Estimation of the $Z \to \nu\nu$ background to New Physics searches in ATLAS

Tanya Sandoval

of

Wolfson College

University of Cambridge

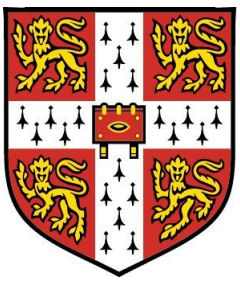

A dissertation submitted to the University of Cambridge
for the degree of Doctor of Philosophy
May 2012

Estimation of the $Z \to \nu\nu$ background to New Physics searches in ATLAS

Tanya Sandoval

Abstract

This thesis describes a series of studies related to searches for new phenomena, beyond the Standard Model of particle physics, in high energy hadron collisions. In such searches, it becomes crucial to identify the Standard Model backgrounds in order to resolve a potential new signal. The thesis presents a method that uses photon events to determine one of such backgrounds, caused by the production of Z boson events. The studies performed to validate the method, both theoretically and experimentally, are presented and the method was shown to be successful as well as to provide reliable results. Theoretically, the method is found to be robust up to a $\sim 10\%$ uncertainty. Experimentally, the method is implemented to estimate the $Z_{\nu\nu}$ + jets background for the SUSY $0\ell + E_{\mathrm{T}}^{\mathrm{miss}}$ + jets search in the ATLAS experiment at the Large Hadron Collider, where this background is one of the most important components for the final sensitivity and is impossible to measure directly. The main experimental results presented are the latest from ATLAS at the time of writing, corresponding to the full dataset of proton-proton collisions delivered by the LHC in 2011 (~ 4.7 fb^{-1}) at $\sqrt{s} = 7$ TeV. Given that this method has been mainstream since 2010, brief comparisons to the results from previous analyses that used smaller datasets with the same $\sqrt{s}$ are also given, as well as additional cross-checks that support the robustness and validity of the method. The results presented here have contributed to the determination of the world's best limits with respect to SUSY models, which currently exclude equal mass squarks and gluinos below 1.4 TeV.

Declaration

This dissertation is the result of my own work and includes nothing which is the outcome of work done in collaboration except where specifically indicated in the text. This dissertation has not been submitted for another qualification to this or any other university and does not exceed the word limit for the respective Degree Committee.

Tanya Sandoval

Acknowledgements

I would like to thank all those who have provided the support and guidance that has enabled me to complete this degree.

In providing the financial support, I would like to thank the Mexican Science and Technology Council (CONACYT) and the University of Cambridge.

Very specially, I would like to thank my supervisors: Andy Parker and Stefan Ask, without whom this thesis would not exist! Andy: thanks for always having faith on me in the first place, supervising me since the start of my PhD and enabling the opportunity to work in the ATLAS experiment and CERN – this has been an incredibly rewarding and memorable experience for me. Stefan: thanks for starting so many different projects with me, and for transmitting your enthusiasm and knowledge of the subject. Stefan started working with me on a project that was his idea, probably without knowing he was going to spend uncountable hours on a project that was my idea – this thesis! How to forget the winter night of 2010 at CERN, when our results were not making sense and yet we stayed trying to make them work, despite the snow storm outside and time – in the end, we didn't get it on that day but rather after a couple of months!

Thanks to James Stirling and Meg Shea for their collaboration to make my first journal publication happen; to TJ Khoo, without whom the best plots and sophistication in this thesis would not have been possible; to Nick Barlow, for teaching me how to fix segmentation faults, make nice plots and helping in my work for the ATLAS Silicon Tracker; to Chris Lester for making me believe in the importance of this project and not give up on it at the times when the results did not make sense; to Gareth Jones, for being always a personal tutor to me since my undergraduate studies at Imperial College. A big thanks also to the entire Cambridge High Energy Physics group and all the people at CERN who worked with me to make this project a reality. To my friends at Wolfson College, Cambridge and CERN, thanks for making my time there so much fun.

Last but not least, I would like to deeply thank my parents Luz Maria and Jose Manuel, and my family and friends in Mexico, for their love and support; for always being there, making me laugh and cheering me up, especially during the most challenging times of my PhD.

Preface

Finding out how our Universe works has never been a bad idea. In fact, it is the quest for a deeper understanding of nature that has given us many of the things we now take for granted in modern life. The LHC, at present the world's most powerful particle collider, has been built for this purpose – to answer some very profound questions about the nature of matter, and it is offering one of the closest possibilities for a ground-breaking discovery, as it has been deliberately designed to journey into uncharted waters, reaching energies in its particle collisions never achieved before in Earthly laboratories. For physicists like me, the main motivation lies in the incompleteness of our current best theory of particle physics: the Standard Model (SM). With its state-of-the-art technology, ATLAS, the world's largest particle detector finally began taking LHC data in 2009 and with it, the searches for New Physics that can either complement or disprove the Standard Model.

In the hype of the searches for new physics at all the LHC experiments, this thesis primarily concerns the presentation of a relatively new and sophisticated method (called here "`ZfromGamma`") to estimate the amount of Z bosons which decay to neutrinos ($Z_{\nu\nu}$) in data. In this case, $Z_{\nu\nu}$ is no longer considered a new process but rather a tarnisher of potential new signals. Moreover, the fact that neutrinos are involved in the final state, makes it one of the most challenging backgrounds to identify and quantify experimentally, for which the searches suffering the most from this background currently rely on its estimate.

While based at CERN, I started this project in 2010 because at the time the SUSY searches had began analysing data and the primary concern then was how to resolve a potential new signal from all the particles we already knew; in other words, how to estimate the SM background. There was of course simulation (MC), but given that data/MC discrepancies had been found in some cases, in particular when modeling multi-jet events, which was one of the SUSY signatures searched for, the ultimate goal was to estimate all the backgrounds from *data* itself. On the other hand, at the time ATLAS as a detector was still being understood and calibrated, so when the first publications for new physics searches took place (between the end of 2010 and beginning of 2011), most based their background prediction on MC. After this however, the "era" of the data-driven methods for background estimation began and nowadays it is considered the default way to quantify a background, while MC is used only as a "cross-check".

During this time, there was also the need to design a method to estimate a particular background which was *unmeasurable* in ATLAS: this was $Z_{\nu\nu}$. Simultaneously, the other multi-purpose experiment at the LHC, CMS had already taken the initiative in designing such method, so this was another motivation for someone in ATLAS to take over this project. The enterprise was challenging: no such studies had been initiated in ATLAS before and so it was basically "starting from zero". Indeed, the challenges became a reality and the project took a good amount of "trial and error" and dedication before it worked and looked the way it is presented in the following chapters – perhaps the thesis as a whole does not necessarily reflect that.

Regarding the thesis structure, Part I starts with Chapter 1 where the presentation of the SM and the possibility for a new Beyond-the-Standard-Model (BSM) theory, called Supersymmetry (SUSY), to solve some of its problems are given. It is then explained why the precise estimation of SM backgrounds are an essential part of the search strategy in all BSM searches like SUSY. In addition, Chapter 2 provides the description of the experimental setup used based on ATLAS and the LHC. Part II starts with Chapter 3, where the motivations for a dedicated $Z_{\nu\nu}$ background study and the need of a method to estimate it are introduced. A method inspired from the possibility of using experimentally easier processes, of similar properties, is proposed, given that one process can be used to estimate the other if their relationship is well-known. Several key advantages and evidence, such as a guaranteed simple relationship with Z bosons, the possibility for large statistics and being data-driven given its clean signature in ATLAS, are given to justify the choice of a photon based sample as the experimentally easier process to estimate the $Z_{\nu\nu}$ background. With this, `ZfromGamma` is formally introduced as as promising method to estimate not just the $Z_{\nu\nu}$ background, but any other Z boson related background, as long as the Z/γ cross-section ratio ($R_{Z/\gamma}$) is well-known. Though in principle, this is enough theoretically, experimentally additional corrections need to be considered, such as photon efficiencies, acceptance and purity. Therefore, the experimental method suggested is based on the idea of a control sample (here referred to as Control Region, CR) and the use of a Transfer Function (TF) to make the Z/γ conversion. Given the knowledge required of $R_{Z/\gamma}$ (not just at parton-level, but also at reconstruction level) for the method to be competitive in experiments, the dedicated theoretical studies performed are presented in Chapter 4 and, despite some variations observed, the overall theoretical uncertainty on $R_{Z/\gamma}$ is determined to be reducible up to 10%. With such positive outcome, the motivation to pursue the method experimentally in ATLAS followed and this work is presented in Chapter 5. The idea was to make `ZfromGamma` as data-driven as possible in order to free the results from as many theoretical uncertainties. The chosen

search to test the method is the SUSY "0ℓ" search, one of the searches with the highest SUSY-reach at the LHC and which relies on the prediction of the $Z_{\nu\nu}$ background, given its major contribution to the selected events where SUSY is searched for. The sections in Chapter 5 are hence dedicated to detailing the experimental framework and event selections implemented to define the photon-based control sample (CR1a), as well the procedures to determine the conversion factor - the Z/γ Transfer Function ($\mathrm{TF}_{Z_{\nu\nu}}$). With the determination of $\mathrm{TF}_{Z_{\nu\nu}}$, the first main cross-check of the results is done by comparing the results directly against simulated $Z_{\nu\nu}$ data and indeed excellent agreement within the estimated uncertainties is found. The final section in this Chapter is then dedicated to showing the relevance of the `ZfromGamma` results to the chosen BSM search and how they were actually used, since a sophisticated procedure, based on a combined fit of all the background estimates, is implemented. In addition, the `ZfromGamma` results are also shown to be consistent with an alternative method based on a $Z_{\ell\ell}$ control sample (CR1b). Given the absence of a potential SUSY signal, the limits set by the 0ℓ analysis are also discussed, as well as the impact of the `ZfromGamma` results on the SUSY mass reach. Lastly, Part III is Chapter 6, which gives the concluding remarks and outlook for both `ZfromGamma` and SUSY, a review of the latest results from CMS at the time of writing and the possible further improvements to the method. For `ZfromGamma`, perhaps the main conclusion is that the method demonstrated to be successful at estimating the $Z_{\nu\nu}$ background to new physics searches in ATLAS since 2010, and despite no signs of SUSY or other BSM physics found so far at the LHC, the searches continue and therefore, this method will remain crucial in determining if there are signs of new physics at all.

The appendices mainly concern the presentation of past results, which were provided to the 0ℓ analysis since 2010. With this, the reader can follow how the method evolved and improved with time, as well as realise the existence of other uses of the method other than for $Z+\text{jets}$ background estimation. The last appendix lists the most common acronyms used throughout the thesis.

Contents

"To my parents Luz Maria and Jose Manuel, and the memory of my brother Jose Manuel Jr. – thank you for everything."

Part I.

Foundation

Chapter 1.

Theoretical Background

The theoretical basis for the research performed in this thesis is the Standard Model – our current best theory of particle physics which has been successful at describing almost all experimental results to date, but that remains incomplete in the sense that several aspects are left unexplained or poorly understood. It is this 'incompleteness' and the possibility to find new physics at the present particle colliders which motivates the research in this thesis.

The aim of this chapter is to summarise the theoretical background required to understand the contents in this thesis. Section 1.1 starts by outlining some key concepts of the Standard Model (SM), followed by a more specific subsection on Quantum Chromodynamics (QCD) applied to hadron colliders. The information for these parts was mainly extracted from references [1–4]. The section finishes by highlighting some of the current problems of the SM, despite its success, in order to motivate the search for new physics. The information for this part was mainly extracted from [5] to quote recent results. Section 1.2 then follows to introduce Supersymmetry (SUSY) - the theory chosen as a promising extension to the SM that could solve some of its problems, potentially at the energies of the Large Hadron Collider (LHC). The section starts by summarising the theoretical aspects of SUSY based on [5, 6], followed by the phenomenological aspects and current search strategy in ATLAS. Throughout this chapter, the reader is assumed to be familiar with some of the concepts and notation used in the references aforementioned.

1.1. Overview of the Standard Model

1.1.1. Key features

Three of the four known fundamental forces in nature – the electromagnetic, weak and strong, which are thought to account for the dynamics of subatomic particles – are described by this *simple* model; *simple* because only a few of these particles appear to be fundamental.

QFT - The model is formulated as a relativistic quantum field theory where particles represent excitations of spacetime fields and forces result from the exchange of the gauge bosons. All the dynamics, particle content and symmetries of the theory are described by a *renormalisable* Lagrangian (see below). The kinetic terms (quadratic in the fields) are associated to the propagators, while the other terms represent interaction vertices (conserved currents). Fermions are represented by spinor fields, gauge bosons by vector fields and the Higgs boson by a scalar field.

Symmetry - The particles and interactions are partly the result of symmetry principles. The symmetries of the theory are realised by transformations which leave the SM *action* invariant, leading to conserved current and charges (Noether's theorem). Invariance under spacetime translations and rotations represent the *global* symmetries of the Poincaré group, leading to conservation of energy-momentum and angular momentum; while invariance under gauge (phase) transformations represent the *local* symmetries of $\mathrm{SU}(3) \times \mathrm{SU}(2)_L \times \mathrm{U}(1)_Y$ – the SM group – leading to other conserved quantities like colour and electric charge. The three sub-groups represent the interactions due to the three fundamental forces: $\mathrm{SU}(2)_L \times \mathrm{U}(1)_Y$ a unified version of the electromagnetic and weak forces, referred to as the electroweak force, and $\mathrm{SU}(3)$ the strong force. The purely electromagnetic interaction (QED) involving only electrically charged particles is represented by the group $\mathrm{U}(1)$, while the purely strong interaction (QCD) involving only quarks and gluons is represented by $\mathrm{SU}(3)$. Each subgroup has an associated coupling strength and gauge field, as represented in Table 1.1, and the particles can be interpreted as the *irreducible representations* (multiplets) of these symmetry groups.

Group	Coupling constant	Gauge field
SU(3)	$g_s = \sqrt{4\pi\alpha_S}$	G^a_μ
U(1)	$e = \sqrt{4\pi\alpha}$	A_μ
$\mathrm{SU}(2)_L$	$g = e/\sin\theta_W$ $\quad \sin^2\theta_W = g'^2/(g^2+g'^2)$	W^a_μ
$\mathrm{U}(1)_Y$	$g' = e/\cos\theta_W$	B_μ

Table 1.1.: *Common notation used for the SM coupling constants and associated gauge fields, where α_S is the strong coupling, α the electromagnetic coupling, θ_W the weak mixing angle and e the electromagnetic charge.*

QED and QCD sectors - Both of these sectors are described by the same lagrangian structure:

$$\mathcal{L} = \bar{\psi}(i\not{D} - m)\psi - \tfrac{1}{4}(F^{(a)}_{\mu\nu})^2 \tag{1.1}$$

where ψ is the fermion (spinor) field, $\not{D}$ the covariant derivative and $F^{(a)}_{\mu\nu}$ the gauge-invariant field strength tensor, defined in terms of the gauge fields in Table 1.1 as in Equations 1.2-1.3. The first term then represents the kinetic and interaction terms of fermions and the second is the gauge boson kinetic term. However, the different properties of the symmetry groups representing QED and QCD, such as dimensions, commutativity, lead to different physics. In QED, the force is mediated by one massless gauge boson - the photon A_μ, while in QCD there are eight - the gluons G^a_μ, where $a = 1, .., 8$. The non-abelian nature of SU(3) is manifested by the additional term in Equation (1.3), allowing for gluon self-interactions.

$$\text{QED:} \qquad F_{\mu\nu} = \partial_\mu A_\nu - \partial_\nu A_\mu \tag{1.2}$$

$$\text{QCD:} \qquad F^a_{\mu\nu} = \partial_\mu G^a_\nu - \partial_\nu G^a_\mu - g_s f_{abc} G^b_\mu G^c_\nu \tag{1.3}$$

The corresponding gauge covariant derivatives are defined as:

$$\text{QED:} \qquad D_\mu = \partial_\mu + ieQA_\mu \tag{1.4}$$

$$\text{QCD:} \qquad D_\mu = \partial_\mu + ig_s T_a G^a_\mu \tag{1.5}$$

where Q is the generator of U(1) (the electromagnetic charge) and T_a are the SU(3) group generators (the colour charge) of a particular representation (quarks are in the *fundamental* representation while gluons are in the *adjoint* representation). QCD is also different from QED in that that the first term of Equation (1.1) requires a

summation over three additional fields, which represents the colours a quark can have, *i.e.* $\psi_a, a = 1, 2, 3$.

Electroweak sector - This sector has some significant differences with respect to the QED/QCD sectors. In terms of field content, an isotriplet of gauge fields W^i_μ $(i = 1, 2, 3)$ couples with strength g to the weak-isospin $\mathrm{SU}(2)_L$ current, while a single gauge field B_μ couples to the weak-hypercharge $\mathrm{U}(1)_Y$ current with strength $g'/2$. T^i and Y are the group generators respectively, such that they relate to the $\mathrm{U}(1)$ generator as $Q = T^3 + Y/2$. The $\mathrm{SU}(2)_L$ current only has left-handed components so it couples to doublets of left-handed fermions, *e.g.* for the ith lepton family, $\psi_{iL} = \binom{\nu_i}{l_i^-}_L$. $\mathrm{SU}(2)_L$ is non-abelian so the corresponding field strength $W^i_{\mu\nu}$ contains additional W^i_μ self-coupling terms, as with the gluons in QCD.

Unlike the purely QED/QCD sectors discussed above, the electroweak sector allows for the Higgs mechanism to yield the masses of the *massive* SM particles, while still preserving gauge invariance and renormalisation. The masses are revealed by *spontaneous symmetry breaking* of the electroweak group $\mathrm{SU}(2)_L \times \mathrm{U}(1)_Y$ when a non-zero vacuum expectation value (vev) of the Higgs field is chosen. Due to this symmetry breaking, the components of the Higgs field are turned into "Goldstone bosons" which are "absorbed" by the other fields in order to acquire mass (or additional degrees of freedom). For the SM, the choice of Higgs field is an isospin $\mathrm{SU}(2)_L$ doublet of complex scalar fields ϕ with hypercharge $Y = 1$, and neutral vev $\phi^0 = \sqrt{\frac{1}{2}}\binom{0}{v}$. This ensures that the photon remains massless and the electroweak bosons become massive. A key feature is that other choices for the representation of the Higgs field lead to different mass relations to those in Equations 1.6-1.8, which do not necessarily fit the experimental results, *e.g.* masslessness of the photon, the W/Z ratio, etc.

The electroweak sector of the SM is summarised by the Lagrangian in Equation (1.9), where L represents a left-handed fermion doublet, and R a right-handed fermion singlet, and G_1 and G_2 the arbitrary fermion-Higgs couplings. After the Higgs mechanism, the gauge boson mass terms, Equations 1.6-1.8, follow from the fourth term in Equation (1.9), the fermion masses from the last term, and a neutral Higgs field $H(x)$ with mass m_H is the only remnant from the Higgs doublet.

$$W^{\pm} = (W^1 \mp iW^2)/\sqrt{2} \quad \longrightarrow \quad M_W = \tfrac{1}{2}vg \tag{1.6}$$

$$A_\mu = \cos\theta_W B_\mu + \sin\theta_W W^3_\mu \quad \longrightarrow \quad M_A = 0 \tag{1.7}$$

$$Z_\mu = -\sin\theta_W B_\mu + \cos\theta_W W^3_\mu \quad \longrightarrow \quad M_Z = \tfrac{1}{2}v\sqrt{g^2 + g'^2} \tag{1.8}$$

$$\mathcal{L} = -\tfrac{1}{4}W^i_{\mu\nu}W_i^{\mu\nu} - \tfrac{1}{4}B_{\mu\nu}B^{\mu\nu} \quad \left\{ \begin{array}{l} W^{\pm},\, Z,\, \gamma \text{ kinetic} \\ \text{terms and} \\ \text{self-interactions} \end{array} \right. \tag{1.9}$$

$$+\bar{L}\gamma^\mu \left(i\partial_\mu - g\tfrac{1}{2}T_i W^i_\mu - g'\tfrac{Y}{2}B_\mu\right) L \quad \left\{ \begin{array}{l} \text{lepton and quark} \\ \text{kinetic terms} \\ \text{and their} \\ \text{interactions with} \\ W^{\pm},\, Z,\, \gamma \end{array} \right.$$

$$+\bar{R}\gamma^\mu \left(i\partial_\mu - g'\tfrac{Y}{2}B_\mu\right) R$$

$$+\left|\left(i\partial_\mu - g\frac{1}{2}T_i W^i_\mu - g'\frac{Y}{2}B_\mu\right)\phi\right|^2 - V(\phi) \quad \left\{ \begin{array}{l} W^{\pm},\, Z,\, \gamma \text{ and Higgs} \\ \text{masses and their} \\ \text{interactions} \end{array} \right.$$

$$-\left(G_1\bar{L}\phi R + G_2\bar{L}\phi_c R + h.c.\right). \quad \left\{ \begin{array}{l} \text{lepton and quark} \\ \text{masses and their} \\ \text{interactions} \\ \text{with Higgs} \end{array} \right.$$

Observables - The main theoretical predictions relevant to particle physics experiments are *decay rates* and *cross sections*, both of which are derived from the transition probability between an initial and final state. For example, the differential cross-section may be written in symbolic form as:

$$\mathrm{d}\sigma = \frac{|\mathcal{M}|^2}{F}\mathrm{dLips} \tag{1.10}$$

where $\mathcal{M}$ is the Lorentz-invariant amplitude or "matrix element" encoding the physics of the process – the type of interaction, particles involved and the mediator

of the interaction (propagators) as found in the SM Lagrangian, As for F, the initial flux, and dLips, the "Lorentz-invariant phase space factor", they merely serve to impose kinematic constraints on the initial and final states respectively. A key feature of the SM theory is however, that $\mathcal{M}$ cannot be solved exactly but rather *approximated* by the technique of *perturbation theory*, whereby a series expansion of $\mathcal{M}$ is done. The leading-order (LO) term in the series represents the largest contribution to the result, whereas the inclusion of higher-order terms are corrections that make the results more accurate.

Renormalisation - As mentioned, the transition amplitude $\mathcal{M}$ is calculated with perturbation theory and the consequence is that the result is only an approximation to the real value. A more accurate result is obtained by including higher-order terms from the perturbation series, which is equivalent to adding more intricate Feynman diagrams as illustrated in Figure 1.1. The problem is that the effect of such corrections can sometimes be significant, *e.g.* the Lamb shift or charge-screening, and their calculation is also technically challenging. Moreover, the value of the loop four-momentum in the Feynman diagrams is unrestricted, so many of these corrections can result in divergent integrals. The idea of *renormalisation* therefore came to "rescue" the SM by proving that such divergences cancel out when the observables are redefined in terms of measured values rather than "bare values". For this, a *scale* μ characteristic of the experiment must be chosen to relate the observable to its bare value. This is equivalent to having a single Feynman diagram with a *running coupling*. Equation (1.11) exemplifies the renormalised/running version of the QED coupling resulting in the charge screening effect – as the energy scale Q^2 increases, so does the coupling. The evolution of the couplings with the energy scale $\beta(\alpha) = \partial\alpha/\partial\ln(\mu)$ is often referred to as the Renormalisation Group Equations (RGEs).

$$\text{QED:} \qquad \alpha(Q^2) = \frac{\alpha(\mu^2)}{1 - \frac{\alpha(\mu^2)}{3\pi}\log\frac{Q^2}{\mu^2}} \tag{1.11}$$

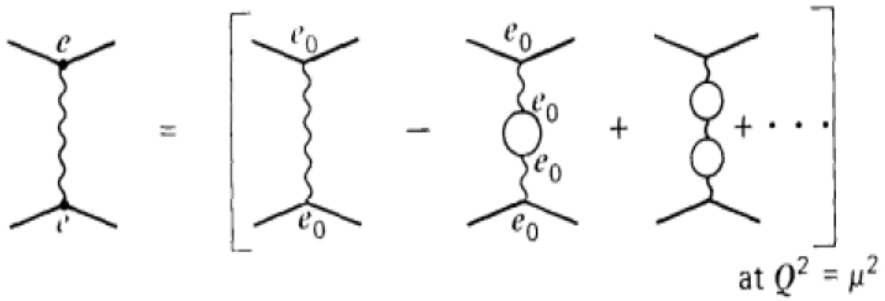

Figure 1.1.: *Pictorial representation of higher-order corrections to the γ propagator when calculating a cross-section. From [1].*

1.1.2. QCD at Hadron Colliders

At the LHC we have proton-proton collisions, *i.e.* mainly strong interactions which determine the final state. Hence, for this thesis, understanding the role of QCD at hadron colliders was crucial. This section summarises some of these concepts.

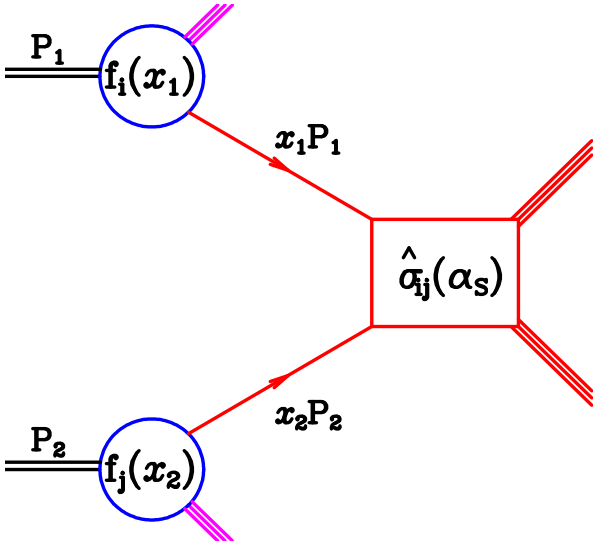

Figure 1.2.: *The parton model description of a hard scattering process. From [3].*

Cross section - Although quarks are always found in confined states (hadrons), at high energies (high-momentum transfer Q^2) a hadron appears as a sea of quasi-free point-like quarks and gluons (partons) and so, the cross section is dominated by the scattering of quasi-free constituent partons – this is the idea behind the *parton model*. Consequently, one requires the knowledge of the partons momentum distribution - the *parton distribution functions* (PDFs). For a hadron-hadron collision, as illustrated in Figure 1.2, if the two incoming hadrons have four-momenta P_1 and P_2, the

cross-section can be written as:

$$\sigma(P_1, P_2) = \sum_{i,j} \int \mathrm{d}x_1 \mathrm{d}x_2 f_i(x_1, \mu^2) f_j(x_2, \mu^2) \hat{\sigma_{ij}}(p_1, p_2, \alpha_s(\mu^2), Q^2/\mu^2) \qquad (1.12)$$

The i and j indices represent the parton types and $p_1 = x_1 P_1$ and $p_2 = x_2 P_2$ the momenta of the partons which participate in the hard-scattering. The PDFs $f_i(x_1, \mu^2)$ represent the probability of finding a parton of type i in the parent hadron, carrying a fraction x_1 of its momentum, defined at a *factorization scale* $\mu \sim Q$. The short-distance (high Q^2) cross section for the process is $\hat{\sigma}_{ij}$ and, since in this regime the strong coupling α_s is small, $\hat{\sigma}_{ij}$ can be calculated using perturbation theory as in QED – as a power series in α_S. The break-down of the perturbative approach is at low Q^2, where α_S is large. Clearly, the effective parton-parton centre-of-mass (c.o.m.) energy $\sqrt{\hat{s}}$ is only a fraction $\sqrt{x_1 x_2}$ of the total c.o.m. energy $\sqrt{s}$ and since the PDFs decrease rapidly with x, probing high $\sqrt{\hat{s}}$ values implies accumulating correspondingly large integrated luminosities.

PDFs - As previously defined, the PDFs are functions of x and Q^2 and are directly related to the *structure functions* $F_i(x, Q^2)$. Being non-perturbative, the structure functions have been extracted from data, an example of which is shown in Figure 1.3(a). In this figure, the parton model prediction of Bjorken scaling ($F_i(x, Q^2) \to F_i(x)$ at high Q^2) is observed, while the scaling violations become evident at low x, where the gluon density and $q\bar{q}$ sea effects become significant. As for the proton PDFs, they have been determined from fits to a large set of experimental data, as shown in Figure 1.3(b), where some features are that quarks carry about 50% of the proton's momentum (gluons carry the rest) and for up and down-type *valence* quarks $u_\mathrm{v} \sim 2d_\mathrm{v}$. Similarly, for $x < 0.2$ gluons dominate. Due to higher-order corrections, the PDFs also have contributions from virtual $q\bar{q}$ produced by the gluon sea. The uncertainties associated to PDFs can have large effects on cross-section calculations at hadron colliders, *e.g.* prior to HERA data, the uncertainty on Higgs production at the LHC was $\sim \pm 25\%$ [7]; which has now been reduced to $\sim \pm 8\%$ [8].

Running coupling - The running of α_s with Q^2 follows from the same argument as in QED (see Section 1.1). However, due to the gluon loops from QCD, its behaviour turns out to be opposite to that in QED. Mathematically, the difference lies in the coefficient of $\log(Q^2/\mu^2)$ in Equation (1.11), which is *positive* for QCD. Therefore in this case $\alpha_s(Q^2)$ decreases with Q^2 as shown in Figure 1.4, so that it is small for short-distance interactions as in the parton model. The phenomenon is known as

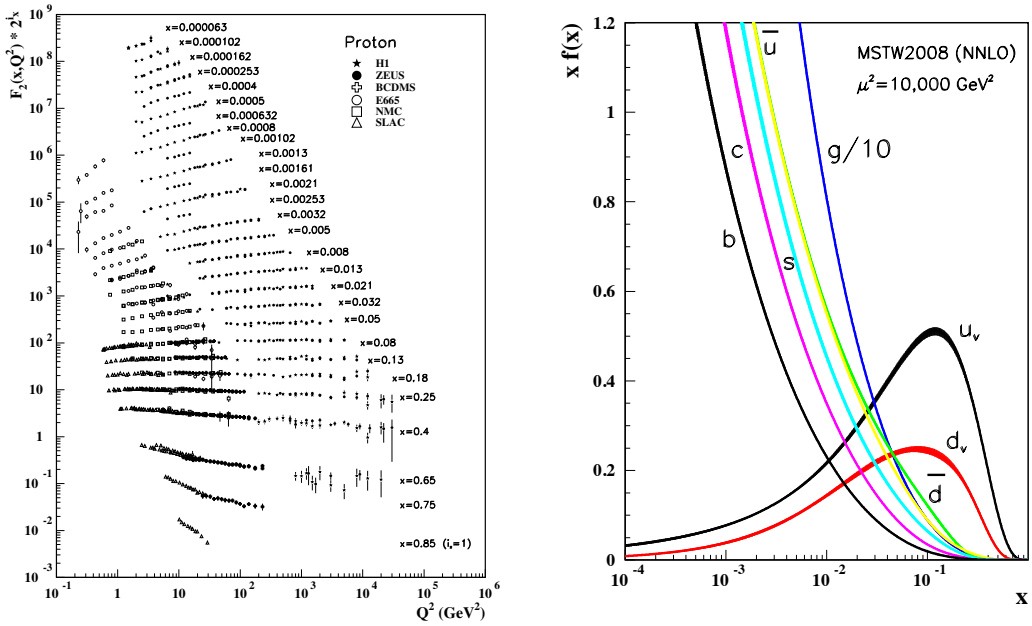

(a) (b)

Figure 1.3.: *(a) The proton structure function F_2^p measured by different experiments. (b) The proton PDFs as determined in the NNLO MSTW2008 global fit (both figures from [5]).*

asymptotic freedom and allows the use of a perturbative approach in this regime. For experiments at the LHC, $\alpha_s \sim 0.1$ and perturbative QCD (pQCD) can be used. A cutoff $Q^2 \sim \Lambda^2$ is normally used to denote the low-energy scale at which partons hadronise (become strongly bound) and such treatment is no longer valid.

Renormalisation and factorisation scales - As previously mentioned (Section 1.1), these scales arise from using a perturbative approach and are defined to play similar roles but at opposite ends of the energy range: through the factorisation scale μ_F, the bare PDFs absorb the long-distance ("infrared", *i.e.* soft and collinear) physics, acquiring a μ_F dependence, whereas through the renormalisation scale μ_R the strong coupling absorbs the short-time ("ultraviolet") physics, acquiring a μ_R dependence. As discussed, the theoretical prediction at fixed-order will have a dependence on these scales, which becomes less important the more higher-order corrections are included.

Confinement and Hadronisation - SU(3) represents the invariance of the strong interaction under unitary transformations in colour space. A consequence of this group structure is *colour confinement* - quarks and gluons are *confined* to bound states of

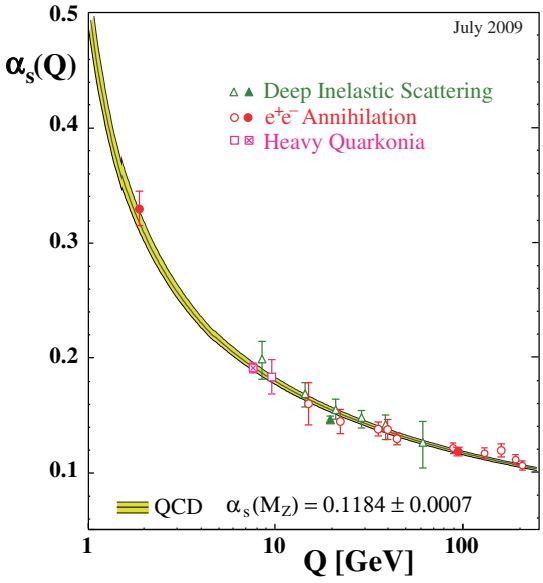

Figure 1.4.: *The 'running' of α_s with the energy scale Q, as measured by different processes. From [5].*

colourless hadrons, so they are never observed as free particles. The hadron picture becomes relevant in the low-energy regime, for which there is little theoretical understanding as it is non-perturbative (although theoretical advances in this area have become available with time, like *lattice* QCD). The *Lund string model* and the *cluster model* are commonly used to explain hadronisation. The general idea is illustrated in Figure 1.5: after scattering, initially the quarks separate at high velocity, but then a colour flux tube forms between them. The energy stored in the flux tube is sufficient to produce $q\bar{q}$ pairs and soft radiation (parton showering). This process continues until quarks are bound into colourless hadrons, generally observed as jets in hadron colliders. The non-perturbative part in this process can be factorised out via the *fragmentation functions* - the final-state analogue of PDFs used for initial-state hadrons.

Underlying Event - Due to the composite structure of hadrons, the underlying event (UE) refers to the processes taking place in a hadron collision in addition to the primary hard-scattering - the hadron can be viewed as bunches of incoming partons as depicted in Figure 1.6. The UE includes initial (ISR) and final state radiation (FSR), multiple interactions (scattering between other parton pairs from the same hadron pair), beam remnants (a fragment of the hadron not taking part in the ISR or hard-scattering) and pileup (when more than one hadron in the beam interacts

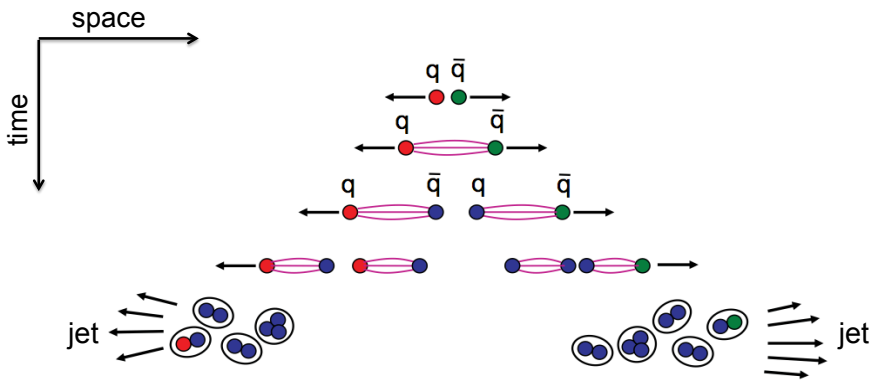

Figure 1.5.: *Schematic representation of parton showering and hadronisation in the Lund string model.*

in a given bunch crossing). Some of these can be modeled with pQCD. Depending on the analysis, UE contributions can sometimes be significant [9].

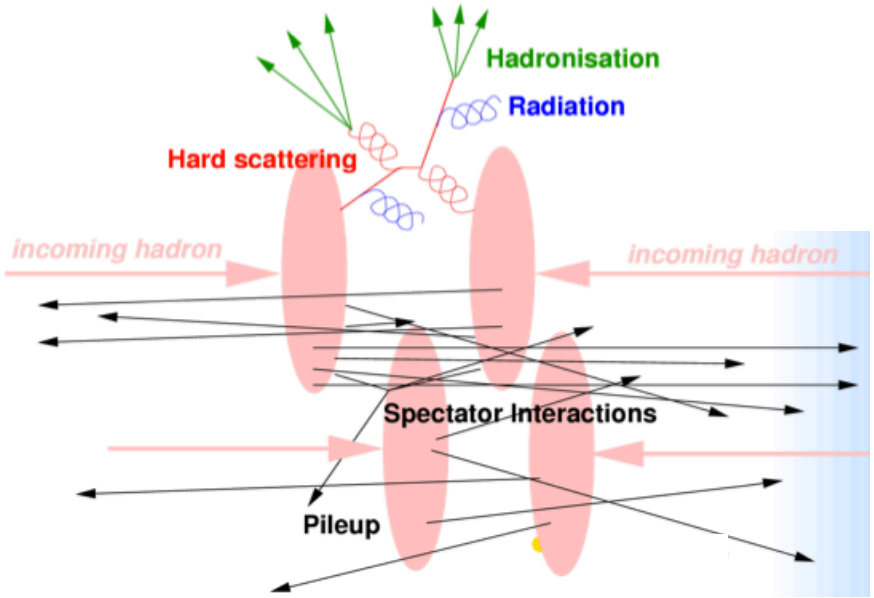

Figure 1.6.: *Pictorial representation of the underlying event in a hadron-hadron collision. Each hadron can be pictured as a 'beam' of partons, which is why other interactions occurs apart from the hard-scattering like ISR/FSR. In addition, other hadrons from the beam can collide in the same bunch-crossing causing 'pileup'.*

1.1.3. Problems of the Standard Model

The scientific community's confidence in the SM theory today is the result of the progressive confirmation by experiment of many of its predictions. Some of these tests have been precise enough to validate even radiative corrections - the value of the QED coupling has been tested to 0.37 ppb from the $e^{\pm}$ magnetic moment [10], the Z boson mass to 23 ppm from $e^+e^- \to$ hadrons [11] and Fermi's constant to 8.6 ppm from the muon lifetime [12]. Similarly the agreement of numerous QCD and electroweak predictions with data has been remarkable, as exemplified for hadron collider physics in Figure 1.7. However, there are still many aspects of the model which are poorly understood, most likely indicating the presence of *new physics*. Recalling Fermi's theory of beta decay (1933) which treated the interaction as pointlike and yet had great phenomenological success, the SM can similarly be regarded as an *effective field theory* at the energies probed so far. This section lists some of the aspects for which the model has little or no coverage at all.

Free parameters - The predictive power of the SM appears to depend on the input of 19 fundamental parameters, listed in Table 1.2, and whose values need to be well-measured. Some of them have large theory uncertainties (*e.g.* no radiative corrections available) or are experimentally limited by precision or at most constrained from data. Moreover, many depend on the input values of other free parameters, leading to differences and correlations in global fits. To avoid such problems, it would be desirable to have a model involving fewer fundamental parameters, from which the others could be derived.

The SM free parameters	
3	gauge couplings g_s, g, g'
9	fermion masses
3	fermion CKM mixing angles
1	CKM phase
2	Higgs vev and quartic coupling v, λ
1	QCD CP-violating parameter θ

Table 1.2.: *The SM 19 fundamental parameters whose values are chosen to fit the data. Measurements exist for the couplings, fermion masses and V_{ij} [5], but only limits for v, λ and θ. The latter is constrained by measurements of the neutron electric dipole moment [14].*

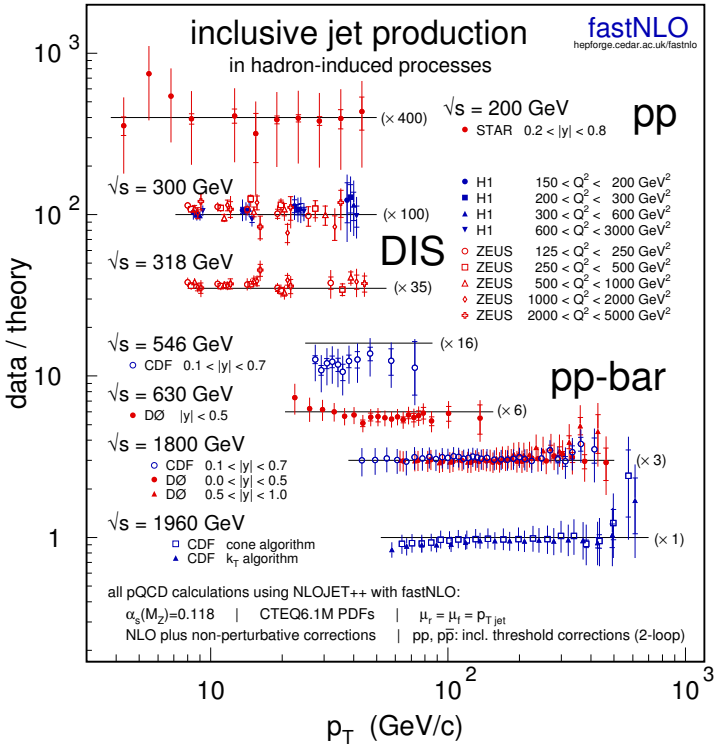

(a)

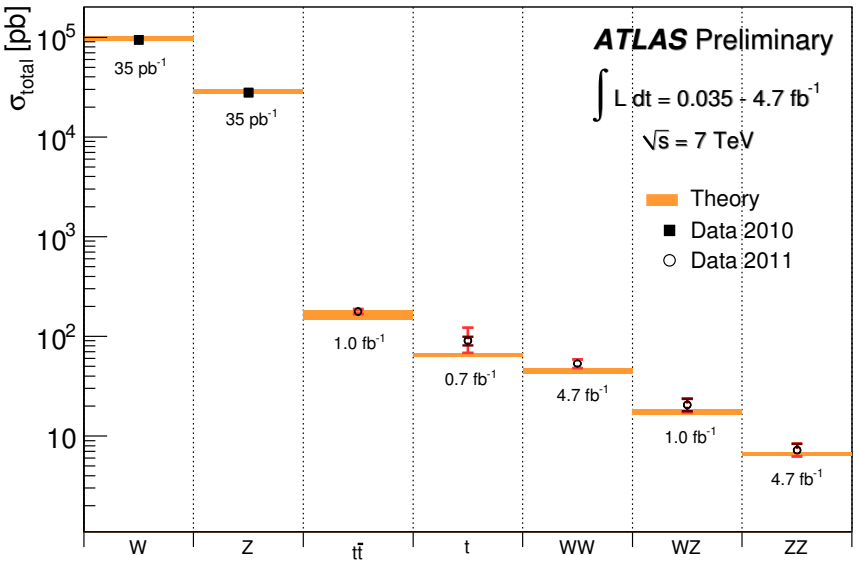

(b)

Figure 1.7.: *(a) A compilation of QCD data-over-theory ratios for inclusive jet cross sections measured in different hadron-induced processes at different center-of-mass energies (from [5]). (b) Summary of several Standard Model measurements in ATLAS compared to the theoretical expectations (from [13]). All theoretical expectations are calculated at NLO or higher.*

Neutrino oscillations - There is now convincing experimental evidence for neutrino masses ($m \lesssim 2$ eV [5]) and yet neutrinos are assumed massless in the SM. Moreover, with 3 light Majorana neutrinos, there would be 9 additional free parameters from their masses, mixing angles and phases.

Precision tests deviations - Some measurements show relatively large discrepancies from the SM prediction, like the measurement of the anomalous magnetic moment of the muon by 2.5σ [5].

Exclusion of gravity - Being a fundamental interaction, it seems unnatural that it is excluded from a framework which describes the other interactions.

Choice of gauge group - The choice $\mathrm{SU}(3) \times \mathrm{SU}(2)_L \times \mathrm{U}(1)_Y$ is rather arbitrary and perhaps a different group structure could explain better the new physics or the poorly understood sectors. A famous example is the Georgi-Glashow model (1974) [15] with $\mathrm{SU}(5) \supset \mathrm{SU}(3) \times \mathrm{SU}(2) \times \mathrm{U}(1)$ allowing for lepton/baryon number violation like proton decay. Although the latter has tight limits set by experiments [16], the model sheds light on gauge coupling unification, as well as charge quantisation.

Origin of mass - The model assumes this is due to the Higgs mechanism but as of the time of writing, only limits have been set on the existence of the Higgs boson. Some recent ATLAS studies exclude at 95% CL the mass ranges 112.9-115.5 GeV, 131-238 GeV and 251-466 GeV, while the range 124-519 GeV is expected to be excluded in the absence of signal [17].

Matter-Antimatter asymmetry - The amount of CP-violation in the SM cannot account for the large imbalance observed in the universe, *e.g.* the baryon-to-photon ratio is too big ($\eta \sim 10^{-10}$ [5]). Similarly, the latest constraints on the QCD "θ parameter" ($|\theta| < 10^{-10}$ [5, 14]) yield no significant CP-violation in QCD ("strong CP problem").

Naturalness/Hierarchy problem - Even assuming the existence of the Higgs boson, unless there is an "unnatural" fine-tuning cancellation of its radiative corrections, the Higgs mass value diverges (more details in Section 1.2.1).

Dark matter and dark energy - Plenty of cosmological evidence, like recent CMB results, yield a small baryon density in the universe ($\Omega_\mathrm{b} = 0.0227 \pm 0.0006$ [18]) but still much larger than the density of *luminous* matter. This indicates most baryons are optically *dark*. Moreover, the total matter density ($\Omega_\mathrm{m} = 0.133 \pm 0.006$) suggests that most matter in the universe ($\sim 83\%$) takes a cold, weakly-interacting, non-baryonic form, referred to as *cold dark matter* Ω_cdm, so that $\Omega_\mathrm{m} = \Omega_\mathrm{cdm} + \Omega_\mathrm{b}$. In

addition, dark energy is needed to explain both the flatness of the universe and the observed accelerated expansion. Overall, with respect to the total mass-energy density, dark-matter constitutes $\sim 23\%$ and dark-energy $\sim 72\%$ [18]. These huge proportions of the universe are clearly not covered by the SM.

1.2. Overview of Supersymmetry

This section aims to provide a summary of Supersymmetry (SUSY) to cover some basic concepts and ideas relevant to the work presented in this thesis, and particularly relevant to Section 5.6. The summary is given in three parts: Section 1.2.1 presents the motivation for the theory; Section 1.2.2 introduces the MSSM, being the simplest and most widely-studied SUSY model; and Section 1.2.3 discusses the phenomenology expected at hadron colliders, in particular at the LHC, as well as the most popular types of SUSY searches performed in ATLAS. The content and notation used in Sections 1.2.1-1.2.2 are mainly based on references [5, 6, 19].

1.2.1. Motivation

The current problems of the SM discussed in Section 1.1.3 made clear that there is a need of an extension or theory which can solve at least one of these problems - this is the motivation behind BSM theories like Supersymmetry (SUSY). SUSY is a very popular BSM theory because: (i) it can potentially solve more than one of these problems, (ii) the first signs of it are expected at the energies of current particle colliders, and (iii) its beautiful mathematical structure respects the fundamental principles of the SM, like gauge invariance and symmetry. Although other BSM theories exist, few of them are as appealing as SUSY.

Initiated around the 1970's, SUSY was postulated as the only possible extension of the spacetime symmetries in the SM by transforming fermions into bosons and vice versa [20, 21]. However, if this symmetry was exact, each SM particle would have a superpartner with the same quantum numbers and mass, only differing by half a unit of spin. Because no such particles have been observed so far, if it exists, SUSY must be a *broken* symmetry. SUSY has the nice property of offering solutions to the following major SM problems, if it shows up at the TeV scale:

Naturalness/Hierarchy problem - As discussed in Section 1.1.3, the large hierarchy of energy scales between the electroweak and Planck scale seems unnatural. Rather, new physics is expected to appear just after the electroweak scale where the SM becomes ill-defined, *e.g.* when the Higgs mass gets unacceptably large loop corrections. With SUSY representing the new physics, the UV corrections are cancelled by the superpartners equivalents, as illustrated in Figure 1.8(a). For the remaining corrections to be acceptable, the superpartners masses must be around the TeV scale.

Gauge coupling unification - The evolution of the three SM couplings is determined by the particle content . Currently these couplings do not meet at a common energy scale, but this would be theoretically appealing as it could involve a single unified gauge group rather than the current SM product group. With the addition of SUSY at the electroweak scale, convergence of the couplings (potentially including that of gravity) is projected at some high-energy scale, *e.g.* 10^{16} GeV [6], Figure 1.8(b).

Dark matter - This problem was already discussed in Section 1.1.3. With SUSY, many models, *e.g.* with R-parity conserved (Section 1.2.2) predict the existence of a stable weakly interacting massive particle (WIMP), which could make up for the observed dark matter or at least some of it.

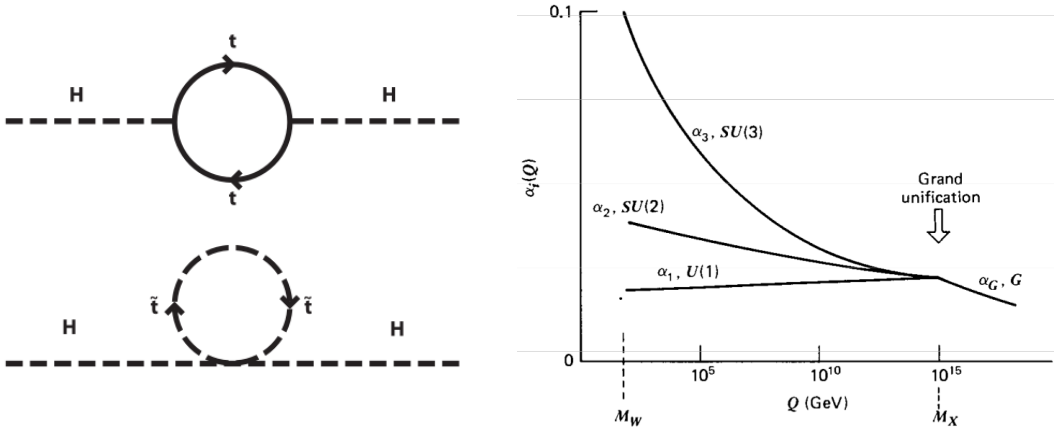

(a) (b)

Figure 1.8.: *(a) Cancellation of the largest corrections to the Higgs boson mass from the top quark loop via its scalar superpartner loop. The remaining contributions are logarithmic. (b) Expected unification of gauge couplings at high-energies with SUSY, from [1].*

1.2.2. The MSSM

The Minimal Supersymmetric extension of the SM (MSSM) consists of the addition of one SUSY partner for every SM particle and an enlarged Higgs sector. The superpartners fields are paired with the SM fields via *superfields*, as shown in Table 1.3. Two Higgs doublets, with vev's v_u and v_d, are required (to cancel gauge anomalies introduced by the higgsinos and to give masses to the up-type and down-type quarks separately). The *unbroken* MSSM Lagrangian is like the SM Lagrangian but with the addition of a *superpotential* – a function of superfields, where the μ parameter is introduced as the mass parameter of the Higgs sector. As in the SM, all the terms in the MSSM Lagrangian must be renormalisable and satisfy the SM $\mathrm{SU}(3) \times \mathrm{SU}(2)_L \times \mathrm{U}(1)_Y$ gauge invariance, as well as the experimentally-observed B-L conservation (B =baryon number, L =lepton number). For the SUSY-breaking part, all allowed *soft* terms, *i.e.* those which do not introduce quadratic divergences, are added by hand (see below). To generate nonzero neutrino masses, additional structure is needed, as discussed in [5].

Field Content of the MSSM						
Superfields		Bosons	Fermions	SU(3)	$\mathrm{SU}(2)_L$	$\mathrm{U}(1)_Y$
Gauge						
gluon/gluino	$\hat{G}$	g	$\tilde{g}$	8	1	0
gauge/gaugino	$\hat{V}$	$W^{\pm}$, W^0	$\tilde{W}^{\pm}$, $\tilde{W}^0$	1	3	0
	$\hat{V}'$	B	$\tilde{B}$	1	1	0
Matter						
slepton/lepton	$\hat{L}$	$\tilde{L} = (\tilde{\nu}, \tilde{e}^-)_L$	$(\nu, e^-)_L$	1	2	-1
	$\hat{E}^c$	$\tilde{E} = \tilde{e}^+_R$	$\tilde{e}^c_L$	1	1	-2
squark/quark	$\hat{Q}$	$\tilde{Q} = (\tilde{u}_L, \tilde{d}_L)$	$(u, d)_L$	3	2	1/3
	$\hat{U}^c$	$\tilde{U}^c = \tilde{u}^*_R$	u^c_L	3	1	4/3
	$\hat{D}^c$	$\tilde{D}^c = \tilde{d}^*_R$	d^c_L	3	1	-2/3
higgs/higgsino	$\hat{H}_d$	H^i_d	$(\tilde{H}^0_d, \tilde{H}^-_d)_L$	1	2	-1
	$\hat{H}_u$	H^i_u	$(\tilde{H}^+_u, \tilde{H}^0_u)_L$	1	2	1

Table 1.3.: *The field content of the MSSM and their $SU(3) \times SU(2)_L \times U(1)_Y$ quantum numbers (only one generation of quarks and leptons is shown). The superfield notation is also shown. For each lepton, quark and Higgs super-multiplet, there is a corresponding antiparticle multiplet of charge-conjugated fermions and their associated scalar partners (also not shown).*

R-parity and LSP: A consequence of imposing B-L conservation in the MSSM is R-parity conservation (RPC). Since R-parity is defined as $R = (-1)^{3(B-L)+2S}$ for a

particle of spin S, R-parity differentiates SM from SUSY particles (the first have $R = 1$ whereas the second have $R = -1$). Hence, with RPC, sparticles could be produced from SM interactions in pairs, *e.g.* $pp \to \tilde{g}\tilde{g}$. The sparticles would then decay (possibly via a cascade) into a SM particle plus another lighter sparticle, *e.g.* $\tilde{g} \to \bar{q}\tilde{q}$. Being stable, the lightest SUSY particle (LSP) would be produced at the end of the decay chain, *e.g.* $\tilde{q} \to q\tilde{\chi}_1^0$. Given cosmological and experimental constraints (see Section 1.1.3), the LSP must also be weakly-interacting.

Symmetry breaking: This is one of the least understood sectors of the theory and hence the one generating the largest number of extra parameters (~ 100 [5]). Unlike the Higgs mechanism in the SM, in SUSY the breaking terms $\mathcal{L}_{soft}$ are explicitly added to the Lagrangian. They consist of the following: (i) trilinear scalar interactions $\frac{1}{3!}\tilde{A}_{ijk}\phi_i\phi_j\phi_k +$ h.c.; (ii) bilinear scalar interactions $\frac{1}{2}\tilde{b}_{ij}\phi_i\phi_j +$ h.c.; (iii) scalar mass-squares $m_{ij}^2\phi_i^\dagger\phi_j$ and (iv) gaugino masses $\frac{1}{2}M_a\lambda^a\lambda^a +$ h.c. They are referred to as "soft" terms because the breaking scale is related to the electroweak symmetry breaking scale in order to guarantee a solution to the hierarchy problem. Two sectors are defined: the visible (MSSM particles) and the hidden (new particles decoupled from the visible sector). Messenger particles mediate these two sectors and transmit to the visible sector the SUSY-breaking originated in the hidden sector. The most popular models of soft SUSY-breaking are:

- **Gravity-mediated:** these are the most widely-studied models. The messenger is Planck scale physics but there is no role for the gravitino $\tilde{G}$ in the phenomenology unless it is the LSP. A constrained-model example is mSUGRA (see "Phenomenological Models" below).
- **Gauge-mediated:** the messengers have $\mathrm{SU}(3)\times\mathrm{SU}(2)_L\times\mathrm{U}(1)_Y$ quantum numbers and SUSY breaking is transmitted via the SM gauge interactions; often $\tilde{G}$ is the LSP. A constrained-model example is GMSB (see "Phenomenological Models" below).

Other mechanism also explored, although less than the previous two, is:

- **Extra Dimensions:** visible and hidden sectors are on two separate branes and messengers live on the "bulk".

Physical states: Analogous to the SM, after electroweak (EW) symmetry is broken, the MSSM fields mix to form the physical mass states listed in Table 1.4. In practice (due to phenomenological constraints from FCNCs), the mixing of the lighter two sfermion generations is neglected and taken to be "mass-degenerate". In contrast, due to the large mass of the SM third-generation, a significant L-R mixing can take place for third

generation squarks, allowing them to be distinguishable from the other generations and much lighter – analogous to the *seesaw mechanism* in neutrinos. A typical SUSY mass spectrum is illustrated in Figure 1.9. As for the Higgs sector, using two Higgs doublets results in 5 physical (spin-0) Higgs bosons: two charged $\tilde{H^{\pm}}$, two neutral CP-even h^0 and H^0 ($m_h < m_H$), and one neutral CP-odd A^0. Their masses depend only on $\tan\beta = v_u/v_d$ and one of the Higgs masses (typically m_A).

$\tilde{B}^0$, $\tilde{W}^0$, $\tilde{H}_u^0$, $\tilde{H}_d^0$	$\rightarrow$	neutralinos:	$\tilde{\chi}_1^0$, $\tilde{\chi}_2^0$, $\tilde{\chi}_3^0$, $\tilde{\chi}_4^0$
$\tilde{W^{\pm}}$, $\tilde{H}_u^+$, $\tilde{H}_d^-$	$\rightarrow$	charginos:	$\tilde{\chi}_1^{\pm}$, $\tilde{\chi}_2^{\pm}$
$\tilde{\tau}_{\mathrm{L}}$, $\tilde{\tau}_{\mathrm{R}}$	$\rightarrow$	stau:	$\tilde{\tau}_1$, $\tilde{\tau}_2$
$(\tilde{t}_{\mathrm{L}}, \tilde{t}_{\mathrm{R}}), (\tilde{b}_{\mathrm{L}}, \tilde{b}_{\mathrm{R}})$	$\rightarrow$	stop, sbottom:	$(\tilde{t}_1, \tilde{t}_2), (\tilde{b}_1, \tilde{b}_2)$

Table 1.4.: *Mixing in the MSSM. Line combinations of neutral gauginos and higgsinos form neutralinos, whereas the charginos result from charged gauginos and higgsinos.*

Phenomenological Models

The MSSM introduces 124 parameters of which only 18 are purely SM [5]. Fortunately, it is possible to make useful predictions at low-energies (electroweak scale) by constraining this parameter space from the *direct* and *indirect* experimental results to date, as well as other simplifying assumptions. *Indirect* constraints come from the relic dark-matter density and precision electroweak data. These restrict the nature of the LSP and suppress lepton number violation, FCNCs and additional sources of CP-violation. *Direct* constraints have been obtained from direct SUSY searches, *e.g.* at LEP, the Tevatron and LHC. As for the additional simplifying assumptions, the following are typically the approaches taken:

Constrained Models: In these, a particular SUSY-breaking mechanism and unification at the GUT scale are assumed, *e.g.* the *top-down* approach assumes a unified gaugino mass at high-energies so that the low-energy masses are related, *e.g.* $M_3 \sim 3.5M_2$, $M_1 \sim 0.5M_2$ [5]. Within these type of models, the most popular are:

- **mSUGRA:** the scalars, gauginos and A-term masses (m_0, $m_{1/2}$, A_0 respectively) unify at the GUT scale. With this, the number of parameters dramatically reduces to 5 (plus the 18 from the SM):

$$m_0,\ A_0,\ m_{1/2},\ \tan\beta,\ \mathrm{sign}(\mu)$$

The RGEs are then used to predict values of the parameters at the electroweak scale, *e.g.* first two squark generations are roughly degenerate while the third is lighter; sleptons are lighter than squarks and the LSP is the lightest neutralino $\tilde{\chi}_1^0$, as shown in Figure 1.9. Although perhaps too simplistic, this model is one of the most widely used at present colliders to set exclusion limits on SUSY (*e.g.* see Section 5.6.3).

- **GMSB:** an effective mass scale $\Lambda \sim 100$ TeV determines the low-energy scalar and gaugino masses through loop effects. A light gravitino is the LSP but the NLSP is really what determines the phenomenology, *e.g.* typically the NLSP is lightest neutralino or stau, which then decays into its superpartner plus gravitino $\tilde{\chi}_1^0 \to \gamma/Z + \tilde{G}$ or $\tilde{\tau}_{\mathrm{R}}^{\pm} \to \tau^{\pm}\tilde{G}$. Different choices of NLSP lead to a variety of final states, *e.g.* a long-lived $\tilde{\chi}_1^0$ decaying outside detector leads to $E_{\mathrm{T}}^{\mathrm{miss}} + \text{leptons} + \text{jets}$, whereas $\tilde{\chi}_1^0 \to \gamma\tilde{G}$ occurring inside detector leads to final states of $E_{\mathrm{T}}^{\mathrm{miss}} + \gamma$. The number of SUSY parameters in this model is six:

$$F_m,\ M_m,\ N_5,\ C_{grav},\ \tan\beta,\ \mathrm{sign}(\mu)$$

  where F_m is the SUSY-breaking scale, M_m the messenger scale, N_5 the number of messenger fields and C_{grav} the couplings for decays into $\tilde{G}$.

- **AMSB:** this is a special type of extra-dimensions gravity-mediated model where the SUSY-breaking is communicated through the *conformal anomaly* [22]. Typically the LSP is a wino $\tilde{W}^0$ and charginos behave like a stable massive particles.

Simplified ("Toy") Models: These models take a different approach to constrained models by focusing on a subsector of the SUSY spectrum. In this case, the simplifying assumptions are on the masses, hierarchies and decay-chains of particles.

RPV: Models with R-parity violation (RPV) exist but since they allow an unacceptably fast proton decay [16] and do not provide a dark matter candidate, RPC models have been more favoured. R-parity violating scenarios also have the disadvantage of introducing more parameters than in RPC scenarios since B-L violation is allowed. Yet, they successfully incorporate neutrino masses and escape many bounds set by the RPC-based searches, which is why these models are still studied. The RPV terms in the Lagrangian allow the LSP and other sparticles to decay to SM ones. However, phenomenological constraints derived from data have been used to set severe limits on the couplings of these terms.

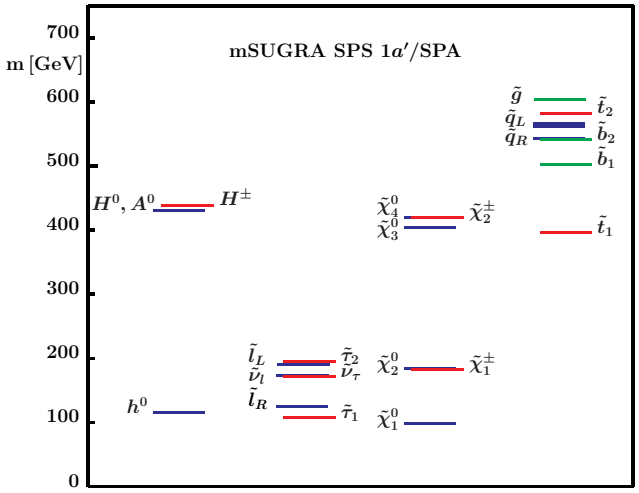

Figure 1.9.: *Mass spectrum of a reference point in mSUGRA, (SPS 1a'). The masses of the first two generations are denoted collectively as* $\tilde{q}$, $\tilde{\ell}$ *and* $\tilde{\nu}_l$ *from [1].*

Problems of the MSSM

Paradoxically, although this is the most accepted model in SUSY, the MSSM has its own problems: the 'μ-problem', similar to the SM hierarchy problem already discussed, requires μ to be of the order of the electroweak scale, which is known to be much smaller than the Planck scale. Moreover, as will be discussed in Chapter 6, the present experimental limits on SUSY are now strong enough to re-evaluate whether SUSY can still address the fine-tuning issue with respect to the Higgs mass or the relic density from cold dark matter. This part will be discussed further in the closing chapter.

1.2.3. Searches at the LHC

Phenomenology

Because of the higher c.o.m. energy, the SUSY mass reach at the LHC will largely exceed that from LEP and the Tevatron. In pp collisions, coloured sparticles, namely squarks and gluinos, are expected to be the most copiously produced, as suggested by Figure 1.10. The diverse MSSM phenomenology which motivates the different SUSY searches at the LHC is exemplified in Figure 1.11. RPC scenarios are characterised by sparticle pair-production (with the dominant hard-process depending on the mass-hierarchy assumed, as shown in Table 1.5) and missing energy from the LSP which is stable and weakly-interacting. In addition, with RPC, the breaking mechanism determines the nature of the LSP/NLSP, which in turn determines the final state. In the RPV scenario, the final state is determined by whether the sparticles are long- or short-lived. Unlike in e^+e^- colliders, in hadron colliders the c.o.m. energy of the colliding partons $\sqrt{\hat{s}}$ is not known but rather its probability density as determined from PDFs (see Section 1.1.2). Since most of the beam remnants escape undetected in the beam pipe, only conservation of momentum in the plane transverse to the beam direction can be used to infer this imbalance – hence the definition of missing transverse energy $E_{\mathrm{T}}^{\mathrm{miss}}$. The key point is that the RPC final-state signature is $E_{\mathrm{T}}^{\mathrm{miss}} + X$, where X depends on more specific model details like the breaking mechanism and the nature of LSP/NLSP.

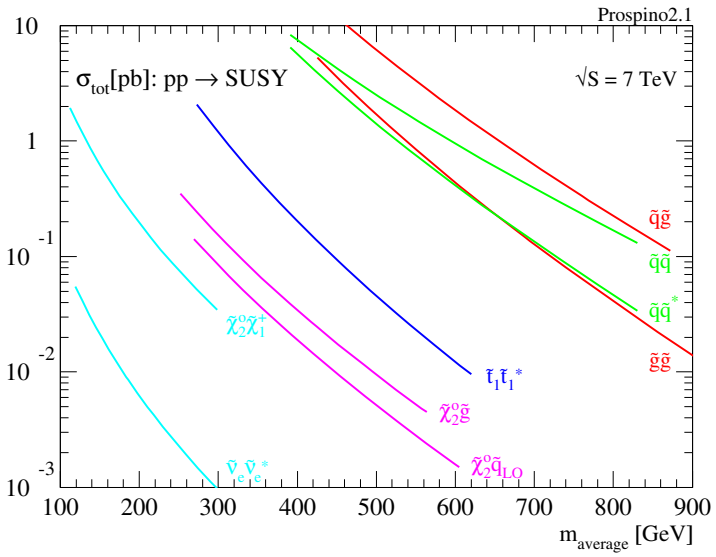

Figure 1.10.: *Total cross-section (in picobarns) for sparticle production as a function of mass, representative of the LHC. Clearly the cross-section is highest for light squarks and gluinos. From [23].*

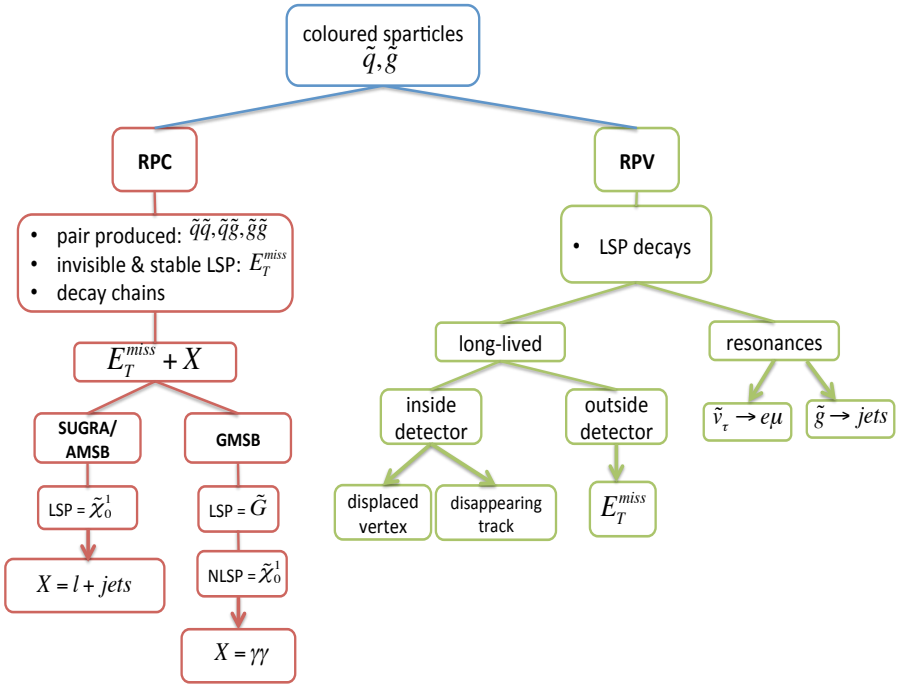

Figure 1.11.: *Schematic chart illustrating the diverse SUSY (MSSM) phenomenology expected at the LHC which motivates the search for different final-state signatures.*

Mass hierarchy	Dominant process	canonical SUSY	
		Typical decays	Final-state signature
$m_{\tilde{q}} \ll m_{\tilde{g}}$	$pp \to \tilde{q}\bar{\tilde{q}}$	$\tilde{q} \to q\tilde{\chi}_1^0$	$E_{\mathrm{T}}^{\mathrm{miss}} + 2\mathrm{j}$
$m_{\tilde{q}} \approx m_{\tilde{g}}$	$pp \to \tilde{q}\tilde{g}$	$\tilde{q} \to q\tilde{\chi}_1^0$ $\tilde{g} \to \bar{q}\tilde{q}/q\bar{\tilde{q}} \to \bar{q}q\tilde{\chi}_1^0$	$E_{\mathrm{T}}^{\mathrm{miss}} + 3\mathrm{j}$
$m_{\tilde{q}} \gg m_{\tilde{g}}$	$pp \to \tilde{g}\tilde{g}$	$\tilde{g} \to \bar{q}\tilde{q}/q\bar{\tilde{q}} \to \bar{q}q\tilde{\chi}_1^0$	$E_{\mathrm{T}}^{\mathrm{miss}} + 4\mathrm{j}$

Table 1.5.: *Squark and gluino pair-production is expected to dominate SUSY processes at the LHC (see Figure 1.10) and the dominant hard-process depends on the mass-hierarchy assumed. In the canonical scenario, their typical decays lead to signatures of $E_{\mathrm{T}}^{\mathrm{miss}}$ from neutralinos and a number of high-p_{T} jets from the daughter quarks after hadronisation, although soft jets from ISR and FSR may increase the jet multiplicities.*

In the popular "canonical scenario" (RPC, mSUGRA-breaking with $\tilde{\chi}_1^0$ as LSP), assumed in Table 1.5, the following applies:

- **Neutralinos:** Being non-coloured, their direct production at the LHC is suppressed. There are four of them, all electrically-neutral. They are Majorana (their own antiparticles) and appear in the cascade decays of heavier sparticles. As mentioned, the lightest is the LSP (the source of $E_{\mathrm{T}}^{\mathrm{miss}}$), produced at the end of the decay-chain.

The heavier neutralinos typically decay to lighter neutralinos via on-shell Z or charginos via on-shell $W^{\pm}$. The subsequent decay of Z and $W^{\pm}$ can result in final-states involving leptons and neutrinos.

- **Charginos:** There are two types, each of which can be positively- or negatively-charged. The heavier one can decay to the lighter one via an on-shell Z. Both can decay to neutralinos via an on-shell $W^{\pm}$. Again, the subsequent decay of Z and $W^{\pm}$ can result in final-states involving leptons and neutrinos, as shown in Table 1.6.
- **Squarks:** They decay to their SM partners (quarks) plus charginos or neutralinos. Each daughter quark undergoes hadronisation and is seen in its final-state as a high-p_{T} jet, as shown in Table 1.5, although additional (softer) jets from ISR and FSR may increase the jet multiplicities (see Section 1.1.2).
- **Gluinos:** Having only colour-charge, they can only decay to quarks plus squarks. Since they are also Majorana, they decay to $\bar{q}\tilde{q}$ or $q\bar{\tilde{q}}$ with equal probability. Their final-states hence relate to those from squarks described above.
- **Sleptons:** If light enough, they are more likely to be produced in the decays of charginos ($\rightarrow \tilde{\ell}^{\pm}\nu$) and neutralinos ($\rightarrow \tilde{\ell}^{+}\tilde{\ell}^{-}$).

Search Strategy

As this thesis is based on data from the ATLAS experiment at the LHC, the rest of this section is specific to ATLAS, although for CMS –the other multi-purpose experiment at the LHC– the results and strategies are very similar. This section also focuses on the RPC-based searches (often referred to here also as "$E_{\mathrm{T}}^{\mathrm{miss}} + X$"), as these are the types of searches in which this thesis specialises. The strategy described however, also applies to other BSM searches.

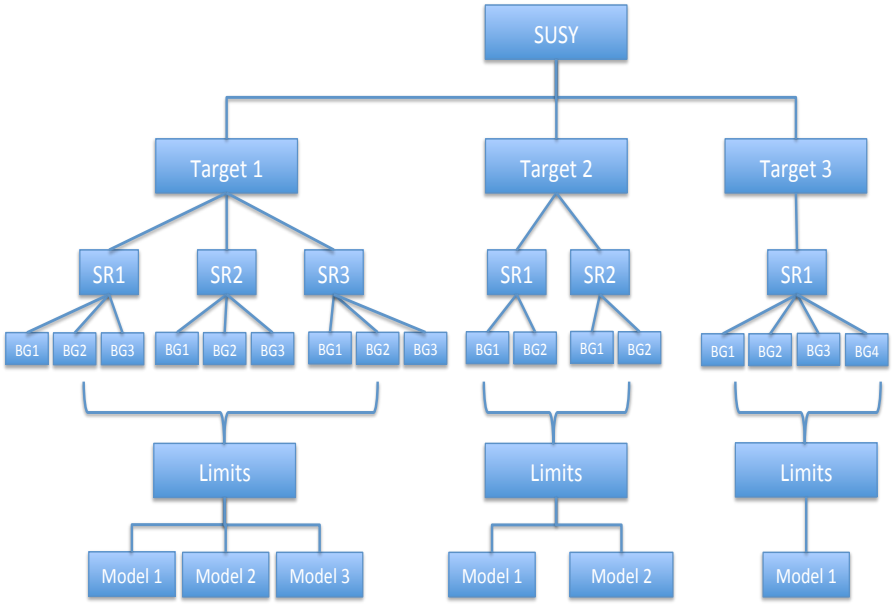

Figure 1.12.: *Schematic chart illustrating the general search strategy used when looking for BSM signals like SUSY. First, the search is split into different final-state targets. For each of the targets, a number of Signal Regions (SRs) are defined, and for each of these, the different SM backgrounds (BGs) are estimated. If no excess is found above the SM expectation in the SR, the information from all SRs is combined to set the best limits on different SUSY models.*

The typical experimental strategy for a BSM search like SUSY is illustrated in Figure 1.12, where the following steps are illustrated:

i. **Target search:** Given the different possible final-state signatures, in ATLAS the SUSY searches are split according to final-state signature and the trade-off between model-sensitivity and model-independence. Table 1.6 shows the main $E_{\mathrm{T}}^{\mathrm{miss}} + X$ searches currently targeted in ATLAS. The first four target general squark-gluino pair-production but cover different final-states. The searches for b-jets final-states target specifically the production of third generation squarks, which given its sizable mass-state mixing, could be the lightest and most accessible at the LHC. The dilepton and diphoton searches are meant to be sensitive to direct gaugino pair-production, *e.g.* if squarks and gluinos are heavier than the lightest neutralino and chargino.

ii. **Signal Region definition:** For each search target, one or more *Signal Regions* (SRs) are defined, which are simply event selections that maximise sensitivity to BSM models while maintaining enough statistics for a meaningful signal. The

RPC ($E_{\mathrm{T}}^{\mathrm{miss}} + X$) SUSY- Search Targets						
X						
0ℓ +jets	multijets	1ℓ + jets	2ℓ + jets	0ℓ + b-jets	1ℓ + b-jets	$\gamma\gamma$
$pp \to \tilde{q}\tilde{q}/\tilde{q}\tilde{g}/\tilde{g}\tilde{g}$				$pp \to \tilde{b}\tilde{b}/\tilde{g}\tilde{g}$	$pp \to \tilde{t}\tilde{t}/\tilde{g}\tilde{g}$	$pp \to \tilde{\chi}_i^0\tilde{\chi}_j^{\pm}$, $\tilde{\chi}_2^0\tilde{\chi}_2^0$
$\tilde{q} \to q\tilde{\chi}_1^0$ $\tilde{g} \to \bar{q}\tilde{q}/q\bar{\tilde{q}}$ short cascades	$\tilde{q} \to q\tilde{\chi}_1^0$ $\tilde{g} \to \bar{q}\tilde{q}/q\bar{\tilde{q}}$ long cascades	$\tilde{q} \to q\tilde{\chi}^{\pm}$ $\tilde{g} \to q\bar{q}'\tilde{\chi}^{\pm}$	$pp \to \tilde{\chi}_i^0\tilde{\chi}_j^{\pm}/\tilde{\chi}_2^0\tilde{\chi}_2^0$ $\tilde{\chi}_i^{\pm} \to l^{\pm}\nu\tilde{\chi}_j^0$ $\tilde{\chi}_i^{\pm} \to l^{\pm}\nu\tilde{\chi}_j^0$ $\tilde{\chi}_i^0 \to l^{\pm}l^{\mp}\tilde{\chi}_j^0$ $\tilde{\chi}_i^{\pm} \to l^{\pm}l^{\mp}\tilde{\chi}_j^{\pm}$	$\tilde{g} \to \tilde{b}b$ $\tilde{b} \to b\tilde{\chi}_1^0$	$\tilde{g} \to \tilde{t}t$ $\tilde{t} \to b\tilde{\chi}_1^{\pm}$ $\tilde{\chi}_1^{\pm} \to \tilde{\chi}_1^0 l^{\pm}\nu$	$\tilde{\chi}_1^0 \to \gamma\tilde{G}$
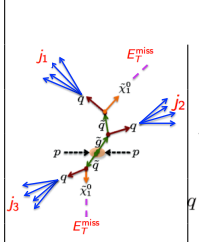	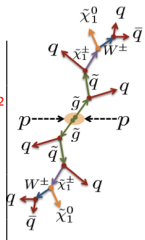	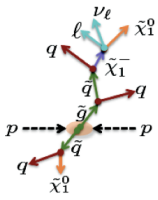	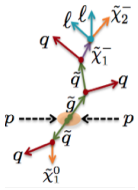			

Table 1.6.: *Main decay channels and final-state signatures targeted in RPC searches in ATLAS. In the "multijets" search, the target is final-states with* $\geq$ 6*-8 jets.*

RPC ($E_{\mathrm{T}}^{\mathrm{miss}} + X$) SUSY- Signal Regions							
Requirement	0ℓ +jets	multijets	1ℓ + jets	2ℓ + jets	0ℓ + b-jets	1ℓ + b-jets	$\gamma\gamma$
# jets, $p_{\mathrm{T}}(j_i)$	✔	✔	✔	✔	✔	✔	-
$E_{\mathrm{T}}^{\mathrm{miss}}$	✔	-	✔	✔	✔	✔	✔
$\Delta\phi(j_i, E_{\mathrm{T}}^{\mathrm{miss}})$ $E_{\mathrm{T}}^{\mathrm{miss}}/m_{\mathrm{eff}}$ m_{eff}	✔	-	✔	-	✔	✔	-
other		ΔR_{jj} $E_{\mathrm{T}}^{\mathrm{miss}}/\sqrt{H_T}$	m_T	m_{ll} SS,OS	# b-jets	m_T # b-jets	$p_{\mathrm{T}}(\gamma)$ $E_T^{\mathrm{iso}}(\gamma)$
discriminating variable	m_{eff}	$E_{\mathrm{T}}^{\mathrm{miss}}/\sqrt{H_T}$	m_{eff}	$E_{\mathrm{T}}^{\mathrm{miss}}$	m_{eff}, m_{CT}	m_{eff}	$E_{\mathrm{T}}^{\mathrm{miss}}$

Table 1.7.: *Similarities and differences in the definition of the SRs for the different RPC searches. Requirements on* $E_{\mathrm{T}}^{\mathrm{miss}}$ *and jets are common, while others are specific to the search target.* ΔR_{jj} *is the jet-jet separation,* $H_T = \sum p_{\mathrm{T}}(j_i)$*, "SS,OS" is same/opposite-signs,* m_{CT} *the co-transverse mass and the other variables are defined elsewhere in the text.*

new physics is therefore searched in the SRs as an excess of events over the SM background expectation. Usually more than one SR is defined to be sensitive to different models. Table 1.7 summarises the main characteristics defining the SRs for the RPC searches, from which is clear that requirements on $E_{\mathrm{T}}^{\mathrm{miss}}$ and jets are common.

iii. Background Estimation Even in the SRs, the great difference in cross-sections between BSM and most SM processes (*e.g.* for SUSY $\sim$ 1 pb versus $\sim$ 80 mb) makes the distinction of new signals very challenging. Therefore, resolving non-SM excesses is only possible when all the corresponding backgrounds have been identified and estimated. The backgrounds contribute differently depending on the search target, as shown in Table 1.8, but also depending on the SR, hence why each background has to be estimated for each SR, as illustrated in Figure 1.12. Different background-estimation techniques are used, though those derived from real data, known as *data-driven*, are much more preferred over Monte Carlo simulation. Data-driven estimates make use of *Control Regions* (CRs), samples associated to a particular background process, from which predictions in the SR can be obtained. In the case of SUSY RPC searches, the main backgrounds come from true $E_{\mathrm{T}}^{\mathrm{miss}}$ sources, *e.g.* $W(\rightarrow \ell\nu) + \text{jets}$, as well as from fake $E_{\mathrm{T}}^{\mathrm{miss}}$ sources, *e.g.* jet-energy mismeasurements (often referred as the 'QCD background'). As this thesis specialises in an estimation method for the $Z + \text{jets}$ background, this topic will be covered in full detail over the following chapters.

RPC ($E_{\mathrm{T}}^{\mathrm{miss}} + X$) SUSY- Main SM Backgrounds						
0ℓ +jets	multijets	$1\ell + \text{jets}$	$2\ell + \text{jets}$	$0\ell + b$-jets	$1\ell + b$-jets	$\gamma\gamma$
W/Z	QCD	$t\bar{t}$	$t\bar{t} + t$	$t\bar{t}$	$t\bar{t}$	QCD
$\bar{t}t + t$	$t\bar{t}$	W/Z	Z	W/Z	W/Z	W
QCD	W/Z	diboson	diboson	diboson	diboson	$t\bar{t}$
		QCD	fake lep	QCD	QCD	Z

Table 1.8.: *Dominant SM contributions to the RPC SUSY searches in ATLAS ($t\bar{t} + t$ means $t\bar{t}$ plus single top production). Searches requiring large $E_{\mathrm{T}}^{\mathrm{miss}}$ in their SRs suffer more from real-$E_{\mathrm{T}}^{\mathrm{miss}}$ backgrounds, while those requiring large jet multiplicities suffer more from QCD backgrounds. When only $t\bar{t}$ is shown, it means the single top contribution is negligible.*

iv. **Excess search:** As mentioned, the data is then compared to the SM background expectation in each of the SRs to search for non-SM excesses, after considering all the associated experimental uncertainties, *e.g.* jet-energy scale and resolution, trigger, efficiencies, etc; as well as theoretical uncertainties, *e.g.* PDFs, renormalisation scale, etc.

v. **Limit setting:** Finally, if no excess is found, model-independent limits (on the so-called "effective SUSY cross-section" $\sigma_{SUSY} \times A \times \varepsilon$ where A is acceptance and ε is efficiency) are set by combining the information of all SRs, using different statistical methods. In ATLAS, the statistical method is usually the CL_s method at 95% confidence level [24]. The results are then interpreted with respect to either simplified and constrained models, examples of which were discussed in Section 1.2.2. Usually, if there is more than one SR, the one with best expected limit is chosen to maximise the reach.

Chapter 2.

ATLAS and the LHC

Having covered the necessary theoretical background in the previous chapter, the aim now is to summarise the experimental setup used for the experimental studies presented in Chapter 5. First, Section 2.1 gives an overview of the LHC machine as this is the particle collider which produces the collision events of the data used. For this part, the main references used were [25–27]. Section 2.2 then follows with a brief description of ATLAS – the particle detector used to record and measure the LHC collision events. For this, the main references used were [28, 29].

2.1. The LHC

The Large Hadron Collider (LHC) is at present the world's highest energy particle accelerator. It currently collides head-on beams of protons and, for a short time at the end of the year, lead ions. The LHC aims to be sensitive to new physics, but the rate of events of a given type N_{event} is fixed by the cross section of the relevant scattering process σ_{event} and the luminosity $\mathscr{L}$:

$$N_{\text{event}} = \mathscr{L}\sigma_{\text{event}} \tag{2.1}$$

Indeed, the rarer the event, the smaller σ_{event} is, and so, achieving the highest luminosity is a top priority for the LHC, since unlike σ_{event} which is fixed, $\mathscr{L}$ can be optimised from beam parameters according to the equation:

$$\mathscr{L} \sim \frac{f_r N_b^2 n_b}{4\pi\sigma^2} F \tag{2.2}$$

where f_r is the machine revolution frequency (set by the synchrotron radius and the speed of light c), N_b the number of protons per bunch, n_b the number of bunches per beam, σ the transverse beam size at the interaction point (IP), and F the reduction factor due to the crossing angle at the IP (if the collisions[1] are not exactly head-on). The beam size σ is frequently expressed in terms of its beta (amplitude) function at the IP ($\beta^\star$), the normalised transverse emittance ε_N (an energy-invariant measure of the phase space occupied by the particles of the beam as it travels, reflecting the quality of the initial bunch preparation) and the relativistic gamma factor $\gamma_r = E/m$ as $\sigma^2 = \beta^\star \varepsilon_N / \gamma_r$. Therefore, to optimise the luminosity, the beam should have the largest number of bunches, with the highest population, colliding at locations where the beam optics provides the lowest possible $\beta^\star$. At the LHC, the lowest $\beta^\star$ happens at four IP's, as shown in Figure 2.1(a), each of which houses a particle detector: ATLAS and CMS are the largest and multi-purpose detectors, aimed for the LHC's design peak luminosity (10^{34} cm^{-2}s^{-1}); LHCb is smaller and dedicated to B-physics, so in order to have cleaner signatures (less pileup, see Section 2.2.4), it aims at a lower peak luminosity (10^{32} cm^{-2}s^{-1}) by locally defocussing the beams at its IP (higher $\beta^\star$). ALICE is dedicated to the heavy-ion runs, so it only operates at the peak luminosity during this time.

To understand better why the LHC is the most powerful collider nowadays, Table 2.1 compares its design beam parameters to those of the Tevatron, which used to be the most powerful.

2.1.1. Operation Cycle

An ideal LHC beam cycle is shown in Figure 2.1(b). For the "proton run", before being injected into the LHC, protons are subject to various stages of acceleration and beam preparation. First, they are accelerated from the proton source to energies of ~ 50 MeV at the CERN Linear Accelerator (LINAC2). Then, they are transferred to successive proton synchrotrons for further acceleration, bunch structure definition and setting the filling scheme: from the Proton Synchroton Booster (PSB, 1.4 GeV) to the Proton Synchroton (PS, 25 GeV) and then to the Super Proton Synchroton (SPS, 450 GeV). After this, they are injected into the LHC in the form of two oppositely-circulating beams, each of which is in a separate pipe throughout most of the ring, except around the IP's where the same pipe is shared. Placed along the ring, superconducting (2 K, liquid He) dipole magnets ensure the beam's fixed orbit, while quadrupoles provide

[1] Throughout the text, the term "collision" will be used to refer to one proton-proton interaction.

the transverse focusing and RF cavities the accelerating voltage. Throughout the pipe, ultra-high vacuum systems minimise proton collisions with gas molecules and particles produced by synchrotron radiation. The magnetic field in the dipole magnets is then increased to 8.3 T (ramping) as the protons are accelerated to the maximum collision energy, which in 2010 and 2011 was 7 TeV (3.5 TeV per beam). At this energy, the beams are squeezed as much as possible to achieve a low $\beta^\star$, after which stable beams for physics may be declared. This is the period during which the experiments record data for physics analyses. The data-taking period usually lasts as long as the beam's luminosity lifetime ($\sim$ 15 hours [30]).

	Tevatron (Fermilab)	LHC (CERN)	
		Design	Oct-2011
Physics start date	1987	2009	-
Particles collided	$\bar{p}p$	pp	-
Circumference (km)	6	27	-
Beam energy (TeV)	0.98	7.0	3.5
Peak luminosity ($10^{33}\text{cm}^{-2}\text{s}^{-1}$)	0.402	10	3.5
Bunch spacing (ns)	396	25	25
N_b (10^{12})	p:2.6, $\bar{p}$:0. 9	0.115	0.140
n_b	36	2808	1380
f_r (Hz)	47700	11245	-
$\beta^\star$ (m)	0.35	0.55	1
γ_r	1045	7461	-
ε_N (μm rad)	-	3.75	-
σ (μm)	66	16	-
F	1	0.85	-
Magnetic field (T)	4.4	8.3	-

Table 2.1.: *Nominal Tevatron parameters [31, 32] compared to those from the LHC design [26, 33] and values observed for fill 2219 on Oct-2011 [27]. The symbols are defined elsewhere in the text.*

2.1.2. Performance

A historical overview of the LHC since it started operation is shown in Table 2.2. The progress in machine development has clearly led to the optimisation of the beam parameters and more uninterrupted operations. Figure 2.2 shows the *integrated luminosity*

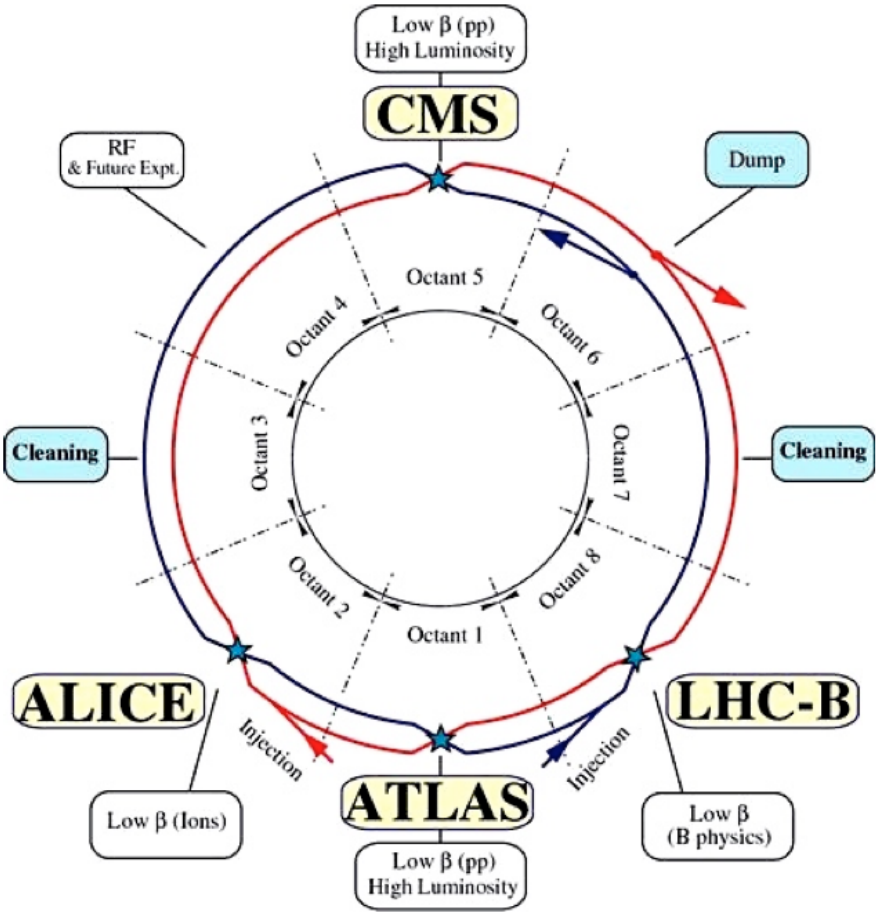

(a)

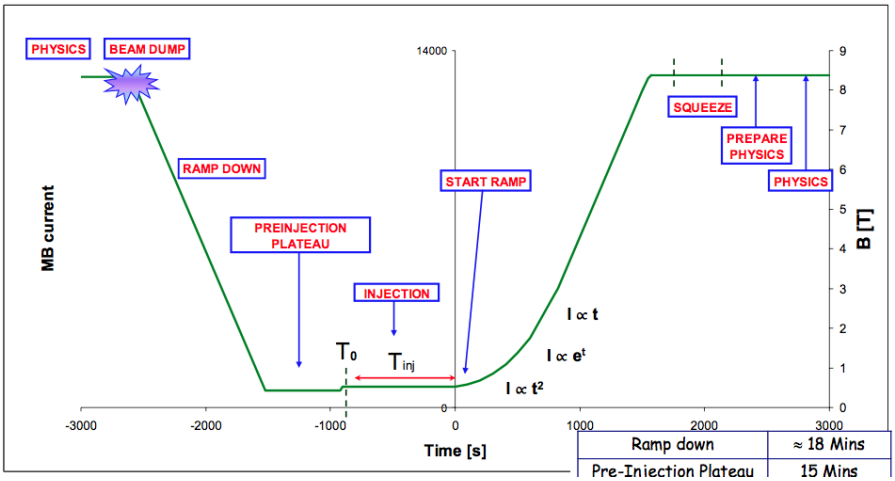

(b)

Figure 2.1.: *(a) Layout of the LHC and the particle detectors along it (from [26]) and (b) the LHC's nominal operation cycle.*

(the integral of the instantaneous luminosity over time, which is a measure of the size of the dataset) delivered by the LHC to the different experiments in 2011. The peak luminosities achieved so far, shown in Figure 2.2(b), are the result of a progressive optimisation of beam parameters as shown in Tables 2.1 and 2.3. There are limitations, however, in how much the integrated luminosity can be optimised. Some limitations are intrinsic to the LHC design and beam, *e.g.* the beam optics, magnets and vacuum systems performance, the vacuum degradation due to the beam presence, the beam long-range interactions, etc. Other limitations are related rather to the LHC operation – problems may be encountered at different stages of the cycle of Figure 2.1(b). A common problem for example has been unexpected "beam dumps", caused by "UFOs" (Unidentified Falling Objects), "SEUs" (Single Event Upsets) and overheating of the magnet system, amongst others. To illustrate this, Figure 2.3 shows the amount of time typically taken by each of the LHC operation stages. As for the optimisation of the *recorded* luminosity, this depends instead on to the performance of the LHC experiments and will be discussed for the case of ATLAS in Section 2.2.4.

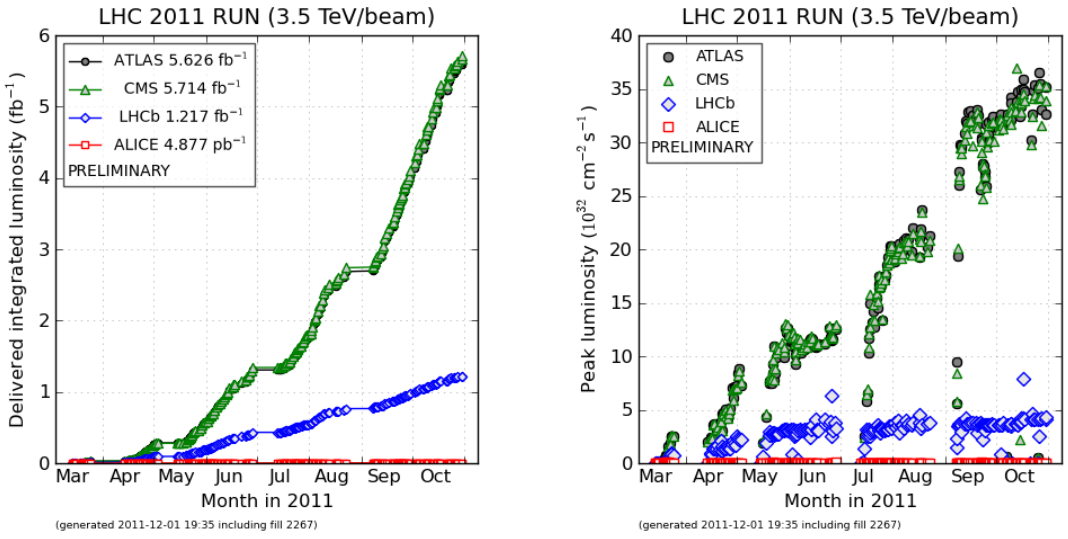

(a) (b)

Figure 2.2.: *Cumulative (a) and peak (b) luminosities versus day during stable beams delivered by the LHC to the experiments in 2011, from [34].*

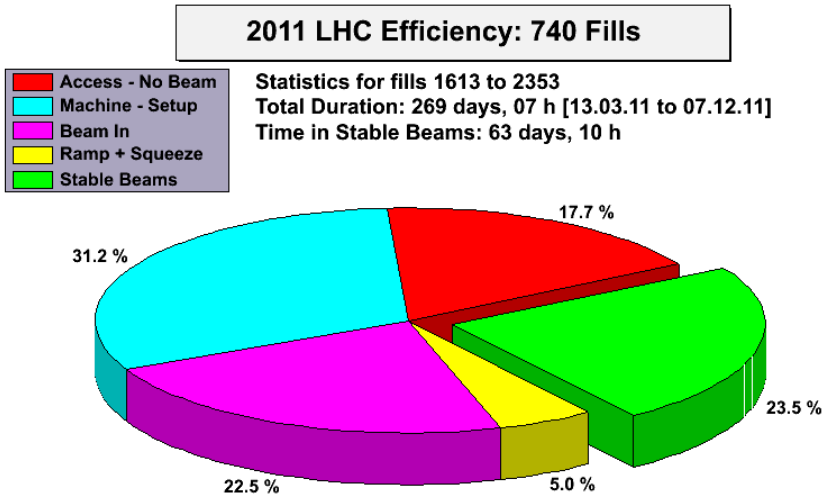

Figure 2.3.: *A pie chart of the LHC performance in 2011. The machine setup appears to take the longest, followed by the beam injection which roughly equals the time taken to recover from problems in operation and technical stops. Stable beams have been on only for about a quarter of the total operation time (from [27]).*

Date	Event
Sep 2008	First beam circulations halted by a destructive magnetic quench (S34 incident)
Oct 2008 - Oct 2009	Recovered from "S34 incident"
Nov 2009	Circulating beam commissioning is resumed
Dec 2009	First *pp* collisions at the injection energy (450 GeV/beam), subsequently reaching 1.18 TeV/beam
Dec 2009- Feb 2009	Christmas shutdown.
Mar 2010	First *pp* collisions at 3.5 TeV/beam.
Oct 2010	Operation with $\beta^\star = 3.5$ m, 150 ns, $n_b = 368$, $\mathscr{L} > 10^{32}\text{cm}^{-2}\text{s}^{-1}$. End of 2010 *pp* run achieving $\sim 45\text{pb}^{-1}$ of recorded data.
Nov 2010	Start of the heavy ion run.
Dec 2010	End of heavy ion run and Christmas shutdown.
Mar 2011	Beginning of the 2011 *pp* run at 3.5 TeV/beam, with 75 ns.
Apr 2011	Bunch spacing decreased to 50 ns. The LHC surpasses the record peak luminosity from the Tevatron.
Jun 2011	ATLAS and CMS reach $\sim 1\text{fb}^{-1}$ of recorded data (2011 target),
Aug 2011	$\beta^\star = 1.5$ m, 50 ns, $n_b = 1380$, $\mathscr{L} > 10^{33}\text{cm}^{-2}\text{s}^{-1}$
Sep 2011	Technical stop. $\beta^\star = 1.0$ m
Oct 2011	End of 2011 *pp* run achieving ~ 5 fb^{-1} of delivered data.

Table 2.2.: *LHC timeline since the first beam circulation in 2008 until the end of the 2011 pp run. Numerical values are taken from [27].*

Fill number	Date	Bunch spacing (ns)	n_b	Peak $\mathscr{L}$ ($10^{33}\text{cm}^{-2}\text{s}^{-1}$)	N_b per beam (10^{14})
1635	18 Mar 2011	75	32	0.030	0.038
1645	22 Mar 2011	75	200	0.252	0.243
1712	15 Apr 2011	50	228	0.237	0.285
1749	30 Apr 2011	50	624	0.716	0.756
1815	29 May 2011	50	1092	1.268	1.330

Table 2.3.: *Example LHC peak luminosity performances resulting from different beam parameters, from [27]*

2.2. The ATLAS Detector

2.2.1. Coordinate System and Kinematic Variables

ATLAS has a right-handed coordinate system, as shown in Figure 2.4(a). The origin (centre of detector) is at the IP; the x-axis points towards the centre of the LHC ring, the y-axis upwards and the z-axis along the beam pipe. Cylindrical coordinates (r, ϕ) are used in the transverse plane (ϕ being the azimuthal angle around the beam pipe).

As discussed in Section 1.1.2, in a hadron collider the partons of the incoming beams do not have a fixed momentum but rather a spectrum described by the PDFs. The overall process is relativistic and the centre of mass of the parton-parton scattering is normally boosted with respect to that of the parent hadrons. It is therefore convenient to describe the final state by variables which transform simply under Lorentz boosts. For this purpose, the variables used are the rapidity y, transverse momentum p_{T} and azimuthal angle ϕ. In terms of these variables, the four-momentum of a particle may be written as

$$p^{\mu} = (E, p_x, p_y, p_z) \tag{2.3}$$

$$= (m_T \cosh y, p_T \sin\phi, p_T \cos\phi, m_T \sinh y) \tag{2.4}$$

where the transverse mass is $m_T = \sqrt{p_T^2 + m^2}$. The rapidity, defined as

$$y = \frac{1}{2} \ln \left[\frac{E + p_z}{E - p_z} \right] \tag{2.5}$$

has the nice property of being additive under boosts (a class of Lorentz transformations) along the z-direction and differences in rapidity are also boost-invariant. In the ultra-relativistic limit ($m \to 0$) the rapidity equals the pseudorapidity η:

$$\eta = -\ln \tan(\theta/2) \tag{2.6}$$

In ATLAS it is experimentally more convenient to use η since the polar angle θ from the beam direction is measured directly in the detector. It is also standard to use the transverse energy,

$$E_T = E \sin\theta \tag{2.7}$$

rather than p_{T}, since the former is what is actually measured in the ATLAS calorimeters (see Section 2.2.5). In the η-ϕ plane, the variable ΔR,

$$\Delta R = \sqrt{(\Delta\eta)^2 + (\Delta\phi)^2} \tag{2.8}$$

is often used to define separation distances between physics objects (see Section 2.2.5).

In ATLAS the collisions are practically head-on[2], so for each event, an unknown proportion of the energy from the incoming protons escapes along the beam-pipe and if "invisible" particles (those not possible to detect with ATLAS) are created in the final state, their net momentum can only be constrained in the transverse (x-y) plane by defining a missing transverse-energy vector $\mathbf{E}_{\mathrm{T}}^{\mathrm{miss}}$, which at a basic level is defined as:

$$\mathbf{E}_{\mathrm{T}}^{\mathrm{miss}} = -\sum_{i} \mathbf{p}_{\mathrm{T}}(i) \tag{2.9}$$

where the sum runs over the transverse momentum p_{T} ($p_{\mathrm{T}} = p/\cosh\eta = p\sin\theta$) of all visible final state particles; however the actual $E_{\mathrm{T}}^{\mathrm{miss}}$ definitions typically implemented in ATLAS are more complicated than this (see for example Section 2.2.5).

All other transverse variables are similarly defined with respect to this plane.

2.2.2. Detector Components

ATLAS is a hybrid system of detectors with different technologies to be able to detect and measure different particles. It has four major systems, each of which is divided into sub-systems, arranged concentrically in a cylindrical structure, as shown in Figure 2.5. The low-η central region of these components are termed "barrel" (B) regions, whilst the high-η forward regions are referred as the "end-caps" (EC). Despite ATLAS having a nearly 4π coverage in solid angle as a whole, the particle *acceptance* is limited by the geometry of its subsystems as outlined in Table 2.4. A description of each of the subsystems now follows.

[2]The beams meet in ATLAS at a half crossing angle of ~ 142.5 μrad [26].

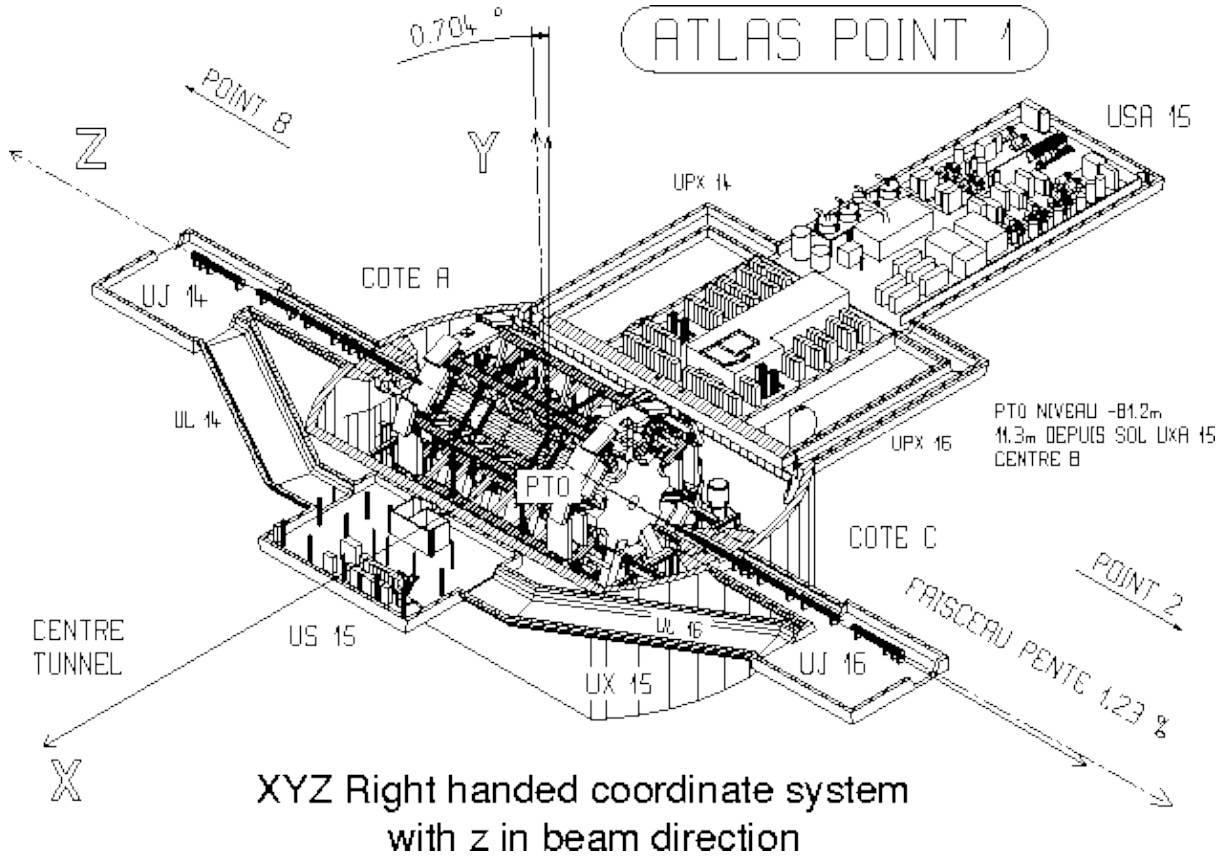

(a)

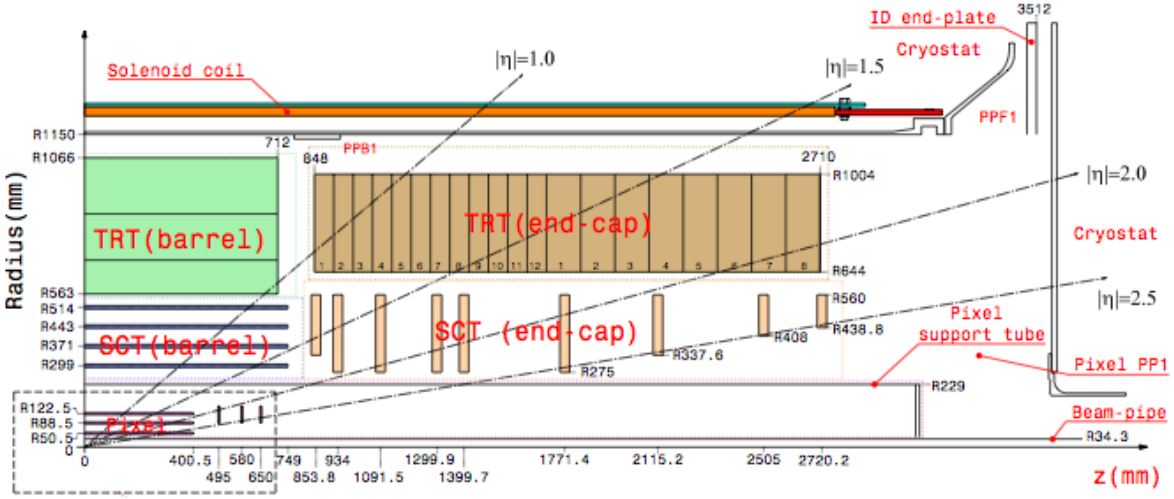

(b)

Figure 2.4.: *Plan views of ATLAS showing the (a) x, y, z and (b) r, η coordinates (from [35] and [36]). The general tilt of the LHC tunnel causes the y-axis to be slightly different from the vertical while high $|\eta|$ values refer to regions of the detector close to the beam pipe.*

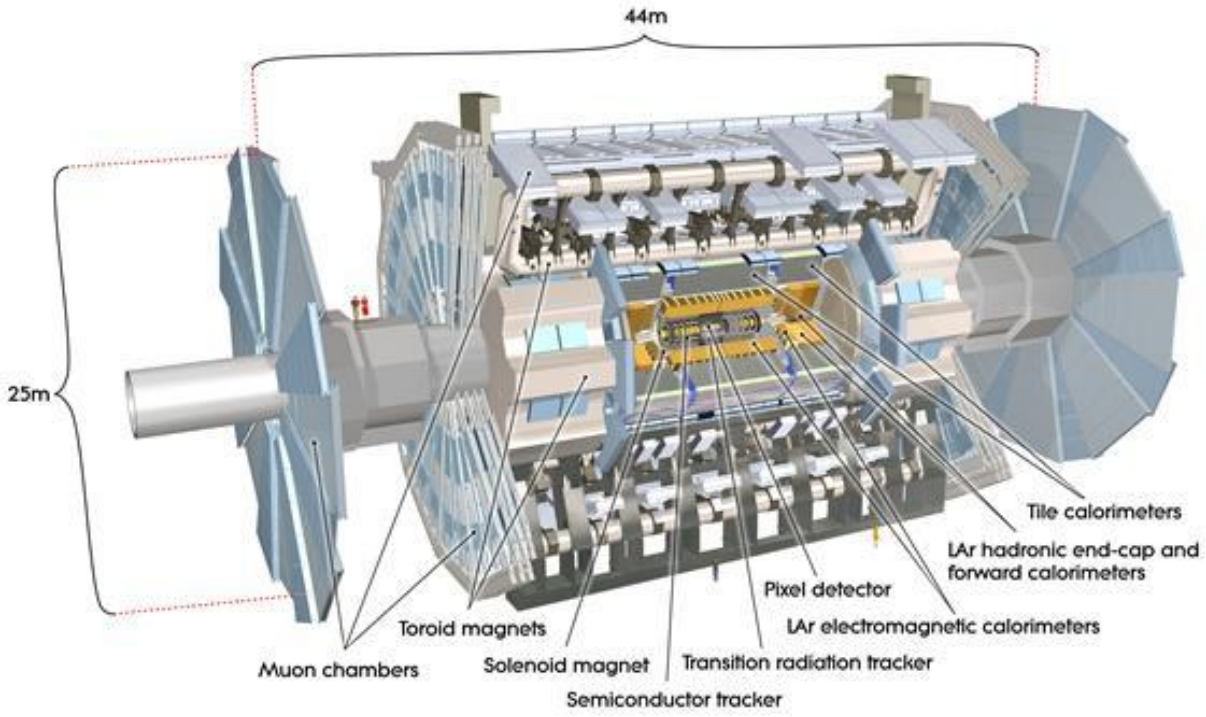

Figure 2.5.: *Computer generated image illustrating the different components of the ATLAS detector, from [37].*

System	Subsystem	$\lvert\eta\rvert$ Acceptance			Design resolution
		Barrel	Endcap	Overall	
ID	Pixel	< 2.5	1.7-2.5	< 2.5	$\sigma_{p_T}/p_T = 0.05\% p_T \oplus 1\%$
	SCT	< 1.4	1.4-2.5		
	TRT	< 0.7	0.7-2.5		
Calorimeters	Presampler	< 1.52	$1.5 - 1.8$	< 1.8	-
	ECAL	< 1.475	$1.375 - 3.2$	< 3.2	$\sigma_E/E = 10\%/\sqrt{E} \oplus 1.2\%$
	HCAL Tile	< 1.0	0.8-1.7	< 4.9	$\sigma_E/E = 50\%/\sqrt{E} \oplus 3\%$
	HCAL LAr		1.5-3.2		
	Forward		3.1-4.9		$\sigma_E/E = 100\%/\sqrt{E} \oplus 10\%$
MS	Tracking	< 1.0	1.4-2.7	< 2.7	$\sigma_{p_T}/p_T = 10\%$ at 1 TeV.
	Trigger	< 2.4			
Magnets	Toroid	< 1.3	1.6-2.7	< 2.7	-
	Solenoid	< 2.5		< 2.5	

Table 2.4.: *Design acceptance [28] and resolution [36] of ATLAS subsystems. The energy resolution is parametrized as $\sigma_E/E = (a/\sqrt{E}) \oplus c$, where a is the sampling term and c the constant term.*

Inner Detector

The Inner Detector (ID) is the tracking system. It specialises in the reconstruction of charged particle tracks and vertices, as well as measuring momentum. It is crucial to measure the impact parameter of short-lived particles (e.g B hadrons and τ leptons). It uses a combination of three subsystems, which, in order from closest to furthest from the IP are:

- Pixel subdetector - made of semiconductor (Si) pixels, it has the highest resolution and it provides 3 precision measurements per track. The innermost layer (termed the "b-layer") provides precision vertexing, which is crucial, *e.g.* for b-quark tagging and photon conversions identification.
- Semiconductor Tracker (SCT) - made of silicon microstrips, it provides 8 precision measurements per track.
- Transition Radiation Tracker (TRT) - made of straw tubes filled mainly with Xe gas, it provides 36 additional measurements per track and additional discrimination between electrons and hadrons, via the detection of X-rays produced by transition radiation.

Lastly, a superconducting central solenoid (CS) magnet wraps the ID to provide a bending magnetic field (~ 2 T).

Calorimeters

After the ID and CS, the system of electromagnetic (EM) and hadronic calorimeters follows (see Figure 2.5), which is of particular importance in this thesis to understand the measurements of photons and jets. Recent performance results with 2010 and 2011 data can be found in [38–40] and the design report at [41].

Overall, the calorimeters provide energy measurements of particles from the electromagnetic and hadronic showers they generate as they traverse their material, with a resolution which improves with energy (the resolution of ATLAS calorimeters is quoted in Table 2.4). High-energy electrons and photons predominantly lose energy from their electromagnetic interactions with matter (*e.g.* bremsstrahlung $e \to \gamma e$ and pair production $\gamma \to e^+e^-$ respectively), which are characterised by narrow showers in ATLAS EM calorimeter (ECAL), as exemplified in Figure 2.12(a). In contrast, jets (hadrons) typically produce

a broader energy deposit from their strong interactions with the calorimeter material, with significant leakage into the hadronic calorimeter (HCAL). The amount of material traversed by the showers is measured longitudinally in terms of radiation lengths χ^0 (EM case) and nuclear interaction lengths (hadronic case).

In order from innermost to outermost, the calorimeter system of ATLAS is composed of the following:

Presampler - consists of a thin liquid argon (LAr) layer which corrects for energy loss in the material before the calorimeters.

EM Calorimeter (ECAL) - consists of a sampling calorimeter of lead and LAr with an accordion geometry (to prevent cracks). Figure 2.6 shows a sketch of one of the barrel modules, where it can be seen it consists of three longitudinal layers, in order of decreasing granularity: "Layer 1" ($|\eta| < 1.4$, $1.5 < |\eta| < 2.4$) segmented into high granularity strips in the η direction to discriminate EM objects from hadrons; "Layer 2", with a thickness of several χ^0 to collect most of the energy from the EM showers, and "Layer 3" to correct leakage beyond the ECAL from high-energy showers.

Hadronic Calorimeter (HCAL) - consists of an iron-scintillator tile calorimeter in the range $|\eta| < 1.7$ and two copper-LAr end-cap calorimeters ($1.5 < |\eta| < 3.2$). The acceptance is further extended up to $|\eta| < 4.9$ by two tungsten-LAr forward calorimeters.

Magnet System

The system of superconducting magnets (kept at temperatures of ~ 4.8 K) consists of two subsystems: a thin central *solenoid*, already mentioned, that provides a magnetic field of ~ 2 T to the ID; and three air-core *toroids* (one barrel "BT" and two end-caps "ECT") that provide the magnetic field to the muon spectrometer.

Muon Spectrometer (MS)

This system specialises in stand-alone triggering and momentum measurement of muons. The direction of the magnetic field from the toroid magnet system is largely perpendicular to the muon trajectory to exert the maximum bending force. Precision measurements of the tracks are given by the Monitored Drift Tubes (MDTs), while the larger pseudora-

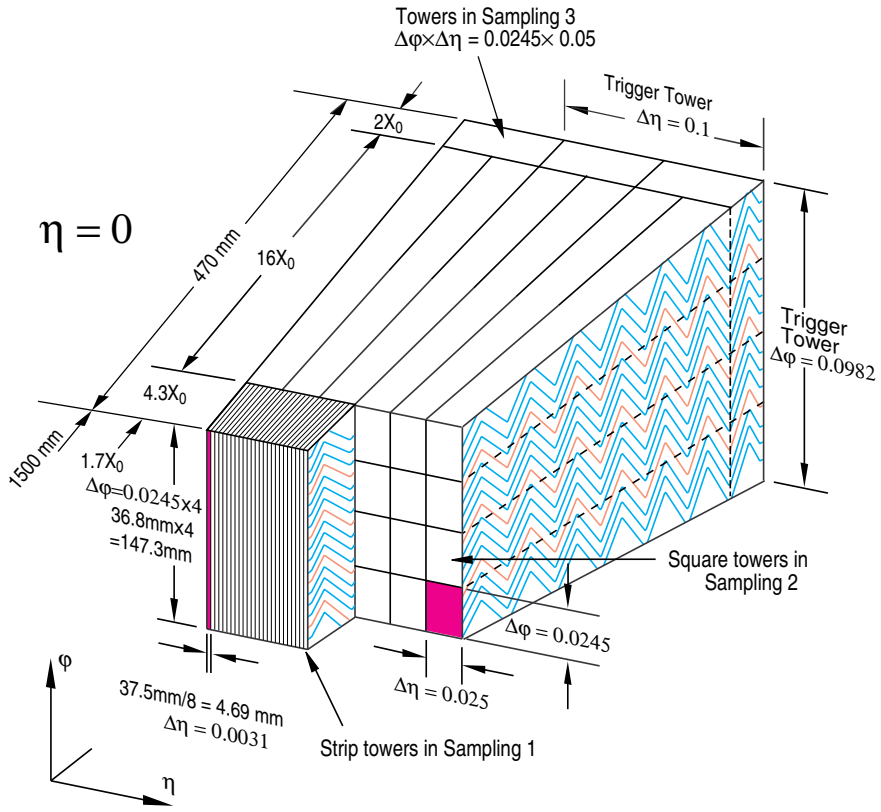

Figure 2.6.: *Sketch of a barrel module from ATLAS ECAL, from [36]. The three layers are visible. The granularity in η and ϕ of the cells in each layer and of the trigger towers is also shown.*

pidities are served by the Cathode Strip Chambers (CSCs) of higher-granularity. The independent trigger system is served by Resisitive Plate Chambers (RPCs) in the barrel and ThinGap Chambers (TGCs) in the end-caps. Full details of the MS can be found in [42].

2.2.3. Trigger

The trigger system in ATLAS is designed to reduce the event rate from the LHC design bunch-crossing rate ($\sim$ 40 MHz) to a more manageable recording rate of $\sim$ 200 Hz. It is composed of three levels, as illustrated in Figure 2.7, to sequentially improve the decision of keeping or rejecting events. Level-1 (L1) is hardware-based and makes the first decision in < 2.5 μs by using information from the calorimeter and muon systems. It also provides Regions of Interest (RoIs) – regions of the detector potentially containing physics objects, like μ, e, γ, jets and $E_{\mathrm{T}}^{\mathrm{miss}}$– for the subsequent trigger levels. The other two levels are the Level-2 (L2) and the Event Filter (EF). Collectively known as the High Level Trigger (HLT), they are software-based triggers that consider the decision more carefully by accessing more event information. Limits on the output bandwidth for the three levels are set by the "trigger menu" - a programmable list of selection criteria (thresholds) to define trigger decisions. The menu has to be constantly redefined to cope with the increasing LHC luminosities. Hence, some large-output triggers need to be "prescaled", meaning that a reduction factor is applied on the fraction of accepted events. An example of this is shown in Figure 2.8.

In this thesis, the main triggers used are single-photon triggers, such as those shown in Table 2.5. As will be noted in Section 5.3.2, different triggers were used to guarantee an unprescaled trigger throughout the dataset being analysed. In general, the L1 trigger is able to compute the transverse energy of electromagnetic clusters. The photon identification is then done at the HLT, using similar variables to those used offline for identification and isolation (see Section 2.2.5 and more details in [43]). The photon triggers are typically labelled by their E_{T} threshold and type of identification requirement (*loose* and *tight* being the most common).

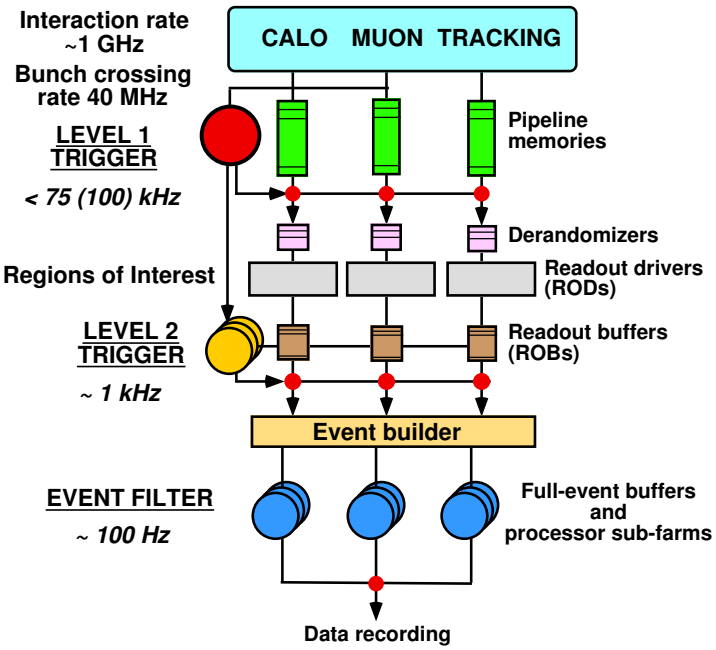

Figure 2.7.: *Diagram of ATLAS Trigger/DAQ system [28]. If an event is accepted by the L1 trigger, the data is piped to the Readout Drivers (RODs) and then the Readout Subsystem (ROS). Events subsequently selected by L2 are transferred to the event-builder, after which the Event Filter can make the final decision to record the event.*

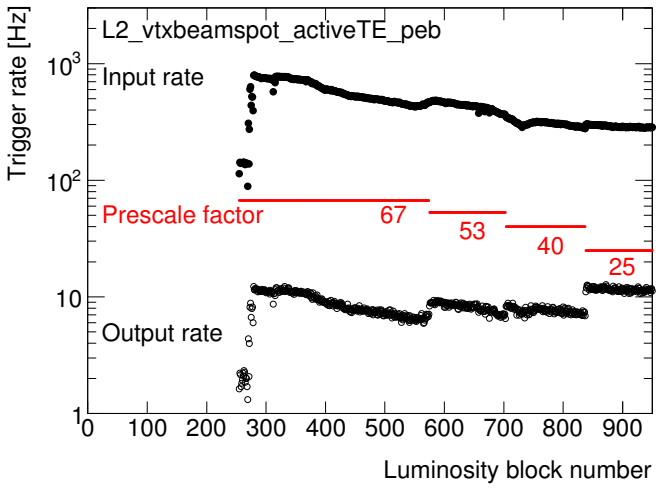

Figure 2.8.: *Adjustment of the L2 trigger output rate for an arbitrary trigger menu by setting prescale factors. The "Luminosity block number" on the x-axis represents a time unit used in ATLAS. From [44].*

Trigger	Offline E_{T} cut	Efficiency
`g20_loose`	25 GeV	$99.13^{+0.20}_{-0.30}$
`g60_loose`	65 GeV	$99.7^{+0.09}_{-0.1}$
`g80_loose`	85 GeV	100^{+0}_{-3}

Table 2.5.: *Examples of the photon triggers used and their estimated efficiencies. Uncertainties are statistical only. In the trigger name, "*`g`*" is for "gamma", the number represents the* E_{T} *threshold and "*`loose`*" the type of ID requirement. From [43].*

2.2.4. Performance

Of the total luminosity delivered by the LHC to ATLAS, $\sim 94\%$ has been recorded, as shown in Figure 2.9. Indeed, all subsystems have been close to 100% efficient, as shown in Table 2.10.

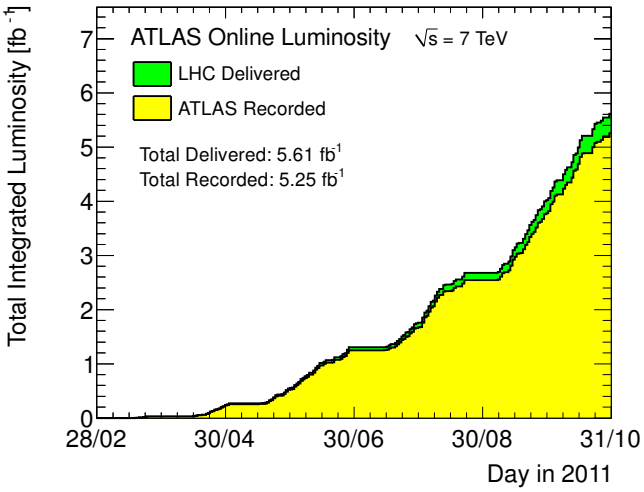

Figure 2.9.: *Cumulative luminosity versus day delivered to (green), and recorded by ATLAS (yellow) in the 2011 p-p run (from [13]). The luminosity is determined in ATLAS from "van-der-Meer scans", where the two beams are scanned against each other in the horizontal and vertical planes to measure their overlap function.*

ATLAS 2011 p–p run

Inner Tracking			Calorimeters				Muon Detectors				Magnets	
Pixel	SCT	TRT	LAr EM	LAr HAD	LAr FWD	Tile	MDT	RPC	CSC	TGC	Solenoid	Toroid
99.8	99.6	99.2	97.5	99.2	99.5	99.2	99.4	98.8	99.4	99.1	99.8	99.3

Luminosity weighted relative detector uptime and good quality data delivery during 2011 stable beams in pp collisions at √s=7 TeV between March 13th and October 30th (in %), after the summer 2011 reprocessing campaign

Figure 2.10.: *Luminosity weighted relative fraction of good quality data delivery by the various ATLAS subsystems between March 13th and October 30th, corresponding to the 2011 recorded dataset (from [13]).*

Pileup

Dealing with pileup is a major experimental challenge for experiments at hadron colliders like the LHC as the beam has a bunch structure. In this context, pileup refers to the cases where more than one inelastic *pp* collision per bunch crossing happens inside the detector. Pileup can be "in-time" if it is caused by the IP bunch crossing or "out-of-time" if it is caused by neighbouring bunch crossings. For 2010 data, the number of reconstructed vertices n_{vtx} was considered a good measure of the amount of pileup in the event. Currently, a more refined procedure based on the mean number of pileup interactions (or equivalently, the mean of the poisson distribution on the number of interactions per crossing) $\langle\mu\rangle$ is used instead (applicable to 2011 data). It is calculated from the instantaneous luminosity as:

$$\langle\mu\rangle = \mathscr{L}\frac{\sigma_{\text{inel}}}{n_b f_r} \tag{2.10}$$

where n_b is the number of bunches per beam, f_r is the machine revolution frequency and σ_{inel} the total inelastic *pp* cross-section, which for $\sqrt{s} = 7$ TeV is ~ 71.5 mb [13, 45]. Therefore, using the LHC design beam parameters from Table 2.1, $\langle\mu\rangle \sim 19$. However, the actual average for 2011, prior the September 2011 technical stop when $\beta^\star$ was reduced from 1.5 m to 1.0 m (see Table 2.2), was ~ 6.3 as shown in Figure 2.11(a).

Equation (2.10) clearly states that pileup increases with luminosity, so this is an increasingly important matter to consider in the physics analyses of ATLAS as its impact on the results can be significant. For example, there is a significant impact on track reconstruction, simply because tracks are more difficult to reconstruct in a busy environment and selecting the correct primary vertex becomes more challenging. As will be shown in Chapter 5 and Appendix C, the comparisons of data with theory from Monte Carlo simulation can also be affected, and since the real pileup conditions change constantly, this cannot be implemented in the MC production accurately nor immediately. An event display of the typical pileup environment after $\beta^\star$ was reduced to 1 m is shown in Figure 2.11(b) for a $Z \to \mu\mu$ candidate event.

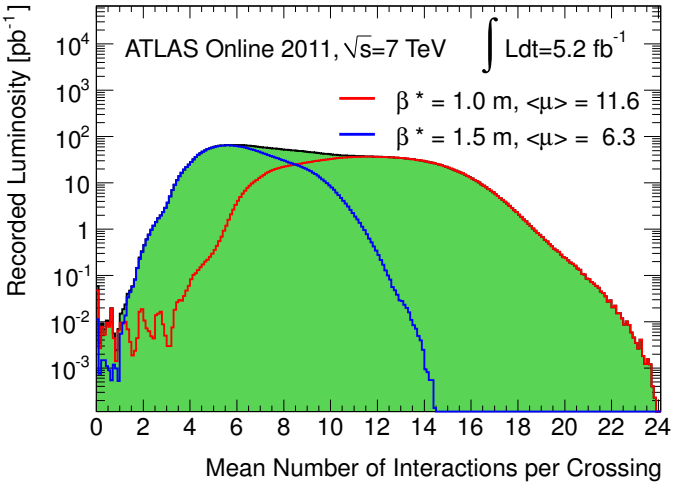

(a)

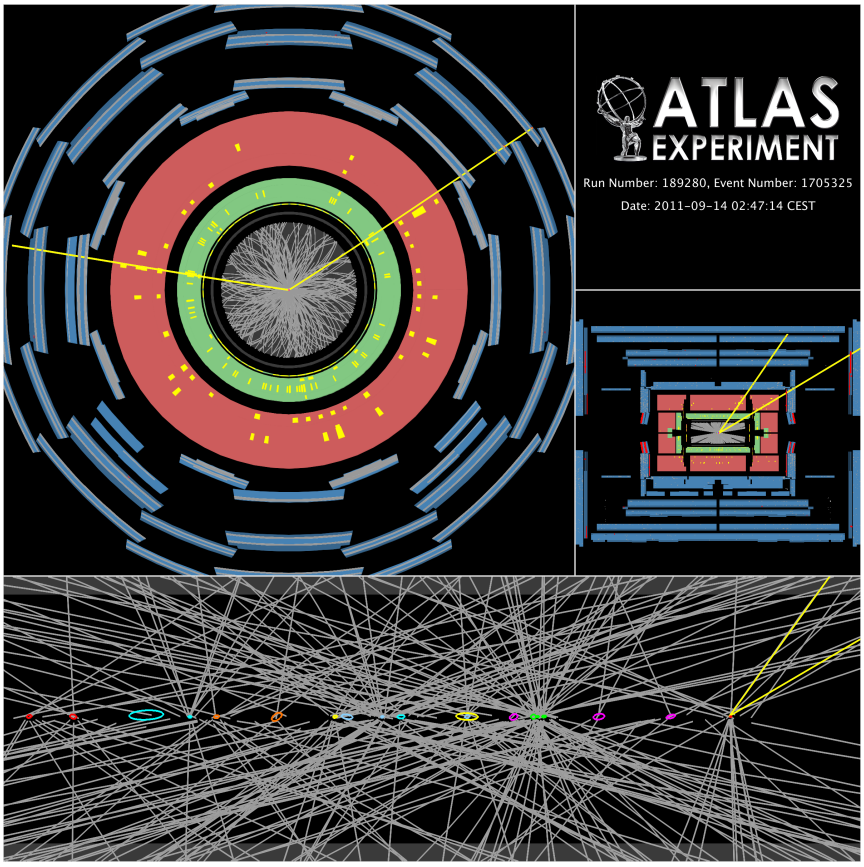

(b)

Figure 2.11.: *(a) Luminosity-weighted distribution of the mean number of interactions per crossing for 2011, for data taken before and after the September technical stop, when $\beta^\star$ was reduced. The entries at $\mu \sim 0$ arise from pilot bunches that were present during many of the early LHC fills (the luminosity in these is significantly smaller than in the main bunches). (b) Event display illustrating a high pileup scenario (20 reconstructed vertices) in a $Z \to \mu\mu$ candidate event. Both figures are from [13].*

2.2.5. Physics Object Definition

For physics objects to be defined for the purpose of physics analysis, the following procedures follow:

i. **Reconstruction:** this is the process whereby the raw data digits, such as times and voltages, and other signals from the hardware in the detector are reconstructed into tracks and energy deposits to deduce the physics of the event, *e.g.* the track particles must have followed and their four-momenta.

ii. **Identification:** this is the process whereby, based on certain criteria, the reconstructed tracks, energies and their profiles (*e.g.* shower shapes) are used to define particle candidates or physics objects like photons, electrons, muons, jets and $E_{\mathrm{T}}^{\mathrm{miss}}$.

iii. **Other Requirements:** The above can be regarded as the basic requirements for object definition but, in general, each physics analysis sets their own additional criteria as a further refinement of the object. Examples of these requirements are the energy scale, quality, acceptance, isolation, overlap removal, etc. Depending on the purpose of the analysis, the criteria for some objects might be looser or tighter, *e.g.* a photon cross-section measurement might require a more precise definition of photons than say, a $Z \to ee$ measurement.

A general summary for the above points that characterise the main physics objects in ATLAS, and which are mainly referred to in this thesis now follows (other object definitions, *e.g.* for b-jets, taus, etc. can be found in other references like [39, 46]).

Photons

i. **Reconstruction:** Photon candidates are formed from clusters of energy deposits reconstructed in the ECAL with $E_{\mathrm{T}} > 2.5$ GeV (above the electronic noise level, which typically is < 1 GeV [36]). An algorithm attempts to match these clusters to tracks reconstructed in the ID. Clusters without matching tracks are classified as *unconverted* photon candidates, while clusters with matched tracks are considered electron candidates. Hence, to recover photons from conversions, clusters matched to pairs of tracks originating from reconstructed conversion vertices in the ID are considered *converted* photon candidates. To increase the reconstruction efficiency of converted photons, conversion candidates where only one of the two tracks is reconstructed (and does not have any hit in the *b-layer*, see Section 2.2.2) are also

retained [47]. The final energy measurement is made with the ECAL, in a cluster size that depends on whether the photon is converted or unconverted. A specific energy calibration is then applied separately to account for upstream energy loss in front of the ECAL (see "Calorimeter Presampler" in Section 2.2.2) and both lateral and longitudinal leakage. Clusters are removed if their barycenter lies in the transition between the Barrel and Endcap regions of the ECAL (also known as the "crack" region, corresponding to $1.37 < |\eta| < 1.52$, see Table 2.4), where larger uncertainties related to efficiency measurements are expected. Similarly, clusters containing cells overlapping with problematic regions of the calorimeter readout or with very noisy cells are also removed.

ii. **Identification:** Shape variables computed from the lateral and longitudinal energy profiles of the electromagnetic shower in the ECAL are used to discriminate signal from background. The definitions of these variables can be found in [48] and examples are shown in Figure C.3. Different selection criteria with respect to these variables are applied to determine the photon identification, *e.g.* "loose" or "tight" (see Section 5.3.1 and more details in [48, 49]). The criteria do not depend on the candidate's E_{T} but on its pseudorapidity η (to take into account variations in the thickness of the upstream material and in the calorimeter geometry). True prompt photons are expected to have small hadronic leakage (typically below 1-2%) and narrow shower profiles, with respect to background candidates, *e.g.* from jets or π^0, as exemplified in Figure 2.12.

iii. **Other Requirements:** The main other requirement for photons is *isolation*, which further suppresses the main background from π^0 (or other neutral hadrons decaying to $\gamma\gamma$). The experimental isolation requirement is based on the energy deposited in the calorimeters (ECAL and HCAL) in a cone of radius $\Delta R = \sqrt{(\Delta\eta)^2 + (\Delta\phi)^2}$ around the photon candidate. In order to make the measurement of $E_{\mathrm{T}}^{\mathrm{iso}}$ directly comparable to parton-level theoretical predictions, a few corrections, obtained from simulation, are made to remove the energy of the photon itself that leaks into the isolation cone and to subtract the estimated contributions from the underlying event and pileup. After this subtraction, the remaining fluctuations are dominated by electronic noise from the calorimeter measurement. Additional details on $E_{\mathrm{T}}^{\mathrm{iso}}$ can be found in [48, 49]. Apart from isolation, other requirements are normally applied on photons, such as on the energy scale, quality, and acceptance (see Section 5.3.1).

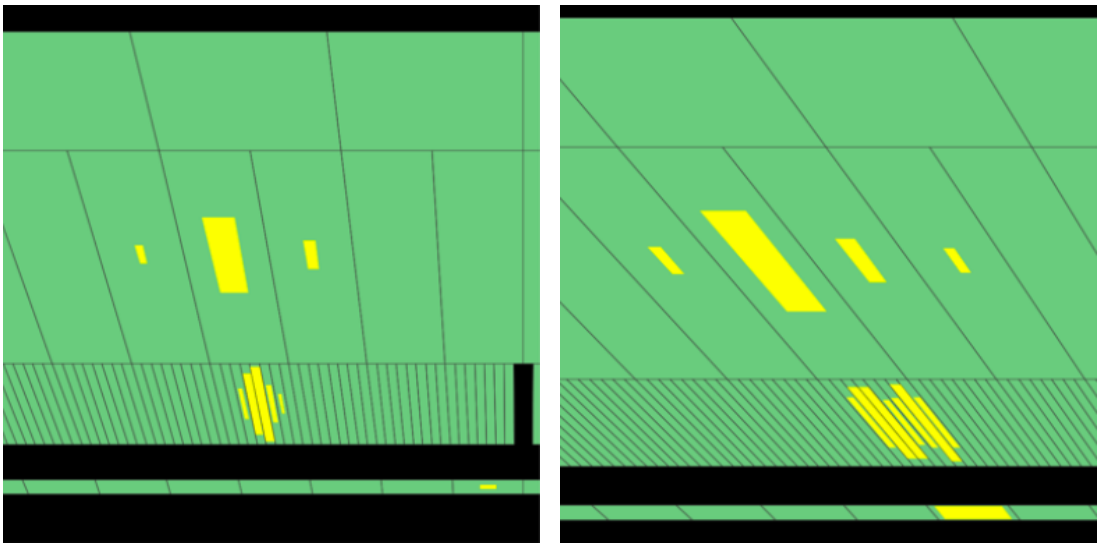

(a) (b)

Figure 2.12.: *Event display of (a) a prompt photon candidate ($E_{\mathrm{T}} = 32$ GeV and $E_{\mathrm{T}}^{\mathrm{iso}} = 178$ MeV) and (b) a π^0 candidate ($E_{\mathrm{T}} = 21$ GeV and $E_{\mathrm{T}}^{\mathrm{iso}} = 6.2$ GeV) in ATLAS ECAL, from [50]. In "Layer 1", the photon shows one peak and a narrow shower, while the π^0 shows two peaks from its decay into $\gamma\gamma$ and hence a broader profile.*

Electrons

Being also an "egamma" object, the procedures to define electrons are, to a general level, very similar to those for photons. However, some important differences are that in the reconstruction the electron candidates are *always* associated to energy clusters with matched ID tracks, and losses from bremsstrahlung must be considered. As for identification, this is based on track-cluster matching and the use of the TRT subdetector (see Section 2.2.2) to further aid in the discrimination against photon conversions and charged hadrons over a wide energy range (between 0.5 and 100 GeV) [47].

Muons

i. **Reconstruction:** Muons as reconstructed by an algorithm which looks for stand-alone tracks in the ID and the MS, which are then combined using a chi-square matching procedure [51].

ii. **Identification:** Two types of muons are generally used: "combined" muons are made from tracks that have been independently reconstructed in both the MS and

ID with the "STACO" algorithm, while "segment-tagged" muons use the MS to tag ID tracks as muons, without requiring a fully reconstructed MS track [51].

iii. **Other Requirements:** Usually muons are required to fulfil acceptance, quality and isolation requirements, *e.g.* for isolation, $\sum p_{\mathrm{T}}$(tracks) in a cone of $\Delta R < 0.2$ must be less than 1.8 GeV.

Jets

i. **Reconstruction:** Jet candidates are reconstructed from topological clusters (built from calorimeter cells) which attempt to reconstruct the three-dimensional shower topology of each particle.

ii. **Identification:** The algorithm most commonly used in ATLAS currently is the infrared and collinear-safe "anti-k_{T}", with a distance parameter of $R = 0.4$ [52] (however, other alternatives like cone algorithms, have been used in the past). The jet four-momenta are constructed from a sum over their constituents, treating each as an $(E, \mathbf{p})$ four-vector of zero mass.

iii. **Other Requirements:** The measured jet p_{T}, as determined at the electromagnetic scale, systematically underestimates that of the hadron-level jet and is mainly due to the non-compensating nature of the calorimeter (lower response to hadrons than electrons or photons) and the presence of dead material. Hence, an average correction, determined as a function of jet-p_{T} and η, extracted from MC simulation is normally applied. This calibration procedure is known as "Jet Numerical Inversion Correction" and is what determines the Jet Energy Scale (JES). In addition, the Jet Energy Resolution (JER) in data is matched by "smearing" the MC. Other requirements typically applied are on the acceptance, overlap removal (wrt other physics objects, see below) and quality.

Missing Transverse Energy

This is determined offline with an object-based algorithm from all measured and identified physics objects, as well as any remaining energy deposits in the calorimeter. An example algorithm is `MET_Simplified20_RefFinal` (used also in this analysis, see Section 5.4.1), where the energy clusters are associated to high-p_{T} objects in the following order: electrons, jets and muons; and any remaining clusters are included in a so-called "CellOut" term.

The $E_{\mathrm{T}}^{\mathrm{miss}}$ is therefore given by the following formula:

$$(E_{\mathrm{T}}^{\mathrm{miss}})_{\mathrm{x(y)}}^{\mathrm{RefFinal}} = (E_{\mathrm{T}}^{\mathrm{miss}})_{\mathrm{x(y)}}^{\mathrm{RefEle}} + (E_{\mathrm{T}}^{\mathrm{miss}})_{\mathrm{x(y)}}^{\mathrm{RefJet}} + (E_{\mathrm{T}}^{\mathrm{miss}})_{\mathrm{x(y)}}^{\mathrm{RefMuo}} + (E_{\mathrm{T}}^{\mathrm{miss}})_{\mathrm{x(y)}}^{\mathrm{CellOut}}, \tag{2.11}$$

where each term is computed from the negative of the sum of calibrated cluster energies inside the corresponding objects. The physics objects used for Equation (2.11) must have passed some criteria like the ones defined above (full details can be found in [53]).

Overlap Removal

When candidates passing the object definitions overlap with each other (definition-wise), a classification is required to remove all but one of the overlapping objects. All overlap criteria are based on the simple geometric variable $\Delta R = \sqrt{\Delta\phi^2 + \Delta\eta^2}$, based on previous studies [46]. They are generally applied in the following order:

1. If an electron and a jet are found within $\Delta R < 0.2$, the object is interpreted as an electron and the overlapping jet is ignored.
2. If a muon and a jet are found within $\Delta R < 0.4$, the object is treated as a jet and the muon is ignored.
3. If an electron and a jet are found within $0.2 \leq \Delta R < 0.4$, the object is interpreted as a jet and the nearby electron is ignored.

Part II.

Estimation of the $Z \to \nu\nu$ background to New Physics searches in ATLAS

Chapter 3.

Introduction

Having covered the necessary theoretical and experimental foundation in the first part, this second part presents the main work carried out both theoretically and experimentally in three chapters: Chapter 3 (this chapter) serves as the formal introduction and motivation to the main subject of the thesis. Chapter 4 then follows to present the Theoretical Studies, and Chapter 5 the Experimental Studies.

For this chapter, the introduction starts with Section 3.1 where the idea of using experimentally simpler processes, like prompt photon production, to calibrate experimentally-harder processes, like Z boson production is posed. Section 3.2 then follows to explicitly outline the experimental challenges involved when it comes to measurements of the Z boson decaying to neutrinos ($Z_{\nu\nu}$) and their importance for background estimates in Beyond the Standard Model (BSM) searches. In Section 3.3, the motivation for specifically choosing $\gamma + \text{jets}$ events to calibrate Z boson production is given. Finally, Section 3.4 summarises `ZfromGamma`- the method/algorithm designed for this purpose.

3.1. Calibrating physics processes via cross-section ratios

Given two processes A and B and their differential cross sections $d\sigma/dx$ versus some observable x, we define the cross section ratio $R_{A/B}(x)$ simply to be the ratio:

$$R_{A/B}(x) = \frac{d\sigma(A)/dx}{d\sigma(B)/dx}. \tag{3.1}$$

Henceforth the A/B subscript and the argument x, are only printed as required by context. As an alternative shorthand, the notation A/B may be used when the processes are of primary concern rather than the ratio itself.

If the two processes are kinematically similar in some regime, then the cross section ratio may have various nice properties, such as a relatively simple functional form (which may be approximately constant), cancellation of uncertainties and minimal dependence on other parameters. Ratios are hence of great utility within experimental analyses, with applications such as:

1. To estimate experimentally *difficult* Standard Model (SM) backgrounds to new physics searches by using experimentally *easier* processes. Their theoretical ratio R can be used to translate between the two processes, as has been done for the $Z_{\nu\nu}$+jets and $W_{\ell\nu}$+jets backgrounds via the $Z_{\nu\nu}/\gamma$, $Z_{\nu\nu}/Z_{\ell\ell}$ and $W/Z_{\ell\ell}$ ratios [54, 55]. An astute choice for the calibrating process can minimise statistical uncertainties, *e.g.* when estimating Z boson using W boson and photon measurements [56].

2. To make precision measurements of SM physics (focusing in regions of phase space where new physics is not expected or has been excluded by other searches), *e.g.* the W/Z ratio measurement [57]. This is facilitated by the cancellation of systematic uncertainties associated to the individual cross sections in the numerator and denominator.

3. To cross-check direct cross section measurements of one process with respect to another similar process, *e.g.* various flavours of leptonic Z boson decays, $Z_{\ell\ell}$ ($\ell = e, \mu, \tau$).

4. Conversely to point 2 above, to test for signs of new physics (focusing in the unexplored regions of phase space). The precision of these measurements is well suited to detecting discrepancies with the SM predictions.

This thesis is primarily concerned with addressing point 1 above, with points 2 and 3 being complementary aspects of the method to be discussed. Specifically, it covers a method in which Z boson production is regarded as the experimentally difficult process and photon production as the *calibrating* process (the reasons to choose photons will be discussed in Section 3.3). The power of the method is illustrated by calibrating the most experimentally challenging manifestation of the Z boson: where it decays to a pair of *invisible* neutrinos ($Z_{\nu\nu}$). This forms a particular important background to Beyond-the-Standard-Model (BSM) searches targeting $E_{\mathrm{T}}^{\mathrm{miss}}$ signatures. Its application to and results

for one such search, namely the ATLAS SUSY search for squarks and gluinos in the "zero lepton" channel (here abbreviated as 0ℓ where $\ell = e, \mu$, see Section 1.2.3) [54, 58] are presented. However, the generality of the method means that it can be adapted to any suitable BSM search or used for other purposes, *e.g.* for points 3 and 4 above, so this thesis is intended to serve as a general "manual" for estimating/calibrating Z boson rates from photon events.

3.2. The challenging $Z_{\nu\nu}$ background

When searching for BSM signals (S), the SM processes become a background (B). The predominant search strategy (Section 1.2.3) has been to test the data for an excess of events above the SM expectation. Although different significance tests exist to resolve new signals, they all require first the determination of the total background with sufficient *precision*. Fundamental to this strategy is also to perform the search in regions of phase-space optimised for discovery (event selections characterised by a large S/B yield), referred to as Signal Regions (SRs). However, the disparity between BSM and most SM cross-sections means that even in the SRs the SM backgrounds can contribute significantly to the event counts in the presence of signal. Such arguments motivate the dedicated background studies in ATLAS such as the one presented here.

The $Z_{\nu\nu}$ background is experimentally challenging for the 0ℓ search mainly because of the following reasons:

- **Invisible neutrinos:** The complication when invisible particles are produced in the final-state of an event is that the individual values of their energy-momentum vectors are unknown. From momentum conservation along the transverse plane (see Section 2.2.1), it is only possible to obtain a total $E_{\mathrm{T}}^{\mathrm{miss}}$ vector ($-\sum_i p_{i\mathrm{T}}$), which includes all sources of transverse momentum imbalance in the event (true and fake):

$$E_{\mathrm{T}}^{\mathrm{miss}} = \not{E}_{\mathrm{T}}^{\mathrm{true}} + \not{E}_{\mathrm{T}}^{\mathrm{fake}} \tag{3.2}$$

  The only expected sources of true $E_{\mathrm{T}}^{\mathrm{miss}}$ ($\not{E}_{\mathrm{T}}^{\mathrm{true}}$) from SM processes are neutrinos, which at the LHC are mostly produced in the leptonic decays of the weak bosons $W \to \ell\nu$ ($\sim 22\%$), $Z(\to \nu\nu)$ ($\sim 20\%$) and heavy-flavour quarks $b \to \ell\nu$ ($\sim 11\%$ [5]).

  However, a fake component ($\not{E}_{\mathrm{T}}^{\mathrm{fake}}$) is also expected due to experimental effects, *e.g.* systematic errors like jet mismeasurements or non-collision backgrounds like

cosmic rays. The key point is that it is not possible to tell apart the different components.

- **Irreducibility:** A background becomes *irreducible* if it has exactly the same final-state as the targeted signature in the BSM search, making it impossible, even in a perfect detector, to entirely eliminate its contribution from the total event count. Only an *estimate* for it can be made. Consequently, irreducible backgrounds tend to be amongst the most dominant contributions to the total background. Clearly, for all BSM searches involving $E_{\mathrm{T}}^{\mathrm{miss}}$ + jets and no leptons, like the 0ℓ search, $Z_{\nu\nu}$ is the irreducible SM background – $Z_{\nu\nu}$ events typically pass the SR selections due to the invisible Z recoiling with large p_{T} against the hadronic activity to produce substantial true $E_{\mathrm{T}}^{\mathrm{miss}}$.

One potential source of estimates for SM backgrounds is of course Monte Carlo (MC) simulation. But, despite the sophistication and versatility of MC event generators nowadays, there remain technical and theoretical limitations, *e.g.* calculation of multileg matrix-elements and their use in simulation of SM background events to new physics searches. Various examples of disagreement between data and simulation demonstrate the pitfalls of relying only on limited matrix-elements and parton showering when probing extreme regions of phase space, *e.g.* those involving multijets and $E_{\mathrm{T}}^{\mathrm{miss}}$ [59]. It is hence essential to use *data-driven* methods, i.e. those that extract background estimates from data instead of purely from simulation. How much the method relies on data may be to a greater or lesser extent, *e.g.* the data may be used purely for normalisation, but it may also drive other details of the estimate. Insofar as the method to be discussed here makes use of MC to some extent, *e.g.* to determine the cross section ratio $R_{Z/\gamma}$, it can be considered as rather *partially* data-driven.

3.3. Using γ events to calibrate Z boson normalisation

It is most straightforward to choose the calibration process to be as similar as possible to the process to be estimated. In principle, for $Z_{\nu\nu}$ + jets the first such option would be $Z_{\ell\ell}$ + jets ($\ell = e, \mu$). Being a well-understood process that can be cleanly measured, by treating the lepton pair momentum as an estimator of the true $E_{\mathrm{T}}^{\mathrm{miss}}$, an event sample of pseudo-$Z_{\nu\nu}$ + jets events can be produced, where the theoretical cross section ratio only

differs by the branching ratio. In practice, however, the number of $Z_{\ell\ell}$ + jets events in control samples tends be too small to do this with sufficient precision ($Br(Z_{\ell\ell}) \sim 6.7\%$ versus $Br(Z_{\nu\nu}) \sim 20\%$). Indeed, the smallest theoretical uncertainty is expected from using $Z_{\ell\ell}$ ($\sim 0.01\%$ [60]), but the fundamental problem is that the poor statistics of this process could lead to quite the opposite, *e.g.* by requiring extrapolations from looser to harder selections (as has been done in the 0ℓ search for this calibrating process [54]). The next option would be to use the other weak boson, $W_{\ell\nu}$, but in this case the modest gain in statistics with respect to $Z_{\ell\ell}$ is counteracted by larger theoretical uncertainties with respect to $Z_{\nu\nu}$ and reduced purity in the experimental event selection.

But one vector boson remains: the photon γ. Having a much higher production rate with respect to $Z_{\ell\ell}$ and $W_{\ell\nu}$ (there is no branching ratio suppression for photon production), as shown in Figure 3.1(a), it offers the best statistics, and thus is a good alternative as long as the theoretical uncertainties can be kept at a competitive level. As will be shown in Chapter 4 and Section 5.5.3, and illustrated in Figure 3.1(b), the Z boson and γ production processes become very similar at high boson p_{T} ($p_{\mathrm{T}} \gg m_Z$). At this point, the only expected difference in rate comes from their electroweak couplings to quarks, which are very well determined. Given that the Z and γ η distributions converge at high boson p_{T}, the dependence of the cross-section ratio on the p_{T},

$$R_{Z/\gamma} = R_{Z/\gamma}(p_{\mathrm{T}}) = \frac{\mathrm{d}\,\sigma(Z + \mathrm{jets})/\,\mathrm{d}\,p_{\mathrm{T}}}{\mathrm{d}\,\sigma(\gamma + \mathrm{jets})/\,\mathrm{d}\,p_{\mathrm{T}}} \tag{3.3}$$

makes this a natural parameterisation for the ratio determination. The ratio will also prove to be robust with respect to both theoretical uncertainties and experimental effects, which should be similar for both processes and therefore cancel in the ratio. Furthermore, the event selections of BSM searches like 0ℓ are characterised by high-p_{T} requirements, where $R_{Z/\gamma}$ is relatively constant with respect to event kinematics (see Figure 3.1(b)).

Therefore, given all the reasons above, it can be concluded that the *measured* rate of γ + jets production, coupled with theoretical knowledge of the ratio of Z and γ SM cross-sections can be used to accurately predict the $Z_{\nu\nu}$ background.

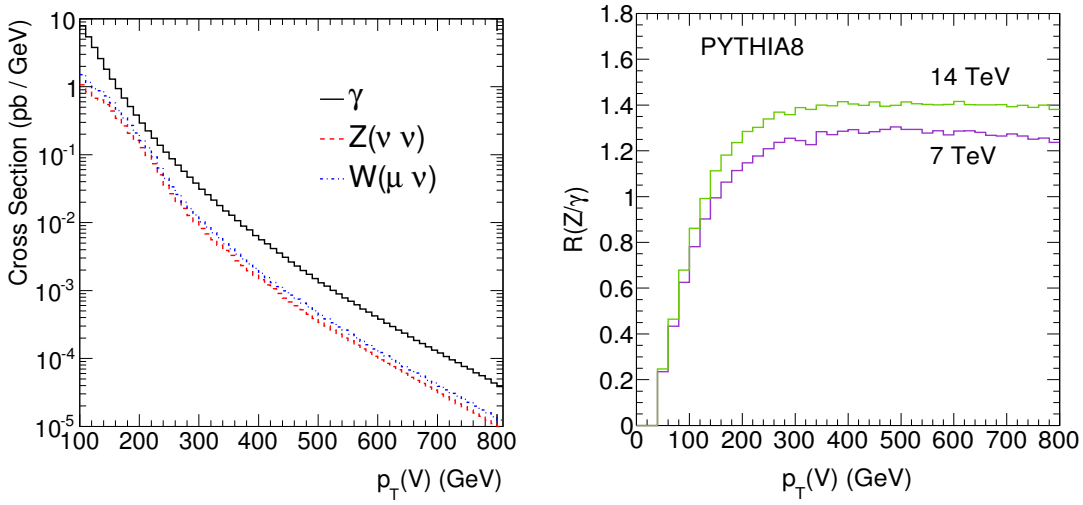

(a) (b)

Figure 3.1.: *(a) Differential cross section as a function of vector boson* p_{T} *for the processes* $pp \to V + X$ *with* $V = Z_{\nu\nu}, W_{\ell\nu}$ *and* γ *at* $\sqrt{s} = 7$ TeV *based on LO* $V + 1$ *parton Matrix Elements. The* $\gamma +$ *jets process yields the largest rate; and (b)* Z/γ *ratio showing the simple relationship at high* p_{T} *where a plateau is reached. Both plots are from* `PYTHIA8`.

3.4. `ZfromGamma` Method Overview

Although theoretically only the knowledge of $R_{Z/\gamma}(p_{\mathrm{T}})$ is enough to translate between the two processes, experimentally additional corrections need to be considered. The experimental method suggested here will be referred throughout the thesis as "`ZfromGamma`" and is based on the use of a control sample (here referred to as "Control Region" CR) and a "Transfer Function" TF to make the *experimental* Z/γ conversion. The `ZfromGamma` method and its multiple applications are summarised in Figure 3.2. First, an inclusive sample of prompt photon candidate events $(\gamma + X)$ are selected from data as specified in Section 5.3. At this stage, the results can be cross-checked with prompt photon cross section measurements as in references [49, 61] (Appendix B). The next step depends on the process to be calibrated. For example, if aiming for an estimate of inclusive Z boson rates $(Z + X)$, the only additional step would be to apply the Transfer Function TF_Z which has the effect of converting a number of photon events N_γ to Z boson events:

$$N_Z(p_{\mathrm{T}}) = \mathrm{TF}_Z(p_{\mathrm{T}}) \cdot N_\gamma(p_{\mathrm{T}}) \tag{3.4}$$

Hence, for a given p_{T}, TF_Z can be regarded as an overall normalisation factor applied to a control sample of the chosen calibrating process to obtain an estimate for the process

of interest. As will be discussed later, TF_Z mainly depends on the boson p_T and is given by,

$$\mathrm{TF}_Z(\eta, p_\mathrm{T}) \to \mathrm{TF}_Z(p_\mathrm{T}) = \frac{P(p_\mathrm{T})}{A^\gamma(p_\mathrm{T}) \cdot \varepsilon^\gamma(p_\mathrm{T})} \cdot R_{Z/\gamma}(p_\mathrm{T}) \tag{3.5}$$

where $P(p_\mathrm{T}) = (1 - f_{bkg}(p_\mathrm{T}))$ is the *purity* of the sample; $f_{bkg}(p_\mathrm{T})$ being the fraction of events other than direct photon production, *i.e.* the background in the photon sample (Section 5.5.2), $A^\gamma(p_\mathrm{T}) \cdot \varepsilon^\gamma(p_\mathrm{T})$ is a correction to account for experimental effects from the detector acceptance and reconstruction efficiency of reconstructed photons (Section 5.5.1) and $R_{Z/\gamma}(p_\mathrm{T})$ is the cross-section ratio already discussed. $A^\gamma(p_\mathrm{T})$ is by definition the fraction of the photon η distribution at a given p_T that falls within the η range considered in the analysis; while ε^γ and P have both been shown to change little with η [49] (also see Tables B.1-B.3).

So far, the conversion denoted by Equation (3.5) is agnostic in the decay modes of the Z boson, so the next branch in Figure 3.2 is to represent the possibility to specialise the TF to a particular decay mode: assuming that the Z boson decays invisibly to neutrinos, but retaining inclusiveness in the rest of the event ($Z_{\nu\nu} + X$). In order to simulate the $Z_{\nu\nu}$ kinematics, the prompt photon γ_1 has to be "neutrinofied", meaning that its p_T is treated as the true $E_\mathrm{T}^\mathrm{miss}$ in $Z_{\nu\nu}$ events ("$p_\mathrm{T}(\gamma_1) \to \not{E}_\mathrm{T}^\mathrm{true}$" in Figure 3.2). Then, the TF has to be scaled by the $Z_{\nu\nu}$ branching fraction ($\mathrm{TF}_{Z_{\nu\nu}}$ in Figure 3.2).

For an estimate of $Z_{\nu\nu}$ *background* given a tighter event selection, *e.g.* for a BSM search, the TF needs to be computed in a suitable Control Region ($\mathrm{TF}^\mathrm{CR}_{Z_{\nu\nu}}$ in Figure 3.2), and to define the Control Region (CR) it may be sufficient to replicate the SR selection, after applying the neutrinofication step (Section 5.4). Applying $\mathrm{TF}^\mathrm{CR}_{Z_{\nu\nu}}$ to the photon events selected in the CR therefore results in the $Z_{\nu\nu}+\mathrm{jets}$ background estimate. This is acceptable as long as: (i) the SR selection is tighter than the $\gamma + X$ sample selection, and (ii) the statistics of the $\gamma + X$ sample at the SR are large enough in order to avoid extrapolations, *e.g.* from a looser selection. In general, both (i) and (ii) straightforwardly apply. One potential complication arises when multiple SR selections lie in kinematic regions with differing values/forms for $R_{Z/\gamma}(p_\mathrm{T})$. In such cases, one might need to determine $R_{Z/\gamma}(p_\mathrm{T})$ separately for each SR, or account better for the variation of the ratio with respect to other kinematic quantities. This is particularly important when aiming to minimise theoretical uncertainties.

The method just described will be referred throughout this thesis simply as "`ZfromGamma`". Regarding its historical background, the first developments were done by CMS in 2008 [62],

and the first attempt to implement it in ATLAS was in 2010 for the first SUSY 0ℓ search [63]. These results were presented at the Moriond'11 conference and hence are considered the first of their kind in ATLAS. They are summarised in Appendix C.1. However, it was only in 2011 that a robust theoretical assessment became available in two studies: $Z/\gamma + 2$ jets NLO studies [64] and the calculation of associated uncertainties, experimental effects and robustness of the $R_{Z/\gamma}$ ratio [56]. The second of these two is what is presented in Chapter 4. The method has since become the mainstream to estimate the $Z_{\nu\nu}$ background in the multiple analysis rounds of the SUSY 0ℓ search in ATLAS. In chronological order, results have been provided for the Moriond'11 [58], PLHC'11 [65], EPS'11 [54] and Moriond'12 [66] conferences, which are documented in Appendices C.1, C.2, C.3 and Chapter 5 respectively. Methods similar to this have also been implemented in other experiments like CMS (Section 6.1.1) and CDF (*e.g.* WW/ZZ search [67]).

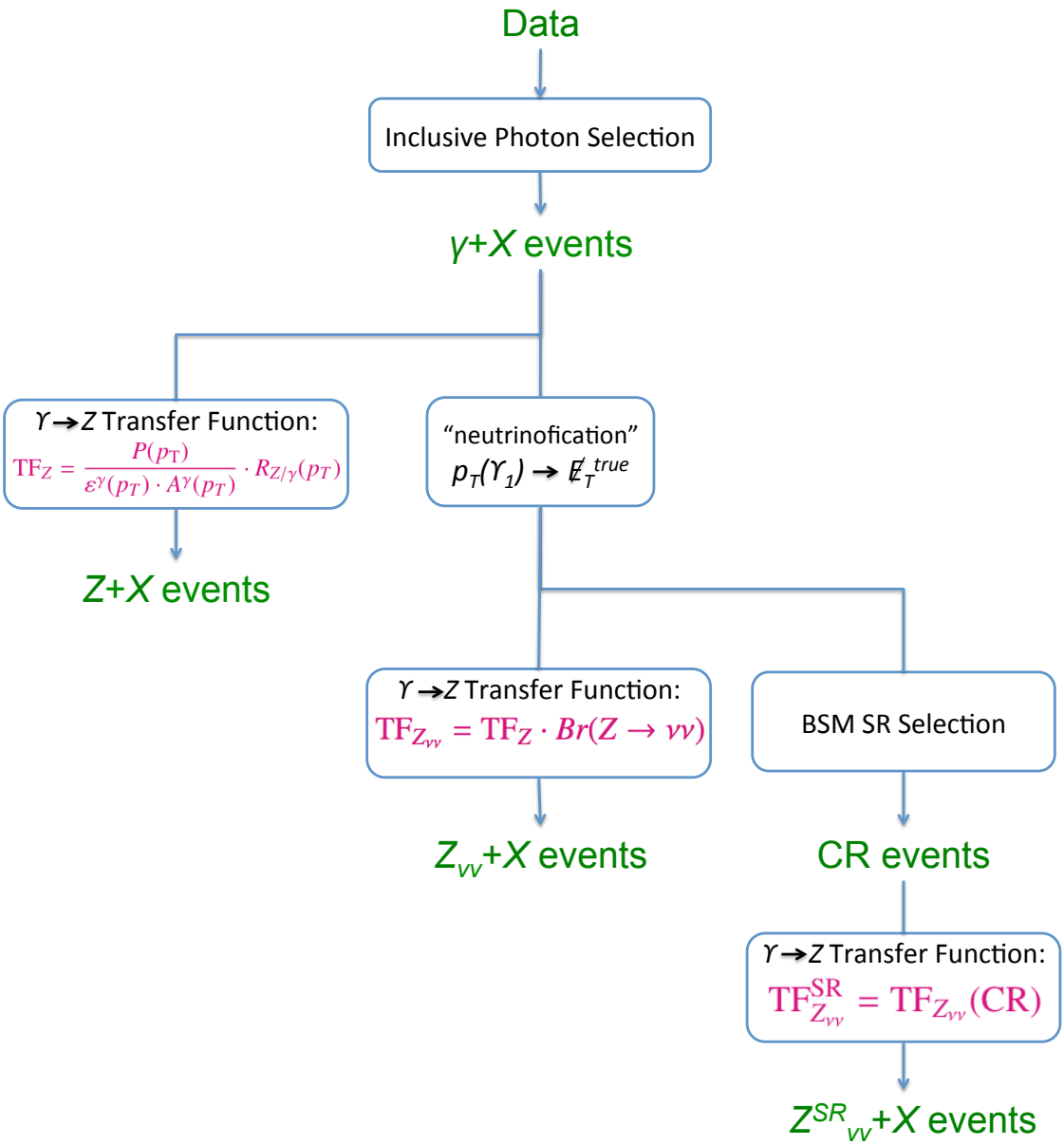

Figure 3.2.: *Schematic charts summarising the different applications of the* `ZfromGamma` *method and steps required for each. The leftmost part of the diagram illustrates how to get a general estimate of inclusive Z rates from inclusive γ rates; the centered and rightmost parts correspond to more specific estimates of $Z_{\nu\nu}$ events and $Z_{\nu\nu}$ + jets background in a BSM $E_{\mathrm{T}}^{\mathrm{miss}}$ + jets search respectively. The meaning of the variables and abbreviations are specified elsewhere in the text.*

Chapter 4.

Theoretical Studies

The aim of this chapter is to present the main theoretical work carried out for this thesis. This work was done in collaboration with S. Ask, M. A. Parker, M. E. Shea and W. J. Stirling from the University of Cambridge and was published in 2011 [56]. This chapter is hence merely a summary of this reference and the specific contributions from the author are specified at the end of this introduction.

The motivation for these theoretical studies arose from the need to know precisely the relationship between the Z boson and γ, specifically their production cross-section ratio, in order to implement the `ZfromGamma` method described in Chapter 3. Moreover, it was necessary to show that this ratio was robust with respect to experimental effects and event selections for the method to be considered competitive. In addition, as pointed in Section 3.4, at the time of the first implementation there were few theoretical studies available.

The structure of this chapter is as follows: Section 4.1 presents the motivation for determining the Z/γ cross-section ratio in such detail. Sections 4.2 and 4.3 present the studies of this ratio for final states involving 1, 2 and 3 hadronic jets, using both the leading–order parton shower Monte Carlo program `PYTHIA8` [68] and the leading–order matrix element program `GAMBOS` [69]. This enabled an understanding of the underlying parton dynamics in both processes, and to quantify the theoretical systematic uncertainties in the ratio. Section 4.4 presents the extension of these parton-level studies to full event simulation and how, using a typical set of experimental cuts from an ATLAS SUSY 0ℓ search, the net theoretical uncertainty in the ratio is estimated to be of order $\pm 7\%$, while uncertainties associated with full event simulation are found to be small. Lastly, Section 4.5 presents a summary of these studies where the highlight is a quoted overall accuracy of the method, excluding statistical errors, of order 10%.

Supervised by S. Ask and M. A. Parker, the author performed most of the PYTHIA-related work and plots, specifically in Section 4.3.1 (Figures 4.4, 4.5); Section 4.3.2 (Figures 4.7, 4.8) and Section 4.3.3 (Figure 4.11); the plots in Section 4.4 were made by the author in collaboration with S. Ask and all the other plots not quoted above *e.g.* GAMBOS and MSTW08 related, were made by M. E. Shea and W. J. Stirling.

4.1. The Z/γ Ratio

Although the Z and γ cross sections have a simple theoretical relationship at high vector boson p_T, care is needed when estimating the theoretical ratio of Z and γ SM cross sections. Especially for more than one jet, there are matrix element contributions to the cross section that may not be included in parton shower Monte Carlos such as PYTHIA [68, 70] or HERWIG [71]. In addition, it is important to quantify the theoretical *uncertainty* on the ratio (from the choice of PDFs, QCD scales etc.), since this will propagate through to the overall uncertainty on the background estimate. A detailed theoretical study of the $V+$ jets ($V = \gamma, Z$) cross sections and uncertainties is therefore required, to supplement the information from Monte Carlo event simulation. Finally, it is important to establish how well the theoretical precision survives under conditions closer to the experimental analysis, *e.g.* including effects from full event simulation, jet reconstruction, detector acceptance, experimental cuts etc.

Since our main interest is in estimating the missing E_T distribution in events with multijets, we focus primarily on the inclusive vector–boson (Z or γ) transverse momentum (p_T) distributions, particularly at high $p_T \gg M_Z$. We first analyse the ratio of the $Z+1$ jet and $\gamma + 1$ jet p_T distributions from a general theoretical perspective using a program for up to and including 3 jets based on exact leading–order parton–level matrix elements. We then reproduce these results using PYTHIA8 [68, 70] (at parton level). This establishes that the ratio of the two process cross sections is theoretically robust, particularly at high p_T. We predict the value of the cross section ratio using 'typical' experimental cuts, and estimate its theoretical uncertainty. We then consider the corresponding 2– and 3–jet cross sections, again comparing the exact leading–order matrix element results with those obtained from PYTHIA8. Finally, we use our results to assess the systematic uncertainties on the missing transverse energy + jets background obtained from the photon + jets cross section using this method. The ratios predicted by the two alternative approaches, based on "pure" matrix elements or parton showers, are illustrated as well as used to

constrain the systematic uncertainties related to the commonly used, and also more optimal, scenario where matrix elements are matched with the parton shower used in the MC simulation. In the following sections, V refers to the vector bosons Z or γ.

In a recent paper [64], a similar study was carried out for the $V + 2$ jets cross sections using two approaches: next–to–leading order in pQCD applied at parton level, and exact leading–order matrix elements interfaced with parton showers (ME+PS) as implemented in `SHERPA` [72]. Agreement between our results and those of [64] confirms that over much of the relevant phase space, and particularly for inclusive quantities, the effect of higher–order corrections on the leading–order Z, γ cross section ratios is small. In our study, we consider also the 1– and 3–jet ratios and, more importantly, we extend the analysis to hadron level using `PYTHIA8`. This allows for an analysis similar to the ones within the LHC experiments. We also examine the dependence of the ratios on the parton distribution functions, since these receive different weightings in the Z and γ cross sections and therefore do not exactly cancel in the ratio. Of course ultimately one would wish to evaluate all these cross sections consistently at next–to–leading order, using the methods described in [64] for the 2–jet case.

4.2. V+jets production in leading–order perturbative QCD

In the Standard Model, the coupling of photons and Z bosons to quarks q are, respectively,

$$-ieQ_q\gamma^\mu \qquad \text{and} \qquad \frac{-ie}{2\sin\theta_W\cos\theta_W}\gamma^\mu(v_q - a_q\gamma_5), \tag{4.1}$$

where Q_q, v_q and a_q, are respectively the electric, vector and axial neutral weak couplings of the quarks, and θ_W is the weak mixing angle. For hadron collider processes such as $q\bar{q} \to V+ng$ or $qg \to qV+(n-1)g$, both of which contribute to $V+n$ jets production, the matrix elements squared will contain factors of Q_q^2 or $(v_q^2 + a_q^2)/4\sin^2\theta_W\cos^2\theta_W$ for γ or Z respectively. The only other difference in the matrix elements comes from the non–zero Z mass[1], which will appear in the internal propagators and phase space integration. Sample Feynman diagrams for $V + 1$ jet production are shown in figures 4.1(a,b), and for $V + 2$ jet production in figures 4.1(c–f).

[1]For the purposes of this discussion, we treat the Z as an on–shell stable particle. In practice, Z decay will also form part of the matrix elements.

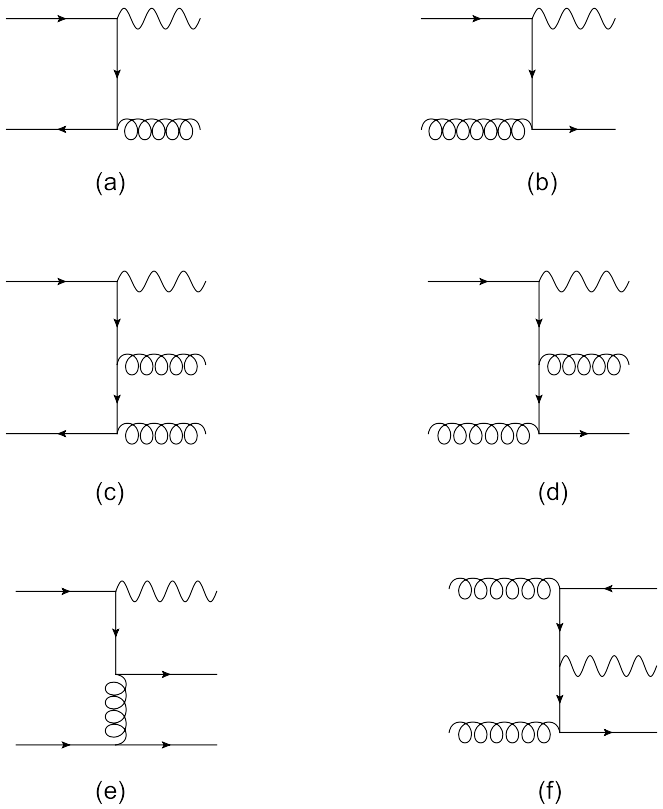

Figure 4.1.: *Sample Feynman diagrams for $V + 1, 2$ jets production, where $V = \gamma, Z$.*

For high $p_T(V)$ ($\gg M_Z$) production we would therefore expect the Z and γ cross sections to be in the ratio

$$R_q = \frac{v_q^2 + a_q^2}{4 \sin^2 \theta_W \cos^2 \theta_W Q_q^2}. \tag{4.2}$$

Substituting $\sin^2 \theta_W = 0.2315$, we obtain $R_u = 0.906$ and $R_d = 4.673$. In practice, of course, the cross sections will receive contributions from *all* quark flavour types, and so $R = \sigma(Z)/\sigma(\gamma)$ will be a weighted average of the R_u and R_d values, *i.e.*

$$R = \frac{Z_u \langle u \rangle + Z_d \langle d \rangle}{\gamma_u \langle u \rangle + \gamma_d \langle d \rangle} \tag{4.3}$$

in an obvious notation, where $\langle u \rangle$ and $\langle d \rangle$ are the typical values of the u–type and d–type quark parton distribution functions (PDFs) in the cross section. Figure 4.2(a) shows R as a function of the ratio $\langle d \rangle / \langle u \rangle$. We would expect that where large x values are probed, for example at very high $p_T(V)$, the ratio would approach the R_u value since

$d(x)/u(x) \to 0$ as $x \to 1$, *e.g.* suggested by Figure 4.2(b). For moderate p_T values at the LHC, $\langle x \rangle \sim 0.1$, which corresponds to $\langle d \rangle / \langle u \rangle \simeq 0.6$ and therefore $R \simeq 1.4$.

The simple connection (4.3) between the vector boson cross section ratio and the initial state quark flavour is, however, broken for $n_{\rm jets} \geq 2$. Consider for example the sample Feynman diagrams of figure 4.1(e) and (f). For the former 'four–quark' diagrams, the vector boson can be emitted off any of the external quark legs and so the numerator and denominator of the ratio R depend on more complicated products of quark distributions. Because at high x uu scattering will be relatively more dominant than dd scattering, we would expect that the value of R for such processes would be closer to R_u than to R_d, compared to the 1–jet ratio. On the other hand, for the gg–scattering diagrams, figure 4.1(f), the ratio of the corresponding cross sections is (ignoring the Z mass) $R = \sum_q Z_q / \sum_q \gamma_q$, where the sum is over the final state quark (antiquark) flavours, and the dependence on the initial state (gluon) distributions cancels. By way of illustration, with 5 massless flavours we obtain $R = 1.933$. As we shall see below, the four–quark contribution is more important at high p_T than the gg contribution, and the net effect is to reduce R slightly compared to the 1–jet case.

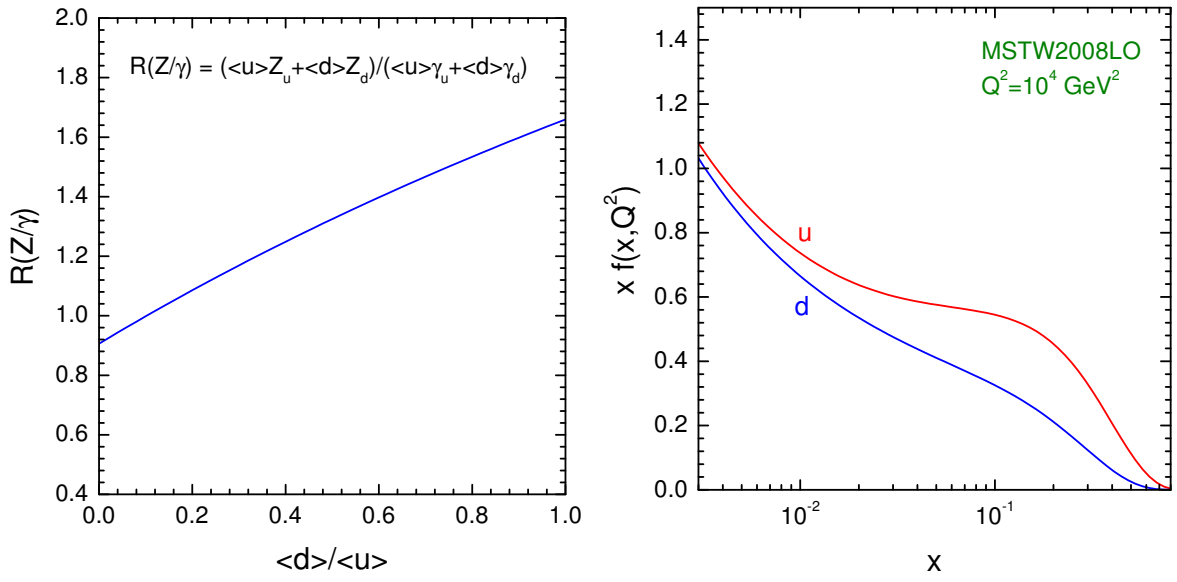

(a) (b)

Figure 4.2.: *(a) Dependence of $R = \sigma(Z)/\sigma(\gamma)$ at the coupling constant level on the ratio of average d and u parton distribution values, see eq. 4.3. (b) u and d quark MSTW2008LO PDFS [73] at $Q^2 = 10^4$ GeV^2.*

Figure 4.3(a) shows the $Z + 1$ jet and $\gamma + 1$ jet cross sections[2] as functions of the vector boson transverse momentum at $\sqrt{s} = 7$ TeV and 14 TeV. Standard PDG values of the electroweak parameters are used, and the PDFs are the leading–order MSTW2008LO set [73] with renormalisation and factorisation scale choice $\mu_R = \mu_F = p_T(V)$, and the Z is treated as an on–shell stable boson. The acceptance cuts are $|y(V, j)| < 2.5$ and $p_T(V, j) > 40$ GeV, where y is the rapidity. Figure 4.3(b) shows the ratio of the Z and γ distributions. We see the expected behaviour of a roughly constant ratio at large $p_T(V) \gg M_Z$ lying between the R_u and R_d values defined above. Although above $p_T \sim M_Z$ the ratio does exhibit a plateau region, at very large p_T we begin to see a slight decrease, as the high–x behaviour of the d/u PDF ratio drives the ratio down towards the R_u value. At 14 TeV, the empirical large–p_T value of $R \simeq 1.4$ is consistent with $\langle d \rangle / \langle u \rangle \simeq 0.6$, see figure 4.2(a). This in turn is consistent with u and d PDFs probed in the $x \sim 0.1$ region, see figure 4.2(b). At the lower collider energy (7 TeV), higher x values are sampled for the same p_T, and the Z/γ ratio decreases slightly, moving towards the R_u value. Note that the ratio curves in figure 4.3(b) can be reasonably well approximated by

$$R = R_0 \left(\frac{p_T^2}{p_T^2 + M_Z^2} \right)^n , \tag{4.4}$$

with $n \approx 1.2$, illustrating the expected Z mass suppression relative to the photon distribution for $p_T < M_Z$.

4.3. Parton level analysis

In order to study the ratio of the Z and γ distributions in a realistic experimental environment, we need to use an event simulation Monte Carlo program. We use `PYTHIA8` for this purpose. At the same time, we want to understand the difference between the scattering amplitudes embedded in `PYTHIA8` and the amplitudes obtained using exact QCD matrix elements for multijet production. For the latter we use the program `GAMBOS`, an adaptation of the Giele et al. `Vecbos` program [69] for $W, Z + n$ jets production, in which the weak boson is replaced by a photon.

First, we compare the `PYTHIA8` and `GAMBOS` results at the parton level. This serves to check the consistency of the results from the two programs, when configured as similarly as possible, and provides a common middle step between the matrix–element (ME)

[2] Expressions for the matrix elements can be found, for example in Chapter 9 of [3].

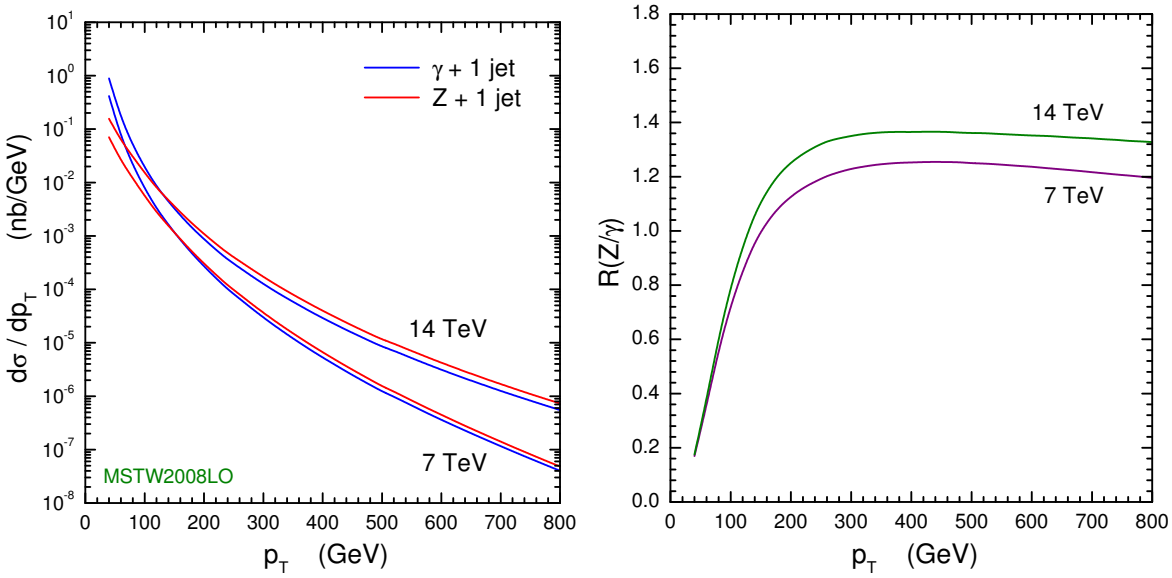

(a) (b)

Figure 4.3.: *(a) Z and γ p_T distributions at $\sqrt{s} = 7$ TeV and 14 TeV, with parameters and cuts as described in the text. (b) Ratio of the Z and γ p_T distributions.*

$V+$ jets results at parton level produced by `GAMBOS` and the results for fully simulated events from `PYTHIA8`.

The `PYTHIA8` results are obtained using the LO ($2 \to 2$) processes, $q\bar{q} \to Vg$ and $qg \to Vq$ where $V = \gamma$ or Z, corresponding to the Feynman diagram types shown in figures 4.1(a,b). Events with ≥ 2 jets are generated by parton showering off the initial and final state partons. This means that processes such as those shown in figures 4.1(c) to 4.1(f) are included, albeit with an approximation to the exact matrix elements, and we can therefore expect differences between `GAMBOS` and `PYTHIA8` results for the Z/γ ratios with ≥ 2 jets.

In order to produce results directly comparable with `GAMBOS`, the following settings are used as default in `PYTHIA8`:

- `PDFs:` MSTW2008LO;
- `Strong:` $\alpha_S(M_Z^2) = 0.13939$, with one loop running;
- `EM:` $\alpha_{EM}(M_Z^2) = 1/127.918$, with one loop running;
- `Weak:` $\sin^2(\theta_W) = 0.2315$;
- `Scales:` Renormalisation and factorisation scales, $\mu_R = \mu_F = p_T(V)$;

- Rapidity, transverse momentum and separation cuts on the final–state Z, γ and jets as described in the previous section.

In the following sub–sections we first compare results for the $V+1$ jet distributions, then discuss the theoretical uncertainties on the corresponding Z/γ ratio, and finally compare the $V+2,3$ jet results from the two programs.

4.3.1. $V+1$ jet results

The LO matrix elements used in the PYTHIA8 processes are the same as those used in GAMBOS for the $V+1$ jet case, and a parton level comparison between the two programs should therefore give identical results. Note that the V and the jet correspond to the outgoing partons of the hard process in PYTHIA8, without any further simulation of the event. The differential Z and γ cross sections and their ratio predicted by PYTHIA8 are shown in figure 4.4 for pp collisions at 7 as well as 14 TeV. The results show the same characteristic features already seen in the GAMBOS predictions in figure 4.3, *i.e.* the Z cross section, excluding any branching ratios, is smaller than the photon cross section at small p_T due to the mass suppression, but is roughly proportional to, and slightly larger than, the γ cross section at $p_T \gg M_Z$. The ratios obtained from PYTHIA8 and GAMBOS are compared in figure 4.5, for 7 TeV and 14 TeV collision energies. Evidently there is good agreement between the two programs, as expected. As seen in the plot, the photon cross sections from the two programs agree perfectly, whereas a small difference between the Z cross sections, $<5\%$, is visible. This difference is due to the way in which the PYTHIA8 generator treats the Z boson as a resonance, in contrast to GAMBOS where the Z is treated as a real particle, and this was confirmed by producing a GAMBOS like process in PYTHIA8 which reproduced the same results. Since the Z boson is generally treated as a resonance in MC programs, this difference is not considered as a source of uncertainty.

4.3.2. Theoretical uncertainties

Having established numerical agreement between the two programs, we can use PYTHIA8 to investigate the theoretical uncertainty on the Z/γ ratio at high p_T. There are a number of sources of these, which we address in turn.

First, we consider the dependence on the PDFs used in the calculation. As argued in section 4.2, the Z/γ ratio at high p_T is sensitive to the d/u parton ratio at large x.

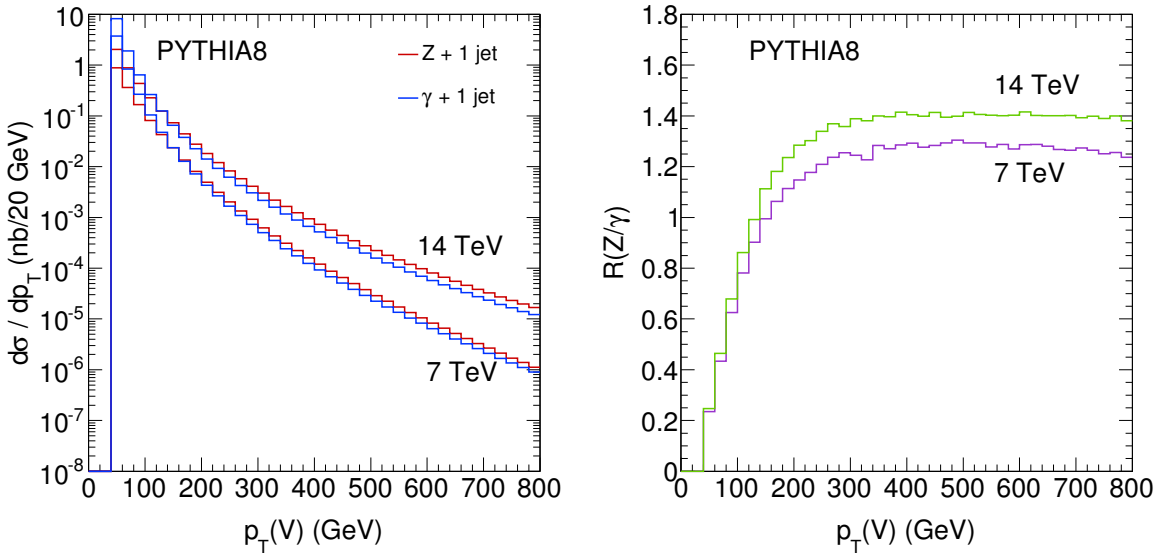

(a) (b)

Figure 4.4.: *(a) Differential cross section as a function of the vector boson p_T for the process $pp \to V + 1$ parton with $V = \gamma, Z$ from* `PYTHIA8`*, and (b) the ratio of these.*

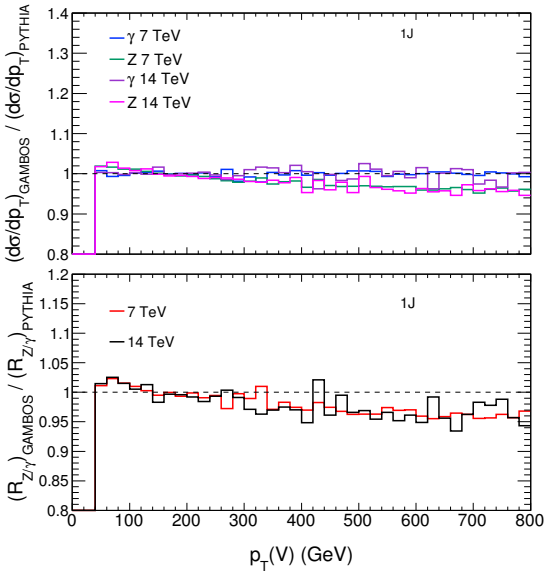

Figure 4.5.: *Effect on the boson p_T and the ratio from using a matrix–element generator (*`GAMBOS`*) and* `PYTHIA8` *at 7 and 14 TeV.*

To study the possible variation in this ratio, we investigate the spread from using the different eigenvectors of the MSTW2008LO set and we compare these predictions with those from two (older) leading–order PDF sets, CTEQ5L [74] and GRV98 [75], shown in figure 4.6. The latter should yield a *conservative* estimate of the PDF dependence. The

impact on the Z and γ distributions and their ratio is shown in figure 4.7. Note that the CTEQ5L and GRV98 PDFs give respectively softer and harder Z and γ p_T distributions, which is an artefact of the underlying quark and gluon PDF behaviour, see figure 4.6(a), but that the effect largely cancels in the ratio. The residual small differences in the cross section ratio can be understood in terms of the corresponding small differences in the d/u ratio for the various sets, shown in figure 4.6(b). We ascribe a conservative $\pm 4\%$ PDF uncertainty to the $R(Z/\gamma)$ ratio at high $p_T(V)$.

In addition to varying the PDFs, we use different choices for the renormalisation and factorisation scales, μ_R and μ_F, in order to mimic the effect of higher–order pQCD corrections not included in either the `PYTHIA8` or `GAMBOS` analyses. In particular, we use multiples of the default scales $\mu_R = \mu_F = p_T(V)$, and two variants of this: the arithmetic and geometric means of the final-state transverse masses in the $2 \to 2$ hard process, $\mu^2_{\text{ari}} = (m^2_{T1} + m^2_{T2})/2 = (2p_T(V)^2 + m(V)^2)/2$ and $\mu^2_{\text{geo}} = m_{T1}m_{T2} = p_T(V)\sqrt{p_T(V)^2 + m(V)^2}$. Note that for the photon, these scales are identical to the default scale $p_T(\gamma)$. Figure 4.8 presents the corresponding impact on the differential cross sections, $d\sigma/dp_T$, as well as the cross section ratio, $R(Z/\gamma)$. The results show that although the variations have significant effects on the differential cross sections, as expected, the Z/γ ratio remains stable in the regime $p_T \gg M_Z$, and for $p_T(V) > 100$ GeV all variations of the ratio are within $\pm 3\%$.

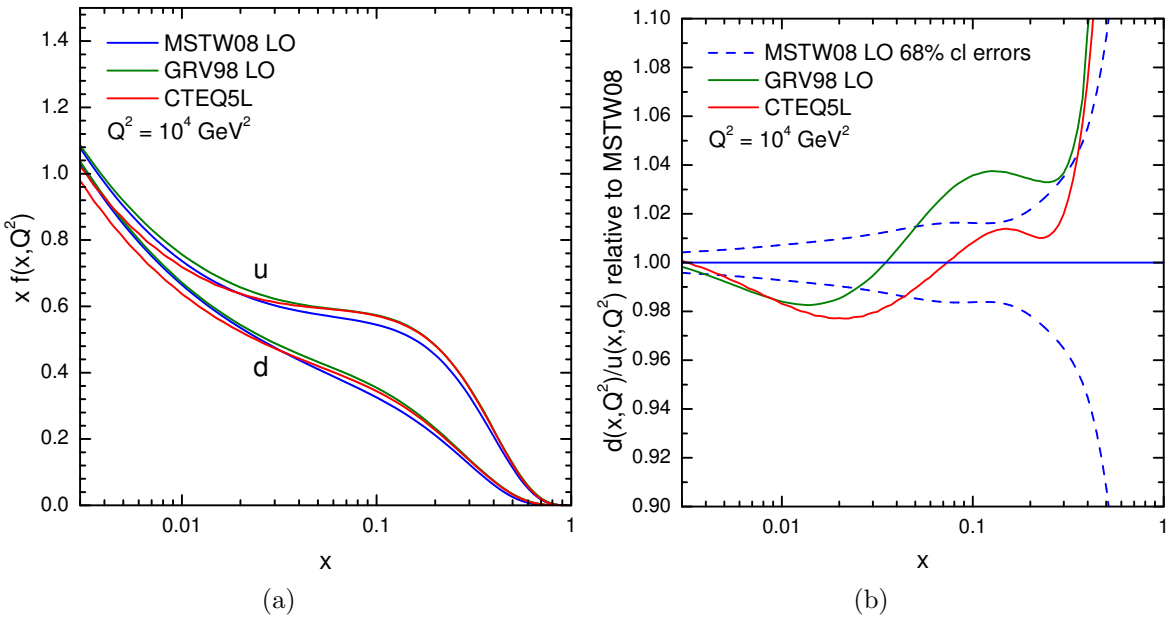

(a) (b)

Figure 4.6.: *(a) Comparison of up and down quark distributions from MSTW2008LO, CTEQ5L and GRV98. (b) d/u ratios compared to MSTW2008LO.*

Indeed the only sizable effect on the ratio related to the scales is observed from the different choices of the scale μ_R, which becomes visible at $p_T \ll M_Z$. Any choice of scale of the form κp_T will of course cancel in the Z/γ ratio, but scales of the form $\kappa\sqrt{p_T^2 + M_V^2}$ will give different results for low $p_T \sim M_V$. The size of this effect was also shown to be consistent with the ratio $\alpha_S(\mu_R(Z))/\alpha_S(\mu_R(\gamma))$ using the same one–loop formula as in `PYTHIA8` and `GAMBOS`, *e.g.* see Figure 4.9. No similar effects are observed from different choices of the factorisation scale μ_F, since the PDFs vary only weakly with the factorisation scale at the x values probed by these cross sections.

Note that in the above analysis we have used the *same* form of scale variation simultaneously in both the numerator (Z) and denominator (γ) cross sections. As pointed out in Ref. [64], this gives a much smaller scale variation than if the scales are varied *independently* in the two cross sections. However, we argue that if we select Z and γ events for which the kinematics of the (colour–singlet) vector bosons and the jets are the same, and if the energies and momenta are large enough such that the Z mass can be neglected (*e.g.* $p_T \gg M_Z$), then the higher–order pQCD corrections to both cross sections should essentially be the same and should therefore largely cancel in the ratio.

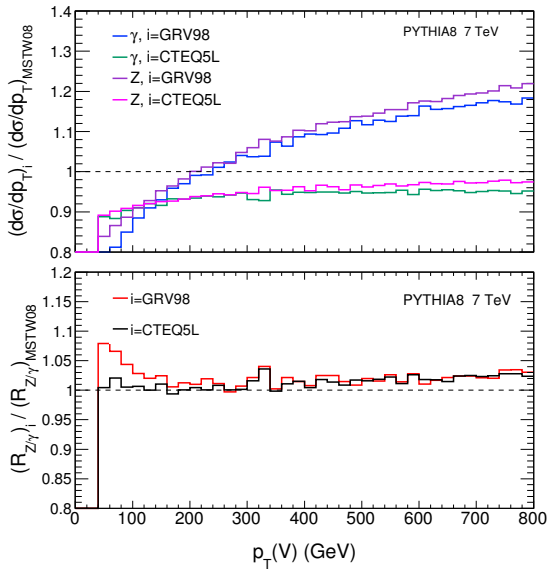

Figure 4.7.: *Effects on (Z, γ) differential cross sections and cross section ratio after varying the PDFs.*

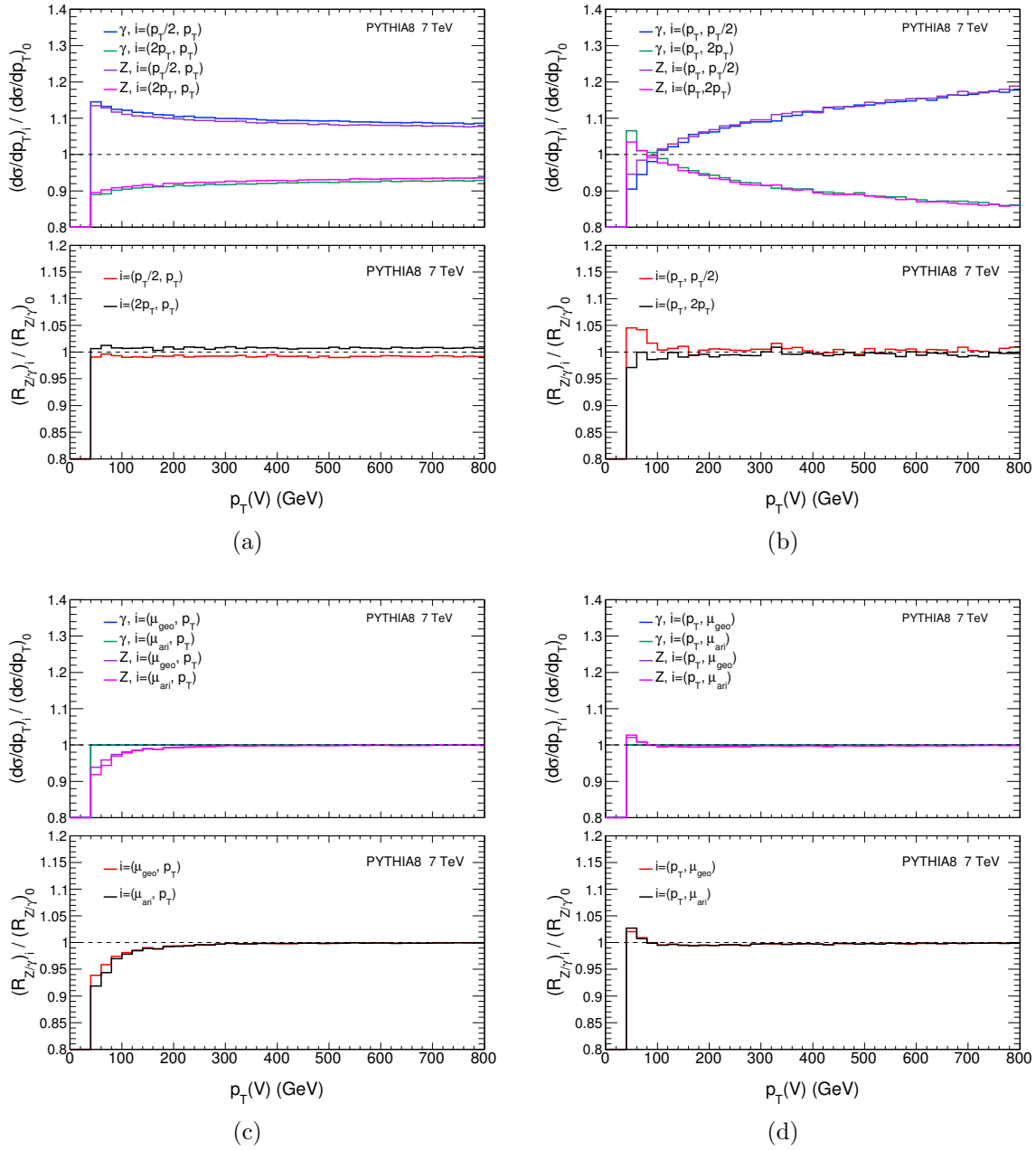

Figure 4.8.: *Effects on (Z, γ) differential cross sections and cross section ratio after varying the scales (μ_R, μ_F). The different μ scales are defined in the text and the denominators correspond to using the default scale choice, i.e. $0 = (p_T, p_T)$.*

4.3.3. $V + 2, 3$ jets results

For the $V + 2$ jets production cross sections there is an additional complication in that the high–p_T photon can be emitted collinearly to a high–p_T quark, with the transverse momentum of the pair being balanced by an 'away side' quark or gluon. For massless

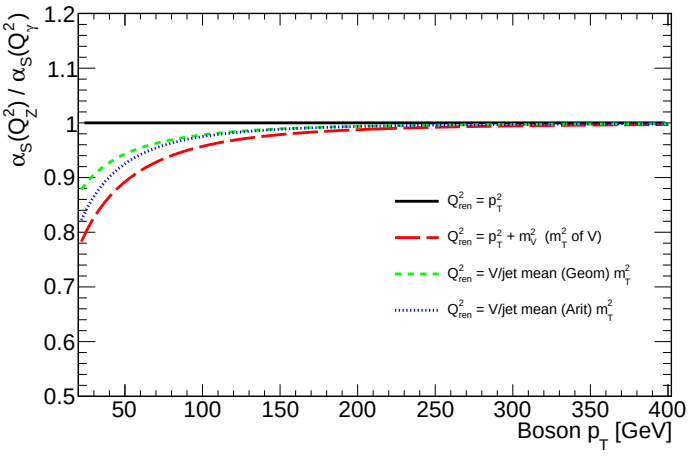

Figure 4.9.: *Expected effect on α_S from using different renormalisation scales Q_{ren} in $R_{Z/\gamma}$. The plot is obtained from a fit to the* PYTHIA8 *MC.*

photons, quarks and gluons the matrix element is singular in this configuration and so the closer the photon is allowed to approach the quark, the smaller the Z/γ ratio becomes, since there is no such collinear singularity for Z production. To regulate the singularity, we impose a $\Delta R(V, j) > \Delta R_{\min}$ isolation cut, where $V = \gamma, Z$ and $j = q, g$.[3] We also, of course, need to impose rapidity, transverse momentum and jet–jet separation cuts on the quark and gluon jets. For illustration, we choose $p_T(j) > 40$ GeV, $|y(j)| < 2.5$ (as for the 1–jet study above), and $\Delta R(j, j) > 0.4$ to represent 'typical' experimental cuts. Figure 4.10(a) shows the ratio of $V + 2$ jet cross sections, as calculated using GAMBOS, for different values $\Delta R_{\min} = 0.05, 0.1, 0.2, 0.4, 0.6$ at 7 TeV. The ratio at high p_T shows the expected dependence on the minimum separation. Note also that the ratio becomes insensitive to the isolation cut when the minimum separation becomes large, since far from the singularity the Z and γ phase space are affected more or less equally. A similar dependence on $\Delta R_{\min}$ is observed for the $V + 3$ jet ratios. From now on we take $\Delta R_{\min} = 0.4$ as our default choice and attribute a $\pm 5\%$ uncertainty of these results based on the difference with respect to $\Delta R_{\min} = 0.6$.

The breakdown of the $Z + 2$ jet GAMBOS cross section at 7 TeV into the different subprocess contributions is shown in figure 4.10(b). We define these to be $q\bar{q} \to Vgg$ scat-

[3]Note that the requirement of photon isolation becomes more subtle beyond leading order in pQCD, since in this case the partonic jets can have non–zero 'width' and the choice of jet algorithm influences the analysis. This issue is addressed in detail in Ref. [64]. In our case we will be studying photon isolation for the full PYTHIA8 event simulation including hadronisation and experimental cuts. Note also that we neglect contributions to the γ cross section involving photon fragmentation functions, *i.e.* $f^{q\to\gamma}(z, Q^2)$. With the strong isolation requirements and high transverse momentum values used in our study, we expect such contributions to be small.

tering (*e.g.* figure 4.1(c)), $qg, gq \to Vqg$ (*e.g.* figure 4.1(d)), $gg \to Vq\bar{q}$ (*e.g.* figure 4.1(f)) and $qq \to Vqq$ (*e.g.* figure 4.1(e)), where a sum over quarks and antiquarks is implied. Note that quark–gluon scattering is by far the most dominant in the kinematic region studied here, and its fractional contribution is roughly independent of $p_T(V)$. The results also show that the second largest contribution in the 2–jets case comes from the qq subprocess, which approximately amounts to 20%. This is in contrast to the 1–jet case, which is dominated by qg and $q\bar{q}$ scattering. The corresponding subprocess breakdown of the $\gamma + 2$ jet cross section is similar.

In figure 4.11(a) we show the $Z/\gamma + 1, 2, 3$ jet `GAMBOS` cross section ratios as a function of $p_T(V)$, with $\Delta R_{\rm min} = 0.4$ and other cuts as before. We see that the 2,3 jet ratios are slightly smaller than the 1 jet ratio at moderate and high p_T. The small difference arises from three effects: (i) the dependence of the 2,3 jet cross sections on $\Delta R_{\rm min} = 0.4$, (ii) the additional qq and gg scattering diagrams, the net effect of which is to decrease the 2,3 jet ratio, as already explained in section 4.2, and (iii) the fact that for a fixed p_T, increasing the number of jets increases the overall invariant mass of the final–state system, and also therefore the values of the parton momentum fractions. This in turn decreases the d/u ratio, and also the Z/γ ratio, see figure 4.2(a).

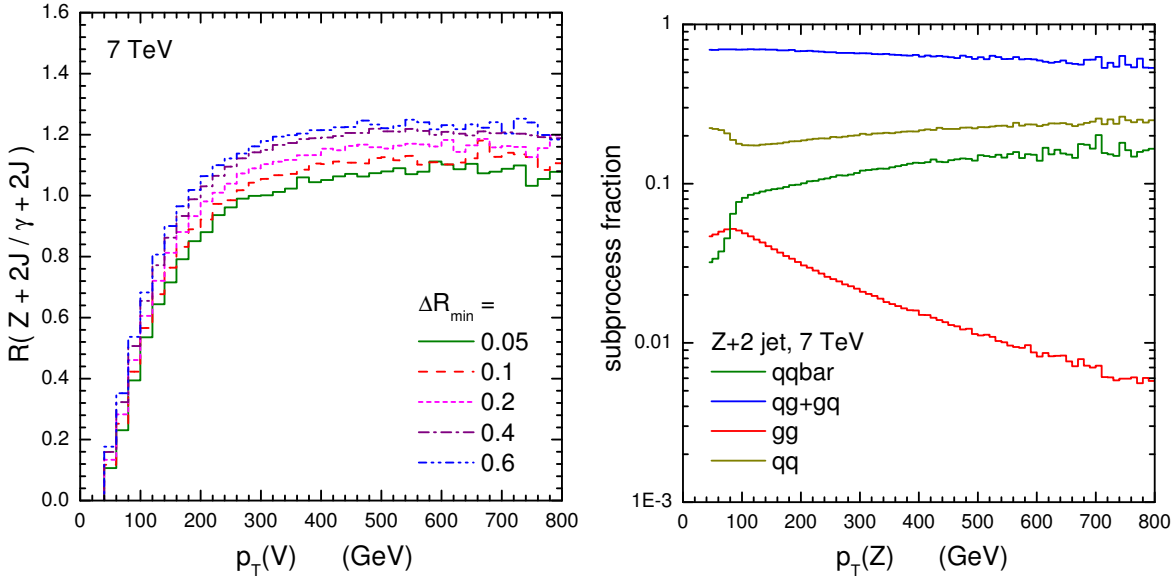

(a) (b)

Figure 4.10.: *(a) Ratio of the $Z + 2$ jets and $\gamma + 2$ jets $p_T(V)$ distributions at 7 TeV, for different values of the $\Delta R(V, j) > \Delta R_{\rm min}$ isolation cut. (b) Breakdown of the $Z + 2$ jet* `GAMBOS` *cross section into the different subprocess contributions defined in the text.*

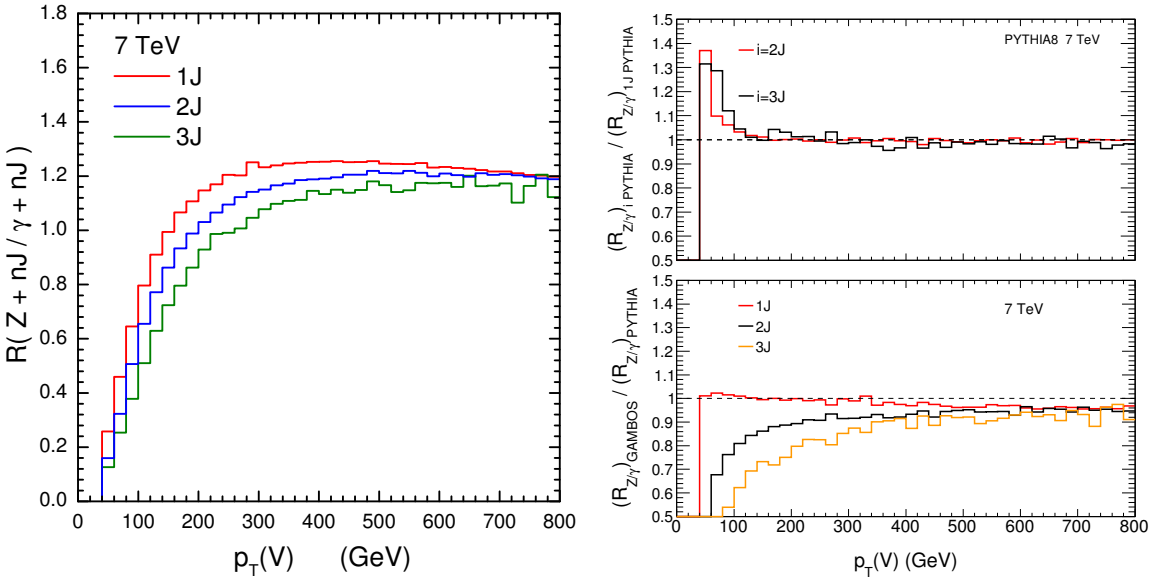

(a) (b)

Figure 4.11.: *(a) $Z/\gamma + 1, 2, 3$ jet* GAMBOS *cross section ratios as a function of $p_T(V)$, with the isolation cut $\Delta R_{\min} = 0.4$. (b) Effect from multijet requirement on the* PYTHIA8 *ratio (upper) and difference with respect to* GAMBOS *(lower).*

For more than one jet, the additional jets in the PYTHIA8 simulation are produced by parton showering. In order to characterise the difference with respect to exact MEs, the following events were used for the 2– and 3–jet results from PYTHIA8 at the parton level, where the aim is to produce events with a similar parton level topology to the GAMBOS events based on the multijet MEs. In the 2–jet case, events were generated with both initial (ISR) and final state radiation (FSR) enabled and only those with exactly 2 jets within the allowed p_T and y acceptance were considered. These jets either correspond to the parton from the hard scatter together with an ISR emission or from events with no accepted ISR emission, but where the hard parton, due to FSR, branches into two partons within the allowed acceptance. In addition, only events with the required $V-$ jet and jet–jet ΔR separation were considered. The same event selection was used for the parton level 3–jet case, where the three jets either correspond to the hard parton together with two ISR emissions, or a FSR branch of the hard parton together with one ISR emission, or two FSR emissions. The multijet ratios from PYTHIA8 were found to be very similar to the one jet case. This is illustrated in the upper plot of figure 4.11(b), which shows the PYTHIA8 $R_{2\text{jet}}/R_{1\text{jet}}$ and $R_{3\text{jet}}/R_{1\text{jet}}$ ratios.[4] The corresponding GAMBOS Z/γ ratios

[4]The large deviation in the first bins is an artefact of the kinematic acceptance. In the 1–jet case, events will populate these bins according to the normal underlying distribution. However, since shower emissions can only occur with p_T smaller than the hard process, the 2,3 jet events will be

are therefore slightly smaller as shown in the lower plot of figure 4.11(b). These results illustrate the difference between the two individual approaches in the multijet case as well as the importance of using a multiparton ME based program in the actual analysis, where the precision related to the ME calculation was discussed above in connection with figure 4.10. By comparing the `GAMBOS` and `PYTHIA8` ratios at high p_T, we can extract correction factors for the `PYTHIA8` ratios to take account of the missing contributions, however, as seen in figure 4.11(b) these correction factors are not large.

4.4. Full event simulation

The ability of `PYTHIA8` to simulate full events was used both to investigate the robustness of the Z/γ cross section ratio as well as its potential use in estimating the $Z_{\nu\nu}$ background in searches for new physics at the LHC. For simplicity, the experimental aspects related to the photon analysis attempt to follow as closely as possible what is commonly used in ATLAS analyses [48, 76], and for the new physics scenario we focus on the SUSY zero–lepton search [58, 65], where SM $Z_{\nu\nu}$ production is one of the main backgrounds. Due to the phenomenological nature of this study, we neglect any experimental photon inefficiencies, apart from the isolation criteria discussed below, as well as any backgrounds (*e.g.* $\pi^0 \to 2\gamma$), which in any case are expected to be relatively small in the high p_T region of interest.

4.4.1. Effects on the ratio

The same `PYTHIA8` processes were used as in the parton–level study, but with the full parton shower, hadronisation, multiple interaction and particle decay simulation enabled. The default settings of v8.150 were used, for which general performance results can be found in [77]. The same selection was used as for the 1–jet parton–level results, here corresponding to an inclusive jet selection. The main differences with respect to the parton–level results come from using the final state boson momentum as well as from using jets reconstructed from the final state particles, rather than being represented by single partons. The jets were reconstructed using the `FastJet` library [52, 78, 79] and were based on all final–state particles except leptons and any photons with $p_T^\gamma > 30$ GeV. The anti–k_t algorithm was used with a R parameter of 0.4, also in accordance with the

peaked toward the upper bin edge. Due to the sharp rise of the ratio at low p_T, the average ratio value in these bins will therefore be significantly different for the higher jet multiplicities.

ATLAS analysis. In the following, these results from full event simulation are referred to as obtained at particle level.

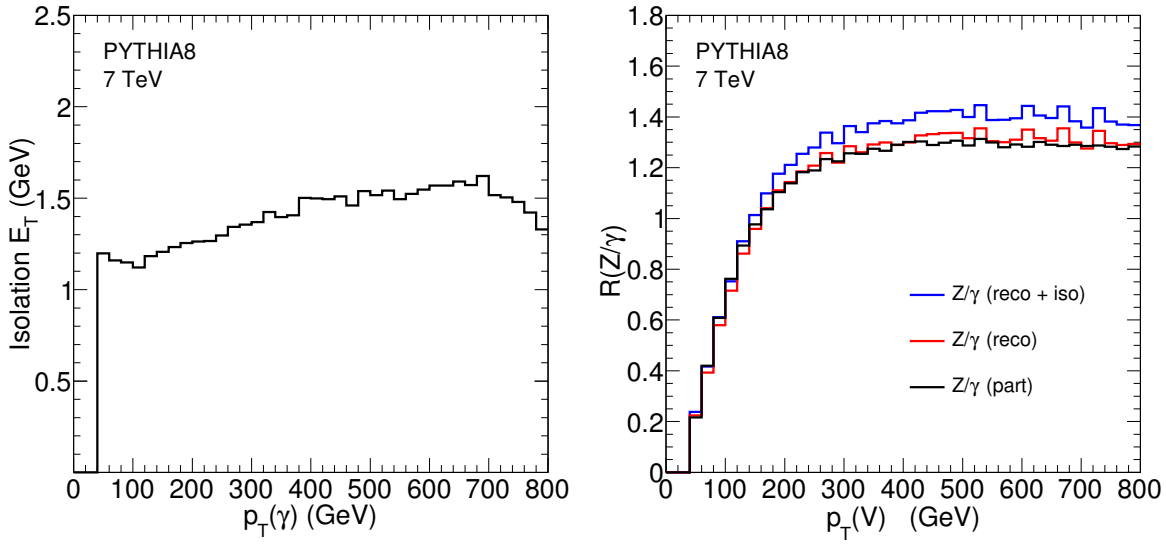

(a) (b)

Figure 4.12.: *(a) Transverse energy inside the photon isolation cone as a function of the photon p_T. (b) Z/γ cross section ratio as a function of the photon p_T. Parton (part) and particle level results (reco) are shown as well as for events passing the isolation criteria (reco + iso).*

The experimental analysis in ATLAS uses a photon isolation criterion in order to suppress QCD background and this quantity was found to be well described at MC generator level. This isolation criterion requires the transverse energy within a $\Delta R[= \sqrt{\Delta\eta^2 + \Delta\phi^2}] = 0.4$ cone around the photon (E_T^{iso}) not to exceed 4 GeV. Since the anticipated use of the ratio here is to estimate the number of Z events from measured γ events, the effect from this isolation requirement is also addressed. The fact that only isolated photons are considered implies an even stronger photon–jet separation than the one used above for the parton level results, ensuring an acceptance where GAMBOS provides robust calculations. The mean transverse energy within the photon isolation cone is shown in figure 4.12(a) as a function of the photon p_T. This plot is based on events which pass the above selection applied to the final state photon as well as the reconstructed jets. A small increase with p_T is shown, but with values well below 4 GeV over the whole range. In spite of the increasing hadronic recoil with larger boson p_T, a relatively constant inefficiency of about 5% was found over the full p_T range.

Figure 4.12(b) shows the Z/γ cross section ratio at parton (part) and particle level (reco) as well as at particle level where the isolation requirement is applied (reco+iso). Good agreement is evident between the results obtained at parton and particle level, where the difference is well below 5% at high p_T, and the increase of the ratio due to the photon isolation criterion is of order 6% at high p_T.

4.4.2. Background estimate for a 0ℓ SUSY search

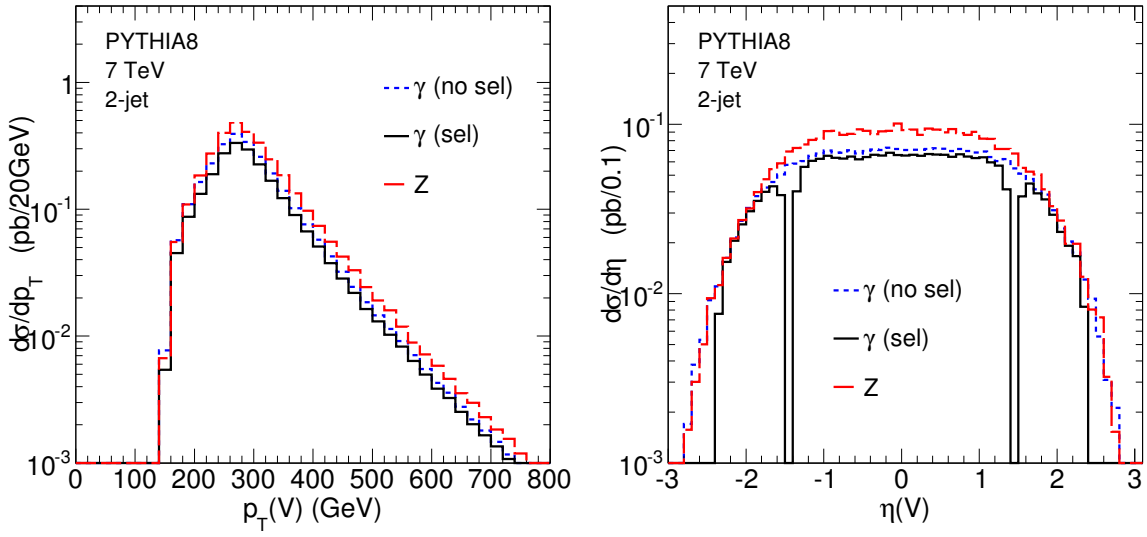

(a) (b)

Figure 4.13.: *(a) Boson p_T and (b) η distributions from events passing the 2–jet SUSY selection. Results from photon events both with (sel) and without (no sel) applying the photon analysis selection are shown together with results from Z events (Z).*

This section demonstrates the estimation of $Z_{\nu\nu}$ background for a zero lepton SUSY search using photon events. This is done using the `PYTHIA8` results and is meant to serve as a general example, since the method could be used also for other new physics searches where $Z_{\nu\nu}$ production contributes with a significant background. The method involves the following steps:

- Photon event selection. Select a photon event sample using a loose enough selection, with respect to the photon and jets, to contain as many events as possible that will pass the final selection. This is represented here by the criteria $p_T(\gamma) > 45$ GeV, $|\eta(\gamma)| < 2.37$, excluding $1.37 < |\eta(\gamma)| < 1.52$ and $E_T^{iso} < 4$ GeV, based on the ATLAS photon analysis [48, 76].

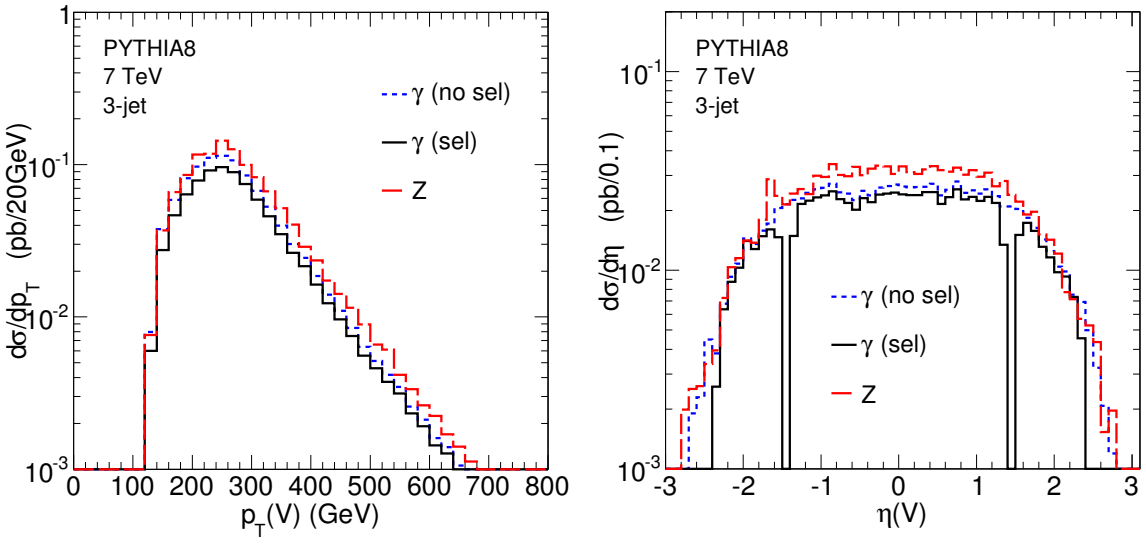

(a) (b)

Figure 4.14.: *(a) Boson p_T and (b) η distributions from events passing the 3–jet SUSY selection. Results from photon events both with (sel) and without (no sel) applying the photon analysis selection are shown together with results from Z events (Z).*

- SUSY event selection. Apply the SUSY selection to the photon events, where the photon p_T represents the missing transverse energy from the Z in the events to be estimated. A 2–jet as well as 3–jet SUSY selection is used, based on the ATLAS search. 2–jet (3–jet): $p_T(j_1) > 120$ GeV, $p_T(j_2) > 40$ GeV, ($p_T(j_3) > 40$ GeV), $|\eta(j_i)| < 2.5$, $p_T(V) > 100$ GeV, $\Delta\phi(V, j_i) > 0.4$, $p_T(V)/m_{eff} > 0.3$ and $m_{eff} > 500$ GeV. Here j_i represents the i^{th} leading jet and m_{eff} is the SUSY discriminating variable used in [58, 65], defined as the scalar sum of the p_T from the jets and the boson in the event.

- Subtract backgrounds and correct for experimental efficiencies. This is represented here only by the isolation efficiency.

- Convert photon events, inside the acceptance of the analysis, to $Z_{\nu\nu}$ events using the cross section ratio, $R(p_T^V) \cdot Br(Z \to \nu\nu)$. As discussed in the previous sections, in an analysis of real LHC data, $R(p_T^V)$ should be based on results from exact multijet MEs and using an appropriate jet selection.

- Correct for acceptance constraints implied by the photon analysis, *e.g.* the $\eta(\gamma)$ selection criteria.

The main intention with this method is that all necessary corrections as well as theoretical input are related to the vector bosons, whereas all requirements with respect to the experimentally more challenging reconstructed jets, are identical for the Z and γ events. As shown in the previous section, the ratio is affected by requiring jets. However, since this effect is a consequence of changing the mixture of couplings imposed by the relevant initial partons together with their PDFs, it is small even for drastically different jet criteria and should be yet smaller with respect to experimental jet uncertainties, such as energy scale and resolution.

The photon event selection imposes some unavoidable criteria which are not experienced by the $Z_{\nu\nu}$ background and therefore has to be corrected for. The implications of this selection on the final sample are, however, relatively mild for the following reasons. The photon p_T requirement is significantly softer than the subsequent selection. A photon isolation criterion, of some kind, is required in order to obtain accurate calculations of the ratio. However, this is often also used in the SUSY selection for more experimental reasons, such as to prevent fake missing transverse energy caused by a high p_T jet, *i.e.* the $\Delta\phi(V, j_i)$ requirement above. In addition, the fact that the Z and γ processes have the same phase space when $p_T \gg M_Z$ means that at high p_T, the η distributions from the γ and Z events converge toward the same distribution, which becomes increasingly central with higher boson p_T. Therefore any acceptance corrections will become the same for the Z as for the γ events.

The SUSY selection, based on the p_T of the boson and jets in the event, is then identical for the two event types and should not require any related corrections. Due to the fact that the bosons are recoiling against the hadrons, the SUSY selection will in principle act as a non–trivial high boson p_T criteria. For this reason the γ events passing the SUSY selection can be converted into Z events based only on the boson kinematics. Again due to the convergence of the Z and γ phase space at high p_T, the cross section ratio becomes insensitive to the particular $\eta(V)$ criteria used and is hence determined by the $p_T(V)$. The precision of this method is therefore mainly related to the photon analysis part, which is expected to be precise at high photon p_T, and the theoretical knowledge of the Z/γ cross section ratio.

In figures 4.13 and 4.14 the boson p_T and η distributions are shown after the 2–jet and 3–jet SUSY selections respectively. The distributions for photon events, with (sel) and without (no sel) passing the photon selection, as well as Z events (Z) are shown. The p_T distributions show that both the SUSY selections mainly select events with a boson p_T in the range 250 to 300 GeV. The η distributions also show the similarity in

shape of the distributions from the Z and γ processes. Both the p_T and η distributions show that the effect from the photon selection, *i.e.* acceptance and isolation requirements, is relatively small also after the SUSY selection and the difference between the Z and γ results is consistent with the cross section ratio at relevant boson p_T values. In the η distributions, the difference from applying the photon selection reflects the impact of the isolation criteria alone and it is shown that the additional jet requirements from the SUSY selections do not change the isolation efficiency dramatically. The results from the 2–jet and 3–jet selections do have slight differences, but the overall characteristics discussed are the same. Figure 4.15 shows the Z p_T distributions from γ events passing the two SUSY selections, converted into $Z_{\nu\nu}$ according to the method outlined above, together with the results obtained from simulating $Z_{\nu\nu}$ directly. Since the `PYTHIA8` ratios do not show any jet multiplicity dependence, the ratio shown in figure 4.12 (reco) was used in this analysis example for both the 2–jet and 3–jet results. As expected, the two distributions agree within the statistical uncertainty of the simulation, which is smaller than 5% in the bulk of the distributions.

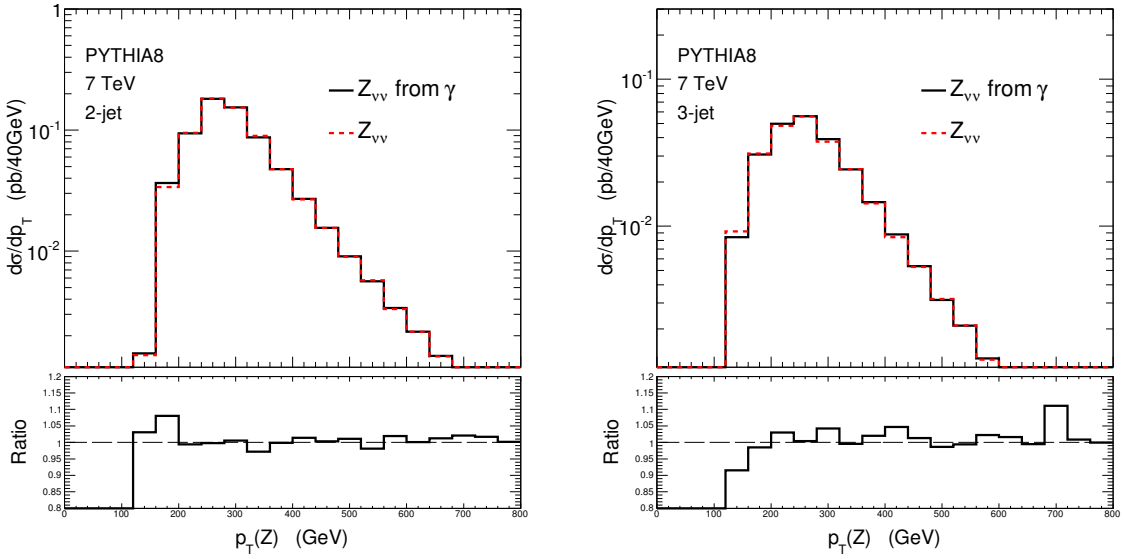

(a) (b)

Figure 4.15.: *Differential cross section as a function of $p_T(Z)$ for $Z \to \nu\nu$ events passing the (a) 2–jet and (b) 3–jet SUSY selection. The predictions using γ events ($Z_{\nu\nu}$ from γ) are compared to results from direct MC simulation of the $Z_{\nu\nu}$ process ($Z_{\nu\nu}$).*

The uncertainties on the final background estimate, related to the experimental aspects of this analysis, are not covered by this study. However, as discussed above, the design of the method should limit the exposure mainly to the corrections from the

Selection	$R^P \cdot Br$	$R^{ME} \cdot Br$	ε_{ME}	ε_μ	ε_{PDF}	ε_{Tot}
2–jet	0.254	0.234	5%	3%	4%	7%
3–jet	0.246	0.207	5%	3%	4%	7%

Table 4.1.: *The overall $R \cdot Br$ values obtained after the SUSY selections, directly from* `PYTHIA8` *(R^P) as well as corrected values with respect to the ME results (R^{ME}). The uncertainties associated with the ME calculation (ε_{ME}), the scales (ε_μ) and the PDFs (ε_{PDF}) are also shown.*

photon event selection, which are expected to be precise at high boson p_T. In addition, as discussed in section 4.4.1, the impact associated with full event simulation on the cross section ratio was found to be small. As shown in figure 4.12(b), the ratio increases, by about 6% in the high p_T region, when including the isolation efficiency, whereas a significantly smaller effect is seen when going from parton to particle level. The final uncertainties on $R(Z/\gamma)$ from such effects are therefore expected to be at the percent level. A theoretical uncertainty, here with respect to the hard process calculations behind $R(Z/\gamma) \cdot Br(Z \to \nu\nu)$, that significantly exceeds 10% is therefore likely to dominate the uncertainty of the method.

Table 4.1 presents the overall $R \cdot Br$ values obtained for the results shown in figure 4.15. This includes both the value from `PYTHIA8` (R^P), that was actually used in the plot, as well as the corrected value (R^{ME}) based on the ME results. The table also includes the uncertainties associated with the ME calculation (ε_{ME}), the scales (ε_μ) and the PDFs (ε_{PDF}), see section 4.3. The results show a total uncertainty of $\pm 7\%$ and indicate that the theoretical uncertainty for results obtained by an appropriately configured MC program, which uses ME amplitudes for the hard jets, should be within 10%. The SUSY selection used in the experimental analysis will evolve with an increasing amount of LHC data. However, such an evolution is expected to effectively imply a harder boson p_T requirement and since the uncertainties in table 4.1 are valid for $p_T(V) > 100$ GeV, the same conclusions should hold also for harder selections.[5]

4.5. Summary

One of the best methods to calibrate the irreducible background from $Z(\to \nu\nu)$+jets, to beyond the SM searches at the LHC, comes from using γ+jets data. The method

[5] At least up to $p_T(V) = 800$ GeV, which is the maximum value included in this study.

utilises the fact that at high boson p_T ($\gg M_Z$) the event kinematics converge for the two processes and the cross sections differ mainly due to the boson couplings. The advantage comes from large statistics, compared to alternative methods using $Z(\rightarrow ee, \mu\mu)$+jets events, together with the clean signature, with respect to experimental efficiencies and background, at high photon p_T. Hence, a precise prediction from theory of the Z/γ cross section ratio, $R(Z/\gamma)$, is required. The similarity between the two processes should allow for a robust prediction of $R(Z/\gamma)$, given careful attention to the modelling of the jets.

The general dependence of $R(Z/\gamma)$ on the mixture of boson couplings, which is determined by the initial state partons of the relevant amplitudes and their corresponding PDFs, has been illustrated. Relatively accurate values can be obtained even using rough approximations in the 1–jet case, whereas a larger set of amplitudes becomes necessary when 2 or more jets are required. The ratios have been studied at parton level using both the (LO) `PYTHIA8` as well as the (multijet ME) `GAMBOS` programs, which allows us to disentangle effects associated with the two approaches. The impact from exact MEs when requiring different numbers of jets was found to be significant, but uncertainties were found to be within 5% for the acceptance from typical experimental cuts. The corresponding uncertainties related to the PDFs and scale choice were found to be less than 4% and 3% respectively.

The `PYTHIA8` MC program was used to investigate effects on $R(Z/\gamma)$ associated with full event simulation as well as performing a proof of principle analysis example. The effects investigated were found to be small and indicate that a theoretical precision[6] at the 10% level is required, in order not to significantly degrade the performance of the method. The total theoretical uncertainty was found to be 7%, indicating that the results obtained by MC simulations, including exact multijet MEs, should be within the 10% level. These results should also hold for similar 2– and 3–jet selections, given that the effective p_T requirement on the boson is harder than that used in the example analysis. Note that all our theoretical cross sections are evaluated in leading–order pQCD. It will be important to check, using for example the techniques of [64], that the ratio predictions are indeed stable – at least to the required accuracy – with respect to higher–order pQCD corrections.

Finally, one type of correction that has not been included in our theoretical study is high-order electroweak corrections. Although these are intrinsically small, and many will again cancel in the Z/γ ratio, there is an important class of correction involving

[6] Again, referring to the hard QCD process calculations behind $R \cdot Br$.

W and Z virtual exchanges that does not cancel in the ratio. The impact on both the Z and γ distributions have been studied in [80, 81]. It was shown that non-cancelling Sudakov-type logarithms $\sim \alpha \log^2(p_T(V)^2/m_W^2)$ appear at high $p_T(V)$, and decrease the $Z/\gamma + 1$ jet ratio by 6% (11%) at $p_T(V) = 300$ (800) GeV [81]. However care is needed in the interpretation of this result, since the emission of *real* W bosons is expected to compensate the virtual Sudakov logarithms to some extent [82, 83]. It is therefore important to carry out a full analysis of higher-order electroweak corrections for the multijet processes and acceptance cuts studied here.

Chapter 5.

Experimental Studies

Given that plenty of advantages and theoretical results from the `ZfromGamma` method have been discussed in the previous two chapters, the remainder of this thesis focuses on presenting the main experimental work carried out to test it in ATLAS. This work was done in collaboration with S. Ask, T. J. Khoo and M. A. Parker from the University of Cambridge who were also members of the ATLAS Collaboration at the time of writing. The specific contributions from the author are specified at the end of this introduction.

As mentioned, the `ZfromGamma` method has provided mainstream results for the SUSY 0ℓ search since the beginning. In chronological order, results have been provided for the Moriond'11 [58], PLHC'11 [65], EPS'11 [54] and Moriond'12 [66] conferences. In this chapter, priority will be given to present the results for Moriond'12 as this is the latest analysis round, corresponding to the largest dataset ($\sim 4.7\text{fb}^{-1}$). However, because of the evolution of this analysis since 2010 (see Section 3.4) and the multiple improvements carried out since, whenever possible brief comparisons will be given with respect to what was done in the previous analyses, and the more comprehensive versions are provided in Appendix C. Other supporting material is: Appendix A to show the plots from the Moriond'12 analysis which were not included in this chapter; Appendix B to summarise the relevant results from official prompt photon cross-section measurements in ATLAS, which are used to compare the results obtain here, *e.g.* Sections 5.3 and 5.5; and Appendix D to present the cross-checks done to validate the method. As for the next sections, the structure is the following: Section 5.1 briefly describes the software framework and provides all the relevant technical references. Section 5.2 details the event samples used from data and simulation. Section 5.3 describes the event selection to extract the inclusive prompt photon sample ($\gamma + X$). The rest of the method is presented in the same order as in the rightmost diagram of Figure 3.2 (for the case of

$Z_{\nu\nu}$ background estimation): Section 5.4 outlines the subsequent selection made on the $\gamma + X$ sample to define the Control Region sample (CR1a). The conversion of this control sample to $Z_{\nu\nu}$ events via a Transfer Function (TF) is detailed in Section 5.5. Finally, Section 5.6 explains the context and relevance of the results within the 0ℓ analysis, as well as compares them to those from the alternative method which uses $Z_{\ell\ell}$ as calibrating sample (see Section 3.3).

Supervised by S. Ask and M. A. Parker, the author performed most of the `ZfromGamma`-related work and plots for Moriond'11, PLHC'11 and EPS'11 found in Appendix C (see Appendix C for additional details), including the R&D that was required for the production of suitable MC samples. For Moriond'12 (presented in the following sections), the plots were done in collaboration with T. J. Khoo: the author provided the `ZfromGamma` algorithm and supervised the implementation of the method for this analysis round while T. J. Khoo took charge of migrating the `ZfromGamma` code to the `ZeroLepton` framework (see Section 5.1), as well as doing the necessary runs to process the Moriond'12 dataset. With respect to the 0ℓ analysis, the author performed most of the work to obtain the CR1a-related results as specified above, except for most of the work presented in Section 5.6 which concerns their implementation into the 0ℓ likelihood function, final background fitting and use for setting limits on SUSY models. However, Section 5.6.3 was also done in collaboration with T. J. Khoo. Similarly, all the results and plots showed from the other 0ℓ CRs and SRs were done by other members from the 0ℓ group in ATLAS.

5.1. Framework

The main technical reference for this analysis can be found at [84], which provides the latest instructions to run the different steps of this analysis, as well as the links to the source code, software specifications and packages, names of samples used, etc. The framework has constantly evolved since its first implementation, Figure 5.1. The first version in 2010 [85] was an adaptation of the `WZJratioAnalysis` framework [86] – a `C++` object-oriented `ROOT`-based package based on the `TSelector` class able to process data in `D3PD` (ntuple) format. The framework was then adapted to process `SUSYD3PD`'s. By 2011, the framework was significantly different from `WZJratioAnalysis` so a new name was given to it (`ZfromGamma`), however, the "tags" (versions) did not come into place until EPS'11 [87].

For the Moriond'12 0ℓ analysis, `ZfromGamma` was migrated to the common `ZeroLepton` framework, which takes the object definitions from a common package to all ATLAS SUSY analyses (`SUSYTools`). This guarantees consistency between analysers, and with other SUSY analyses and ensures that up-to-date object definitions are used. The input histograms for the method are produced within the `C++` code, while extraction of signal region estimates of the Z background is accomplished in post-processing, which is encapsulated within a python script. Details on the implementation are available on the twiki [88].

Analysis	Framework	Release	`SUSYD3PD` tag
Moriond'12	`ZeroLepton-00-00-19`	17	p832
EPS'11	`ZfromGamma-00-00-01`	16	p601/2
PLHC'11	`ZfromGamma`	16	p543
Moriond'11	`WZJratioAnalysis`	15	p305

Table 5.1.: *Details of the frameworks used for the different analysis rounds since 2010, including the ATLAS software release and* `SUSYD3PD` *tag used.*

5.2. Event Samples

5.2.1. Data

The details of the data samples used for the different analyses rounds performed in 2011 are outlined in Table 5.2. As of writing, the Moriond'12 analysis was the most recent result, utilising the complete 2011 dataset, amounting to 4.7 fb^{-1} after application of some Data Quality (DQ) criteria – specifically, the 0ℓ "Good Runs List" (GRL). In all cases, the data corresponds to a c.o.m. energy of $\sqrt{s} = 7$ TeV and the `Egamma` stream. The data files are in `SUSYD3PD` format, made of AODs with the `SUSYD3PDMaker` package [89], with tags specified in Table 5.2.

Data conditions varied throughout the 2011 run, with some of the most important differences highlighted in Table 5.2. Both machine (LHC) and detector (ATLAS) conditions changed in different data periods, with the detector conditions in particular mandating specific cuts that needed to be applied to the photon and 0ℓ selections, amongst these:

1. "LAr Hole" – The loss of six front-end boards (FEBs) in the LAr calorimeter (ECAL, see Section 2.2.2) on April 30th made it impossible to read out cells in the second and third EM calorimeter layers in the region $0 < \eta < 1.4$, $-0.8 < \phi < -0.6$. These were partially recovered during the July technical stop, restoring measurement capability for the second layer. The loss meant that jets, electrons and photons falling into the hole could be partially or wholly unmeasured, introducing a major source of missing energy (see Appendix D.2). For PLHC'11, only data up to Period D was used, none of which was affected by this defect. However, the EPS'11 and Moriond'12 analyses had to introduce cuts to veto spurious missing energy events resulting from mismeasurement in the hole. At EPS'11, this was accomplished by a simple veto of any jets falling in the vicinity of the hole, while a more sophisticated check was used for Moriond'12, whereby for each jet the degree of mismeasurement and its contribution to the $E_{\mathrm{T}}^{\mathrm{miss}}$ was taken into account.

2. "Dead Tile drawers" – Over the course of 2011, the proportion of non-functional Tile calorimeter (HCAL, see Section 2.2.2) cells rose from 0.2% to 5.1%. Such dead cells cause undermeasurement of jet energies, leading to fake $E_{\mathrm{T}}^{\mathrm{miss}}$. Prior to the Moriond'12 iteration, this problem was not considered. For Moriond'12, events with substantial $E_{\mathrm{T}}^{\mathrm{miss}}$ arising from jets pointing to dead Tile drawers were vetoed.

3. "LAr errors" – Noise bursts and other defects in the LAr calorimeter can lead to the identification of false objects or their mismeasurement in other ways. Based on the shapes of the pulses read out from the LAr calorimeter and the status of the hardware, a flag is set that allows veto of events suffering from these issues.

4. "Bad jets" – A fraction of jets in data come from non-collision backgrounds such as beam halo and beam gas events, cosmic rays and calorimeter noise. The ATLAS Jet/Etmiss Combined Performance group provides a recipe for "Jet Cleaning", and additional SUSY-group-specific cuts are used to eliminate events with identified bad jets.

5. "Bad $E_{\mathrm{T}}^{\mathrm{miss}}$" – Due to compensation and noise in the calorimeter cells, occasional events may have a large number of cells measuring negative energies, producing substantial $E_{\mathrm{T}}^{\mathrm{miss}}$. Such events are vetoed.

Event selection requirements based on the above are usually termed "event cleaning" cuts, *e.g.* cuts 3a-3i in Table 5.14.

Analysis	Dates	Run period	Run number	$\langle\mu\rangle$	Peak $\mathscr{L}$ ($10^{30}\text{cm}^{-2}\text{s}^{-1}$)	$\int \mathscr{L}\text{d}t$ (fb^{-1})	SUSYD3PD tag
2011 data, $\sqrt{s} = 7$ TeV							
Moriond'12	22/03-28/06	B2-M10	178044-191933	2.6-17.5	1.3-3600	$4.710 \pm 3.9\%$	p832
EPS'11	22/03-30/10	B2-H4	178044-184169	2.6-7.97	1.3-1260	$1.035 \pm 4.5\%$	p601/2
PLHC'11	22/03-29/04	B2-D7	178044-180481	2.6-7.0	1.3-660	$0.165 \pm 4.5\%$	p543
2010 data, $\sqrt{s} = 7$ TeV							
Moriond'11	30/03-29/10	A-I	152166-167844	1-3.5	1.3-210	$0.035 \pm 11\%$	p832

Table 5.2.: *Details of the data samples used for the different analyses; $\langle\mu\rangle$ represents the peak mean number of interactions per bunch crossing. The integrated luminosity quoted is after the application of the SUSY GRL. Values taken from [13].*

5.2.2. Monte Carlo

Monte Carlo simulated data samples are required not only to compare with data and assess the effectiveness of the method, but also to determine part of the Z/γ TF (Section 5.5). Therefore, samples are required for: (i)"prompt-photon + jets ", (ii) backgrounds to "prompt-photon + jets " and (iii) "$Z_{\nu\nu}$ + jets". The goal of estimating the $Z_{\nu\nu}$ + jets background in $E_{\text{T}}^{\text{miss}}$ + jets SRs drives the need for samples generated with large jet multiplicities.

It is important to note that throughout the different analysis rounds, the availability of suitable MC samples evolved. In particular, substantial R&D studies had to be done to motivate the production of more suitable samples. The samples that were available in the previous analyses are listed in Appendix C. Some of these samples were superseded by more suitable ones and those currently in use are listed in Tables 5.3-5.6. Where possible, the same process is simulated with different generators in order to cross-check the results. A more detailed description of the process in (i), (ii) and (iii) above and their usage is now given.

γ + jets

These samples model the prompt photon signal with an inclusive number of jets. They are mainly used to determine part of the Z/γ TF (Equation (3.5)), such as $R_{Z/\gamma}$, $A^{\gamma}(p_{\text{T}}) \cdot \varepsilon^{\gamma}(p_{\text{T}})$, but also to calculate a few associated uncertainties and assess the impact from different generators.

For Moriond'12, the two main generators used are `ALPGEN` and `SHERPA`, with the details given in Table 5.3. The `SHERPA` samples are produced in inclusive p_{T} slices, with thresholds at 35, 70, 140, 280 and 500 GeV. "Enhancement factors" (intrinsic to the generator to deliberately generate a larger number of events in certain parts of phase space, which are assigned weights so that the correct cross section is obtained when used in the normalisation) are applied to boost statistics for events with 5 or 6 jets. Because the samples overlap, it is necessary to avoid double-counting by removing some of the MC events. This is done by dropping all events from the lower p_{T} thresholds for which the hardest truth photon (`mc_status = 3`, i.e. before showering) is above the next lowest p_{T} threshold.

Samples produced with `ALPGEN` come in two varieties: "standard" and "susyfilt", where the former simply impose a 20 GeV photon p_{T} threshold and the same for the additional partons in the matrix element. The susyfilt samples are similar, but have additional truth-level filter cuts that require the leading photon and jet to have $p_{\mathrm{T}} > 100$ GeV. These requirements improve the statistics for hard prompt photons, as required by this method. The standard and susyfilt samples also overlap, so any events in the standard samples with two truth jets above 100 GeV are vetoed (this is equivalent to vetoing events with a leading photon and a jet above 100 GeV).

In addition to the configuration of the MC generator parameters, *e.g.* related to scales, PDFs, etc., the choice of the α_{em} value is of particular interest for this process. To some extent counter-intuitively, as discussed for example in [64], the correct value assigned to the photon coupling in this process is believed to be the low energy value, $\alpha_{em}(0) \sim 1/137$, instead of the running coupling value, $\alpha_{em}(Q) \sim 1/128$, which is a consequence from selecting events with one real photon only (*e.g.* not including virtual contributions with photons decaying into lepton pairs). This is also what was used for the `SHERPA` samples and it is interesting to notice the good agreement with data obtained, straight from the MC predictions, in the following sections.

Backgrounds to γ + jets

When selecting prompt photon events in data, various background sources can contaminate the selected sample. Hence, samples are required to evaluate the contribution from other SM processes to the photon selection at different stages of the analysis. A variety of samples using different generators are used, detailed in Table 5.5 and Table 5.6.

The dominant low-p_{T} background is from QCD events such as production of $\pi^0 \to \gamma\gamma$. Additionally, electrons from W and top decays can be misidentified as photons. The electron contamination is also highly p_{T}-dependent, due to the electron spectrum peaking around $p_{\mathrm{T}} = m_W/2$[1], and is therefore expected to be small for a photon sample with $p_{\mathrm{T}} > 100$ GeV. Therefore, QCD multijet and W processes form the most important background samples.

$Z_{\nu\nu}$ + jets

These samples are mainly used for the computation of $R_{Z/\gamma}$, but also for a direct comparison with the $Z_{\nu\nu}$ + jets estimate (from γ + jets). Again, multiple generators are used to evaluate the impact of theoretical variations.

To be consistent with the γ + jets samples, `ALPGEN` and `SHERPA` are also used, with details given in Table 5.4. The `SHERPA` samples in this case are not p_{T}-sliced, and include up to 5 jets in the matrix-element. Unfortunately, this hence results in a lack of statistics at high jet multiplicities, rendering the `SHERPA` MC unusable for many of the event selections in the 0ℓ analysis. As for the `ALPGEN` samples, they are similarly divided into "standard" and "susyfilt" samples, and must have overlaps removed in a similar fashion. However, rather than filtering on two truth jets, in this case the leading truth jet and the truth $E_{\mathrm{T}}^{\mathrm{miss}}$are used instead. The MC statistics from `ALPGEN` are found to be adequate, and therefore `ALPGEN` samples are used for the computation of $R_{Z/\gamma}$. Nevertheless, comparisons are made with `SHERPA` wherever possible.

In the following pages, the `SHERPA` γ + jets will be shown only in the plots where a minimal selection for inclusive photon events has been applied, *i.e.* in all figures up to Figure 5.7. This is because of the filtering in the `ALPGEN` γ + jets samples already discussed, which misses a patch of phase space of events with a softer leading jet and photon. After imposing the 0ℓ $E_{\mathrm{T}}^{\mathrm{miss}}$ and leading jet cuts, the `ALPGEN` samples properly describe the data, and are used instead to be consistent with the $Z_{\nu\nu}$ + jets MC.

[1] Although applying jet requirements can have an effect on the lepton p_{T} distribution, the background caused by these events remains negligible.

Sample ID	Name	Cross Section [pb]	Filter Eff.	k-factor	N_{gen}
113714	SherpaY4JetsPt35	$2.248 \cdot 10^{+4}$	1.000	1.000	199999.0
113715	SherpaY4JetsPt70	$1.774 \cdot 10^{+3}$	1.000	1.000	198898.0
113716	SherpaY4JetsPt140	$1.028 \cdot 10^{+2}$	1.000	1.000	199899.0
113717	SherpaY4JetsPt280	$3.997 \cdot 10^{+0}$	1.000	1.000	199997.0
126371	SherpaY4JetsPt500	$1.633 \cdot 10^{-1}$	1.000	1.000	199993.0
106123	AlpgenJimmyGamNp1	$7.411 \cdot 10^{+4}$	1.000	1.000	100000.0
106124	AlpgenJimmyGamNp2	$2.160 \cdot 10^{+4}$	1.000	1.000	99998.0
106125	AlpgenJimmyGamNp3	$5.801 \cdot 10^{+3}$	1.000	1.000	99999.0
106126	AlpgenJimmyGamNp4	$1.360 \cdot 10^{+3}$	1.000	1.000	100000.0
106127	AlpgenJimmyGamNp5	$3.522 \cdot 10^{+2}$	1.000	1.000	99950.0
150090	AlpgenJimmyGamNp1_pt20_susyfilt	$4.699 \cdot 10^{+2}$	0.151	1.000	999893.0
150091	AlpgenJimmyGamNp2_pt20_susyfilt	$4.571 \cdot 10^{+2}$	0.170	1.000	1199697.0
150092	AlpgenJimmyGamNp3_pt20_susyfilt	$2.309 \cdot 10^{+2}$	0.222	1.000	1249891.0
150093	AlpgenJimmyGamNp4_pt20_susyfilt	$8.427 \cdot 10^{+1}$	0.289	1.000	749196.0
150094	AlpgenJimmyGamNp5_pt20_susyfilt	$2.467 \cdot 10^{+1}$	0.363	1.000	269995.0
150095	AlpgenJimmyGamNp6_pt20_susyfilt	$7.260 \cdot 10^{+0}$	0.457	1.000	74900.0

Table 5.3.: *Moriond'12 Monte Carlo samples used to simulate the γ + jets signal, including cross section times filter efficiency, k-factor and the number of generated events in the sample.*

Sample ID	Name	Cross Section [pb]	Filter Eff.	k-factor	N_{gen}
118959	SherpaZ5jetstonunu30GeV	$4.818 \cdot 10^{+3}$	1.000	1.207	1699946.0
144069	SherpaZ5jetstonunu30GeV_weighted	$5.155 \cdot 10^{+3}$	1.000	1.128	984999.0
107710	AlpgenJimmyZnunuNp0_pt20_filt1jet	$3.572 \cdot 10^{+3}$	0.011	1.260	54949.0
107711	AlpgenJimmyZnunuNp1_pt20_filt1jet	$7.387 \cdot 10^{+2}$	0.611	1.260	909848.0
107712	AlpgenJimmyZnunuNp2_pt20_filt1jet	$2.229 \cdot 10^{+2}$	0.882	1.260	169899.0
107713	AlpgenJimmyZnunuNp3_pt20_filt1jet	$6.187 \cdot 10^{+1}$	0.968	1.260	144999.0
107714	AlpgenJimmyZnunuNp4_pt20_filt1jet	$1.563 \cdot 10^{+1}$	0.992	1.260	309899.0
144017	AlpgenJimmyZnunuNp5_excl_pt20_filt1jet	$3.581 \cdot 10^{+0}$	0.998	1.260	185000.0
144021	AlpgenJimmyZnunuNp6_pt20_filt1jet	$9.220 \cdot 10^{-1}$	1.000	1.260	114999.0
144192	AlpgenJimmyZnunuNp1_pt20_susyfilt	$3.683 \cdot 10^{+1}$	0.349	1.260	499898.0
144193	AlpgenJimmyZnunuNp2_pt20_susyfilt	$3.429 \cdot 10^{+1}$	0.296	1.260	399999.0
144194	AlpgenJimmyZnunuNp3_pt20_susyfilt	$1.612 \cdot 10^{+1}$	0.335	1.260	299998.0
144195	AlpgenJimmyZnunuNp4_pt20_susyfilt	$5.481 \cdot 10^{+0}$	0.397	1.260	184998.0
118962	AlpgenJimmyZnunubbNp0_pt20_filt1jet	$3.280 \cdot 10^{+1}$	1.000	1.260	604499.0
118963	AlpgenJimmyZnunubbNp1_pt20_filt1jet	$1.450 \cdot 10^{+1}$	1.000	1.260	280999.0
118964	AlpgenJimmyZnunubbNp2_pt20_filt1jet	$5.240 \cdot 10^{+0}$	1.000	1.260	102000.0
118965	AlpgenJimmyZnunubbNp3_pt20_filt1jet	$1.560 \cdot 10^{+0}$	1.000	1.260	30500.0

Table 5.4.: *Moriond'12 Monte Carlo samples used to simulate the $Z_{\nu\nu}$ + jets signal, including cross section times filter efficiency, k-factor and the number of generated events in the sample.*

Sample ID	Name	Cross Section [pb]	Filter Eff.	k-factor	N_{gen}
105890	AlpgenJimmyttbarlnlnNp0	$3.466 \cdot 10^{+0}$	1.000	1.690	117999.0
105891	AlpgenJimmyttbarlnlnNp1	$3.399 \cdot 10^{+0}$	1.000	1.690	159999.0
105892	AlpgenJimmyttbarlnlnNp2	$2.124 \cdot 10^{+0}$	1.000	1.690	336897.0
117897	AlpgenJimmyttbarlnlnNp3_baseline	$9.470 \cdot 10^{-1}$	1.000	1.690	148000.0
117898	AlpgenJimmyttbarlnlnNp4_baseline	$3.341 \cdot 10^{-1}$	1.000	1.690	60000.0
117899	AlpgenJimmyttbarlnlnNp5_baseline	$1.275 \cdot 10^{-1}$	1.000	1.690	7000.0
105894	AlpgenJimmyttbarlnqqNp0	$1.376 \cdot 10^{+1}$	1.000	1.770	647396.0
105895	AlpgenJimmyttbarlnqqNp1	$1.361 \cdot 10^{+1}$	1.000	1.770	652997.0
105896	AlpgenJimmyttbarlnqqNp2	$8.418 \cdot 10^{+0}$	1.000	1.770	146999.0
117887	AlpgenJimmyttbarlnqqNp3_baseline	$3.776 \cdot 10^{+0}$	1.000	1.770	652495.0
117888	AlpgenJimmyttbarlnqqNp4_baseline	$1.336 \cdot 10^{+0}$	1.000	1.770	118999.0
117889	AlpgenJimmyttbarlnqqNp5_baseline	$5.040 \cdot 10^{-1}$	1.000	1.770	8000.0
117360	st_tchan_enu_AcerMC	$6.970 \cdot 10^{+0}$	1.000	1.000	999295.0
117361	st_tchan_munu_AcerMC	$6.970 \cdot 10^{+0}$	1.000	1.000	999948.0
117362	st_tchan_taunu_AcerMC	$6.970 \cdot 10^{+0}$	1.000	1.000	998995.0
117363	st_schan_enu_AcerMC	$5.000 \cdot 10^{-1}$	1.000	1.000	199899.0
117364	st_schan_munu_AcerMC	$5.000 \cdot 10^{-1}$	1.000	1.000	199850.0
117365	st_schan_taunu_AcerMC	$5.000 \cdot 10^{-1}$	1.000	1.000	200000.0
105500	AcerMC_Wt	$1.574 \cdot 10^{+1}$	1.000	1.000	994897.0
119353	PythiaMadgraph_ttbarW	$1.244 \cdot 10^{-1}$	1.000	1.300	100000.0
119354	PythiaMadgraph_ttbarWj	$8.347 \cdot 10^{-2}$	1.000	1.300	100000.0
119355	PythiaMadgraph_ttbarZ	$9.558 \cdot 10^{-2}$	1.000	1.300	99997.0
119356	PythiaMadgraph_ttbarZj	$8.160 \cdot 10^{-2}$	1.000	1.300	100000.0
119583	PythiaMadgraph_ttbarWW	$1.249 \cdot 10^{-3}$	1.000	1.300	100000.0

Table 5.5.: *Moriond'12 Monte Carlo samples used to simulate the SM background to the γ+jets signal from top quark production, including cross section times filter efficiency, k-factor and the number of generated events in the sample.*

Sample ID	Name	Cross Section [pb]	Filter Eff.	k-factor	N_{gen}
107680	AlpgenJimmyWenuNp0	$6.932 \cdot 10^{+3}$	1.000	1.196	3458883.0
107681	AlpgenJimmyWenuNp1	$1.305 \cdot 10^{+3}$	1.000	1.196	2499645.0
107682	AlpgenJimmyWenuNp2	$3.780 \cdot 10^{+2}$	1.000	1.196	3768632.0
107683	AlpgenJimmyWenuNp3	$1.019 \cdot 10^{+2}$	1.000	1.196	1008947.0
107684	AlpgenJimmyWenuNp4	$2.570 \cdot 10^{+1}$	1.000	1.196	250000.0
144018	AlpgenJimmyWenuNp5_excl_pt20	$5.814 \cdot 10^{+0}$	1.000	1.196	979197.0
144022	AlpgenJimmyWenuNp6_pt20	$1.546 \cdot 10^{+0}$	1.000	1.196	144998.0
144196	AlpgenJimmyWenuNp1_pt20_susyfilt	$1.305 \cdot 10^{+3}$	0.006	1.196	180899.0
144197	AlpgenJimmyWenuNp2_pt20_susyfilt	$3.780 \cdot 10^{+2}$	0.017	1.196	134998.0
144198	AlpgenJimmyWenuNp3_pt20_susyfilt	$1.019 \cdot 10^{+2}$	0.034	1.196	139999.0
144199	AlpgenJimmyWenuNp4_pt20_susyfilt	$2.570 \cdot 10^{+1}$	0.056	1.196	75000.0
107650	ZeeNp0	$6.696 \cdot 10^{+2}$	1.000	1.243	6618284.0
107651	ZeeNp1	$1.346 \cdot 10^{+2}$	1.000	1.243	1334897.0
107652	ZeeNp2	$4.065 \cdot 10^{+1}$	1.000	1.243	2004195.0
107653	ZeeNp3	$1.126 \cdot 10^{+1}$	1.000	1.243	549949.0
107654	ZeeNp4	$2.840 \cdot 10^{+0}$	1.000	1.243	149948.0
107655	ZeeNp5	$7.600 \cdot 10^{-1}$	1.000	1.243	50000.0
109300	AlpgenJimmyZeebbNp0_nofilter	$6.570 \cdot 10^{+0}$	1.000	1.243	409999.0
109301	AlpgenJimmyZeebbNp1_nofilter	$2.480 \cdot 10^{+0}$	1.000	1.243	160000.0
109302	AlpgenJimmyZeebbNp2_nofilter	$8.900 \cdot 10^{-1}$	1.000	1.243	60000.0
109303	AlpgenJimmyZeebbNp3_nofilter	$3.900 \cdot 10^{-1}$	1.000	1.243	30000.0
116250	AlpgenJimmyZeeNp0_Mll10to40_pt20	$3.055 \cdot 10^{+3}$	1.000	1.243	994949.0
116251	AlpgenJimmyZeeNp1_Mll10to40_pt20	$8.491 \cdot 10^{+1}$	1.000	1.243	299998.0
116252	AlpgenJimmyZeeNp2_Mll10to40_pt20	$4.119 \cdot 10^{+1}$	1.000	1.243	999946.0
116253	AlpgenJimmyZeeNp3_Mll10to40_pt20	$8.350 \cdot 10^{+0}$	1.000	1.243	149998.0
116254	AlpgenJimmyZeeNp4_Mll10to40_pt20	$1.850 \cdot 10^{+0}$	1.000	1.243	40000.0
116255	AlpgenJimmyZeeNp5_Mll10to40_pt20	$4.600 \cdot 10^{-1}$	1.000	1.243	10000.0
126013	Sherpa_Wenugamma_1jet	$7.287 \cdot 10^{+1}$	1.000	1.000	399899.0
126014	Sherpa_Wmunugamma_1jet	$7.287 \cdot 10^{+1}$	1.000	1.000	399948.0
126017	Sherpa_Znunugamma	$1.035 \cdot 10^{+0}$	1.000	1.000	100000.0
126018	Sherpa_Wenugamma_highpt	$2.966 \cdot 10^{+0}$	1.000	1.000	299947.0
126019	Sherpa_Wmunugamma_highpt	$2.964 \cdot 10^{+0}$	1.000	1.000	299999.0
126022	Sherpa_Znunugamma_highpt	$2.316 \cdot 10^{+0}$	1.000	1.000	200000.0
117410	AlpgenJimmyWgammaNp0_pt20	$2.133 \cdot 10^{+2}$	1.000	1.000	1459648.0
117411	AlpgenJimmyWgammaNp1_pt20	$5.223 \cdot 10^{+1}$	1.000	1.000	529998.0
117412	AlpgenJimmyWgammaNp2_pt20	$1.726 \cdot 10^{+1}$	1.000	1.000	175000.0
117413	AlpgenJimmyWgammaNp3_pt20	$5.334 \cdot 10^{+0}$	1.000	1.000	264999.0
117414	AlpgenJimmyWgammaNp4_pt20	$1.376 \cdot 10^{+0}$	1.000	1.000	64999.0
117415	AlpgenJimmyWgammaNp5_pt20	$3.444 \cdot 10^{-1}$	1.000	1.000	20000.0

Table 5.6.: *Moriond'12 Monte Carlo samples used to simulate the SM background to the γ+jets signal from vector boson production, including cross section times filter efficiency, k-factor and the number of generated events in the sample.*

Modelling data conditions

Note that each of the listed samples is generally available in more than one software production, depending on the analysis round for which it was used, to reflect the different data-taking conditions discussed in Sections 2.2.4, 5.2.1 and Table 5.2. Some of the MC production details are given in Table 5.7. For example, for Moriond'12, the productions were "mc11b" and "mc11c", which were designed to be compatible with 2011 ATLAS data by applying specific MC event generator and detector simulation settings (more details can be found in [90, 91]). A more refined simulation of the different pileup conditions is done "offline" (at analysis-level) using the ATLAS default *pileup reweighting tool*. This tool calculates an event weight for MC events, based on a given data sample, since when the MC samples are first produced, only a "best-guess" of the data pileup conditions can be made. For PLHC'11 and EPS'11, the introduction of this tool resulted in a MC inefficiency of $\sim 50\%$ (see Section C.2.2). Additionally, some detector conditions such as the LAr hole were not reflected in the MC as the simulation conditions were prepared well in advance of data taking.

For Moriond'12, the data-taking conditions for the entire dataset were already known. Hence it was possible to account for all important detector conditions e.g. the LAr hole and dead tile drawers, as well as to simulate better the pile-up conditions in the corresponding MC productions.

Analysis	Production	Release	$\langle\mu\rangle$
Moriond'12	mc11b/c	17	6.3-11.6
EPS'11	mc10b	16	8
PLHC'11	mc10a	16	8
Moriond'11	mc09	15	1-3.5

Table 5.7.: *Details of the MC production used for the different analyses, including MC production and mean number of interactions per event* $\langle\mu\rangle$*. In all cases, the c.o.m. is* $\sqrt{s} = 7$ TeV *and GEANT4 is used for ATLAS detector simulation. The main difference between mc11b and mc11c is the* `PYTHIA` *tune used to generate the pileup events.*

In all the plots that follow, unless otherwise stated, whenever MC is shown, the normalisation is to the data luminosity and using the cross-sections listed in this section.

5.3. Inclusive Photon Sample ($\gamma + X$)

As mentioned in Section 3.4, for each 0ℓ SR, a photon event sample suitable for estimating the Z boson background is selected in two stages. These two stages are defined so that after the first stage: (i) the resulting sample is common to all SRs; (ii) the selection matches that from the ATLAS prompt photon cross section analysis , *e.g.* [48, 49, 92]; and (iii) a first cross-check can therefore be made with these official results, *e.g.* the efficiency and purity should be the same given the identical event selections. This Section describes the first stage, referred to in this thesis as the *inclusive photon selection* ($\gamma + X$).

5.3.1. Object definitions

The photon object definitions implemented here are identical to the latest used by the ATLAS Standard Model Direct Photon (SMDP) group [93] (based on the ATLAS`egamma` group recommendations [94–96]) as follows:

Preselected photons: Defined as *reconstructed* photons (see Section 2.2.5) which pass the following criteria in Table 5.8:

- Energy Scale - The appropriate electromagnetic energy scale is extracted by using electrons from Z boson decays and the well-known Z-mass shape. The corresponding corrections are applied on the energy of all data candidates using the `EnergyRescaler` tool provided by the `egamma` group [97]. Since the MC does not perfectly reproduce the energy resolution in data, a smearing procedure is also applied to all MC candidates.
- Object Quality - Candidates must satisfy the `egamma` Object Quality selection [94].
- Photon Cleaning - Candidates must pass the `egamma` prescription, based on the LAr cell quality factor and timing (related to selections on some shower shape variables [94]). This removes fake photons associated to noise bursts in the LAr calorimeter.
- Photon Quality - Candidates must pass the SMDP tight `isEM` cuts, recomputed with the `PhotonIDTool` [93] after having applied the `EnergyRescaler` on all relevant discriminating variables.

- η Acceptance[2] - Photons are required to be away from the ECAL barrel/endcap transition region ($1.37 \leq |\eta| < 1.52$) and within the acceptance of the high granularity regions ($|\eta| < 2.5$, see Table 2.4).

Signal photons: Defined as *preselected* photons as above, which in addition pass the following criteria in Table 5.8:

- Identification (ID) - To discriminate the prompt photon signal from the background, cuts are applied on a series of electromagnetic *shower shape variables*, based on the lateral and longitudinal energy profile of the shower in the ECAL. For all analyses, the "RobustTight" identification criterion (referred to here as "tight") was used and the its precise definition can be found in [48]. Overall, this criterion does not depend on the photon p_{T}, but on its η (to take into account variations in the calorimeter geometry and material).

- Isolation - To further discriminate signal from background, an isolation requirement is made on the remaining photon candidates after preselection and identification. This is because the prompt photon signal is expected to be more isolated with respect to hadronic activity than the background, as shown in Figure 5.1[3]. The isolation variable $E_{\mathrm{T}}^{\mathrm{iso}}$ is computed from the transverse energy deposited in the calorimeters in a cone of radius $\Delta R = 0.4$ around the photon candidate. A few corrections are made to $E_{\mathrm{T}}^{\mathrm{iso}}$ to account for the effects associated with the energy of the photon candidate itself, the underlying event and pileup (see Section 2.2.5). The overall correction from these was found to be ~ 900 MeV [49], after which $E_{\mathrm{T}}^{\mathrm{iso}}$ is directly comparable to parton-level theoretical predictions (*e.g.* an experimental $E_{\mathrm{T}}^{\mathrm{iso}} < 3$ GeV cut is similar to applying a theoretical 4 GeV cut).

Prompt photon (γ_1): Defined here as the leading-p_{T} *signal* photon in an event. These are the candidates considered further when resolving overlapping objects, such as jets (see Section 5.4).

As appreciated from Table 5.8, the object definitions have evolved throughout the different analysis rounds to deal with different data-taking conditions (see Section 5.2.1) and improve photon measurements (ID, efficiency, etc).

[2]The photon η used here is the one computed in the second sampling of the LAr calorimeter, which is denoted as η^{s2} in [49] but here referred to simply as η.

[3]At the time, this variable was known to not be perfectly modelled by the MC, hence the lack of a perfect data/MC agreement in the figures.

Reconstructed Photon Definitions				
Cut	Specification			
	Moriond'12	EPS'11	PLHC'11	Moriond'11
Preselected γ				
Energy Scale	"	"	"	rescaling (data) / smearing (MC)
Object Quality	"	"	OQ flag	OQ check (data) / OQ map (MC)
Cleaning	"	OQ, LAr quality & timing	jet cleaning	none
η Acceptance	"	" "	$\lvert\eta^{s2}\rvert < 2.37$ "	$\lvert\eta^{s2}\rvert < 1.81$ & not in crack
Signal γ				
Identification	"	"	"	RobustTight
Isolation	Etcone40 < 5 GeV	"	"	Etcone40 < 3 GeV

Table 5.8.: *Summary of the selection criteria for the different photon definitions used (the " means the definition didn't change with respect to to the previous analysis). The leading p_{T} signal photon in an event defines the prompt photon candidate. The "crack" region and η^{s2} are defined elsewhere in the text and "OQ" stands for Object Quality.*

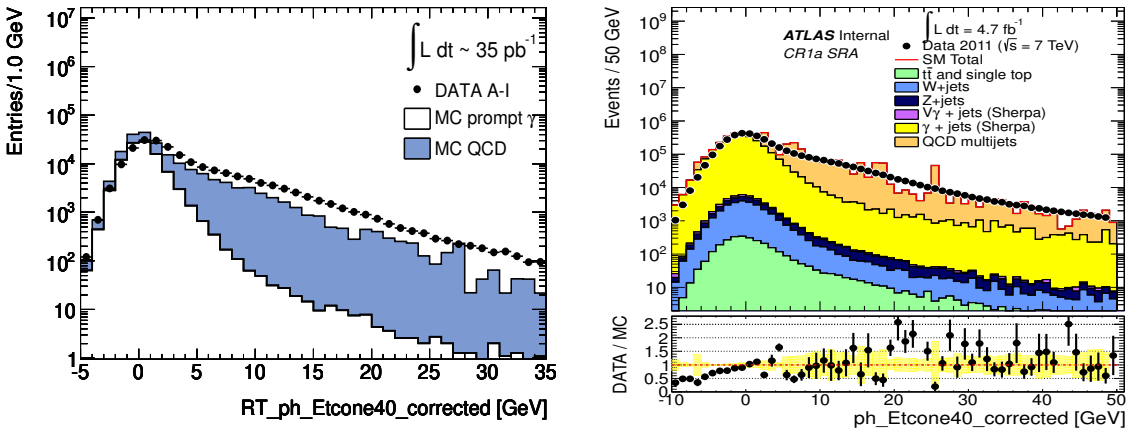

(a) (b)

Figure 5.1.: *Isolation variable $E_{\mathrm{T}}^{\mathrm{iso}}$ distribution for preselected "tight" photon candidates in data and MC. The MC include γ+jets signal and backgrounds to γ+jets, (a) in the Moriond'11 dataset (showing QCD background only) and (b) in the Moriond'12 dataset (showing both QCD and electroweak backgrounds). The width of the $E_{\mathrm{T}}^{\mathrm{iso}}$ spectrum for the signal is driven by noise in the EM calorimeter, which is calibrated to be centred at zero, hence the negative component corresponding to downward fluctuations in the calorimeter cells.*

5.3.2. Event Selection

The event selection performed in this first stage of the analysis is outlined in Table 5.9. Cut 1 is to ensure the same data-quality (DQ) requirements as in the 0ℓ analysis. Events are required to be in the same Good Runs List (GRL), which also determines the total integrated luminosity of the sample, quoted in Table 5.2. With the exception of Cut 1, the event selection is also identical to the latest used by the SMDP group [93]. Cut 2 is the trigger decision, always chosen to be the lowest unprescaled photon trigger in the dataset. Cut 3-4 are general "event cleaning" cuts applied widely in ATLAS analyses. Cut 3 in particular rejects events with bad data quality in the LAr calorimeter [94] (see Section 5.2.1). Cut 4 ensures that the event is a genuine collision event with a well-defined interaction at the primary vertex (PV)[4], as opposed to being from non-collision sources such as cosmic rays. Lastly, Cut 5 ensures the photon candidates are in the $\sim 100\%$ efficient trigger plateau from Cut 2.

$\gamma + X$ Event Selection					
Cut	Description	Specification			
		Moriond'12	EPS'11	PLHC'11	Moriond'11
1	0ℓ GRL (data)	`x-v36-prod10y-08z`	`x-v*-prod*y-0*z`	`x-v*-prod*y-0*z`	N/A
2	Trigger	"	`g80_loose`	`g60_loose`	`g40_loose`
3	Ev. clean - LAr (data)	"	`larError=0`	none	none
4	Ev. clean - leading PV	"	$N_{trk} \geq 5$	"	$N_{trk} \geq 3$
5	$p_{\mathrm{T}}(\gamma_1)$	"	> 85 GeV	> 65 GeV	> 45 GeV

Table 5.9.: *Event selection defining the inclusive prompt photon sample ($\gamma + X$) in the different analysis rounds. In Cut 1,* `x=data11_7TeV.periodAllYear_DetStatus-`*;* `y=_CoolRunQuery-00-04-`*; and* `z=_Susy.xml`*. For the trigger names in Cut 2, "*`g`*" is for "gamma", the number represents the transverse energy threshold and "*`loose`*" the type of ID requirement. Cut 3 checks the LAr DQ flag is not in ERROR (noise burst) or WARNING (noisy) state. In Cut 4, N_{trk} is the number of associated tracks to the PV. In Cut 5, γ_1 represents the prompt photon candidate as defined in Section 5.3.1.*

5.3.3. Results

Table 5.10 shows the number of photon candidates passing the object definitions in Table 5.8, for events that pass the selection in Table 5.9. Only those events with at least

[4]The leading primary vertex is defined as the vertex with the highest $\sum |p_{\mathrm{T}}|^2$ of tracks.

one *signal photon* candidate are kept and these define the "$\gamma + X$ sample". Although it is possible for an event to have more than one signal photon, *e.g.* a diphoton event $\gamma\gamma + Y$, only the highest-p_{T} photon is considered as the prompt photon candidate, and so the total number of candidates equals the total number of events. Figure 5.2 shows the p_{T} and η distributions of the prompt photon candidates in the $\gamma + X$ sample. As expected (see Appendix B), the background reduces with photon p_{T}, shown by the increasing agreement of data with the MC signal. The average jet multiplicity in these events is suggested by the recent SMDP $\gamma +$ jets cross-section measurement results [98], where on average it is found to be between 1.3 and 2.0, and increasing with photon p_{T}.

Number of γ candidates				
Requirement	Moriond'12	EPS'11	PLHC'11	Moriond'11
Preselection	11 951 974	-	-	722 055
Identification	3 926 910	-	-	255 985
Isolation	2 858 432	523 745	230 457	152 602

Table 5.10.: *Cutflow of reconstructed photons in data which passed the event selection in Table 5.9 under different object definitions in Table 5.8 for the different analyses. Only those passing up to the isolation requirement are considered part of the $\gamma + X$ sample. It is possible to have events with more than one signal photon (*e.g. *in the PLHC'11 dataset, 71 events are diphoton events) but for the purposes of this analysis, only the leading p_{T} one is considered the prompt photon. The '-' means the information was not available at the time of writing.*

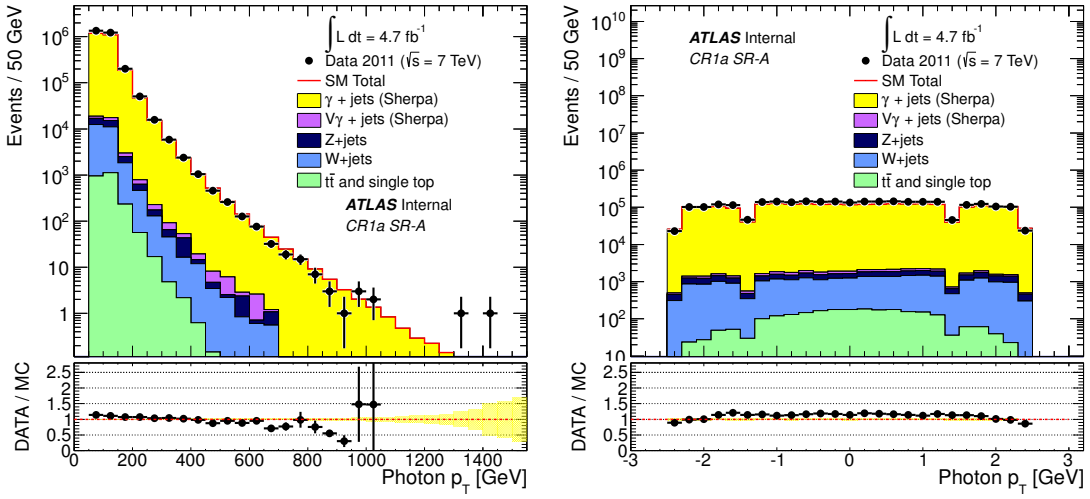

Figure 5.2.: *Moriond'12 leading-p_{T} photon (prompt photon candidate) (a) p_{T} and (b) η distributions from data and MC after the $\gamma + X$ selection. The number of events in these plots is quoted in Table 5.10.*

5.3.4. Comparison with SM prompt photon results

The event sample obtained after the inclusive photon selection ($\gamma + X$) was used for cross checks with respect to official results from ATLAS prompt photon cross-section measurements. These comparisons serve both to validate the selection procedure as well as to provide reference results before the final selection is applied. The final selection (Section 5.4), motivated by the new physics search and specific to this analysis, is expected to only have small effects on several properties of the photon event sample, particularly those related to efficiencies and backgrounds. It is therefore very valuable to establish a reference before the final selection, which can confirm this expectation and be verified by other independent analysis results.

Two measurements of the prompt photon cross-section have been made in ATLAS: one in 2010 with 880 nb^{-1} [48] and an update of it in 2011 with 35 pb^{-1} [49]. A summary of the 35 pb^{-1} analysis (referred to here as the "SM analysis") is provided in Appendix B, as this is the main reference used in this analysis. However, more recent updates exist (albeit unpublished), such as [92] (1.08 fb^{-1}). To ease comparison with the 35 pb^{-1} analysis results, the rest of this section will present the Moriond'11 results (Appendix C.1), since this is the analysis round which corresponds to roughly the same luminosity. Despite the results being relatively old, the main conclusions also hold for the more recent updates. As seen in Sections 5.3.1-5.3.2, the event selection and object definitions have changed little since then, so in practice, the main change simply comes down to an increase in luminosity.

Acceptance and Efficiency ($A^\gamma \cdot \varepsilon^\gamma$) - The acceptance A^γ derives from the limited fiducial region in which photons can be properly reconstructed in ATLAS (η requirements in Table 5.8). Given that the same photon p_T and η acceptance as in [49] are used, no additional acceptance corrections are necessary. As discussed in Appendix B, the efficiency at this stage refers to the *overall* photon efficiency of reconstruction and identification, *i.e.* $\varepsilon^\gamma = \varepsilon^\gamma_\text{rec} \cdot \varepsilon^\gamma_\text{id}$. Usually the isolation criterion is not taken into account in the efficiency of the photon results in [49], but instead included in the theoretical predictions with which they are compared. Therefore, here an additional efficiency $\varepsilon^\gamma_\text{iso}$ is defined with respect to the isolation requirement. This is, however, closely related to the Control Region selection (Section 5.4) and becomes only relevant when calculating the TF, therefore its discussion is left until Section 5.5.1.

The reconstruction inefficiency $(1 - \varepsilon^{\gamma}_{\text{rec}})$ is caused by limitations of the reconstruction algorithm, acceptance loss due to dead calorimeter cells and object quality requirements. In [48, 49], $\varepsilon^{\gamma}_{\text{rec}}$ was estimated from prompt photon MC as a function of η and p_{T}, and found to be relatively constant within the relevant photon acceptance, slightly decreasing with larger p_{T} and with some variation in η (see Figure B.2).

The dominant source of the identification inefficiency $(1 - \varepsilon^{\gamma}_{\text{id}})$ is the *tight* photon identification requirement. Here as well, $\varepsilon^{\gamma}_{\text{id}}$ was estimated in [48, 49] from prompt photon MC and found to be relatively constant within the relevant photon acceptance, but unlike $\varepsilon^{\gamma}_{\text{rec}}$, $\varepsilon^{\gamma}_{\text{id}}$ increased with p_{T} (see Figure B.3). As a cross check, the shower shape variables, plots of which are shown in Figure C.3, were investigated in data and MC and found to be consistent with the SM analysis results. These variables were also compared before and after the final Moriond'11 0ℓ selection (see Section 5.4) and found not to change significantly, even suggesting a higher efficiency after the final selection, as expected due to the higher photon p_{T} in the final sample (see Section 5.4.3).

Overall, the relatively stable behaviour of the efficiency, especially at high photon p_{T}, indicates that the efficiency estimated in the SM analysis should also be representative after the final selection in this analysis, as long as the resulting p_{T} and η distributions are folded in. This, together with the high precision expected from estimating these efficiencies using MC, as done in this analysis, should allow for a relatively precise comparison between the final efficiency estimate and the SM analysis results.

Purity (P) - As shown in the SM analysis, the expected purity $(1 - f_{bkg})$ is very high when requiring a high photon p_{T} ($\sim 99\%$, see Table B.3) . This is mainly due to the isolation criterion, which becomes more efficient at high p_{T} because harder jets tend to be more collimated and it is less likely for a π^0 to remain isolated. This is in contrast to the tight identification requirement, which can more efficiently reject background at lower p_{T} (*e.g.* the rejection power is better for softer π^0, because the first layer of the LAr calorimeter can more easily resolve the two photons produced in the π^0 decay).

Figure 5.1 shows the isolation energy ($E^{\text{iso}}_{\text{T}}$) distribution for the Moriond'11 and Moriond'12 samples of preselected tight photon candidates. It indicates the concentration of QCD background in the tail region at large $E^{\text{iso}}_{\text{T}}$ values. The results also demonstrate a slight disagreement between data and MC for this variable, which is

characterised by data being shifted toward larger values by ~ 2 GeV (this will be discussed further in Section 5.5.1 in connection to the isolation efficiency). Similar distributions for different photon p_{T} ranges are shown in Figure B.5 to illustrate how the QCD background propagates to larger $E_{\mathrm{T}}^{\mathrm{iso}}$ values as the photon p_{T} increases. At high photon p_{T}, the remaining background consists primarily of electrons, *e.g.* from $W_{e\nu}$ decays, faking a photon. However, this background is also at the 1% level for photon p_{T} requirements which are significantly above $m_W/2$ [99].

Figure 5.3 shows the photon p_{T} distribution of candidates passing the object definitions in Table 5.8, for events that pass the selection in Table 5.9. Figure 5.3(a) corresponds to *preselected* photons, where the sample can be seen to be still highly contaminated by QCD background (a purity of about 20%) in an approximately even distribution over the whole p_{T} range. Figure 5.3(b), on the other hand, shows the same distribution after the full prompt photon selection, *i.e.* including the tight identification and the photon isolation requirements. Despite the LO precision of the `PYTHIA` MC, the overall trend is consistent with the results found in the SM analysis, where for $p_{\mathrm{T}}(\gamma_1) > 100$ GeV the purity exceeds 90%, and the background becomes negligible at $p_{\mathrm{T}}(\gamma_1) \sim 200$ GeV.

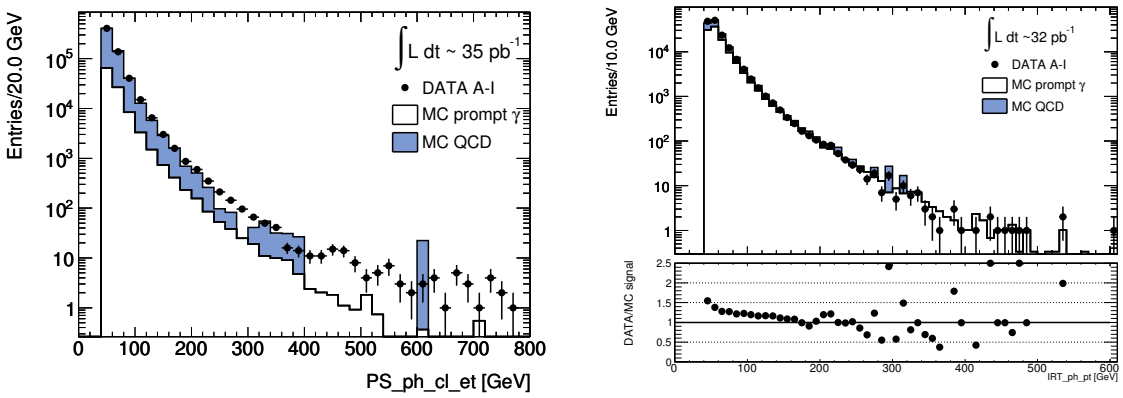

(a) (b)

Figure 5.3.: *Moriond'11 p_{T} distribution of photon candidates passing the (a) preselection and (b) prompt photon definitions in Table 5.8. The MC shown is the γ + jets signal and QCD background from* `PYTHIA` *(see Appendix C.1.2).*

Signal yield (N_γ) - The signal yield results obtained were also found consistent with those in [49]. As an example, in the Moriond'11 dataset the number of observed prompt photon candidates $N_{\mathbf{A}}^{\mathrm{obs}}$ in the $(|\eta|, p_{\mathrm{T}})$ range $([0.60; 1.37), [45; 55)$ GeV) was 32 272. In this $(|\eta|, p_{\mathrm{T}})$ bin, the expected purity is $\sim 90\%$. For the same $|\eta|$ range

but higher p_{T} range $[200; 400)$ GeV, the expected purity is $\sim 100\%$ and $N_{\mathbf{A}}^{\mathrm{obs}}$ was 185. These numbers can be compared with the SM analysis equivalent quoted in Table B.3. A small difference is expected from the different GRLs used and the slightly higher luminosity in the Moriond'11 dataset (see Section B.1).

5.4. Control Region Sample (CR1a)

The steps shown in Figure 3.2 required to go from the "$\gamma + X$ events" to the "CR events" are of course a simplified version – in practice a few more steps are required as shown in Figure 5.4, which consist of *additional* object definitions and event selections (on top of those defining the $\gamma + X$ sample). The details of these requirements are described in this Section, but beforehand it is helpful to define more precisely the following concepts which are constantly used in the following pages:

Signal Region (SR) - Defined by an event selection optimised for discovery, *i.e.* with sufficient sensitivity to a BSM model. In the case of the SUSY 0ℓ analysis, the aim is to maximise sensitivity to the production of heavy SUSY particles decaying into jets and neutralinos, leading to final-states of $E_{\mathrm{T}}^{\mathrm{miss}} + \text{jets}$. In the various 0ℓ analyses, several SRs are defined, typically differentiated by jet multiplicity and thresholds on the discriminating variables, *e.g.* m_{eff} cut, defined below.

Control Region (CR) - Defined by an event selection as similar as possible to the SR (to minimise the uncertainties arising from extrapolation to the SR while maintaining an adequate statistical weight) and enriched in the chosen calibrating process, *i.e.* of high-purity. Measurements in a CR are used to estimate a particular background in the SR via the TF (Section 5.5). Example of CRs in the 0ℓ analysis are shown in Table 5.11 and the detailed definitions are discussed until Section 5.6.

CR1a - This is the Control Region based on the $\gamma + \text{jets}$ sample, used to estimate the $Z_{\nu\nu} + \text{jets}$ background in the 0ℓ analysis. More specifically, it is the $\gamma + X$ event sample, as defined in Section 5.3, which also passes the additional requirements described in Sections 5.4.1 and 5.4.2 (see Figure 5.4).

CR1b - This is the alternative CR to CR1a based on a $Z_{\ell\ell} + \text{jets}$ sample as outlined in Table 5.11.

Channel - This term is used to refer to the ensemble of a SR and its corresponding CRs, *e.g.* for Moriond'12, six channels are defined, where each SR has five associated CRs.

CR	SR Background	CR process	CR selection
CR1a	$Z_{\nu\nu}$ + jets	γ+jets	Isolated photon
CR1b	$Z_{\nu\nu}$ + jets	$Z_{\ell\ell}$ + jets	$\lvert m(\ell,\ell) - m(Z)\rvert < 25$ GeV
CR2	QCD jets	QCD jets	Reversed $\Delta\phi$ cut
CR3	$W_{\ell\nu}$ + jets	$W_{\ell\nu}$ + jets	30 GeV $< m_T(\ell, E_{\mathrm{T}}^{\mathrm{miss}}) <$ 100 GeV, b-veto
CR4	$t\bar{t}$ and single-t	$t\bar{t} \to bbqq'\ell\nu$	30 GeV $< m_T(\ell, E_{\mathrm{T}}^{\mathrm{miss}}) <$ 100 GeV, b-tag

Table 5.11.: *Control Regions used in the 0ℓ analysis, indicating the main SR background targeted, the process used to calibrate the background, and main CR cuts used to select this process. The meaning of the selections and variables can be found in Section 5.6 and [100].*

5.4.1. CR1a Object Definitions

As indicated in Figure 5.4, these additional requirements are conjunctively referred to as 'CR1a Object Definition' because within the context of the 0ℓ analysis they only apply to CR1a, *i.e.* in the rest of the 0ℓ analysis, prompt photon events are ignored[5]. The CR1a object definition then consists of the following:

i. **γ_1-jet Overlap Removal:** Experimentally, this step is required when the jets in photon events need to be defined. This is because in ATLAS photons are also reconstructed as jets, as suggested by Figure 5.5. So, to prevent the reconstructed photon from being double-counted as a jet, a γ_1-jet *overlap removal* procedure is required. The recipe used here is to remove any jets with $\Delta R < 0.2$ of the prompt photon candidate γ_1. It was found that varying the critical ΔR value between 0.1 and 0.4 introduces negligible bias, as is to be expected given the prior application of photon isolation criteria in the identification cuts.

ii. **$\boldsymbol{E}_{\mathbf{T}}^{\mathbf{miss}}$ definition:** As discussed in Section 3.2 and outlined in Equation (3.2), the total $E_{\mathrm{T}}^{\mathrm{miss}}$ vector can be split into its true ($\not{E}_{\mathrm{T}}^{\mathrm{true}}$) and fake ($\not{E}_{\mathrm{T}}^{\mathrm{fake}}$) components. In SM processes, the only expected $\not{E}_{\mathrm{T}}^{\mathrm{true}}$ is from neutrinos and anything else is considered $\not{E}_{\mathrm{T}}^{\mathrm{fake}}$ arising from experimental effects. From now on, the variable $E_{\mathrm{T}}^{\mathrm{miss}}$ and it's components $\not{E}_{\mathrm{T}}^{\mathrm{true}}$ and $\not{E}_{\mathrm{T}}^{\mathrm{fake}}$ will be assumed to represent those in $Z_{\nu\nu}$ + jets events and their primed versions ($E_{\mathrm{T}}^{\mathrm{miss}\prime}$, $\not{E}_{\mathrm{T}}^{\mathrm{true}\prime}$, $\not{E}_{\mathrm{T}}^{\mathrm{fake}\prime}$) those in γ + jets events. Hence, to simulate the $E_{\mathrm{T}}^{\mathrm{miss}}$ in $Z_{\nu\nu}$ + jets events from the γ + jets sample, the

[5]Cross-checks have made to verify that the γ + jets contribution to the 0ℓ SRs can be safely neglected (see Section D.2).

following applies:

$$E_{\mathrm{T}}^{\mathrm{miss}} = \not{E}_{\mathrm{T}}^{\mathrm{true}} + \not{E}_{\mathrm{T}}^{\mathrm{fake}} \tag{5.1}$$

$$= p_{\mathrm{T}}(\gamma_1) + \not{E}_{\mathrm{T}}^{\mathrm{fake}\prime} \tag{5.2}$$

$$= p_{\mathrm{T}}(\gamma_1) + E_{\mathrm{T}}^{\mathrm{miss}\prime} \tag{5.3}$$

Equation (5.2) follows since the prompt photon p_{T} is used to simulate the $\not{E}_{\mathrm{T}}^{\mathrm{true}}$ in $Z_{\nu\nu}$ events ($\not{E}_{\mathrm{T}}^{\mathrm{true}} = p_{\mathrm{T}}(\gamma_1)$) and the same experimental effects are expected to contribute equally to $\not{E}_{\mathrm{T}}^{\mathrm{fake}}$ in both types of events ($\not{E}_{\mathrm{T}}^{\mathrm{fake}} = \not{E}_{\mathrm{T}}^{\mathrm{fake}\prime}$). Equation (5.3) follows since $\not{E}_{\mathrm{T}}^{\mathrm{true}\prime} \sim 0$ is expected in $\gamma +$ jets events (although it would still be possible to have neutrinos in the event, *e.g.* from $\gamma + b$-jets).

Some subtlety enters in the definition of the $E_{\mathrm{T}}^{\mathrm{miss}\prime}$ due to the $E_{\mathrm{T}}^{\mathrm{miss}}$ definition used in the 0ℓ analysis (`MET_Simplified20_RefFinal`, see Section 2.2.5), which does not explicitly reconstruct terms for photons or taus (as mentioned, the 0ℓ analysis neglects these objects in the event selection). Given that ATLAS reconstruction ordinarily identifies clusters belonging to photons as jets as well, and furthermore photons may be misidentified as electrons (*e.g.* when a conversion track is present, see Section 2.2.5), the clusters corresponding to a prompt photon are typically calibrated as though they originated from electrons or hadronic jets. Particularly in the case of jets, the numerical inversion jet calibration scheme (EMJES) used in all the analyses up to Moriond'12 does not separately scale electromagnetic and hadronic clusters, but applies a single p_{T}- and η-dependent scaling factor to all clusters. As the EMJES scaling factor is always larger than the corresponding electromagnetic scale, photon clusters can be weighted high relative to the energies that would be appropriate for genuine photons. Hence, a momentum imbalance is introduced, producing $\not{E}_{\mathrm{T}}^{\mathrm{fake}\prime}$ opposite in ϕ to the leading photon. While this $\not{E}_{\mathrm{T}}^{\mathrm{fake}\prime}$ can be substantial in magnitude, it is typically aligned with the leading jet in the event, and thus photon events tend not to pollute the 0ℓ signal regions, due to a cut on such event configurations ("$\Delta\phi$ cut" in Table 5.14, see Section 5.4.2). This is clearly illustrated in Figure 5.6 where different $E_{\mathrm{T}}^{\mathrm{miss}}$ algorithms are plotted and, although the effect on $Z_{\nu\nu} +$ jets events is negligible (Figure 5.6(a)), that in $\gamma +$ jets is not (Figure 5.6(b)).

Prior to Moriond'12, the solution to this problem was to simply use a different $E_{\mathrm{T}}^{\mathrm{miss}}$ reconstruction algorithm as shown in Table 5.12, which calibrated all calorimeter clusters appropriately, either by discriminating clusters based on location rather than

by object association (`MET_LocHadTopo`), or by associating photons appropriately (`MET_Simplified20withTightPhotons_RefFinal`). For Moriond'12, to increase the consistency with the 0ℓ analysis, the `MET_Simplified20_RefFinal` definition was retained, but the contribution of the jet or electron matched to γ_1 was removed from the $E_{\mathrm{T}}^{\mathrm{miss}}$ calculation, rather than being partially cancelled by removing $p_{\mathrm{T}}(\gamma_1)$ ($\not{E}_{\mathrm{T}}^{\mathrm{true}} = p_{\mathrm{T}}(\gamma_1)$ in Equation (5.3)). This new procedure was found to be in agreement with the previous procedure, as shown in Figure 5.7.

In summary, both the γ_1-jet overlap removal and $E_{\mathrm{T}}^{\mathrm{miss}\prime}$ redefinition can be regarded as being required for purely experimental reasons, while the $\not{E}_{\mathrm{T}}^{\mathrm{true}}$ redefinition is intrinsic to the method. After the application of these requirements, the result is a suitable $E_{\mathrm{T}}^{\mathrm{miss}}$ + jets sample which can be used for the '0ℓ Object Definition and Event Selection', described in the next Section.

$\boldsymbol{E_{\mathrm{T}}^{\mathrm{miss}}}$ **components in CR1a**				
$E_{\mathrm{T}}^{\mathrm{miss}}$ component	Moriond'12	EPS'11	PLHC'11	Moriond'11
$\not{E}_{\mathrm{T}}^{\mathrm{fake}}$	`MET_Simplified20_RefFinal`	„	`MET_Simplified20 withTightPhotons_RefFinal`	`MET_LocHadTopo`
$\not{E}_{\mathrm{T}}^{\mathrm{true}}$	$\sum \gamma_1$-matched jets and electrons	„	„	$p_{\mathrm{T}}(\gamma_1)$

Table 5.12.: *Names of reconstruction algorithms used to compute $\not{E}_{\mathrm{T}}^{\mathrm{fake}}$ (the one used for Moriond'12 being the same as in the 0ℓ analysis) and the meaning of $\not{E}_{\mathrm{T}}^{\mathrm{true}}$ in CR1a throughout the different analysis rounds.*

5.4.2. 0ℓ Object Definitions and Event Selection

As shown in Figure 5.4, the following requirements are the last needed to define CR1a, and are applied on the $E_{\mathrm{T}}^{\mathrm{miss}}$ + jets sample defined in the previous Section. They are referred to as "0ℓ Object Definitions and Event Selection" (and together simply as "0ℓ Selection") because they are exactly those defining the 0ℓ SRs. As mentioned in Section 3.3, one of the advantages of the γ + jets sample is that the large statistics make it possible to apply the SRs selections directly, without needing extrapolations from looser cuts.

i. **0ℓ Object Definitions:** These define the 0ℓ requirements for jets, electrons, muons and $E_{\mathrm{T}}^{\mathrm{miss}}$, as well as overlap-removal procedures between these objects. The specific

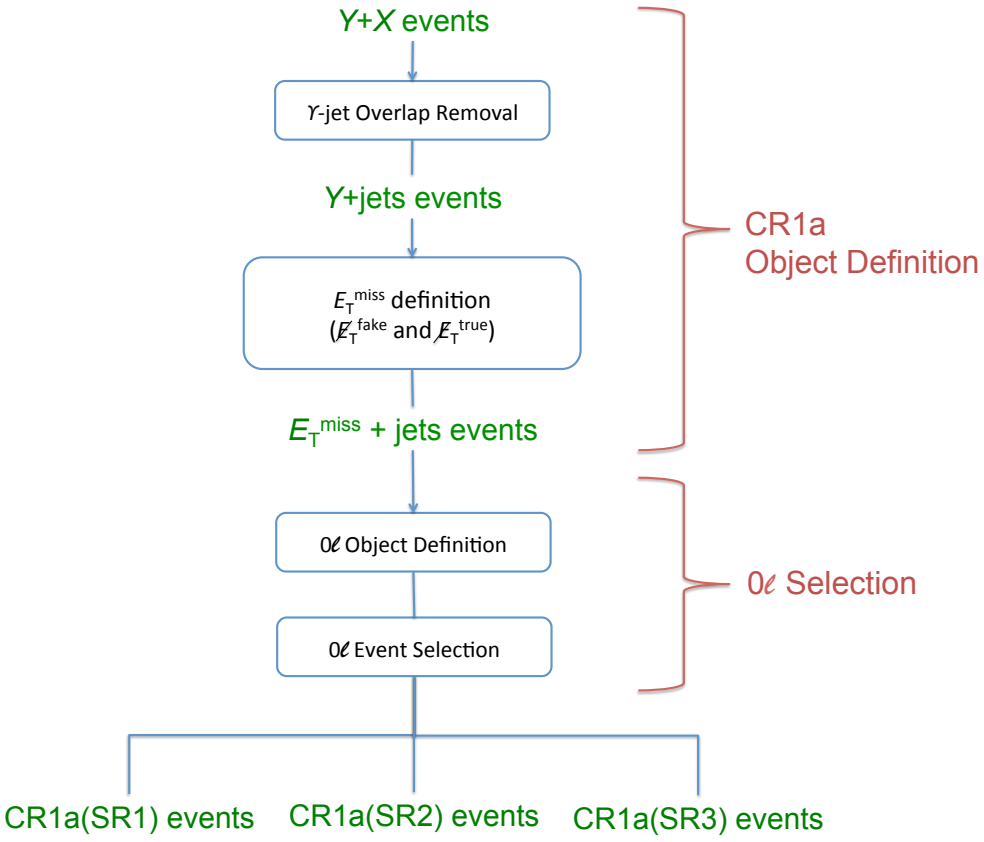

Figure 5.4.: *Schematic chart outlining the additional steps needed to define CR1a. First, an additional object definition specific to CR1a is required (an overlap removal between the prompt photon candidate and jets in the event and a redefinition of the* $E_{\mathrm{T}}^{\mathrm{miss}}$ *variable), after which an appropriate* $E_{\mathrm{T}}^{\mathrm{miss}}$ *+ jets sample is defined. At this point, the* 0ℓ *object definitions and event selections can be applied directly, which finally results in the definition of the CR1a sample (one for each SR). CR1a events are the input for the TF to get the* $Z_{\nu\nu}$ *background estimate. The meaning of the variables and abbreviations in the diagram are specified elsewhere in the text.*

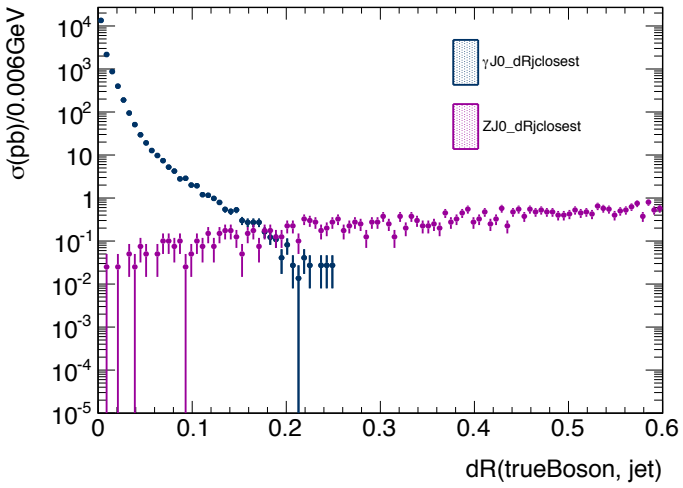

Figure 5.5.: *The distribution of the ΔR variable between the true vector boson V ($V = Z_{\nu\nu}, \gamma$) and the closest reconstructed jet in V + jets MC before V-jet overlap removal. In the γ + jets case, before overlap removal, almost all events have the closest jet within $\Delta R < 0.2$ because the γ is also reconstructed as a jet, while the $Z_{\nu\nu}$ + jets sample does not suffer from this problem. After overlap removal, these jets are discarded and the closest jet is then well separated from the boson. The MC is from* `PYTHIA` *samples listed in Section C.1.*

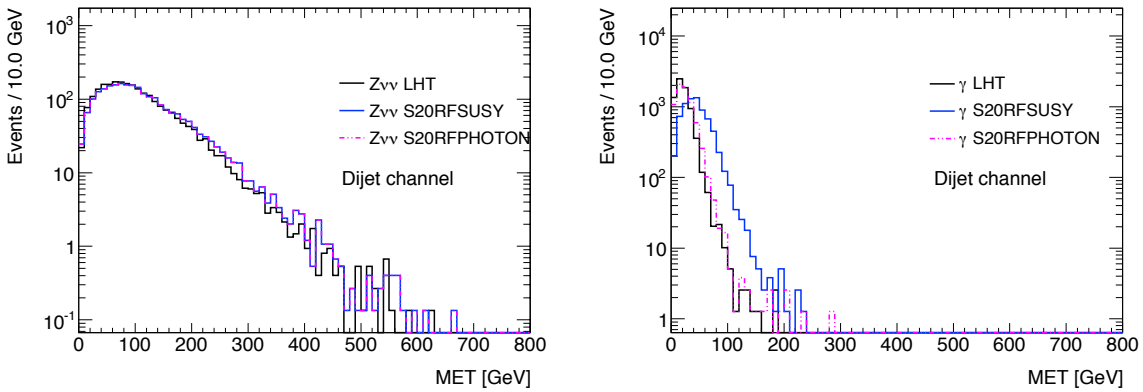

(a) (b)

Figure 5.6.: *Effect of three different $E_{\mathrm{T}}^{\mathrm{miss}}$ reconstruction algorithms on MC (a) $Z_{\nu\nu}$ + jets and (b) γ + jets in the PLHC'11 0ℓ dijet channel (see Appendix C.2). 'LHT' is for* `MET_LocHadTopo`*, 'S20RFSUSY' for* `MET_Simplified20_RefFinal` *and 'S20RFPHOTON' for* `MET_Simplified20withTightPhotons_RefFinal` *(see Table 5.12). The MC is normalised to the PLHC'11 luminosity.*

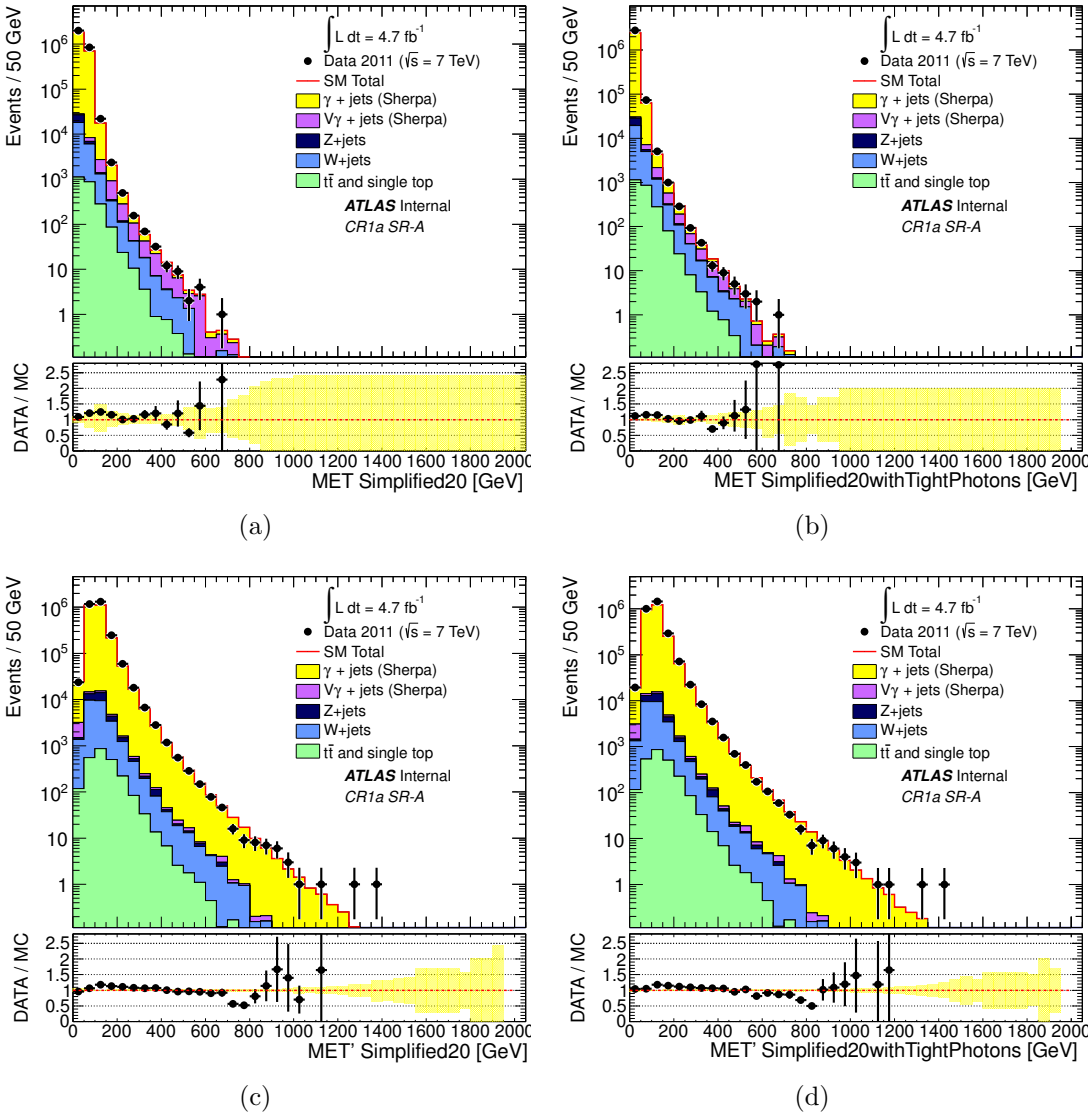

Figure 5.7.: *Moriond'12 Comparison of different* $E_{\mathrm{T}}^{\mathrm{miss}}$ *algorithms from Moriond'12 (specified on the x-axis) in the* $\gamma+X$ *sample. The definitions are as follows:* `MET_Simp20`*: standard SUSY definition, photons not explicitly reconstructed.* `MET_Simp20wTP`*: SUSY definition, but identifying tight photons and calibrating their clusters appropriately.* `METp_Simp20`*: as for* `MET_Simp20`*, but with the contribution of a jet or electron matched to* γ_1 *removed.* `METp_Simp20wTP`*: as for* `MET_Simp20wTP`*, but with the contribution of* γ_1 *removed. In (a) and (b), a noticeable tail is visible. This is due to backgrounds with genuine* $E_{\mathrm{T}}^{\mathrm{miss}}$ *from a* $W \to e\nu$ *decay, where the electron fakes a photon. The broadening of the* $E_{\mathrm{T}}^{\mathrm{miss}}$ *spectrum due to the miscalibration of photon clusters is also evident. After removing the photon contribution, the resulting simulated* $E_{\mathrm{T}}^{\mathrm{miss}}$ *distribution is mostly independent of the reconstruction algorithm, as demonstrated in (c) and (d). Figures (c) and (d) hence represent the* $Z_{\nu\nu}$*-like* $E_{\mathrm{T}}^{\mathrm{miss}}$ *to be used for the subsequent* 0ℓ *selection.*

object definitions have evolved throughout the different analysis rounds, and the details can be found in the corresponding analysis documentation [63, 100–102] (see also Section 2.2.5 for a general overview).

ii. 0ℓ Event Selection / SRs: The 0ℓ SRs are ultimately defined by cuts on a discriminating variable called the *effective mass* m_{eff}. For a channel which selects events with n jets, m_{eff} is defined to be the scalar sum of the transverse momenta of the leading n jets together with $E_{\text{T}}^{\text{miss}}$:

$$m_{\text{eff}}(\text{incl.}) \equiv \sum_{i=1}^{n} |\mathbf{p}_{\text{T}}^{(i)}| + E_{\text{T}}^{\text{miss}}, \tag{5.4}$$

Hence, through this variable, stringent requirements on $E_{\text{T}}^{\text{miss}}$ and jets can be applied, which is why it is a powerful discriminant between SUSY signals and most SM backgrounds.

The 0ℓ SRs have evolved throughout the different analysis rounds and the details can be found in the corresponding analysis documentation [63, 100–102]. For Moriond'12 six inclusive channels are defined (labelled A, A', B, C, D and E), characterised by increasing jet multiplicity from 2 to 6 (except for A' which has the same multiplicity as A but is differentiated by a different value of the $E_{\text{T}}^{\text{miss}}$ to m_{eff} ratio). The lower jet multiplicity channels target models of squark pair production with short decay chains, while the high jet multiplicity channels target gluino pair production and/or long cascade decay chains (see Section 1.2.3). The corresponding SRs are summarised in Table 5.13 and shown in full detail in Table 5.14. For the latter, Cuts 3a-5 are for "event cleaning" due to a variety of experimental effects and data-taking conditions (Section 5.2.1), so the actual discriminating cuts only start from Cut 7 onwards. In order to make this distinction, the expression '0ℓ preselection' will be used to refer to the application of all cuts up to and including Cut 6 ("0ℓ veto"). Cut 14 is the"$\Delta\phi$ cut" – a requirement on the smallest of the azimuthal separations between the $E_{\text{T}}^{\text{miss}}$ vector and the reconstructed jets. For channels A, A' and B, the selection requires $\Delta\phi > 0.4$ using up to three leading jets. For the other channels an additional requirement $\Delta\phi > 0.2$ is placed on all jets with $p_{\text{T}} > 40$ GeV. Requirements on $\Delta\phi$ and $E_{\text{T}}^{\text{miss}}/m_{\text{eff}}$ (Cut 15) are designed to reduce the background from multi-jet processes. The last cut (Cut 16) uses "m_{eff}(incl.)" rather than m_{eff}, which sums over *all* jets with $p_{\text{T}} > 40$ GeV, as it has been found to improve the QCD jet background rejection [100].

In summary, to define CR1a, all the requirements from Table 5.14 have to be applied on the $E_{\mathrm{T}}^{\mathrm{miss}}$ + jets sample previously defined, with the exception of Cut 2 (a different trigger requirement was already applied when defining the $\gamma + X$ sample in Section 5.3). Since there is more than one SR, the result is one CR1a sample per SR. From now on, unless otherwise stated, the expression 'CR1a sample' will be frequently used to refer to all these CR1a samples, rather than just one. Similarly, the expression '0ℓ selection' will be used to refer to the combined '0ℓ object definition and event selection'.

This concludes all the addtional object definitions and event selections required by the method, since the CR1a sample is what is needed to calculate the TF and get the $Z_{\nu\nu}$ + jets background estimate. Therefore, the remainder of this Section is dedicated to discussing a few results and features observed in the CR1a sample.

Requirement	Channel					
	A	A'	B	C	D	E
$E_{\mathrm{T}}^{\mathrm{miss}}$ [GeV] >	160					
$p_{\mathrm{T}}(j_1)$ [GeV] >	130					
$p_{\mathrm{T}}(j_2)$ [GeV] >	60					
$p_{\mathrm{T}}(j_3)$ [GeV] >	–	–	60	60	60	60
$p_{\mathrm{T}}(j_4)$ [GeV] >	–	–	–	60	60	60
$p_{\mathrm{T}}(j_5)$ [GeV] >	–	–	–	–	40	40
$p_{\mathrm{T}}(j_6)$ [GeV] >	–	–	–	–	–	40
$\Delta\phi(\mathrm{jet}_i, E_{\mathrm{T}}^{\mathrm{miss}})_{\mathrm{min}}$ >	0.4 ($i = \{1, 2, (3)\}$)			0.4 ($i = \{1, 2, 3\}$), 0.2 ($p_{\mathrm{T}} > 40$ GeV jets)		
$E_{\mathrm{T}}^{\mathrm{miss}}/m_{\mathrm{eff}}(N_j)$ >	0.3 (2j)	0.4 (2j)	0.25 (3j)	0.25 (4j)	0.2 (5j)	0.15 (6j)
m_{eff}(incl.) [GeV] >	–/1400/1900	–/1200/–	–/–/1900	900/1200/1500	–/–/1500	900/1200/1400

Table 5.13.: *Moriond'12 analysis 0ℓ channels (where the SRs are defined by the last cut). Note that m_{eff} constructed from the leading N jets is used in the $E_{\mathrm{T}}^{\mathrm{miss}}/m_{\mathrm{eff}}$ cut while that constructed from all jets with $p_{\mathrm{T}} > 40$ GeV is used for the final m_{eff}(incl.) cut. The three m_{eff} selections listed in the final row denote the 'loose', 'medium' and 'tight' selections respectively (but not all channels possess three SRs).*

5.4.3. Comparison with SM prompt photon results

In Section 5.3.4, the SM analysis results (Appendix B) were shown to apply to the $\gamma + X$ sample. This was of course expected, given the identical object definitions and event

Cut	Description	Channel					
		A	A'	B	C	D	E
1	DQ (data)	Run / lumi block appears in SUSY GRL `data11_7TeV.periodAllYear_DetStatus-v36-prod10_CoolRunQuery-00-04-08_Susy.xml`					
2	Trigger	EF_j75_a4_EFFS_xe45_loose_noMu (data period B) / EF_j75_a4tc_EFFS_xe45_loose_noMu (K $\geq$ data period $\geq$ D) / EF_j75_a4tc_EFFS_xe55_noMu (data period $\geq$ L) / None (MC)					
3a	Ev. clean - jets (data)	No Looser bad jets after jet-lepton overlap removal with $p_{\mathrm{T}} > 20$ GeV and any η					
3b	Ev. clean - jets (data and MC)	Reject if leading up to 2 selected jets with $p_{\mathrm{T}} > 100$ GeV after overlap removal possess (chf < 0.02 and $\lvert\eta\rvert < 2.0$) or (chf < 0.05 and emf > 0.9 and $\lvert\eta\rvert < 2.0$)					
3c	Ev. clean - jet timing	Energy-weighted mean time of leading N selected jets after overlap removal in N jet analysis $\lvert\langle t\rangle\rvert < 5$ ns.					
3d	Ev. clean - LAr hole	'Smart' LAr hole veto					
3e	Ev. clean - cosmics	No selected muons after overlap removal with (fabs(mu_staco_z0_exPV) ≥ 1) or (fabs(mu_staco_d0_exPV) ≥ 0.2)					
3f	Ev. clean Bad muon veto	No selected muons before overlap removal with sqrt(mu_staco_cov_qoverp_exPV)/fabs(mu_staco_qoverp_exPV) ≥ 0.2					
3g	Bad MET_MUON	Veto event if $(MET\_MUON/E_{\mathrm{T}}^{\mathrm{miss}}) \times \cos(MET\_MUON\_phi - MET\_phi) > 0.5$					
3h	Ev. clean Bad tile drawers	Veto event if any selected jet with $p_{\mathrm{T}} > 40$ GeV and $BCH\_CORR\_JET > 5\%$ satisfies $\Delta\phi < 0.2$					
3i	Bad $MET\_CellOut$	Veto event if $(MET\_CellOut/E_{\mathrm{T}}^{\mathrm{miss}}) \times \cos(MET\_CellOut\_phi - MET\_phi) > 0.5$					
4	Ev. clean - LAr (data)	larError == 0					
5	Ev. clean - Prim. vtx.	Leading primary vertex with > 4 tracks					
6	Lepton veto	No selected e/μ after overlap removal with $p_{\mathrm{T}} > 20/10$ GeV.					
7	$E_{\mathrm{T}}^{\mathrm{miss}}$ [GeV] $>$	> 160					
8	$p_{\mathrm{T}}(j_1)$ [GeV] $>$	130					
9	$p_{\mathrm{T}}(j_2)$ [GeV] $>$	60					
10	$p_{\mathrm{T}}(j_3)$ [GeV] $>$	–	–	60	60	60	60
11	$p_{\mathrm{T}}(j_4)$ [GeV] $>$	–	–	–	60	60	60
12	$p_{\mathrm{T}}(j_5)$ [GeV] $>$	–	–	–	–	40	40
13	$p_{\mathrm{T}}(j_6)$ [GeV] $>$	–	–	–	–	–	40
14	$\Delta\phi(\mathrm{jet}_i, E_{\mathrm{T}}^{\mathrm{miss}})_{\mathrm{min}} >$	0.4 ($i = \{1, 2, (3)\}$)			0.4 ($i = \{1, 2, 3\}$), 0.2 ($p_{\mathrm{T}} > 40$ GeV jets)		
15	$E_{\mathrm{T}}^{\mathrm{miss}}/m_{\mathrm{eff}}(N_j) >$	0.3 (2j)	0.4 (2j)	0.25 (3j)	0.25 (4j)	0.2 (5j)	0.15 (6j)
16	m_{eff}(incl.) [GeV] $>$	–/1400/1900	–/1200/–	–/–/1900	900/1200/1500	–/–/1500	900/1200/1400

Table 5.14.: *Full version of Table 5.13 detailing the event selection, including "event cleaning" cuts. The SRs are defined by cut 16. The main variables are defined elsewhere in the text and the rest in [100].*

selections used up to that point. However, in the CR1a sample the validity of these results is not immediately obvious. Although the photon acceptance and efficiencies are mainly determined by the $\gamma + X$ selection, some minor effects from the 0ℓ selection in CR1a could be expected.

However, as the 0ℓ selection emphasises hard jet activity balanced by the total $E_{\mathrm{T}}^{\mathrm{miss}}$ vector (*i.e.* mainly the boson p_{T} in the case of CR1a and $Z_{\nu\nu}$ + jets), it predominantly selects events with hard photons that are well-separated from the leading jets. Hence, in principle no photon reconstruction biases should be introduced by such selection. It is therefore reasonable to compare the photon acceptance and efficiency in CR1a with the SM analysis results. Supporting cross-checks were done, in particular for the first analysis rounds when the method was being validated, to show this assumption was acceptable. In fact, for the Moriond'11 analysis, part of the Z/γ TF (*e.g.* $A^{\gamma} \cdot \varepsilon^{\gamma}$ and purity) used the SM analysis results directly (see Section C.1). As an example, Figure 5.8 shows the effect of the 0ℓ selection on a shower shape F_{side} (the fraction of the energy deposited in the first layer of the ECAL, in seven strips centred around the first maximum that is not contained in the three core strips [48]) which is relevant to $\varepsilon_{\mathrm{id}}^{\gamma}$. This shows that the 0ℓ selections have a rather *beneficial* impact on $\varepsilon_{\mathrm{id}}^{\gamma}$ since slightly higher values are expected from the resulting narrower shape. Therefore, the value of $\varepsilon_{\mathrm{id}}^{\gamma}$ taken from the SM analysis would be rather conservative on CR1a. An equivalent comparison for a different shower shape variable is shown in Appendix C.1.4. The overall lack of data/MC agreement in shower shapes had already been observed in the SM analyses, *e.g.* see [49], and understood to be the result of MC mismodelling, for which correction factors based on the average differences with respect to data were applied in their estimation of $\varepsilon_{\mathrm{id}}^{\gamma}$.

5.4.4. Results

The Moriond'12 numbers of events in data passing the full CR1a selection for the various SR channels are quoted in Table 5.15. The good statistics of CR1a are evident and this nice feature is more obvious when comparing it with the other 0ℓ CRs (see Section 5.6.2). The corresponding $p_{\mathrm{T}}(\gamma_1)$ distributions for the loosest SR per channel are shown in Figure 5.9, where the expected high purity is suggested by the MC. The $p_{\mathrm{T}}(\gamma_1)$ range and average across all channels is specified in Table 5.16 and compared to those in previous analyses.

The CR1a m_{eff} distributions (prior to Cut 16) for each channel are shown in Figure 5.10, compared to `ALPGEN` MC (the distributions for the SRs and other CRs can be found in

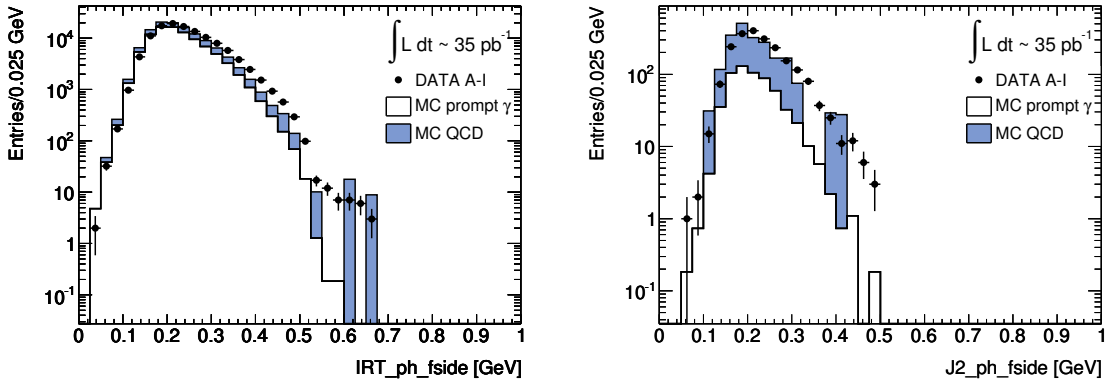

(a)

(b)

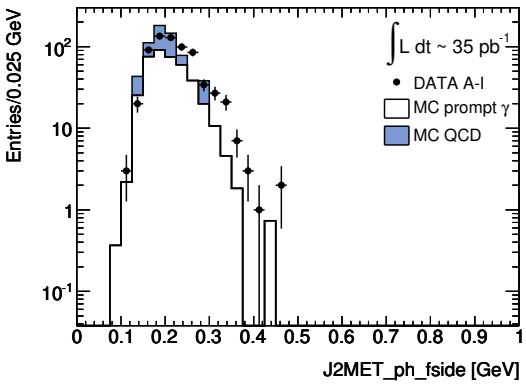

(c)

Figure 5.8.: *PLHC'11 Effect of the* 0ℓ *selections on a shower shape distribution used for the "tight" identification* F_{side}*: (a)* $\gamma + X$ *sample; (b)* $E_{\mathrm{T}}^{\mathrm{miss}}$ *+ jets sample with* 0ℓ *Dijet selection and (c)* $E_{\mathrm{T}}^{\mathrm{miss}}$ *+ jets sample with* 0ℓ *Dijet selection and* $E_{\mathrm{T}}^{\mathrm{miss}}$ *cut (the* $E_{\mathrm{T}}^{\mathrm{miss}}$ *+ jet sample is as defined in Figure 5.4). The MC shown is from* `PYTHIA` *(Section C.1.2).*

[100]). A slight difference in the slopes of the m_{eff}(incl.) distributions can be observed, which is believed to be due to `ALPGEN` mismodelling of the photon p_{T} and/or hadronic activity. When the hard cuts on $E_{\text{T}}^{\text{miss}}$ and $E_{\text{T}}^{\text{miss}}/m_{\text{eff}}$ are applied, this causes the MC to overshoot the data [100].

For the purpose of presentation of the Moriond'12 plots, data-driven scaling factors were applied to the MC to match the data in all the SRs and other CRs, except for CR1a and CR2. In the case of CR1a, this was because the data-MC agreement was considered good enough; whereas for CR2 it was because the corresponding background estimate (QCD/multi-jet) was mostly data-driven. As will be discussed in Section 5.6, these scaling factors have no impact on the final Moriond'12 0ℓ results because the background normalisation was handled by a fit to data.

Moriond'12 CR1a Event Counts											
SR	A		A'	B	C			D	E		
m_{eff}(incl.) cut [GeV]	1400	1900	1200	1900	900	1200	1500	1500	900	1200	1400
CR1a / Z/γ+jets	81	9	155	6	201	45	6	3	74	24	10

Table 5.15.: *Moriond'12 CR1a data event counts for all 0ℓ SRs.*

CR1a $p_{\text{T}}(\gamma_1)$	Moriond'12	EPS'11	PLHC'11	Moriond'11
Range [GeV]	85-1410	85-960	70-590	50-550
Average [GeV]	296-889	225-509	220-460	250

Table 5.16.: *Ranges and average values of the prompt photon p_{T} in all the CR1a samples (one CR1a per SR) in the different analysis rounds. The corresponding distributions for Moriond'12 are shown in Figure 5.9.*

For illustration, the event display of the event with the highest value of $p_{\text{T}}(\gamma_1)$ and m_{eff}(incl.) entering CR1a A, A' and B is shown in Figure 5.11, indicating that this event is most likely a genuine prompt photon event, and not due to fake sources like non-collision backgrounds. The event displays and details of all other events in this dataset with $p_{\text{T}}(\gamma_1) > 1$ TeV are shown in Appendix A.1.

Having obtained the CR1a event sample, it is now possible to proceed to the next stage of the method, which is its conversion into a $Z_{\nu\nu}$ + jets background estimate. This is done with the Z/γ TF, which is the subject of the next section.

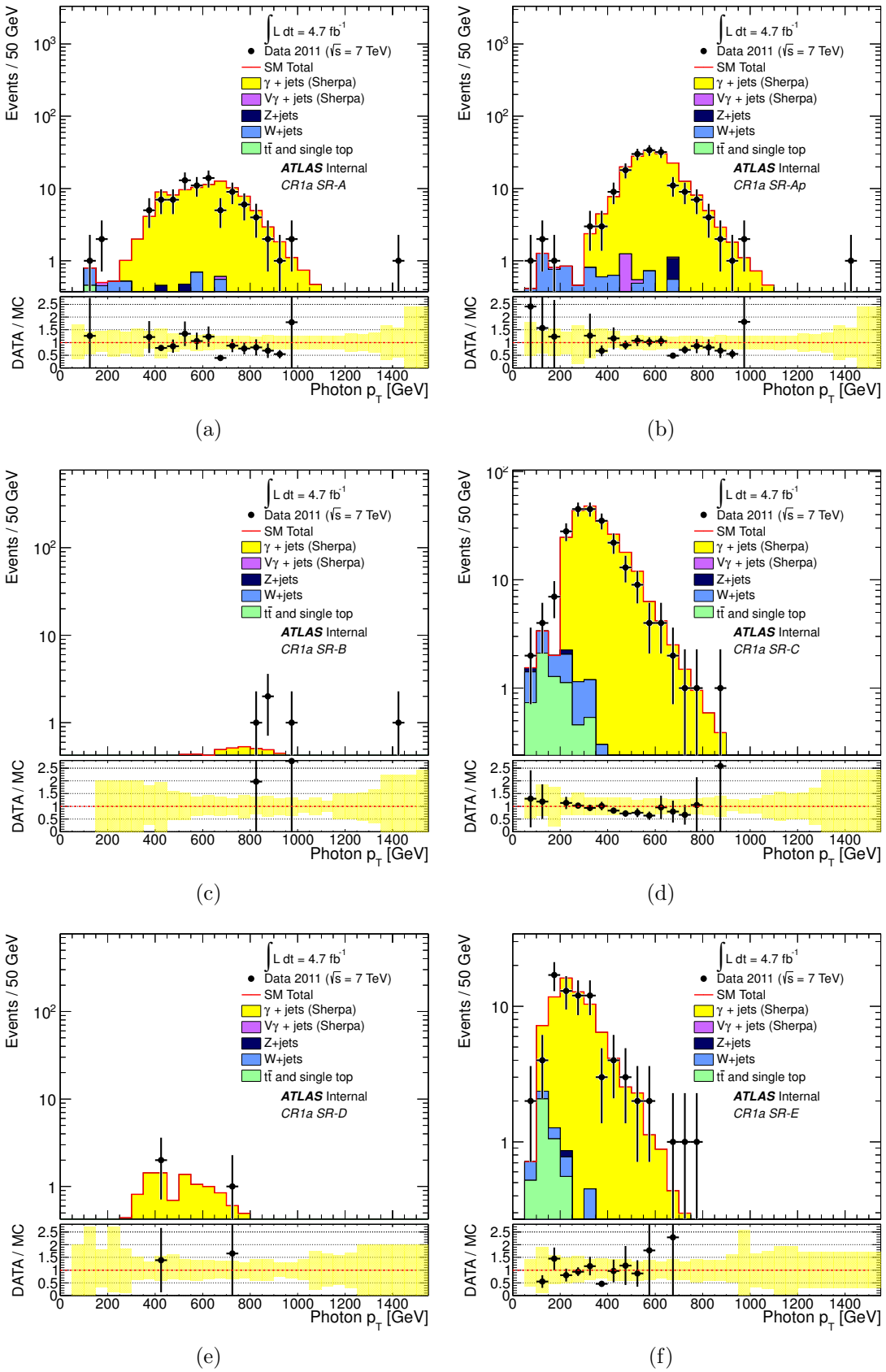

Figure 5.9.: *Moriond'12 CR1a prompt photon p_{T} distributions for the loosest SRs per channel (A: 1400, A': 1200, B: 1900, C: 900, D: 1500, E: 900). All selection criteria in Table 5.14 have been applied applied. The MC is from* `ALPGEN` *and the normalisation is to the data luminosity.*

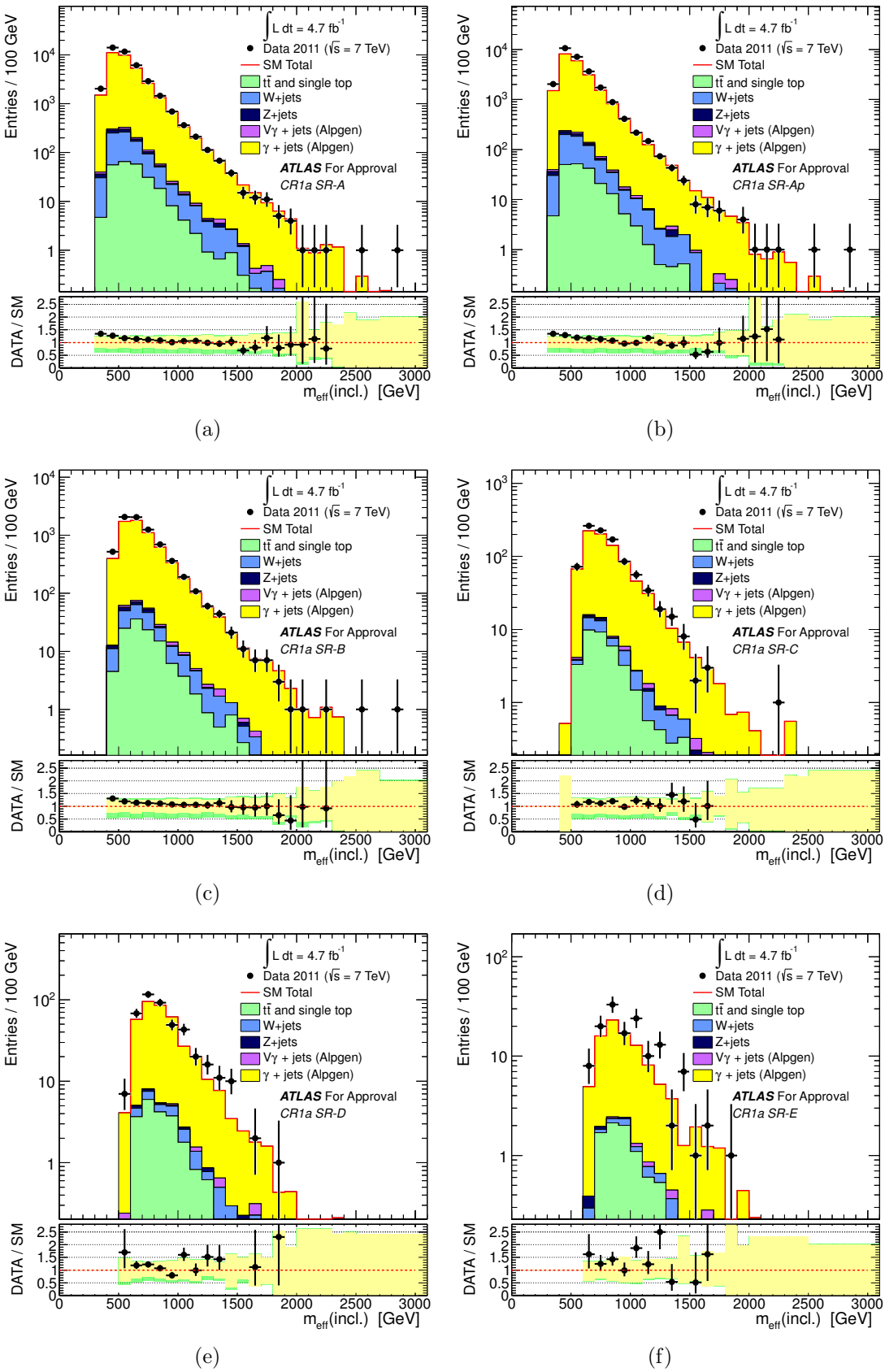

Figure 5.10.: *Moriond'12 CR1a* $m_{\text{eff}}(incl.)$ *distributions. All selection criteria in Table 5.14 prior to the final* $m_{\text{eff}}(incl.)$ *cut have been applied. The MC is from* ALPGEN *and the normalisation is to the data luminosity.*

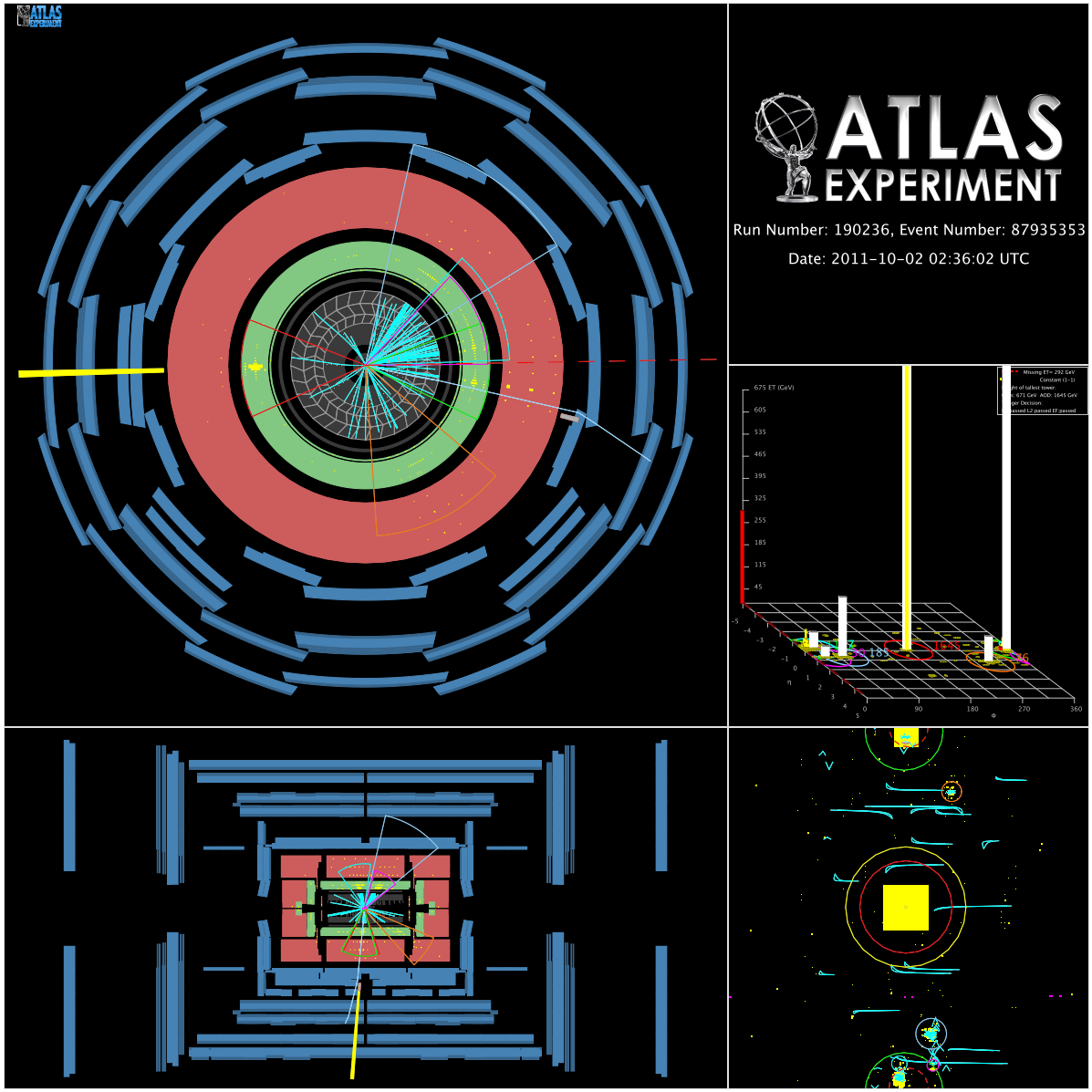

Figure 5.11.: *Moriond'12 Event display of the highest $p_{\mathrm{T}}(\gamma_1)$ event (*1407 GeV*) entering CR1a A, A' and B. There is a single photon of good quality, and the jets in the event are similarly good. The leading jet in the collection is that reconstructed from the photon clusters, and is over-calibrated to have $p_{\mathrm{T}} = 1645$ GeV. This over-calibration generates most of the the $E_{\mathrm{T}}^{\mathrm{miss}}$, which points opposite to the photon, and aligns perfectly with the second leading jet (leading hadronic jet). More details of this event can be found in Table A.1.*

5.5. Transfer Function ($\mathbf{TF}_{Z_{\nu\nu}}$)

In the 0ℓ analysis, the measurements in the CRs are used to derive background expectations in a SR through the use of Transfer Functions (TFs). Technically, the TFs are defined as the ratio of expected event counts in the CRs and SR, and also between CRs (to estimate CR contamination by other SM processes). The TF therefore provides a conversion factor of "SR events per CR event", as expressed by the equation:

$$\begin{aligned} \mathrm{N(SR, est, proc)} &= \mathrm{N(CR, obs, proc)} \cdot \mathrm{TF} \\ &= \mathrm{N(CR, obs, proc)} \cdot \left[\frac{\mathrm{N(SR, raw, proc)}}{\mathrm{N(CR, raw, proc)}} \right], \end{aligned} \tag{5.5}$$

where N(SR, est, proc) is the SR estimate for a particular background process, N(CR, obs, proc) is the observed number of data events in the CR for the calibrating process chosen, and N(SR, raw, proc) and N(CR, raw, proc) are "raw" estimates of the contributions from the processes in the SR and CR respectively[6]. Similar equations containing TFs from CR to CR ("cross-TFs") enable the background estimates to be normalised coherently across all the CRs (Section 5.6.1). The TFs are estimated using data-driven techniques wherever possible, otherwise MC simulation is used. Given that the TF is a ratio, it has the advantage of having some systematic uncertainties largely cancelling, *e.g.* that on the Jet Energy Scale (JES) in MC.

In this thesis, the SR background component of interest is $Z_{\nu\nu}$ + jets and the CR is CR1a. As presented in Section 3.4, the corresponding $Z_{\nu\nu}/\gamma$ TF is defined as:

$$\mathrm{TF}_{Z_{\nu\nu}}(p_{\mathrm{T}}) = \frac{P(p_{\mathrm{T}})}{A^{\gamma}(p_{\mathrm{T}}) \cdot \varepsilon^{\gamma}(p_{\mathrm{T}})} \cdot R_{Z/\gamma}(p_{\mathrm{T}}) \cdot Br(Z \to \nu\nu) \tag{5.6}$$

To properly account for the effects of the 0ℓ object and SR event selection, this TF has to be evaluated after the full CR1a selection (Sections 5.3-5.4):

$$N_{Z_{\nu\nu}}(\mathrm{SR}, p_{\mathrm{T}}) = \mathrm{TF}_{Z_{\nu\nu}}(\mathrm{SR}, p_{\mathrm{T}}) \cdot N_{\gamma}(\mathrm{CR1a}, p_{\mathrm{T}}) \tag{5.7}$$

The procedure can hence be regarded as a map from the CR to the SR, as illustrated in Figure 5.12. For brevity, from now on "TF" will be often used to refer to that from CR1a.

[6]These raw estimates need not be normalised to any particular luminosity or calibrated to other physics processes, but should be weighted by cross-section, and the normalisation convention should be consistent between SR and CR.

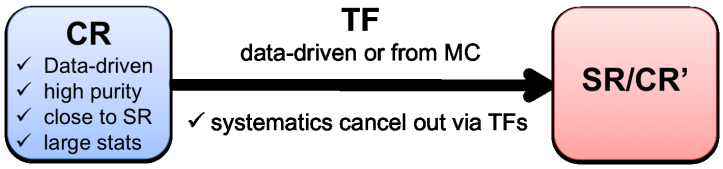

Figure 5.12.: *Schematic diagram showing the effect of the TF as a map from an 'ideal' CR to a SR or to another control region CR′ (the latter case is referred as a 'cross-TF'). The 'ideal' TF would be fully calculated from data. Being a ratio, the TF has the advantage of cancelling some of the associated systematics errors.*

The next subsections will be dedicated to explain the method for estimating each of the factors in Equation (5.6) and their associated systematic uncertainties (in order of appearance).

5.5.1. Efficiency and Acceptance

The $A^{\gamma}(p_{\mathrm{T}}) \cdot \varepsilon^{\gamma}(p_{\mathrm{T}})$ factor in the TF is needed to correct for the effects from the $\gamma + X$ selection in CR1a, which are absent from the $Z_{\nu\nu}$ + jets background events in the SRs.

Rather than obtaining the acceptance and efficiencies separately, a single $A^{\gamma}(p_{\mathrm{T}}) \cdot \varepsilon^{\gamma}(p_{\mathrm{T}})$ function is obtained from prompt photon MC by taking the ratio of the $p_{\mathrm{T}}(\gamma_1)$ distributions in CR1a with and without the $\gamma + X$ selection step applied, *i.e.* :

$$A^{\gamma}(p_{\mathrm{T}}) \cdot \varepsilon^{\gamma}(p_{\mathrm{T}}) = \frac{N^{\gamma}_{\mathrm{reco}}(p_{\mathrm{T}})}{N^{\gamma}_{\mathrm{truth}}(p_{\mathrm{T}})}. \tag{5.8}$$

When the $\gamma + X$ selection is not included, the truth photon four-vector is used for γ_1-jet overlap removal, and to define $\not{E}_{\mathrm{T}}^{\mathrm{true}}$ (Equations 5.1-5.3). The `ALPGEN` $A^{\gamma}(p_{\mathrm{T}}) \cdot \varepsilon^{\gamma}(p_{\mathrm{T}})$ function in each channel at different stages of the CR1a selection is shown in Figure 5.13, where the yellow/orange (bottom) line is the closest to the full CR1a selection (a common 900 GeV m_{eff} cut is used instead of the SR cut one to maintain reasonable statistics). The results were cross-checked with `SHERPA` and very good agreement was found.

For complementary purposes, to get an idea of how much acceptance is lost from the photon η cuts in the $\gamma + X$ selection step (see Table 5.8), an example of the estimated value of A^{γ} alone is shown in Table 5.17 for the relevant $p_{\mathrm{T}}(\gamma_1)$ range in channel A (see Figure 5.9(a) and Table 5.16) and for the two selected $|\eta|$ regions used in the SM analysis [48, 49]. From this, it is clear the loss is less than $\sim 10\%$. Given the practically flat $|\eta|$ distribution (Figure 5.2(b)), both estimates are clearly consistent with each other.

Analysis	$\|\eta\|$ region	CR1a $\langle A^{\gamma}(p_{\mathrm{T}})\rangle$ for SR-A
All others	< 2.37	0.92-0.96
Moriond'11	< 1.81	0.74

Table 5.17.: *Mean acceptance of true photons for the η cuts used in [48, 49]. The first applies to all analyses except Moriond'11.*

Comparison with SM prompt photon results

Identification and reconstruction efficiencies ($\varepsilon^{\gamma}_{\mathbf{rec}}$, $\varepsilon^{\gamma}_{\mathbf{id}}$) - As suggested by the discussion in Section 5.3.4, the combined efficiency $\varepsilon^{\gamma}_{\mathrm{rec}} \cdot \varepsilon^{\gamma}_{\mathrm{id}}$ is relatively constant for high-p_{T} photons, such as those selected in CR1a. Although the efficiency varies slightly between the central and forward η regions, this only implies an effect of $\sim 2\%$ on the overall value, which according to the results from the SM analysis is $\sim 86\%$, close to the high-p_{T} values seen in Figure 5.13 (black line).

Isolation efficiency ($\varepsilon^{\gamma}_{\mathbf{iso}}$) - As mentioned in Section 5.3.4, this efficiency is not calculated explicitly in the SM analysis but becomes important here at this stage. The efficiency of the isolation requirement $\varepsilon^{\gamma}_{\mathrm{iso}}$ tends to decrease with increasing hadronic activity, which is amplified when requiring more reconstructed jets or a higher photon p_{T} – both requirements of the 0ℓ selection and particularly accentuated in Moriond'12. While the required separation between the $E_{\mathrm{T}}^{\mathrm{miss}}$ and jets in the 0ℓ selection ($\Delta\phi$ cut in Table 5.14) implies an isolated photon, the requirement is not as hard as the $E_{\mathrm{T}}^{\mathrm{iso}}$ cut used (see Section 5.3.1). Therefore, the net effect is a reduced $\varepsilon^{\gamma}_{\mathrm{iso}}$, which must be estimated in this specific context. This was done by comparing with the $E_{\mathrm{T}}^{\mathrm{iso}}$ distribution from prompt photon MC passing the 0ℓ selection but bypassing the $\gamma + X$ selection (again, truth photon information was used for the 0ℓ selection in this case). Typical values were found to be between 80% and 90%.

As discussed in Section 5.3.4 a slight data/MC disagreement was observed in the $E_{\mathrm{T}}^{\mathrm{iso}}$ distribution (Figure 5.1(b)), consistent with a ~ 2 GeV 'shift'. To understand this difference, the efficiency of two different $E_{\mathrm{T}}^{\mathrm{iso}}$ cuts (3 and 5 GeV) was studied using the $\gamma + X$ sample, and the resulting discrepancy between the data and MC was used to set an uncertainty estimate on $\varepsilon^{\gamma}_{\mathrm{iso}}$. In the Moriond'12 analysis, a preliminary estimate determined that the discrepancy was under 5%, and this figure was hence set as the relative uncertainty. On repetition of the investigation with

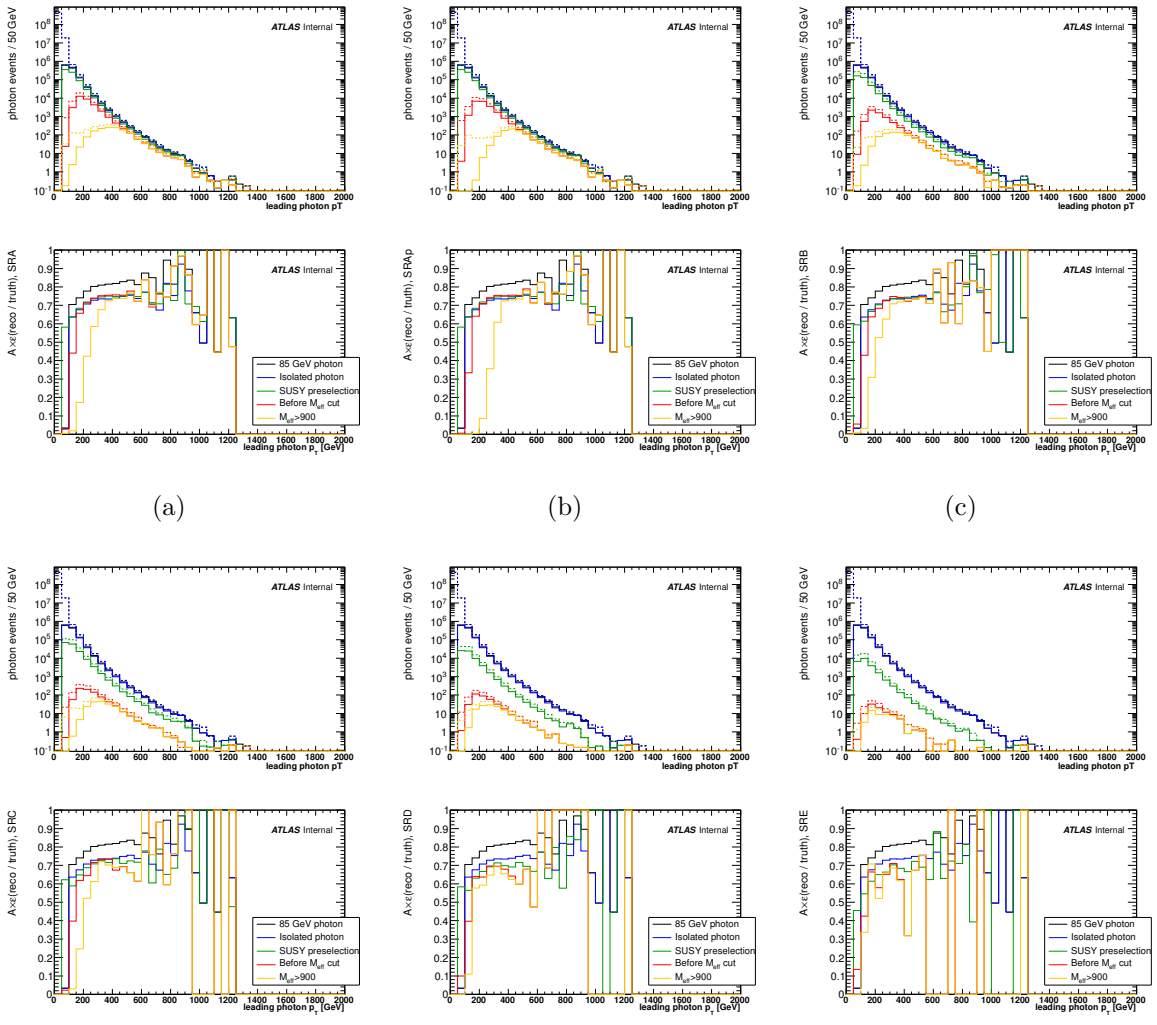

Figure 5.13.: *Moriond'12 distributions of truth and reconstructed $p_{\mathrm{T}}(\gamma_1)$ (upper plot) and their ratio $A^{\gamma}(p_{\mathrm{T}}) \cdot \varepsilon^{\gamma}(p_{\mathrm{T}})$ (lower plot) at different CR1a selection stages in every 0ℓ channel (A, A', B, C, D, E) – black line: all cuts from Table 5.9 and the signal photon definition without isolation applied; blue line: all cuts from Table 5.9 and the full signal photon definition applied ('signal photons' are defined in Section 5.3.1); green line: 0ℓ preselection (as defined in Section 5.4.2); red line: full 0ℓ selection except the $m_{\mathrm{eff}}(incl.)$ cut; orange line: full 0ℓ selection including a 900 GeV $m_{\mathrm{eff}}(incl.)$ cut. In the upper plot, dashed lines indicate the truth photon distributions and solid lines the reconstructed ones. The MC is from* `ALPGEN` *and normalised to the data luminosity.*

some analysis improvements, the difference was found to be slightly larger as quoted in Table 5.18. This slight shift in $E_{\mathrm{T}}^{\mathrm{iso}}$ and shower shapes (*e.g.* Figure C.3) was also observed in the SM analysis [49].

Signal Region	Isolation efficiency, $\varepsilon_{\mathrm{iso}}^{\gamma}$		Relative difference,
	$E_{\mathrm{T}}^{\mathrm{iso}} > 3$ GeV	$E_{\mathrm{T}}^{\mathrm{iso}} > 5$ GeV	δ_{ε}
A	0.825	0.885	6.8%
A'	0.838	0.877	4.4%
B	0.807	0.865	6.7%
C	0.796	0.851	6.6%
D	0.758	0.824	8.0%
E	0.740	0.819	9.6%

Table 5.18.: *Moriond'12 efficiency of the $E_{\mathrm{T}}^{\mathrm{iso}}$ cut ($\varepsilon_{\mathrm{iso}}^{\gamma}$), evaluated in CR1a (but with a 900 GeV m_{eff}(incl.) cut applied in all cases) for thresholds of 3 and 5 GeV. The relative difference (with respect to the 5 GeV isolation criteria) determines the uncertainty. The values are taken from* `ALPGEN`.

An overall comparison is then made between the acceptance A^{γ} and efficiencies $\varepsilon_{\mathrm{rec}}^{\gamma} \cdot \varepsilon_{\mathrm{id}}^{\gamma}$ from [49] combined with the $\varepsilon_{\mathrm{iso}}^{\gamma}$ computed above, and the $A^{\gamma}(p_{\mathrm{T}}) \cdot \varepsilon^{\gamma}(p_{\mathrm{T}})$ bin-by-bin results computed from `ALPGEN` MC (Figure 5.13). The difference between the two estimates at high p_{T}, where the ratio is approximately constant, is taken as the final uncertainty (see Table 5.20), and comes out to be significantly larger than the detailed estimates from the SM analysis. The uncertainty with respect to pile-up on $A^{\gamma}(p_{\mathrm{T}}) \cdot \varepsilon^{\gamma}(p_{\mathrm{T}})$ is always estimated as in the rest of 0ℓ analysis (for Moriond'12 this is specified in [100], but see also Section 5.5.5).

In summary, the fact that the SM analysis results agree well with those obtained for CR1a confirms the relatively small impact from the 0ℓ selection step, particularly in the important regime of high photon p_{T}. This is clearly shown in Figure 5.13, where after the application of the $E_{\mathrm{T}}^{\mathrm{iso}}$ cut (blue line), $A^{\gamma}(p_{\mathrm{T}}) \cdot \varepsilon^{\gamma}(p_{\mathrm{T}})$ remains fairly constant (within statistical uncertainties) with respect to the 0ℓ selection. In particular, the final m_{eff}(incl.) cut does not lead to large shifts (only at the highest jet multiplicities is the difference greater than 5%). Applying the m_{eff}(incl.) cut does move the $A^{\gamma}(p_{\mathrm{T}}) \cdot \varepsilon^{\gamma}(p_{\mathrm{T}})$ plateau region to higher values of p_{T}, but Figure 5.14 shows that the total effect once combined with $R_{Z/\gamma}$ is not so substantial. From this and to improve the statistics available, no m_{eff}(incl.) cut was applied when computing the value of $A^{\gamma}(p_{\mathrm{T}}) \cdot \varepsilon^{\gamma}(p_{\mathrm{T}})$. In addition, as $A^{\gamma}(p_{\mathrm{T}}) \cdot \varepsilon^{\gamma}(p_{\mathrm{T}})$ is expected to flatten out at high p_{T}, a *plateau* value was used in the

TF for $p_{\mathrm{T}} > 400$ GeV in SRs A, A', B and for $p_{\mathrm{T}} > 350$ GeV in SRs C, D, E to reduce the impact of statistical fluctuations. For clarity purposes, the plateau line is not shown directly in Figure 5.13 but an equivalent plot displaying it can be found in [100].

5.5.2. Purity

This TF component is not determined directly in these studies for two main reasons: (i) more thorough data-driven estimates have been carried out in the SM analysis already [49, 99], and (ii) the purity of the CR1a sample is expected to be already quite high at this stage. As discussed in Section 5.3.4, the purity indeed increases with p_{T} and the background suppression is mainly related to $E_{\mathrm{T}}^{\mathrm{iso}}$. From MC, QCD is estimated here to contribute 1% to the selected sample for $p_{\mathrm{T}} \sim 200$ GeV and 0% for $p_{\mathrm{T}} > 300$ GeV. This is consistent with the good agreement between photon data and the MC signal in CR1a (Figure 5.9), which in addition supports the conclusion that the background is not significantly increased by the 0ℓ selection. Reference [99] found the electron background to be $\sim 1\%$, which agrees with the MC estimate of electroweak processes in Figure 5.9. Therefore, because the total contamination is expected to be only at the percent level, it is not explicitly accounted for in the $Z_{\nu\nu}$ background estimation. Instead, a 5% uncertainty is assigned, based on the maximum background fraction estimated in [49] within the bulk of the photon p_{T} distribution in CR1a (mean values are specified in Table 5.16). The reason to prefer a purity estimate based on [49] over a direct estimate from MC is because the former uses more sophisticated, *e.g.* data-driven, methods to estimate it and has much smaller associated uncertainties.

5.5.3. Z/γ Ratio

The uncertainties related to the cross section ratio $R_{Z/\gamma}$ have been studied in [56] and were summarised in Chapter 4. The key point from these studies is that many of the theoretical uncertainties, such as the choice of scales and PDFs, are found to largely cancel in the ratio (net impact is less than $\sim 5\%$). It was, however, also shown that this ratio can be sensitive to jet selections and that multi-parton matrix elements should be used to correctly describe all the relevant amplitudes.

For Moriond'12, the availability of more suitable MC samples than in the previous analyses made it possible to estimate $R_{Z/\gamma}$ from fully-simulated ATLAS MC from `SHERPA` and `ALPGEN`. For both generators, 4 to 5 additional partons, besides the boson, in the

matrix-element were simulated (see Section 5.2.2). However, the limited amount of statistics at high p_{T} in these samples, in combination with the large number of required jets, did not allow for the ratio to be determined with a precision better than $\sim 25\%$. Moreover, the Z boson `SHERPA` samples were not only more statistically limited but also a disagreement with respect to data was observed for the leptonic ($Z_{\ell\ell}$) samples *e.g.* when compared to CR1b (see `SHERPA` CR1b m_{eff} plots in [100]). This was thought to be the reason why the $R_{Z/\gamma}$ value computed from `SHERPA` was found lower than the theoretical expectation from [56].

Hence, for the TF, $R_{Z/\gamma}$ was determined with the `ALPGEN` samples, which suffered from neither of these problems. The results is shown in Figure 5.14, where the robustness and convergence of $R_{Z/\gamma}$ with respect to different selections at high p_{T} is observed (although the specific threshold for this varies, depending on the m_{eff}(incl.) cut). The large $R_{Z/\gamma}$ values after the 0ℓ preselection (black line) in the lowest bins are due to generator-level cuts on the photon MC, not applied to the $Z_{\nu\nu}$ MC (see Section 5.2.2). However, the effect vanishes after application of the $E_{\mathrm{T}}^{\mathrm{miss}}$ cut (Cut 7 in Table 5.14). The results were also found to roughly be in good agreement with [56] (see Figure 3.1(b) and Table 4.1). Differences between the selection stages are comparable to the MC statistical fluctuations of the ratio at high p_{T}, for which a 25% theoretical uncertainty is assigned to cover such effects. It should be noted that no NLO/NNLO k-factor was applied when normalising either the photon or Z samples to cross-section. This partly was because no such k-factor was available for the photon sample, but more importantly it is expected that, because the processes are so similar, any higher-order effects will cancel out in the ratio[7], and so the normalisation to data should sufficiently account for these effects. The relevance of the k-factor is discussed further in Section 5.5.4. As $R_{Z/\gamma}$ flattens out at high p_{T}, a *plateau* value was also used as for $A^{\gamma} \cdot \varepsilon^{\gamma}$ in the TF for $p_{\mathrm{T}} > 500$ GeV in SRs A, A', B, for $p_{\mathrm{T}} > 400$ GeV in SR C, and for $p_{\mathrm{T}} > 350$ GeV in SRs D and E to reduce the impact of statistical fluctuations. For clarity purposes the plateau line is not shown in Figure 5.14 but is displayed on the equivalent plot in [100].

It is worth noting that prior to Moriond'12, $R_{Z/\gamma}$ was taken directly from the result in [56] (which used `PYTHIA8` and `GAMBOS`). This approach, however, was not entirely adequate given the hard scales and high multiplicities characterising the 0ℓ selections, in particular that in Moriond'12. The $R_{Z/\gamma}$ taken from [56] did not include the effects of the exact 0ℓ selection, nor of drawing on the full ATLAS simulation. During this time, the overall uncertainty quoted on $R_{Z/\gamma}$ was $\sim 15\%$ (see Appendix C).

[7] Except perhaps for the Sudakov-type corrections, see Section 4.5.

γ vs $Z_{\nu\nu}$ Pseudorapidity

While in principle the Z boson and γ have different η distributions, causing some visible differences in the event kinematics, the effects disappear at high p_{T} (specifically $p_{\mathrm{T}} \gg m_Z$) as the η distributions for the two bosons converge. Moreover, this is always ensured by the 0ℓ selections, as exemplified in Figure 5.15[8]. A similar figure with larger statistics at generator level from `PYTHIA` is shown in Figure 4.14(b). This is the reason to parameterise $R_{Z/\gamma}$ as a function of p_{T} only, while the limited fiducial acceptance of the photons is accounted through the A^{γ} factor described previously.

[8]These plots correspond to the Moriond'11 selection, but the effect is expected to be more robust for the harder Moriond'12 selection.

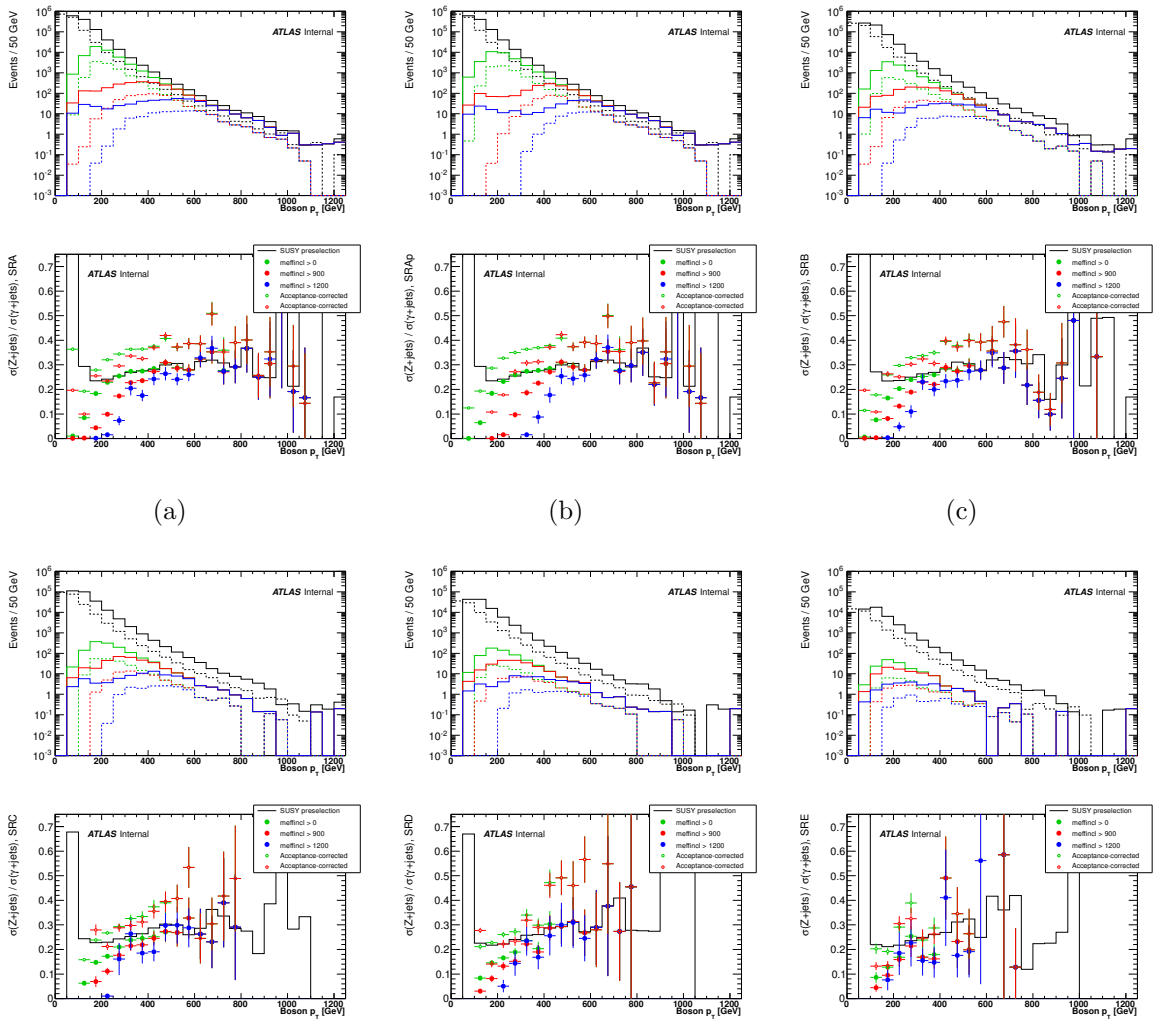

Figure 5.14.: *Moriond'12 distributions of truth $Z_{\nu\nu}$ and γ p_{T} (upper plot) and their ratio $R_{Z/\gamma}(p_{\mathrm{T}})$ (lower plot) at different CR1a selection stages in the 0ℓ channels (A, A', B, C, D, E). The hollow/smaller circles correspond to corresponding solid circles multiplied by the $A^{\gamma}(p_{\mathrm{T}}) \cdot \varepsilon^{\gamma}(p_{\mathrm{T}})$ function in Figure 5.13. In the upper plot, dashed lines indicate the $Z_{\nu\nu}$ distributions and solid lines the γ ones. The MC is from* `ALPGEN` *and normalised to the data luminosity.*

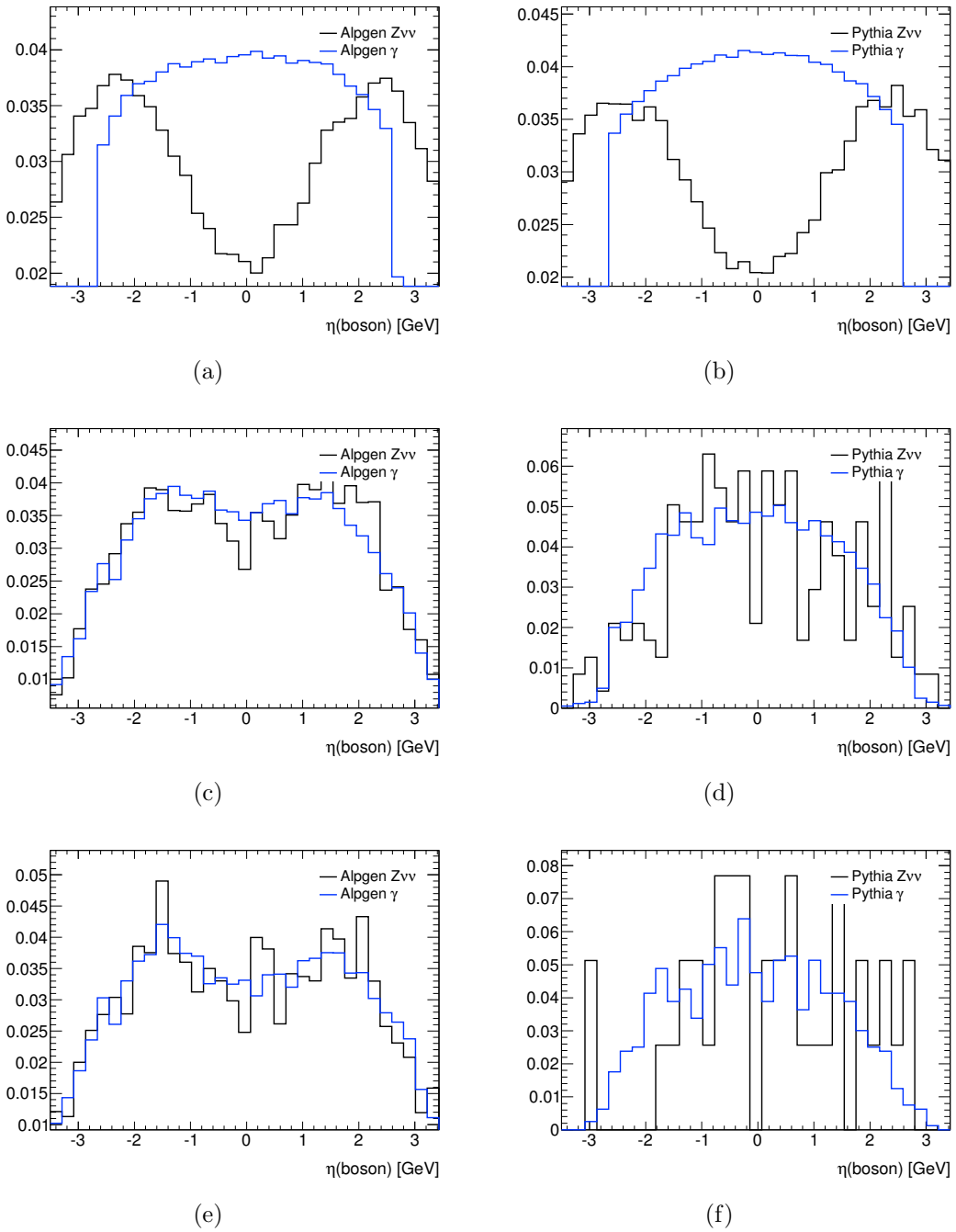

Figure 5.15.: *Moriond'11 pseudorapidity (η) distribution for true γ and $Z_{\nu\nu}$ at different CR1a selection stages, using reconstructed jets from* `PYTHIA` *and* `ALPGEN`*: (a)-(b) after the $\gamma + X$ selection; (c)-(d) after the 0ℓ dijet selection; and (e)-(f) after the 0ℓ three jet selection. The histograms are normalised to unit area to facilitate comparison of shapes and the y-axis has arbitrary units.*

5.5.4. Application of TF/ TF stand-alone estimate of $Z_{\nu\nu}$ + jets

At this stage it is possible to obtain a 'stand-alone' estimate of the $Z_{\nu\nu}$ + jets background in the various SRs by simply applying the TF (Equation (5.6)) on the CR1a event counts. This is a less sophisticated procedure than the one actually implemented in the 0ℓ analysis, in which the TFs of all the CRs are combined to produce a fit where all background processes are simultaneously normalised (see Section 5.6.3). However, by carrying out this more rudimentary approach, it is possible to immediately cross-check the method's estimate directly against simulated $Z_{\nu\nu}$ + jets events. The relevant numerical results obtained from this cross-check are listed in Table 5.19 and the corresponding distributions are shown in Figure 5.16. The main results are the raw CR1a event counts (column 3) and the data-driven $Z_{\nu\nu}$ + jets events estimate (column 5). The latter is obtained from the integrated value of the distribution of black dots in Figure 5.16. This distribution is produced by filling a two-dimensional histogram of m_{eff}(incl.) vs $p_{\text{T}}(\gamma_1)$, and then scaling the m_{eff}(incl.) projected histogram bin-by-bin in p_{T} by the corresponding TF as in Equation (5.7). The rest of the results in Table 5.19 are just cross-checks made with MC to support the validity of the method.

Z + jets data/MC discrepancies

Within the 0ℓ analysis, the $Z_{\nu\nu}$ + jets `ALPGEN` samples included a k-factor of 1.28 (see Table 5.4) to include NNLO corrections to the cross-section, and the `SHERPA` samples a k-factor of 1.20 owing to the running of α_{EM}. However, these k-factors were not applied to this stand-alone $Z_{\nu\nu}$ + jets estimate since no equivalent k-factor was available for the γ + jets MC, but more importantly because the method is primarily data-driven (the MC dependance is based on a ratio where higher order corrections like these should cancel). The $Z_{\nu\nu}$ + jets `ALPGEN` distribution does appear on average higher than data, but this is related to a common trend observed for all the Z boson related `ALPGEN` samples used in the 0ℓ analysis. For this, the 0ℓ analysis applied a scale factor of 0.75 to the normalisation in order to improve the agreement with data, but this is not included in this estimate. As for the discrepancies of $Z_{\nu\nu}$ + jets `SHERPA` with data (columns 6 and 7 in Table 5.19), these were previously observed for $R_{Z_{\nu\nu}/\gamma}$ (Section 5.5.3) and are believed to be due also to an overall normalisation offset (*i.e.* `SHERPA` $Z_{\ell\ell}$ is found to be systematically lower than CR1b data [100]). In addition, given that $Z_{\nu\nu}$ + jets `SHERPA` sample is very statistics-limited at high m_{eff}(incl.), it is not considered reliable for counts below ~ 10 events.

The key point, however, is that these discrepancies with $Z_{\nu\nu}$ MC should not matter, given the data-driven nature of the result actually used for the final $Z_{\nu\nu}$ background estimate.

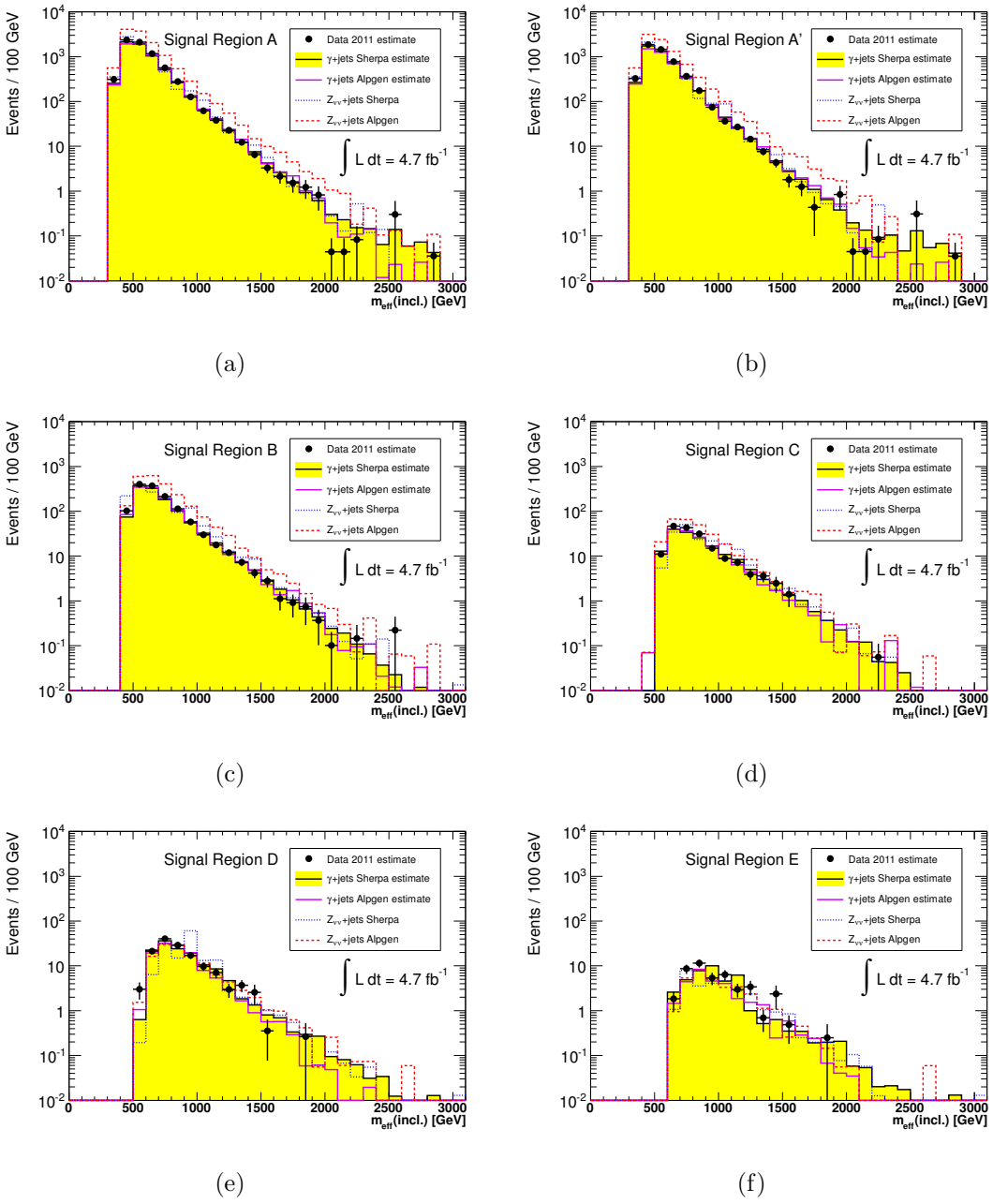

Figure 5.16.: *Moriond'12 $Z_{\nu\nu}$ + jets $m_{\mathrm{eff}}(incl.)$ distributions in the 0ℓ SRs as estimated from data and MC using the CR1a TF, compared directly with $Z_{\nu\nu}$ + jets MC from* `SHERPA` *and* `ALPGEN`*. The labels 'Data 2011' and 'γ + jets Sherpa/Alpgen estimate' indicate the TFs were applied to the CR1a data and MC events, whereas those labeled '$Z_{\nu\nu}$ + jets Sherpa/Alpgen' show the raw MC prediction scaled to the data luminosity.*

SR	m_{eff}(incl.)	CR1a		$Z_{\nu\nu}$ + jets Estimate		$Z_{\nu\nu}$ + jets Signal
		data	Sherpa/Alpgen	data	Sherpa/Alpgen	Sherpa/Alpgen
A	1400	81	97.2 / 95.2	30.6 ± 3.4 (stat.) ± 8.1 (syst.)	37.2 / 36.4	22.3 / 44.2
	1900	9	9.54 / 9.41	3.44 ± 1.15 (stat.) ± 0.912 (syst.)	3.64 / 3.59	1.81 / 4.87
A'	1200	155	179 / 182	60.2 ± 4.83 (stat.) ± 16 (syst.)	70 / 71.3	35.8 / 86.2
B	1900	6	6.32 / 6.59	2.49 ± 1.02 (stat.) ± 0.664 (syst.)	2.59 / 2.69	1.28 / 2.53
C	900	201	230 / 204	62.7 ± 4.42 (stat.) ± 16.7 (syst.)	73.5 / 64.5	70.4 / 80.6
	1200	45	57.4 / 46.2	15.2 ± 2.26 (stat.) ± 4.33 (syst.)	19.2 / 15.5	15.5 / 21.3
	1500	6	14.6 / 11.5	2.06 ± 0.84 (stat.) ± 0.643 (syst.)	4.98 / 3.94	4.35 / 5.89
D	1500	3	11.2 / 7.17	0.896 ± 0.518 (stat.) ± 0.254 (syst.)	3.37 / 2.17	3.01 / 3.64
E	900	74	76.9 / 51.9	20.7 ± 2.41 (stat.) ± 5.69 (syst.)	22.2 / 14.3	17.6 / 17.6
	1200	24	15.7 / 15.5	7.29 ± 1.49 (stat.) ± 2.03 (syst.)	5.1 / 4.58	6.14 / 5.82
	1400	10	9.01 / 6.69	3.12 ± 0.985 (stat.) ± 0.889 (syst.)	2.92 / 1.99	2.71 / 2.34

Table 5.19.: *Moriond'12 CR1a event counts in data and MC for each SR (columns 3-4) and the stand-alone estimate of $Z_{\nu\nu}$ + jets background in the 0ℓ SRs from data and MC (columns 5-6), compared to $Z_{\nu\nu}$ + jets MC (column 7). The MC statistical and luminosity uncertainties are not shown but can be assumed to be small* e.g. *the luminosity uncertainty is* $\sim 3.9\%$.

5.5.5. Summary of TF results and uncertainties

A summary of the CR1a TF results and associated uncertainties is shown in Table 5.20. These, along with the raw CR1a event counts (column 3 in Table 5.19), are the main results provided to the 0ℓ analysis, where they are used as inputs for the final combined background fit (Section 5.6). In Table 5.20, the "Central Value" represents the *expected value* of the TF, defined as the integral of a $Z_{\nu\nu}$ estimate histogram in the SR (Figure 5.16) divided by the integral of the corresponding CR1a histogram (Figure 5.10), *i.e.*

$$\begin{aligned}\langle \mathrm{TF}_{Z_{\nu\nu}} \rangle &= \frac{\langle N_{Z_{\nu\nu}}(\mathrm{SR}) \rangle}{\langle N_{\gamma}(\mathrm{CR1a}) \rangle} \\ &= \frac{\int_0^{\infty} \mathrm{TF}_{Z_{\nu\nu}}(p_{\mathrm{T}}) \cdot N_{\gamma}(\mathrm{CR1a})\, dp_{\mathrm{T}}}{\int_0^{\infty} N_{\gamma}(\mathrm{CR1a})\, dp_{\mathrm{T}}}. \end{aligned} \tag{5.9}$$

Equivalently, these are weighted averages of the TF, where the weight function is the differential cross-section in p_{T}.

As for the TF uncertainties, the procedures to calculate them were as discussed in Section 5.5. Other uncertainties assessed to be consistent with the rest of the 0ℓ analysis, also appearing in Table 5.20, were:

- JES/JER: Jet energy scale and jet energy resolution uncertainties were assessed using the standard ATLAS tools provided by the Jet/ETmiss working group [103]
- Trigger: the corresponding trigger efficiency (`g80_loose` for Moriond'12, see Appendix B.2)
- Pileup: related to the usage of the standard ATLAS pileup reweighing tool, it was estimated from the difference between nominal $\langle\mu\rangle$ and $\langle\mu\rangle \times 0.9$ (see Section 5.2.2). The factor of 0.9 was estimated based on the data/MC mismatch observed for mc11b (see Table 5.7).
- MET CellOut: The uncertainty on the energy of topoclusters which are not associated to physics objects but that contribute to the missing energy (the "CellOut" term in Equation (2.11)). An additional 6.6% pileup uncertainty is also applied, as recommended by the Jet/ETmiss group.

CR1a TF central value and uncertainties											
SR	A		A'	B	C			D	E		
m_{eff}(incl.)	1400	1900	1200	1900	900	1200	1500	1500	900	1200	1400
Central Value	0.377	0.382	0.388	0.414	0.312	0.337	0.343	0.299	0.280	0.304	0.312
f_{bkg}	5%	5%	5%	5%	5%	5%	5%	5%	5%	5%	5%
$\varepsilon^{\gamma}_{\text{iso}}$	5%	5%	5%	5%	5%	5%	5%	5%	5%	5%	5%
$A^{\gamma} \cdot \varepsilon^{\gamma}$	5%	5%	5%	5%	5%	5%	5%	5%	7%	7%	7%
Theory ($R_{Z_{\nu\nu}/\gamma}$)	25%	25%	25%	25%	25%	25%	25%	25%	25%	25%	25%
JES/JER	1.6%	1.9%	1.6%	3.6%	2.7%	10.7%	16.6%	10.7%	5.0%	6.8%	9.2%
Trigger	$< 1\%$	$< 1\%$	$< 1\%$	$< 1\%$	$< 1\%$	$< 1\%$	$< 1\%$	$< 1\%$	$< 1\%$	$< 1\%$	$< 1\%$
Pileup	$< 1\%$	$< 1\%$	$< 1\%$	$< 1\%$	$< 1\%$	$< 1\%$	$< 1\%$	$< 1\%$	$< 1\%$	$< 1\%$	$< 1\%$
MET CellOut	0.3%	0.4%	0.3%	1.0%	0.4%	0.7%	0.9%	1.3%	0.9%	1.0%	1.3%

Table 5.20.: *Moriond'12 CR1a TF expected value for each 0ℓ SR, together with the estimated associated uncertainties. The meaning of the terms are explained elsewhere in the text. The MC statistical uncertainty is included in the 'Theory ($R_{Z_{\nu\nu}/\gamma}$)' uncertainty.*

5.6. Context within the 0ℓ analysis

This final section contextualises this background estimation method within the 0ℓ analysis. The importance and performance of the method will be discussed, and in particular its performance will be compared with that of other CRs, especially CR1b which is the 0ℓ alternative for $Z_{\nu\nu}$ + jets background estimation. For reference, the selections defining the various 0ℓ CRs are detailed in Table 5.21. These have been designed to be as orthogonal as possible to minimise correlations between them and the backgrounds they aim to estimate. They are as close as possible to the SR to maintain adequate statistical weight, while minimising the uncertainties arising from extrapolations to the SRs. Another characteristic is their high purity with respect to the calibration process chosen, exceeding 50% in all cases [54].

In order to be consistent with the documentation in [100], in this section, the presentation of SR and CR results in tables will follow a different format to the one presented in previous sections of this chapter – the SRs will be presented in the following order: SRC loose, SRE loose, SRA medium, SRAp medium, SRC medium, SRE medium, SRA tight, SRB tight, SRC tight, SRD tight, SRE tight.

5.6.1. Overview of relevant 0ℓ results

A summary of the most important results (prior to interpretation) of the 0ℓ analysis is now given. First, the data event counts in the various SRs and CRs are quoted in Table 5.22 (the CR1a row is equivalent to Table 5.15). A sample of the corresponding m_{eff}(incl.) distribution for the electroweak boson production CRs is shown in Figure 5.17 for channel A (a more comprehensive collection is available in [100]).

Transfer factor summary

Next, the central values of the TFs used to translate the CR event counts into SR background estimates are presented in Table 5.23. The values presented for CR1a are the expected values discussed in Section 5.5.5 (Table 5.20) *modified* by a scaling factor to account for the small $Z(\rightarrow ee, \mu\mu, \tau\tau)$ + jets contamination in the SR (the basic CR1a TF discussed in Section 5.5 accounts only for $Z(\rightarrow \nu\nu)$). Such events can evade the lepton veto when the leptons are softer than the threshold for the veto (chosen to ensure adequate reconstruction quality), land outside the detector acceptance or are

simply misidentified or misreconstructed. Hadronically decaying taus make up the largest fraction of this background, as they are resolved as hadronic jets, and furthermore contain a non-negligible real $E_{\mathrm{T}}^{\mathrm{miss}}$component due to the neutrinos from the tau decays. The scaling factor is simply computed from $Z+$ jets `ALPGEN` MC as:

$$R_{Z/Z_{\nu\nu}} = N_{Z\to X}(\mathrm{SR})/N_{Z\to\nu\nu}(\mathrm{SR}) \tag{5.10}$$

and is applied to all CR1a TF values shown within this section.

In the simultaneous normalisation scheme used by the 0ℓ analysis, it is important also to account for cross-contamination from background processes other than the one that is being targeted. This is done by constructing "cross-TFs", which are TFs from CR to CR. For illustration, the ones corresponding to SR A (medium) are shown in Table 5.24. By construction, TF(CR1a $\to$ CR1a), TF(CR1b $\to$ CR1b), TF(CR2 $\to$ CR2), etc., are equal to 1. As the background fraction in CR1a (f_{bkg}) has been assumed to be negligible, TF(CRX $\to$ CR1a) = 0, except for CR1b (see below), as shown by the first row in the Table. As for TF(CR1a $\to$ CRX), these are obtained by combining appropriate TFs from CR1a and CR1b as follows:

$$\begin{aligned}
\mathrm{TF}(\mathrm{CR1a}\to\mathrm{CRX}) &= \frac{N_Z(\mathrm{CRX})}{N_\gamma(\mathrm{CR1a})} \\
&= \frac{N_Z(\mathrm{CRX})}{N_Z(\mathrm{CR1b})}\cdot\frac{N_Z(\mathrm{CR1b})}{N_Z(\mathrm{SR})}\cdot\frac{N_Z(\mathrm{SR})}{N_\gamma(\mathrm{CR1a})} \\
&= \frac{\mathrm{TF}(\mathrm{CR1b}\to\mathrm{CRX})}{\mathrm{TF}(\mathrm{CR1b}\to\mathrm{SR})}\cdot\mathrm{TF}(\mathrm{CR1a}\to\mathrm{SR})\cdot R_{Z/Z_{\nu\nu}}.
\end{aligned} \tag{5.11}$$

e.g. for SR A (medium) in Table 5.24, TF(CR1a $\to$ CR2) = 0.051

Given that a combined fit is used to simultaneously normalise all the background components in the 0ℓ analysis (see Section 5.6.1), when combining CR1a and CR1b results, it has been preferred to avoid introducing too many cross-correlations, so that rather than using the CR1a-CR1b cross-TFs in the fit, they are connected only indirectly via their respective TFs to the SR. In the case of CR1a this makes particular sense as it does not involve any extrapolation from a soft-to-hard region and therefore does not benefit from "short-cutting" the extrapolation by using a soft-to-soft TF. The corresponding entries in Table 5.24 therefore appear empty ("-").

Cut	Control Region				
	1a	1b	2	3	4
1	As for SR Cut 1 (modulo appropriate stream for trigger)				
2	EF_g80_loose	EF_e20_medium (period $\leq$ J) / EF_e22_medium (data period K) / (EF_e22vh_medium1 OR EF_e45_medium1) (period $\geq$ L) OR EF_mu18 (period $<$ J) / EF_mu18_L1J10 (period $\geq$ J)	As for SR cut 2	As for CR1b	As for CR1b
3a-5	As for SR cuts 3a-5, with lepton treated as jet with chf = 1, emf = 0 and excluded from $\vert\langle t\rangle\vert$ for CR3/4. Cut 3g: signal muon(s) used in cut 6a excluded from $E_{\mathrm{T}}^{\mathrm{miss}}$ for CR1b/3/4. Cut 3h: $E_{\mathrm{T}}^{\mathrm{miss}'}$ from cuts $\geq$7 used in CR1a/1b.				
6a	SM Photon selection (see Section 5.3)	Exactly 2 OS selected signal electrons or muons: $p_{\mathrm{T}}(e)$ >25, 20 GeV or $p_{\mathrm{T}}(\mu)$ >20, 20 GeV	As for SR Cut 6	Exactly 1 selected signal electron or muon with $p_{\mathrm{T}}(e)$ >25 GeV or $p_{\mathrm{T}}(\mu)$ >20 GeV	Exactly 1 selected signal electron or muon with $p_{\mathrm{T}}(e)$ >25 GeV or $p_{\mathrm{T}}(\mu)$ >20 GeV
6b	–	–	–	No p_{T} >40 GeV sel. $\vert\eta\vert < 2.5$ jet with JetFitterCombNN $\geq$ 1.8	$\geq$ 1 p_{T} >40 GeV sel. $\vert\eta\vert < 2.5$ jet with JetFitterCombNN $\geq$ 1.8
6c	–	66 GeV $< m(\ell\ell) <$ 116 GeV	–	30 GeV $< m_T(\ell, E_{\mathrm{T}}^{\mathrm{miss}}) <$ 100 GeV	30 GeV $< m_T(\ell, E_{\mathrm{T}}^{\mathrm{miss}}) <$ 100 GeV
Use below:	$E_{\mathrm{T}}^{\mathrm{miss}'} = p_{\mathrm{T}}(\gamma) + E_{\mathrm{T}}^{\mathrm{miss}}$(`Simplified20 withTightPhotons_RefFinal`)	$E_{\mathrm{T}}^{\mathrm{miss}'} = E_{\mathrm{T}}^{\mathrm{miss}} + p_{\mathrm{T}}(\ell\ell)$	–	Treat lepton as a jet	Treat lepton as a jet
7-13	As for SR cuts 7-13				
14	SR cut 14	No cut	$\Delta\phi < 0.2$: i={1,2,(3)}(A, A', B) / $p_{\mathrm{T}} > 40$ GeV jets (C,D,E)	No cut	No cut
15	SR cut 15	No cut	SR Cut 15	No cut	No cut
16	SR cut 16	SR Cut 16	SR Cut 16	SR cut 16	SR cut 16 / 1500 GeV (A/B(tight))

Table 5.21.: *Moriond'12 event selections defining the 0ℓ CRs. For SR cuts referenced, see Table 5.14. From [100].*

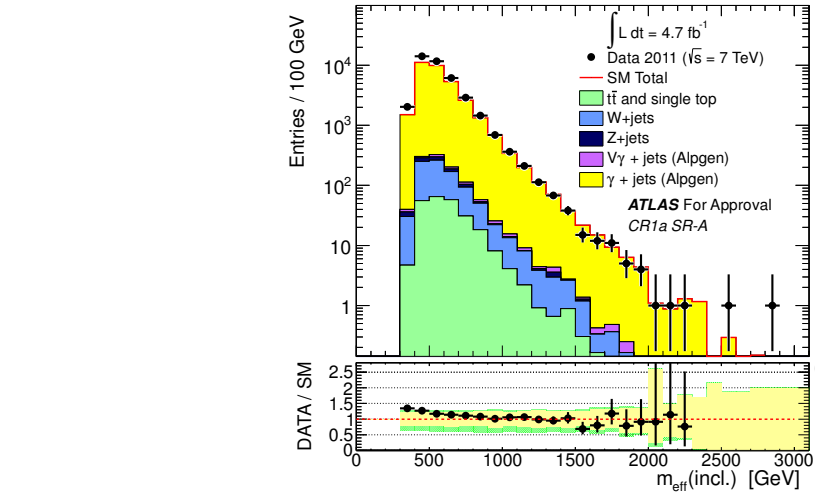

(a)

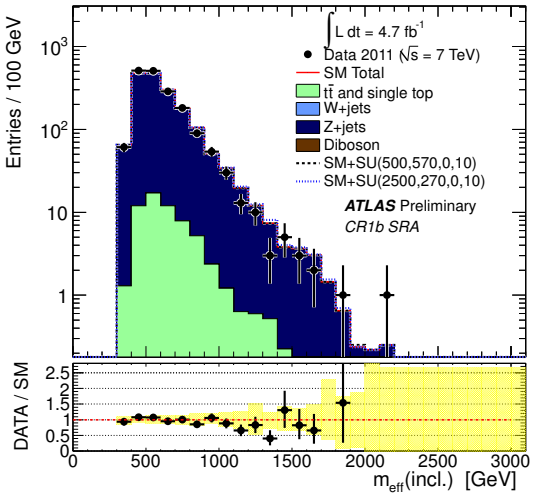

(b)

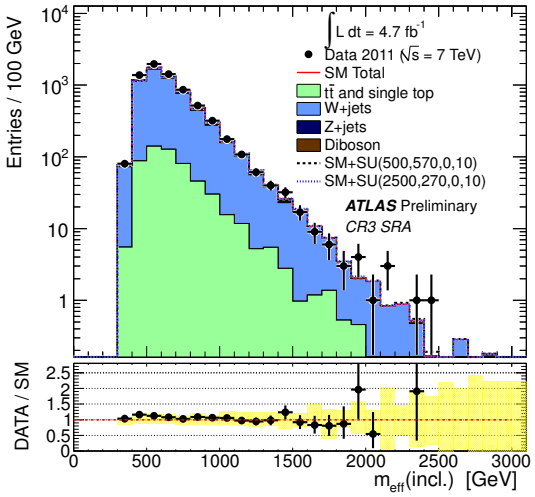

(c)

Figure 5.17.: *Moriond'12 $m_{\text{eff}}(incl.)$ distribution in data and MC for (a) CR1a, (b) CR1b and (c) CR3 in channel A. Though the purity of CR1a is slightly worse than CR1b, the statistics are much better, especially once the $m_{\text{eff}}(incl.)$ cuts are applied, while with respect to to CR3, although the statistics are comparable, the purity of CR1a is better at any given p_{T}, since CR3 suffers from a relatively large $t\bar{t}$ and single top contamination. From [100].*

CR / Process	Signal Region										
	SRC loose	SRE loose	SRA medium	SRA' medium	SRC medium	SRE medium	SRA tight	SRB tight	SRC tight	SRD tight	SRE tight
SR	210	148	59	85	36	25	1	1	14	9	13
CR1a / Z/γ+jets	**201**	**74**	**81**	**155**	**45**	**24**	**9**	**6**	**6**	**3**	**10**
CR1b / Z/γ+jets	28	0	12	25	6	0	1	1	3	2	0
CR2 / QCD jets	192	243	30	16	42	67	4	5	10	11	29
CR3 / W+jets	234	57	77	178	60	25	10	8	16	13	13
CR4 / $t\bar{t}$+ Single t	164	87	26	63	51	35	18	17	14	13	15

Table 5.22.: *Moriond'12 data event counts in the SR and CRs for each channel. From [100].*

CR / Process	Signal Region										
	SRC loose	SRE loose	SRA medium	SRA' medium	SRC medium	SRE medium	SRA tight	SRB tight	SRC tight	SRD tight	SRE tight
CR1a / Z/γ+jets	**0.35**	**0.29**	**0.39**	**0.42**	**0.37**	**0.34**	**0.32**	**0.4**	**0.35**	**0.3**	**0.32**
CR1b / Z/γ+jets	2.9	6.5	2.5	2.2	2.9	5	5.3	4.2	1.8	2.1	2.7
CR2 / QCD jets	0.0051	0.024	0.036	0.098	0.0026	0.026	0.0021	0.0013	0.0014	0.0028	0.021
CR3 / W+jets	0.36	0.74	0.31	0.19	0.2	0.39	0.25	0.14	0.16	0.26	0.26
CR4 / $t\bar{t}$+ Single t	0.52	0.84	0.35	0.22	0.27	0.54	0.0055	0.0084	0.14	0.17	0.29

Table 5.23.: *Moriond'12 summary of initial (pre-fit) central values of the CRs TFs in every channel. Rows indicate the calibrating region/process, while columns indicate the SR for which the estimate is being made. N.B. TFs from CR1a contain a scaling factor that accounts for the Z background from decays other than to neutrinos, and hence do not exactly match those from Table 5.20. From [100].*

Region	Main CR/Process				
	CR1a / Z/γ+jets	CR2 / QCD jets	CR4 / $t\bar{t}$+ Single Top	CR3 / W+jets	CR1b / Z/γ+jets
CR1a	**1**	**0**	**0**	**0**	**-**
CR2	**0.051**	1	0.4	0.19	0.31
CR4	**0**	0	1	0.071	0
CR3	**0.02**	0	0.46	1	0.12
CR1b	**-**	0	0.032	0	1
SR	**0.39**	0.036	0.35	0.31	2.5

Table 5.24.: *Moriond'12 initial (pre-fit) cross-TFs for SR-A medium. Columns indicate the calibrating region/process, while rows indicate the region for which the estimate is being made. The reason for the CR1a-CR1b cross-TFs being empty is explained elsewhere in the text. From [100].*

Final 0ℓ results

The vulnerabilities from relying on pure MC has been stressed enough by now. Indeed, the full sophistication of the current 0ℓ analysis lies in the use of the data-driven background estimation methods rather than MC. Consequently, this requires a more complicated procedure than simply applying the TFs to the CR event counts, as was done in Section 5.5.4. Rather, *all* the CR measurements (event counts, SR-to-CR and CR-to-CR TFs and associated uncertainties) are combined via a fitting procedure to produce a more sophisticated background estimate, which ensures consistency for all processes and accounts for mutual contamination.

The final 0ℓ results for Moriond'12 are quoted in Table 5.25. These comprise the data event counts and the predicted SM contributions in all SRs, broken down by process as well as in aggregate. For the SM contributions, values in parentheses indicate the initial MC estimates, *i.e. before* the combined fit[9], while the other values are *after* the fit. The fitting procedure is based on a likelihood function built from the Poisson probability density function (pdf) describing the SR (P_{SR}) and its CRs ($P_{i\mathrm{R}}$ where $i = \mathrm{W(CR3)}, \mathrm{T(CR4)}, \mathrm{Za(CR1a)}, \mathrm{Zb(CR1b)}, \mathrm{Q(CR2)}$) and a pdf describing the systematic uncertainties (C_{Syst}):

$$L(\boldsymbol{n}|\mu, \boldsymbol{b}, \boldsymbol{\theta}) = P_{\mathrm{SR}} \times P_{\mathrm{WR}} \times P_{\mathrm{TR}} \times P_{\mathrm{ZRa}} \times P_{\mathrm{ZRb}} \times P_{\mathrm{QR}} \times C_{\mathrm{Syst}}. \tag{5.12}$$

The mean of a CR pdf is then defined as:

$$\lambda_i(\mu, \mathbf{b}, \boldsymbol{\theta}) = \mu \cdot C_{\mathrm{SR}\to\mathrm{iR}}(\boldsymbol{\theta}) + \sum_j C_{j\mathrm{R}\to\mathrm{iR}}(\boldsymbol{\theta}) \cdot b_{j\mathrm{R}}$$

where the index j runs over all CRs, μ is the signal strength, b_{jR} is the background j in Region R and $C_{jR->SR}$ the TF of process j from region R to the SR. For example, the terms $C_{\mathrm{QR}\to\mathrm{QR}}$, $C_{\mathrm{WR}\to\mathrm{WR}}$, $C_{\mathrm{ZRa,b}\to\mathrm{ZRa,b}}$, $C_{\mathrm{TR}\to\mathrm{TR}}$ correspond to the diagonal entries in Table 5.24. The likelihood fit is explained in more detail in [63], including how the correlations in the uncertainties are handled. In general, Table 5.25 shows that the observed SR event counts do not deviate substantially from the predictions of the fit, except in some of the tighter SRs, where fluctuations in both directions are seen. To a certain extent, these may also be due to fluctuations in the CR data driving the SM expectations up or down, *e.g.* due to a lack of statistics at high m_{eff}, as in Figure 5.17(b).

[9] This is the reason for the large discrepancy in the QCD estimate, *e.g.* MC being generally inadequate to properly describe the extreme tails of the $E_{\mathrm{T}}^{\mathrm{miss}}$ in QCD multijet events.

In order to illustrate better which background components are the most significant in each of the SRs, Table 5.26 shows the fraction from the total SM expectation that each background process contributes (again, pre-fit values are shown in parentheses). From this table, it is clear that the $Z+$jets background (here predominantly irreducible $Z_{\nu\nu}+$jets events) are amongst the largest contributions to the total event count, *e.g.* for SRs A medium, Ap medium, C medium, A tight, B tight and C tight, this process in fact represents the largest contribution, and the second largest for the remaining SRs (except for SR E loose and D tight). The overall trend is that this background becomes more dominant with decreasing jet multiplicity.

Finally, the m_{eff}(incl.) distributions (prior to the m_{eff}(incl.) cut) of the SRs in data and MC (`ALPGEN`) are shown in Figure 5.18. The data represents the event counts in Table 5.25, while the MC, the values in parenthesis for each SM contribution (except for QCD where the data-driven estimate is quoted). The `ALPGEN` $W+$jets, $Z+$jets and $t\bar{t}+$jets distributions in the Moriond'12 analysis were scaled respectively by 0.75, 0.78 and 0.73, in addition to the normalisation to the data luminosity, in order to improve the agreement with the data. These scaling factors are within the expected range of systematic uncertainties and were determined by normalisation to all data in CR3, CR1b and CR4 respectively in channel A. As mentioned, the CR1a plots do not have such scaling. The scaling was only cosmetic for the relevant plots and has no impact on the final Moriond'12 0ℓ results, as the background normalisation is handled by the likelihood fit.

Overall, reasonably good agreement is observed between the data and the SM expectation (both the MC and fitted versions), with no significant excesses seen.

Process	Signal Region					
	SRC loose	SRE loose	SRA medium	SRAp medium	SRC medium	SRE medium
$t\bar{t}$+ Single Top	74 ± 13 (75)	66 ± 26 (64)	7 ± 5 (5.1)	11 ± 3.4 (10)	12 ± 4.5 (10)	17 ± 5.8 (13)
Z/γ+jets	**70 ± 22 (61)**	**22 ± 6.4 (13)**	**31 ± 9.9 (34)**	**64 ± 20 (69)**	**17 ± 5.9 (16)**	**8 ± 2.9 (4.4)**
W+jets	62 ± 9.3 (61)	23 ± 11 (23)	19 ± 4.5 (21)	26 ± 4.6 (30)	8.1 ± 2.9 (11)	5.9 ± 3 (4.7)
QCD jets	0.39 ± 0.4 (0.16)	3.7 ± 1.9 (3.8)	0.14 ± 0.24 (0.13)	$1e-06 \pm 0.13$ (0.38)	0.024 ± 0.034 (0.013)	0.8 ± 0.53 (0.64)
Di-Bosons	7.9 ± 4 (7.9)	4.2 ± 2 (4.2)	7.3 ± 3.7 (7.5)	15 ± 7.4 (16)	1.7 ± 0.87 (1.7)	2.7 ± 1.3 (2.7)
Total	$214 \pm 24.9(sys) \pm 13(stat)$	$119 \pm 32.6(sys) \pm 11.6(stat)$	$64.8 \pm 10.2(sys) \pm 6.92(stat)$	$115 \pm 19(sys) \pm 9.69(stat)$	$38.6 \pm 6.68(sys) \pm 4.77(stat)$	$34 \pm 4.47(sys) \pm 5.57(stat)$
Data	**210**	**148**	**59**	**85**	**36**	**25**
local p0 (Gaus. σ)	0.55(-0.14)	0.21(0.8)	0.65(-0.4)	0.9(-1.3)	0.6(-0.26)	0.85(-1)

Process	Signal Region				
	SRA tight	SRB tight	SRC tight	SRD tight	SRE tight
$t\bar{t}$+ Single Top	0.22 ± 0.35 (0.046)	0.21 ± 0.33 (0.066)	1.8 ± 1.6 (0.96)	2 ± 1.7 (0.92)	3.9 ± 4 (2.6)
Z/γ+jets	**2.9 ± 1.5 (3.1)**	**2.5 ± 1.4 (1.6)**	**2.1 ± 1.1 (4.4)**	**0.95 ± 0.58 (2.7)**	**3.2 ± 1.4 (1.8)**
W+jets	2.1 ± 0.99 (1.9)	0.97 ± 0.6 (0.84)	1.2 ± 1.2 (2.7)	1.7 ± 1.5 (2.5)	2.3 ± 1.7 (1.5)
QCD jets	$7.6e-09 \pm 0.0024$ (0.002)	$1.4e-08 \pm 0.0034$ (0.0032)	$5.1e-09 \pm 0.0058$ (0.0023)	$4.4e-08 \pm 0.0072$ (0.021)	0.22 ± 0.25 (0.24)
Di-Bosons	1.7 ± 0.95 (2)	1.7 ± 0.95 (1.9)	0.49 ± 0.26 (0.51)	2.2 ± 1.2 (2.2)	2.5 ± 1.3 (2.5)
Total	$7 \pm 0.999(sys) \pm 2.26(stat)$	$5.39 \pm 0.951(sys) \pm 2.01(stat)$	$5.68 \pm 1.79(sys) \pm 1.51(stat)$	$6.84 \pm 1.7(sys) \pm 2.1(stat)$	$12.1 \pm 4.59(sys) \pm 3.04(stat)$
Data	**1**	**1**	**14**	**9**	**13**
local p0 (Gaus. σ)	0.982(-2.1)	0.955(-1.69)	0.0183(2.09)	0.292(0.548)	0.447(0.133)

Table 5.25.: *Moriond'12 numbers of events in data and fitted background components in each SR. The estimated background values are quoted in the order "expectation ± total uncert. (pre-fit prediction)". For the total background estimates, the two quoted uncertainties are respectively systematic and statistical (MC and CR stats combined). The values in parentheses are the pre-fit predictions, normalised to cross-section and luminosity. For W + jets, Z + jets and $t\bar{t}$ +jets, these predictions are from* `ALPGEN` *scaled by factors explained elsewhere in the text. In the case of QCD, the pre-fit values are from the data-driven estimate. From [63].*

Process	Percentages (%)					
	SRC loose	SRE loose	SRA medium	SRAp medium	SRC medium	SRE medium
$t\bar{t}$+single t	35 (37)	56 (59)	11 (7.5)	9.5 (8.0)	31 (26)	49 (51)
Z/γ+jets	**33 (30)**	**19 (12)**	**48 (50)**	**55 (55)**	**44 (41)**	**23 (17)**
W+jets	29 (30)	19 (21)	29 (31)	22 (24)	21 (28)	17 (8)
QCD jets	0.18 (0.078)	3.1 (3.5)	0.22 (0.19)	8.6×10^{-7} (0.30)	0.062 (0.034)	2.3 (2.5)
Di-Bosons	3.7 (3.9)	3.5 (3.9)	11 (11)	13 (13)	4.4 (4.4)	7.8 (11)

Process	Percentages (%)				
	SRA tight	SRB tight	SRC tight	SRD tight	SRE tight
$t\bar{t}$+single t	3.2 (0.65)	3.9 (1.5)	32 (11)	29 (11)	32 (30)
Z/γ+jets	**42 (44)**	**46 (36)**	**38 (51)**	**14 (32)**	**26 (21)**
W+jets	30 (27)	18 (19)	21 (31)	25 (31)	19 (17)
QCD jets	1.1×10^{-7} (0.028)	2.6×10^{-7} (0.073)	9.1×10^{-8} (0.027)	6.4×10^{-7} (0.25)	1.8 (2.8)
Di-Bosons	25 (28)	32 (43)	8.8 (5.9)	32 (26)	21 (29)

Table 5.26.: *Moriond'12 percentage contributions to the SR background expectation from Table 5.25 for each SM background component. Parentheses indicate the pre-fit values from MC.*

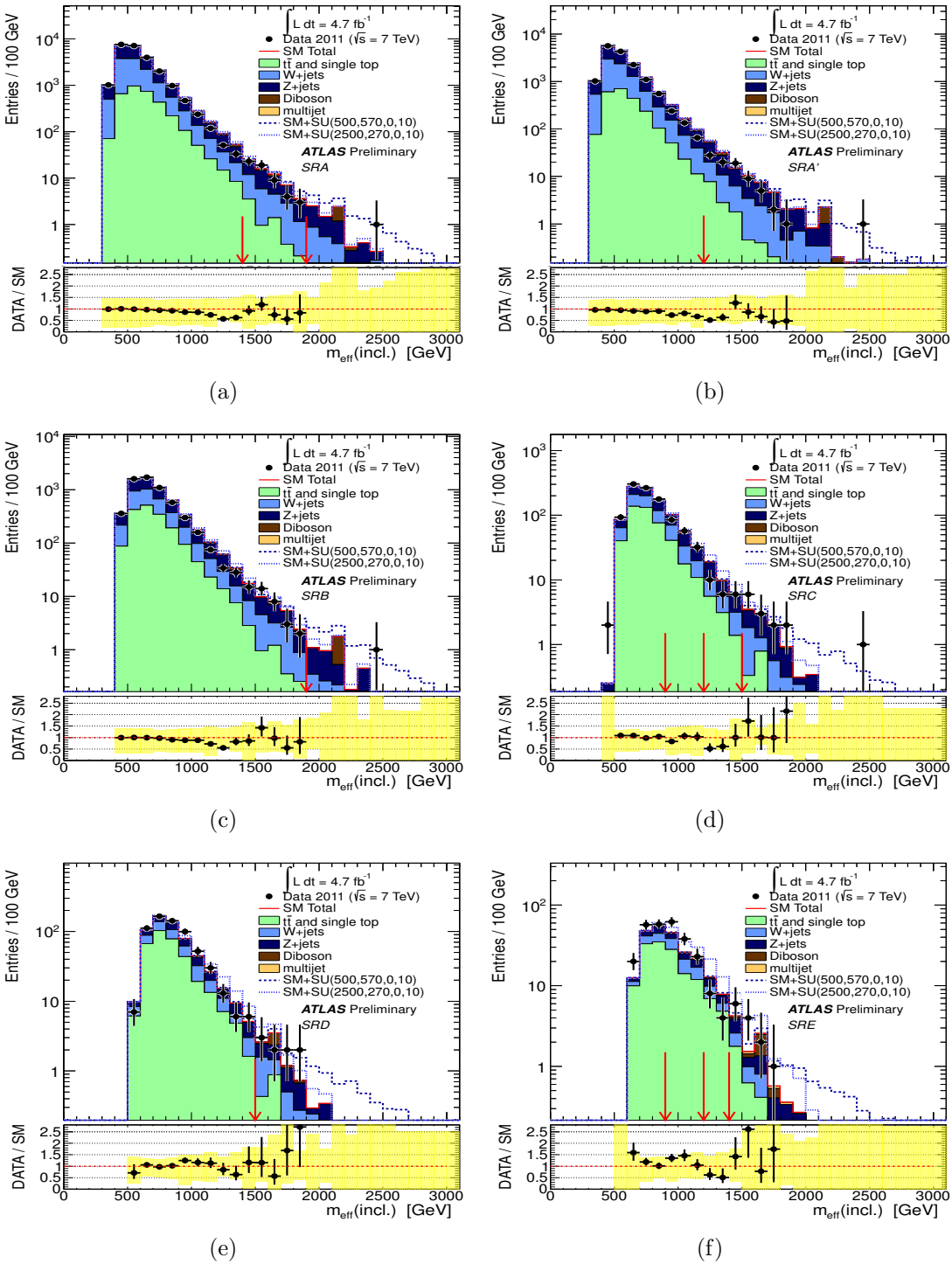

Figure 5.18.: *Moriond'12 $m_{\text{eff}}(incl.)$ distributions in data and MC (ALPGEN) for all the 0ℓ SRs prior to the $m_{\text{eff}}(incl.)$ cut (red arrows indicate the start of a SR). The $W+jets$, $Z+jets$, $t\bar{t}$ and single top contributions have additional scaled factors applied (explained elsewhere in the text). The multi-jet (QCD) contribution is as estimated using the corresponding data-driven method. The dashed-line histograms represent two mSUGRA/CMSSM benchmark model points ($m_0 = 500$ GeV, $m_{1/2} = 570$ GeV, $A_0 = 0$, $\tan\beta = 10$ and $\mu > 0$ and with $m_0 = 2500$ GeV, $m_{1/2} = 270$ GeV, $A_0 = 0$, $\tan\beta = 10$ and $\mu > 0$), which lie just beyond the reach of EPS'11. The yellow band represents the combined JES, JER and MC statistics uncertainties.*

5.6.2. Discussion: Comparisons with other CRs

To understand the relevance of CR1a in the 0ℓ analysis, as well as its advantages over other control samples that could be used to estimate the same background, *e.g.* $Z_{\ell\ell}$ and $W_{\ell\nu}$, a few of comparisons will be made here between CR1a and other CRs, in particular those involving electroweak boson processes, *i.e.* CR1b ($Z_{\ell\ell}$) and CR3 ($W_{\ell\nu}$). The main topics will be the statistics, purity and uncertainties.

CR statistics

In Section 3.3, the theoretical advantages of the γ + jets sample to estimate the Z + jets background over other possibilities like $Z_{\ell\ell}$ + jets and $W_{\ell\nu}$ + jets were discussed. Now the focus is on the experimental evidence supporting such arguments. When examining Table 5.22, the contrast between the available statistics in CR1a and CR1b is starkly evident. This is underlined by the fact that CR1b is the only CR to actually register zero events in data (for the 6-jet channel E), making it effectively unusable (*e.g.* it is disregarded in the 0ℓ likelihood fit for this channel). Maintaining substantial CR statistics is of course critical for providing a robust SR estimate, since the CR statistical uncertainties feed directly into the SR prediction. The comparison with CR3 does not show such drastic differences, and the statistical advantage varies depending on the channel and m_{eff}(incl.) cut. But it is worth bearing in mind that some cuts ($\Delta\phi$ and $E_{\text{T}}^{\text{miss}}/m_{\text{eff}}$ in Table 5.21) are relaxed in the case of the CR3 selection, whereas they are not in CR1a. While the omission of these cuts is not expected to substantially bias the SR predictions, full consistency would favour retaining them.

Magnitude and stability of TFs

A related issue arises from the magnitude of the TFs. From Table 5.23, it can be seen that the only TFs that are larger than 1 are those from CR1b. This feature results from the small branching fraction for $Z_{\ell\ell}$ decays. While at first glance this would not appear to present a problem, one may infer that the CR statistics will always be inferior to the number of events predicted in the SR. Therefore, the CR statistical uncertainty on the estimate will always be intrinsically larger than the Poisson uncertainty on the estimate itself – an undesirable state of affairs.

In contrast, the CR1a TF values are without exception smaller than 0.5, and are in fact much more stable across the SRs relative to other CRs. To illustrate this, Table 5.27 shows the range, mean and standard deviations for the TFs in Table 5.23, broken down by CR. The standard deviation of CR1a is the smallest relative to the mean, at 13%, while the remainder are all in excess of 50%. While a degree of variation is inevitable due to the different kinematic selections of the various 0ℓ SRs, stability is beneficial in that it offers a straightforward sanity check: the feature reflects the $R_{Z/\gamma}(p_{\mathrm{T}})$ plateau at high p_{T} (Figure 3.1(b)), as well as the minimal effect of the 0ℓ selections on the photon acceptance, efficiencies and purity (Section 5.4.3).

CR / Process	Range	Mean	Std. Dev.
CR1a / Z/γ+jets	**0.130**	**0.319**	**0.042**
CR1b / Z/γ+jets	4.700	3.46	1.545
CR2 / QCD jets	0.097	0.0254	0.029
CR3 / W+jets	0.600	0.296	0.167
CR4 / $t\bar{t}+t$	0.835	0.305	0.249

Table 5.27.: *Moriond'12 range (difference between minimum and maximum values), mean and standard deviation of the TFs in Table 5.23, separated by CR/process.*

Purity

A rough estimate of the purity of the various CR selections can be obtained by examining the corresponding m_{eff}(incl.) histogram, *e.g.* Figure 5.17, where the fraction of background at 1 TeV can be seen to be approximately 5% for CR1a and 3% for CR1b, but it is as large as 10% for CR3. Although the contamination can be compensated by an adequate knowledge of the contaminating processes, a purer sample benefits from reduced uncertainties, and is on the whole preferable.

Uncertainties

As an example, Table 5.28 shows the central values of the TFs for all CRs and the absolute values of their associated uncertainties, for the SR A (medium) (the complete collection can be found in [63]). Therefore, column 2 in this table is comparable to column 6 in Table 5.20 with the following caveats:

- The "acc. Z+jets/γ" uncertainty represents a *combined* uncertainty by adding in quadrature the uncertainties in rows 2-4 and 7-8 in Table 5.20 (for simplicity, all these uncertainties are assumed uncorrelated with each other).
- The uncertainties not filled for CR1a are only relevant to other CRs, *e.g.* the b-tag/veto efficiency, and therefore are not assessed.
- The central value quoted in Table 5.28 has the $R_{Z/Z_{\nu\nu}}$ scaling factor applied, as described in Section 5.6.1.
- The "MET CellOut" uncertainty in Table 5.20 appears resolved into its components "cluster" and "pileup" in Table 5.28.

For complementary purposes, Table 5.29 shows the influence of the various CRs uncertainties on the total SM background estimate for each SR. From these numbers, two important details can be noted. Firstly, the degree of correlation between the CR1a uncertainties and those of other CRs is really minimal – those systematics that are correlated (JER, JES, MET CellOut) are essentially negligible, when compared to the remaining uncorrelated systematics unique to CR1a. Secondly, the contribution of CR1a to the total uncertainty budget for the 0ℓ SRs is rather substantial, except where MC or CR statistical uncertainties dominate. This is true at lower jet multiplicities and for softer m_{eff}(incl.) cuts. Essentially, this is due to $Z_{\nu\nu}$ + jets being the dominant background in these SRs, and does not reflect an innate weakness in the estimation method. However, it is clear that reducing the size of the uncertainties associated with CR1a can bring substantial gains in the performance of the 0ℓ analysis as a whole (Section 5.6.3). As the dominant uncertainties can be traced to the lack of $Z_{\nu\nu}$ MC statistics used to compute $R_{Z/\gamma}$, this problem is not insoluble, but merely underlines again the need for more appropriate MC samples. The theoretical studies from Chapter 4 and [64] indicate that it should be possible to decrease this uncertainty from 25% to about 10% under ideal circumstances, *e.g.* where multiparton MEs are used for all selected jets.

Region	Main CR/Process				
	CR1a / Z/γ+jets	CR2 / QCD jets	CR4 / $t\bar{t}$+ Single Top	CR3 / W+jets	CR1b / Z/γ+jets
Central value	0.39	0.036	0.35	0.31	2.5
JER	**0.0032** **0**		0.092 0	−0.021 0	−0.14 0
JES	**0.0052** **−0.0037**		−0.0068 0.027	0.0069 0.017	−0.46 0.9
Pileup			0 0.036	0 −0.014	
l resoln.			−0.0043 0.0094	−0.0039 0.0027	0 −0
Trigger			−0.0019 0.0019	−0.0017 0.0017	−0.028 0.029
b-tag/veto eff.			−0.027 0.04	−0.0032 0.0032	
acc. Z+jets/ γ	**0.11** **−0.11**				
l scale.			−0.0043 0.0057	−0.0052 0.00047	−0.05 −0.034
QCD smear.		0.031 −0.031			
MET CellOut cluster	**0.001** **−0.00072**		0.0015 0.00065	−0.00082 −0.0015	
Top Theory			0.21 −0.21		
l eff.			−0.0024 0.0024	−0.002 0.002	−0.032 0.032
MET CellOut pileup	**0.00029** **−0.00079**		−0.00018 0.0078	−0.00077 $9.4e{-}05$	
PDF			0.0061 −0.0097	−0.0067 0.014	
Z+jets Theory					0.1 −0.1
MC stat.			0.12 −0.12	0.035 −0.035	0.46 −0.46
W+jets Theory				0.025 −0.025	

Table 5.28.: *Moriond'12 initial (pre-fit) uncertainties on the CRs TFs to SR A (medium). From [100].*

Uncertainty	Signal Region										
	SRA medium	SRA tight	SRAp medium	SRB tight	SRC loose	SRC medium	SRC tight	SRD tight	SRE loose	SRE medium	SRE tight
Total	12	2.2	21	2.1	28	8	2.3	2.7	40	7	5.7
CR stat /%	12	27	6.8	24	9.5	15	17	12	3.9	23	7
MC stat /%	16	62	10	62	12	20	26	36	4.5	39	18
l resoln. /%	0.054	2.6	0.043	0	0.076	0.08	0.01	0	0.063	0.2	0.0047
acc. Z+jets/ γ /%	54	14	81	11	59	40	7.6	0.99	2.1	9.5	2.1
MET CellOut cluster /%	0.013	2.7	0.055	0	0.32	0.017	1.8	1.9	0.077	0.16	0.14
MET CellOut pileup /%	0.0056	0	0.011	0	0.15	0.17	0.0026	0	0.022	0.25	0
Top Theory /%	12	2.7	1.2	0	5.9	17	23	13	6.6	15	19
PDF /%	0.024	0.15	0.06	0	0.19	0.32	0.019	0	0.33	1.4	0
BTagWjets /%	0.11	2.7	0.079	0	0.71	0.28	0.014	0	0.13	1.2	0.033
W+jets Theory /%	1.6	0.65	0.88	2	2.8	5	8.7	0.81	0.4	1.2	0.22
l scale. /%	0.097	2.6	0.022	0	0.13	0.12	0.0071	0	0.08	0.21	0
Generic Diboson /%	3.9	11	5.7	12	0.016	0.16	0.017	14	0.052	1.8	4.4
l eff. /%	0.012	2.7	0.053	0	0.16	0.13	0.012	0	0.03	0.18	0
JES /%	0	2.7	0.23	0.61	0.53	0.08	0.8	0	45	1.3	32
Pileup /%	0	2.6	0.023	0.049	0.39	0.63	0.0093	1.4	0.1	0.14	0.007
Trigger /%	0.015	1.8	0.011	0	0.1	0.13	0.0031	0	0.023	0.17	0
JER /%	0	1.5	0	2.1	0.93	3.4	13	17	0.89	0.81	6.4
BTagtop /%	1.1	2.7	0.49	0	9.2	3.3	3.1	4	5.1	7.4	1.3
QCD smear. /%	0.018	1.7	0.0016	0	0.056	0.13	0.0011	0	0.2	0.45	0.014

Table 5.29.: *Moriond'12 breakdown of the influence of various systematic uncertainties in the SRs. The "Total" row shows the absolute uncertainty on the SR prediction. All other rows show the fractional contribution of individual systematics to this number, as follows: 'CR stat' is the uncertainty with all uncertainties besides the statistical uncertainty in the CR switched off, 'MC stat' is the uncertainty coming from limited MC sample sizes; all other entries show the influence of the corresponding systematic uncertainty. 'MC stat' uncertainties are modelled with a log normal pdf shape, while 'CR stat' uncertainties are based on Poisson pdfs. Note: The influence of MC stat. and all systematic uncertainties a Gaussian shape for all underlying prob. density functions. From [100].*

5.6.3. 0ℓ Interpretation and Limits

In the absence of a statistically significant excess, limits are set on contributions to the SRs from new physics, which has been the case in all the 0ℓ analyses to date.

For the purposes of interpretation, a SR measurement is compared with the corresponding background estimate in order to determine the significance of any excesses over the SM expectation, or to test its compatibility with respect to a given signal model[10]. In other words, a hypothesis test is carried out. The so-called *discovery* test regards the SM prediction as the "null" hypothesis, *i.e.* the model to be falsified if the observation is substantially incompatible with it, like an excess. Alternatively, one can test the compatibility of particular BSM model with the observation in order to *exclude* incompatible models. Therefore, *exclusion* tests become of interest when no significant excesses are observed. The ATLAS SUSY Working Group policy has been so far to present both discovery and exclusion results in all cases. In the 0ℓ fitting procedure, any of these hypothesis tests can be performed by just assuming the appropriate signal component in the likelihood function (Equation (5.12)). When searching for an excess it is assumed that the SUSY signal contributes minimally to the CR counts. For the purposes of a discovery test, the CRs are simply treated as signal-free, since no particular signal is assumed. However, it is possible to account for the signal contamination in CRs, and this is indeed done when carrying out an exclusion test on some specific model.

Since no significant excess has been observed until now, in the 0ℓ analysis the focus has been on setting exclusion limits whilst still providing the the p-values for the discovery test, as shown in Table 5.25. For the interpretation to be as generic as possible, *model-independent* limits have been set on the SUSY cross-section times acceptance times efficiency, $\sigma_{\text{SUSY}} \cdot A \cdot \varepsilon$, *i.e.* remaining agnostic about the model kinematics and detector effects. The limits set on $\sigma_{\text{SUSY}} \cdot A \cdot \varepsilon$ are listed in Table 5.30. Such numerical values can be reinterpreted easily by computing $\sigma_{\text{SUSY}} \cdot A \cdot \varepsilon$ for a given signal model and comparing this with the ATLAS limits. The limits on a specific SUSY model are obtained by comparing the observed numbers of events in the SR (s) with the fitted SM background expectation plus SUSY signal process ($s + b$), using the CL_s method [24] to derive 95% Confidence Level (CL) exclusion regions. The SR with the best expected limit at each point in the SUSY parameter space is chosen as the *combined* limit. These procedures

[10] In principle, deficits could also mark new physics destructively interfering with SM particle production, but this is not considered here.

follow the ATLAS Statistics Forum recommendations and are explained in more detail in [100] and [104].

The two main interpretations of the results in the Moriond'12 0ℓ analysis are presented in Figure 5.19. Figure 5.19(a) represents an exclusion region in the MSSM squark-gluino mass plane for a set of simplified SUSY models (see Section 1.2.2) with $m_{\tilde{\chi}_1^0} = 0$ and degenerate gluino and squark masses of the first two generations. All other supersymmetric particles, including the squarks of the third generation, are decoupled by being given masses of 5 TeV. From this, the limit on the gluino mass is approximately $m_{\tilde{g}} \sim 940$ GeV, and on the squark mass $m_{\tilde{q}} \sim 1380$ GeV. As for Figure 5.19(b), it represents an interpretation in an MSUGRA constrained model (see Section 1.2.2) with parameters $\tan\beta = 10$, $A_0 = 0$, $\mu > 0$. From this, the limit on $m_{1/2}$ is above 300 GeV at high m_0 and reaches 680 GeV for low values of m_0 – the inclusion of SRs with larger jet multiplicities improved the reach at large m_0. Equal mass squarks and gluinos are excluded below 1400 GeV in both scenarios. Overall, the increased data sample in the Moriond'12 analysis allowed for the substantial extension of the limits from EPS'11.

	Signal Region					
	SRC loose	SRE loose	SRA medium	SRAp medium	SRC medium	SRE medium
Limit (fb)	$12(13^{+9.3}_{-18})$	$18(15^{+11}_{-20})$	$5.3(6^{+4.3}_{-8.2})$	$6.2(9.2^{+6.7}_{-13})$	$3.7(4.1^{+3}_{-5.7})$	$2.5(3.5^{+2.5}_{-5})$

	Signal Region				
	SRA tight	SRB tight	SRC tight	SRD tight	SRE tight
Limit (fb)	$0.62(1.3^{+0.89}_{-1.9})$	$0.65(1.2^{+0.8}_{-1.8})$	$3.5(2.3^{+1.6}_{-3.2})$	$2.2(1.9^{+1.4}_{-2.7})$	$2.6(2.5^{+1.8}_{-3.5})$

Table 5.30.: *Moriond'12 Approximate observed limits on the model independent cross section at 95 % C.L. based on the CLs method, no signal uncertainties are taken into account. The expected cross section is given in brackets with a $\pm 1\sigma$ deviation in the background.*

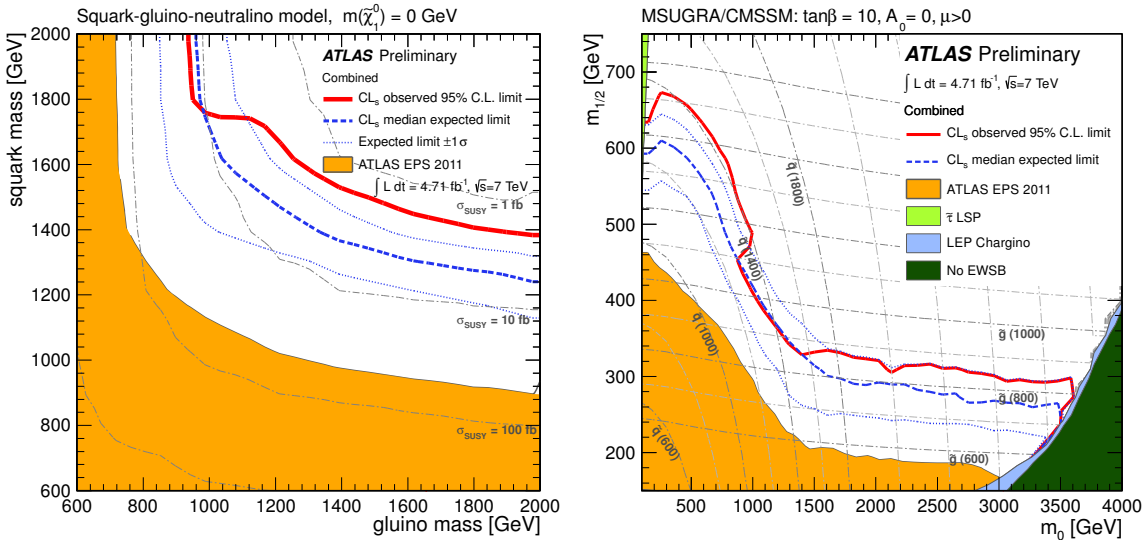

Figure 5.19.: *Moriond'12 95% CL_s exclusion limits obtained in the 0ℓ analysis by using the SR with the best expected sensitivity at each point in (a) a simplified MSSM scenario with only strong production of gluinos and first- and second-generation squarks, and direct decays to jets and neutralinos; and (b) in the (m_0 ; $m_{1/2}$) plane of MSUGRA/CMSSM for* $\tan\beta = 10$, $A_0 = 0$ *and* $\mu > 0$. *The red lines show the observed limits, the dashed-blue lines the median expected limits, and the dotted blue lines the* $\pm 1\sigma$ *variation on the expected limits. The EPS'11 and LEP limits are also shown. From [58].*

Effects of CR1a $Z_{\nu\nu}$ + jets estimate

The reduction of uncertainties in any background estimation method is a high priority. In particular, where a given background component is irreducible, and cannot be eradicated from the SR selection entirely, it is best to ensure that the magnitude of the component is known *precisely*. To illustrate the extent to which this is true, a comparison is made in Figure 5.20 of limits computed assuming a 25% theoretical uncertainty on the ratio $R_{Z/\gamma}$ (as was assumed for Moriond'12) with those assuming a 15% uncertainty. All other parameters were kept unchanged. Two SR selections, SR A (medium) and SR A' (medium) are shown, as these are the ones for which the Z + jets background is most dominant (48% and 55%, see Table 5.26). The limits improve perceptibly when the uncertainty is reduced, by up to 40 GeV in the squark and gluino masses.

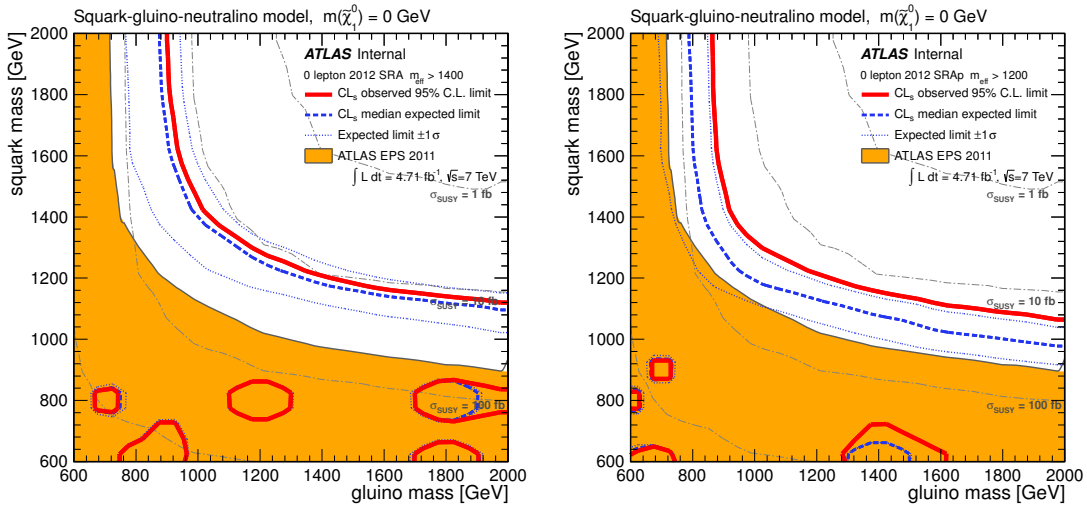

(a) SR A, $m_{\text{eff}} > 1.4$ TeV, $\sigma_{\text{th}} = 25\%$

(b) SR A', $m_{\text{eff}} > 1.2$ TeV, $\sigma_{\text{th}} = 25\%$

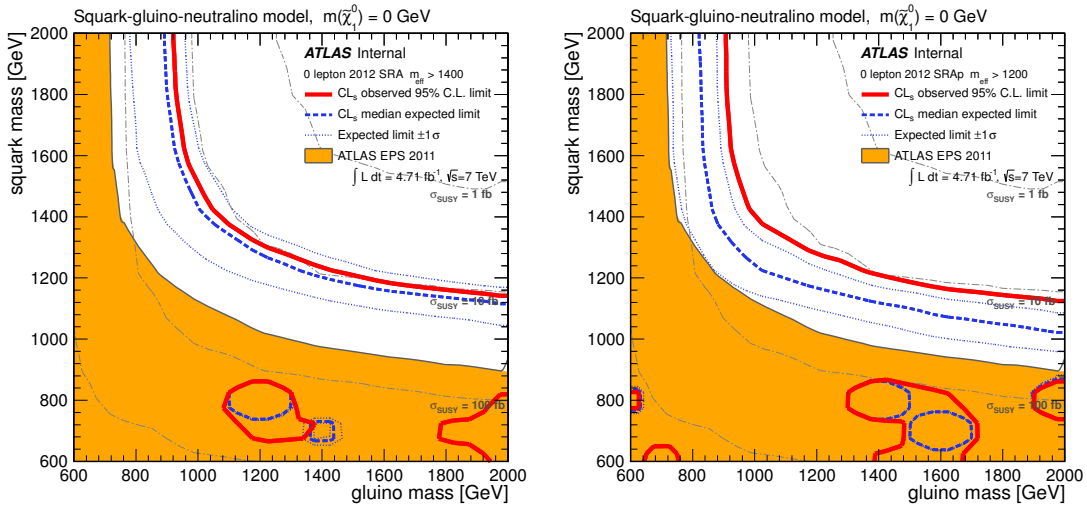

(c) SR A, $m_{\text{eff}} > 1.4$ TeV, $\sigma_{\text{th}} = 15\%$

(d) SR A', $m_{\text{eff}} > 1.2$ TeV, $\sigma_{\text{th}} = 15\%$

Figure 5.20.: *Moriond'12 comparison of limits set using the predicted CR1a Z+jets background estimate from Figure 5.16 with different systematic uncertainties. The red solid and blue dashed lines indicates the observed and expected 95% C.L. excluded regions, while the shaded orange region is the excluded area from EPS'11. The upper two plots show the nominal 25% theory uncertainty, σ_{th}, estimated for Moriond'12. In the lower plots, this magnitude of this uncertainty is reduced to 15%, resulting in a strengthening of the limits by up to 40 GeV in the squark and gluino masses, providing a strong motivation for improving the estimation of the CR1a TFs. The SRs shown are those that are dominated by the $Z_{\nu\nu}$ + jets background due to the less stringent jet multiplicity requirements. The 'holes/loops' shown reflect MC fluctuations or divergences encountered by the fit for those regions of phase space.*

Part III.

Close

Chapter 6.

Conclusions & Outlook

6.1. ZfromGamma

In conclusion, the ZfromGamma method was demonstrated to be successful in estimating the $Z_{\nu\nu}$ background to new physics searches in ATLAS, as well as well-established since 2010. Despite no signs of SUSY or other BSM physics found so far at the LHC (see Section 6.2), the searches continue and therefore, the ZfromGamma method will remain crucial in determining if there are signs of new physics at all.

However, there remains room for improvement: a further reduction in the uncertainties associated with this method would pay substantial dividends in improving the sensitivity and reach of the searches for new physics. In this section, some potential steps that might advance the precision and overall applicability of the method are outlined, but first, to understand some of the motivations behind these, a discussion of analogous CMS results precedes.

6.1.1. CMS results

This part focuses on the "ZfromGamma-like" results from CMS. First, the most comparable studies in CMS to the ATLAS 0ℓ analysis are their so-called "SUSY hadronic searches". The analyses which have used a similar dataset to the Moriond'12 one discussed here are: (i) the "multijets+MHT" search (4.98 fb^{-1}) [105]; (ii) the "MT2" search (4.73 fb^{-1}) [106]; (iii) the "razor" search (4.4 fb^{-1}) [107]; where (i) is the closest with respect to the 0ℓ event selection. From these, (i) and (ii) have used a ZfromGamma-like method to estimate the $Z_{\nu\nu}$ + jets background as overviewed below.

MHT + jets: The baseline selection for this search was $H_T > 500$ GeV, $\not{H}_T > 200$ GeV, at least 3 jets with $p_T > 50$ GeV and $|\eta| < 2.5$ and $\Delta\phi(\not{H}_T, j_1) > 0.5$, $\Delta\phi(\not{H}_T, j_2) > 0.5$ and $\Delta\phi(\not{H}_T, j_3) > 0.3$; where $H_T = \sum p_T$(selected jets). Roughly speaking, H_T is analogous to the 0ℓ m_{eff} and $\not{H}_T$ to the 0ℓ E_T^{miss}. As in the 0ℓ search, $Z_{\nu\nu}$ + jets is usually either the largest or second-largest background to this search, as shown in Figure 6.1, so determining this background is also very important here. For this, a similar method to `ZfromGamma` is used and the plots analogous to CR1a are shown in Figure 6.2 as a function of H_T and $\not{H}_T$. Some systematic data/MC discrepancies can be noticed in Figure 6.2(a) at low H_T ($H_T < 1$ TeV), perhaps due to missing electroweak backgrounds in the MC, as well as in Figure 6.2(b) for medium $\not{H}_T$ (250 GeV $< \not{H}_T <$ 500 GeV). However, the overall data-driven prediction for the total SM background agrees well with the distributions in data (example plots can be found in [105]).

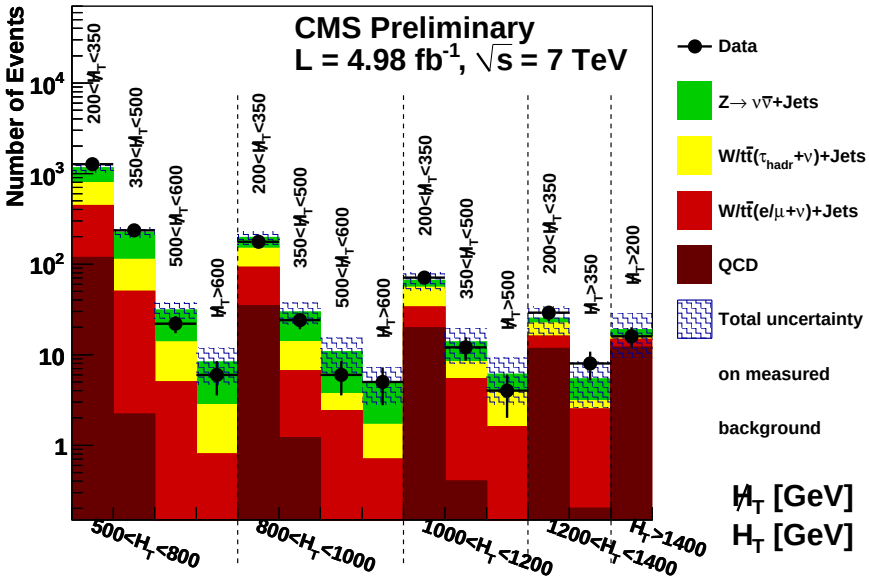

Figure 6.1.: *CMS Moriond'12 "MHT+jets" search. Summary of number of events observed in data and prediction of various backgrounds from data in 14 "search bins" defined in bins of H_T and $\not{H}_T$ (from [105]).*

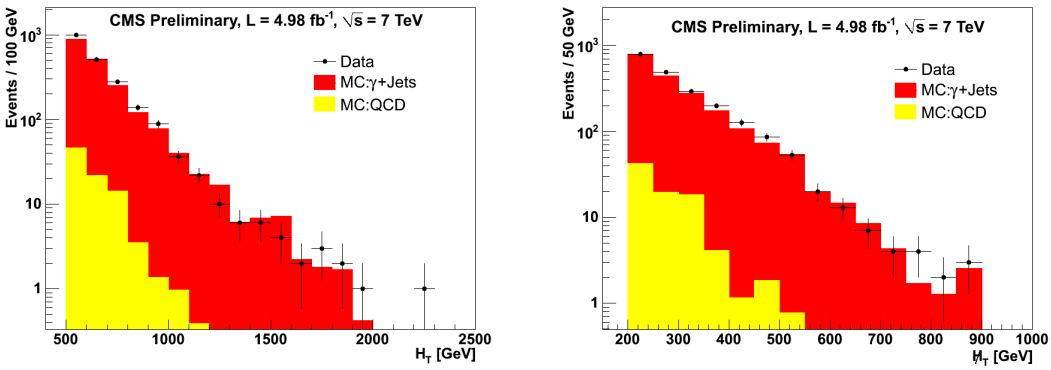

(a) (b)

Figure 6.2.: *CMS Moriond'12 "MHT+jets" search. Comparison of the γ + jets control sample in data and MC: (a) H_{T} and (b) $\not{H}_{\mathrm{T}}$ after all the baseline selection has been applied (from [105]).*

MT2 + jets: This search is based on a different discriminating variable to m_{eff} called m_{T2}, which was in fact used once in the 0ℓ analysis to define one of the Moriond'11 SRs (see Appendix C.1.4). As in the 0ℓ analysis, two control samples are obtained to determine the $Z_{\nu\nu}$ + jets background; one of them being γ + jets and the other $W_{\mu\nu}$ + jets. As in `ZfromGamma`, in both cases, $Z_{\nu\nu}$ is mimicked by removing, respectively, the γ and μ from the event, and adding the corresponding p_{T} to the $E_{\mathrm{T}}^{\mathrm{miss}}$. In the case of γ+jets, the QCD contamination was estimated from MC in the CR (via a shower shape fit). The data to MC comparison of the m_{T2} distribution for the CR is shown in Figure 6.3. The $Z_{\nu\nu}$ background was estimated for each bin in m_{T2} from the number of prompt photon events multiplied by the $R_{Z/\gamma}(m_{\mathrm{T2}})$ from MC. Despite being calculated as a function of m_{T2}, the photon p_{T} is what drives the m_{T2} value, *i.e.* $R_{Z/\gamma}(m_{\mathrm{T2}}(p_{\mathrm{T}})) = R_{Z/\gamma}(p_{\mathrm{T}})$, and so the same features discussed for in previous chapters for $R_{Z/\gamma}(p_{\mathrm{T}})$ apply. The background prediction was found to be in excellent agreement with the MC expectation. The main uncertainties in their estimate come from control sample statistics, the shower shape fit (5%) and $R_{Z/\gamma}$. In particular, for $R_{Z/\gamma}$, the uncertainty was obtained first comparing the photon p_{T} spectra between `MADGRAPH` and `JetPhox NLO` generators, and then comparing the p_{T} dependence of the ratio in MC to the one in data by using $Z_{\ell\ell}$ events (the latter being similar to the `ZfromGamma` "$Z_{\mu\mu}$ cross-check", see Appendix D.1), as shown in Figure 6.4(b). With these, the uncertainty obtained was $< 20\%$ for $m_{\mathrm{T2}} < 275$ GeV and $< 30\%$ for $m_{\mathrm{T2}} > 275$ GeV (the latter being larger due to the limited $Z_{\ell\ell}$ statistics for $p_{\mathrm{T}} > 400$ GeV). In the reference for this analysis [106], there is no mention of photon efficiencies nor acceptance corrections.

As for the alternative method which used $W_{\mu\nu}$, the main challenge was to estimate the relatively large $t\bar{t}$ contamination in the control sample. However, both methods were found to be in good agreement and the weighted average of the two is taken as the final estimate (they are assumed statistically uncorrelated). The uncertainties on the $W_{\mu\nu}$ are not quoted in the reference either. Another feature of this analysis is that the $Z_{\nu\nu}$ background is always comparable to the $W_{\ell\nu}$ and top backgrounds in the SRs (as shown by the SRs plots in [106]).

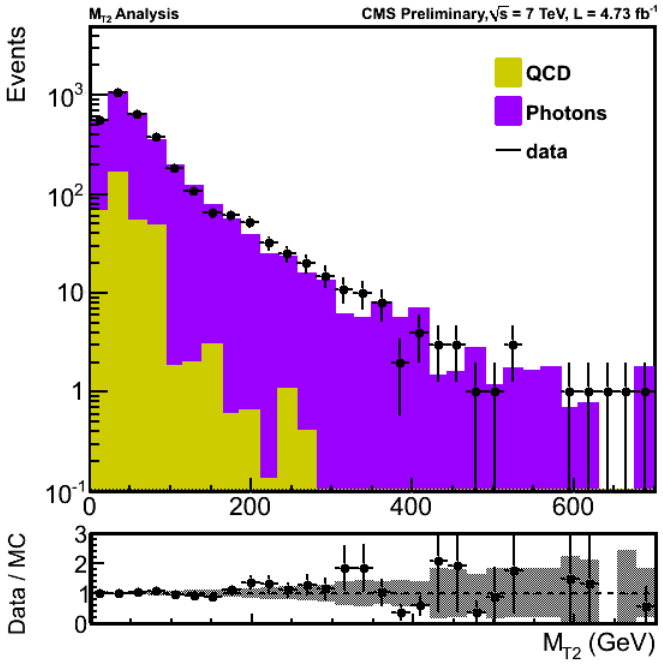

Figure 6.3.: *CMS Moriond'12 "MT2" search. Photon m_{T2} spectrum in data and MC, where the photon was added to the $E_{\mathrm{T}}^{\mathrm{miss}}$-vector to mimic the $Z_{\nu\nu}$ kinematics. (from [106]).*

6.1.2. Outlook

It is possible to further improve the `ZfromGamma` method in a variety of ways. The following is a list with some ideas:

- Overall, the aim would be to reduce each of the uncertainties associated with the method, to help maximise the BSM search reach (see Section 5.6.3).
- Despite the very high purity of the CR1a sample, a proper estimation of the background contamination (f_{bkg}) in the sample should be done (currently, the CMS MT2 search implements a method to do so, see Section 6.1.1). This could *potentially*

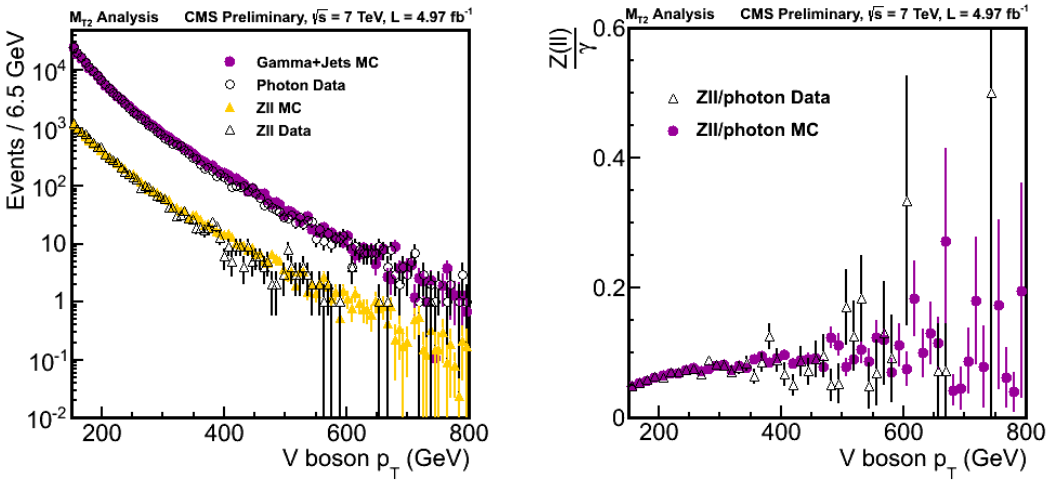

(a) (b)

Figure 6.4.: *CMS Moriond'12 "MT2" search. (a) Vector boson p_{T} for $Z(ee, \mu\mu)$ and $\gamma + jets$ events for data and MC. (b) $Z(ee, \mu\mu)$ to $\gamma + jets$ ratio as a function of vector boson transverse momenta both for data and MC. Only statistical errors are shown (both from [106]).*

reduce the uncertainty on f_{bkg}. For the 0ℓ analysis, this could also determine the cross-TFs to other CRs.

- Obtain $R_{Z/\gamma}$ from data rather than from MC, as currently done in CMS (Figure 6.4(b)), also aiming to reduce further the theoretical uncertainty, especially at low-p_{T}, where the data statistics should not be so limited.

- Evaluate the variation of $R_{Z/\gamma}$ with respect to other kinematic variables *e.g.* as a function of η, m_{eff}, N_{jets}, H_{T}, etc (as done by CMS for m_{T2}, see Section 6.1.1), and determine the thresholds and conditions at which such effects can be safely ignored.

- Determine $R_{Z/\gamma}$ at $\sqrt{s} = 8$ TeV, given that this is the new c.o.m. energy at which the LHC will operate throughout 2012 and that the ratio is expected to slightly increase (see Figure 3.1(b))

- Investigate the effects on $R_{Z/\gamma}$ from electroweak corrections *e.g.* Sudakov logarithms (see Section 4.5), involving W/Z virtual exchanges.

- Look at the possibility of determining from the $R_{Z/\gamma}$ dependence on α_{S}, the renormalisation scale Q_{ren} "chosen" by data *e.g.* from the ratio $\alpha_{\mathrm{S}}(Q_Z^2)/\alpha_{\mathrm{S}}(Q_\gamma^2)$ as illustrated in Figure 4.9.

6.2. SUSY and other BSM

No evidence of SUSY at the LHC has been found up to now, meaning that no excess has been observed above expected backgrounds in the various searches. This has been interpreted as new limits on physically relevant quantities of many BSM models. Figure 6.5 shows a summary of the latest ATLAS SUSY reaches as of Moriond'12. The plot features the different search categories: "Inclusive searches", "Third generation", "Direct gaugino", "Long-lived particles" and "RPV", some of which are described below. The limits so far set by CMS on these models are very similar so they will not be discussed here, but an equivalent plot can be found in [108].

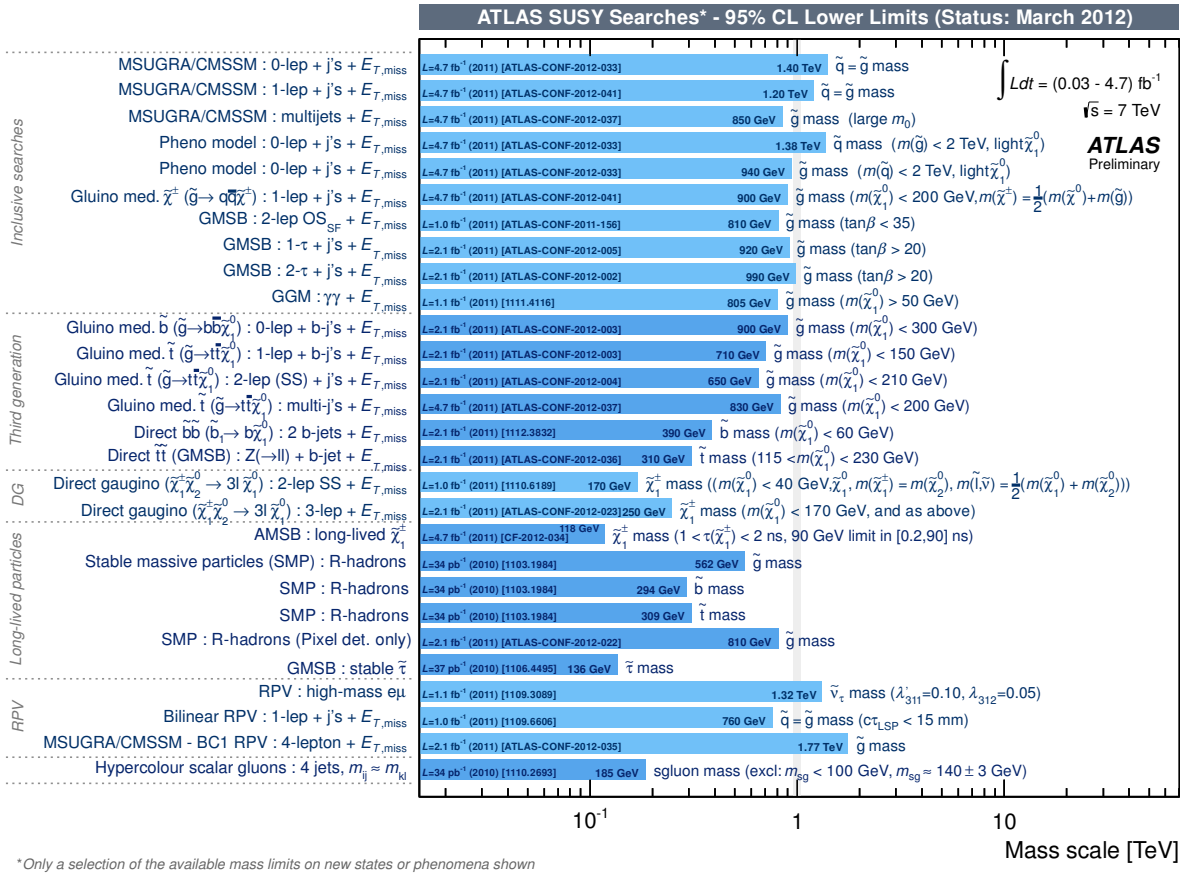

Figure 6.5.: *Mass reach of ATLAS searches for Supersymmetry. Only a representative selection of the available results is shown. The format of each row is "Model name: signature — Luminosity (data sample), [reference] — 95% CL mass exclusion — Observable". Status of figure: Moriond'12 (from [13]).*

RPC searches: The 0ℓ search currently sets the most stringent limits on squark and gluino masses in the constrained and simplified models discussed in Section 5.6.3. For GMSB models, the 2ℓ+jets excludes SUSY-breaking scales of $\Lambda \sim 40$ TeV [109], but the most stringent limits are set by the $\gamma\gamma$ search on the SPS8 breaking-scale up to $\Lambda \sim 145$ TeV and other GMSB models (GGM) [110]. For AMSB models, a search for a long-lived $\tilde{\chi}_1^{\pm}$ decaying inside the ATLAS detector to $\tilde{\chi}_1^0 + \pi^{\pm}$ resulting in final-states of $E_{\mathrm{T}}^{\mathrm{miss}} + 0l +$ jets and a disappearing track sets limits on the $\tilde{\chi}_1^{\pm}$ lifetime between 0.5-2 ns. The $2\ell +$ jets search is able to constrain the masses of charginos up to 200 GeV. The specialised searches for third generation squarks ("b-jet searches") set the most stringent limits on stops and sbottoms in simplified models where the third generation is assumed to be the lightest, while first and second are decoupled from the theory. The highlight of the $0\ell + b$-jet search is to exclude sbottom masses up to 390 GeV [111], while in $1\ell + b$-jet search is to exclude stop masses up to 300 GeV [112].

RPV: In ATLAS these are less popular than the RPC searches, so fewer results are available. Starting with the long-lived particle searches, the $1\ell +$ jets search has also an interpretation in a bilinear RPV (bRPV) mSUGRA model [113], where equal squark and gluino masses below 760 GeV are excluded [113]. A search for a long-lived $\tilde{\chi}_1^0$ which decays to high-p_{T} μ+jets leaving a displaced vertex has set limits on a SUGRA model, excluding 150 GeV squarks for any single displaced vertex. There have been also other searches looking for "resonance" signatures, such as the $\tilde{\nu_\tau} \to e\mu$ search and the scalar gluon search ($\tilde{g} \to$ jets).

Despite no signs of SUSY so far, the searches for it will continue at the LHC this year and with a higher c.o.m. (8 TeV). As discussed in Section 1.2.2, the SUSY parameter space is enormous and many models still remain to be explored. On the other hand, the present experimental limits on SUSY are now strong enough to re-evaluate whether SUSY can still address the problems it aims to solve, which is why alternative BSM theories are simultaneously searched for in ATLAS.

Other BSM

There are many other theories similarly motivated by the improvements they could offer to the SM problems. Given that no sign of SUSY has been observed so far (Section 1.2.3), it is becoming even more appealing now to pursue these alternatives, which in ATLAS

are referred altogether as "Exotics". Figure 6.6 shows a summary of the latest ATLAS Exotics reaches as of Moriond'12, where they have been arranged into six categories: extra dimensions (ED), contact interactions (CI), exotic vector bosons (V'), leptoquarks (LQ), fourth-generation (4^{th} gen.) and 'other', which includes less popular searches (technicolor, Majorana neutrinos, excited quarks, axigluons, etc). However, even in all these many different searches, no new physics signs have showed up either. However, the plan is also to continue these analyses in 2012, as well as other new alternatives.

In conclusion, despite the main outcome from the LHC so far could be seen as only "disproving theories", the reader should not be discouraged – the LHC is a long term experiment and the next few years are really going to show which theories are actually correct.

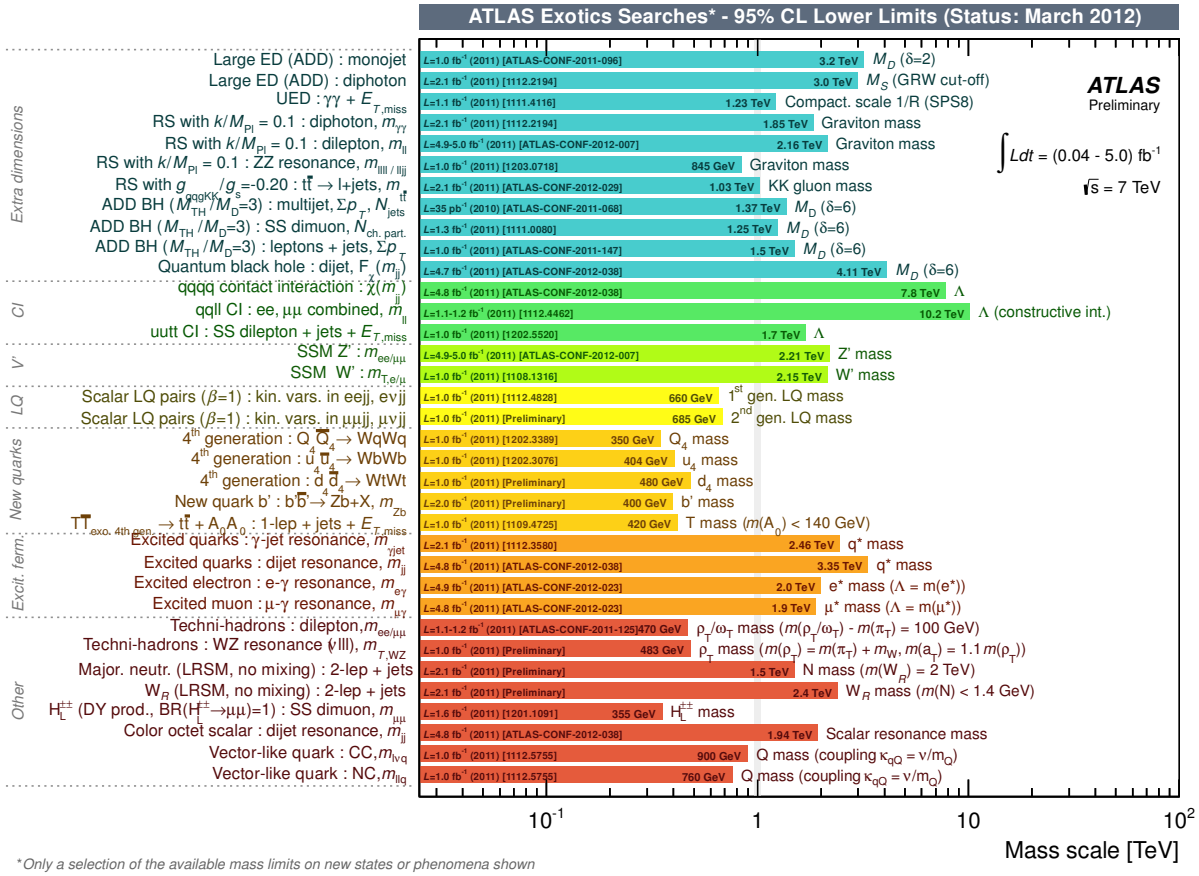

Figure 6.6.: *Mass reach of ATLAS searches for new phenomena other than SUSY. Only a representative selection of the available results is shown. The format of each row is "Model name: signature — Luminosity (data sample), [reference] — 95% CL mass exclusion — Observable". Status of figure: Moriond'12 (from [13]).*

Appendix A.

Supplementary Moriond'12 results

A.1. Event displays

This section shows the details of the event displays of all events in the Moriond'12 dataset with $p_{\mathrm{T}}(\gamma_1) > 1$ TeV. Only the hardest of these events enters CR1a (for SRs A, A' and B). From lowest to highest $p_{\mathrm{T}}(\gamma_1)$ respectively, the event displays are shown in Figures A.1, A.2(a), A.2(b) and 5.11. None of them show 'strange' features to suspect they could originate from fake sources, *e.g.* non-collision backgrounds. Amongst the quantities checked to ensure this are: timing, cell quality, photon quality, no significant dead parts of the detector and the jet quality (*e.g.* timing, charged fraction, EM fraction, etc). Table A.1 outlines some of the details from these events.

Run Number	Event Number	$p_{\mathrm{T}}(\gamma_1)$ [TeV]	$p_{\mathrm{T}}(j_1)$ [TeV]	$p_{\mathrm{T}}(j_2)$ [TeV]	$p_{\mathrm{T}}(j_3)$ [GeV]	$E_{\mathrm{T}}^{\mathrm{miss}\prime}$ [GeV]
189372	37505659	1.008	1.186	0.997	52	147
191426	151155403	1.046	1.238	1.081	48	115
190975	24668402	1.339	1.569	1.280	57	318
190236	87935353	1.406	1.645	1.146	185	297

Table A.1.: *Details for the CR1a events in the Moriond'12 dataset with* $p_{\mathrm{T}}(\gamma_1) > 1$ TeV. *The corresponding event displays are shown in Figures A.1, A.2(a), A.2(b) and 5.11 respectively.* $E_{\mathrm{T}}^{\mathrm{miss}\prime}$ *is as defined in Section 5.4.1.*

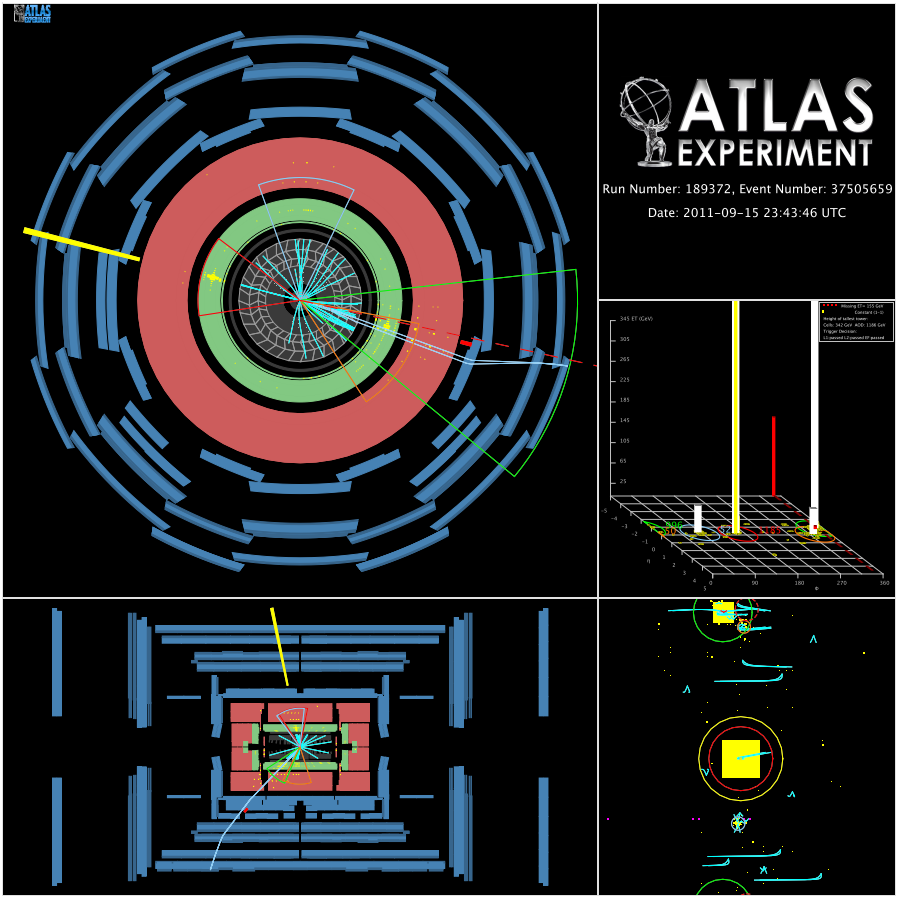

Figure A.1.: *Event displays of the first event in Table A.1 ($p_{\mathrm{T}}(\gamma_1) = 1.008$ TeV).*

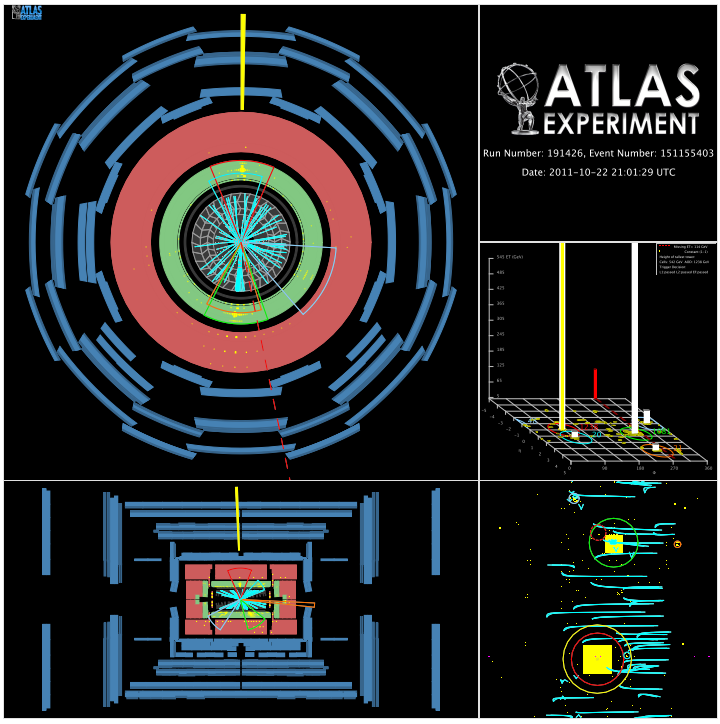

(a)

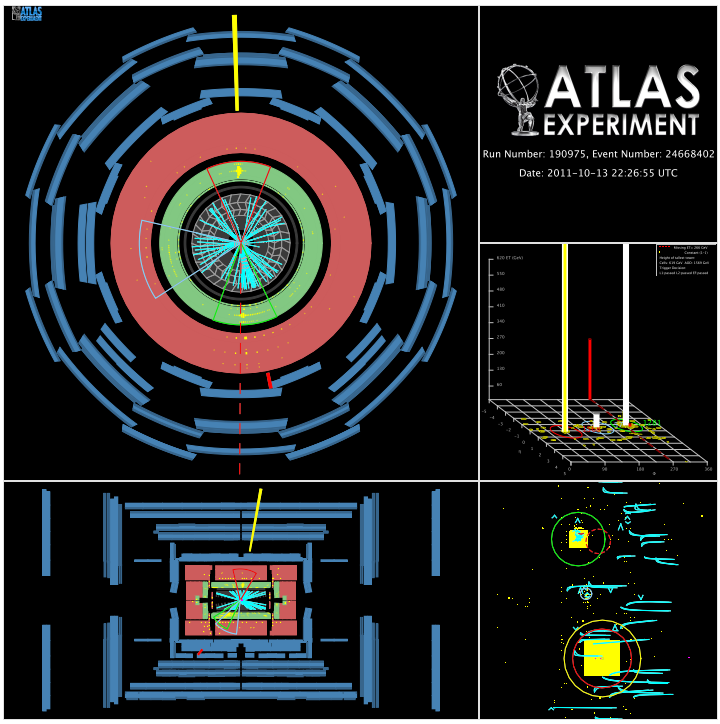

(b)

Figure A.2.: *Event displays of (a) the second ($p_{\mathrm{T}}(\gamma_1) = 1.046$ TeV) and (b) third ($p_{\mathrm{T}}(\gamma_1) = 1.339$ TeV) events in Table A.1.*

Appendix B.

SMDP inclusive prompt photon cross-section measurement ($35\ \mathrm{pb}^{-1}$)

The aim of this section is to summarise some of the results from the latest published ATLAS prompt photon cross-section analysis, performed by the SMDP group, which are relevant to the `ZfromGamma` method and often quoted in the main sections. This analysis corresponds to 35 pb^{-1} and can be found preliminary documented in [76] (data from September-October 2010) and published in 2011 [49]. Further updates of this analysis with more data have been done but not published yet in a journal but rather presented at conferences *e.g.* EPS'11 [92]. Similarly, the first published analysis of this kind from ATLAS was in 2010 with 880 nb^{-1} [48] and its main difference with respect to the 35 fb^{-1} analysis is the exclusion of the region $1.81 \leq |\eta| < 2.37$ in the photon acceptance (see Table 5.8), which at the time suffered from relatively low $\varepsilon_{\mathrm{id}}^{\gamma}$, large shower shape uncertainties and unsuitable MC simulation.

The main contribution from the author to these analyses was in constantly presenting the `ZfromGamma` results to the SMDP group, which were always at the forefront of photon-based analyses, particularly concerning prompt photon events produced in association with jets ($\gamma + \mathrm{jets}$). The `ZfromGamma` results therefore provided useful feedback to this group *e.g.* for the recent SMDP $\gamma + \mathrm{jets}$ cross-section measurement publication [98]. An additional contribution from the author was to produce some of the SMDP EPS'11 plots and results previously mentioned [92], specifically those presented in Section C.3.3.

B.1. Photon Selection

As mentioned in Section 5.3, the event selection and object definitions used for Moriond'11 were practically identical to the those from the SMDP 35 pb^{-1} analysis. This selection is summarised in the corresponding Moriond'11 column in Tables 5.8-5.9. The only significant difference was the DQ criteria (GRL): in [49] fewer 2010 run periods were included (G-I only, amounting to 34.6 ± 1.2 pb^{-1}), whereas the 0ℓ analysis included all (A-I, see Table 5.2). The net loss in luminosity from not using period A-F is ~ 3 pb^{-1} [49].

B.2. Efficiencies

As a part of this study, we compare with the efficiency results in [49] and for this reason we summarise the main results in this section. In the reference, the overall photon efficiency is the product of three individually estimated efficiencies: reconstruction $\varepsilon^{\gamma}_{\rm rec}$, identification $\varepsilon^{\gamma}_{\rm id}$ and trigger efficiency $\varepsilon^{\gamma}_{\rm trig}$.

Trigger Efficiency $\varepsilon^{\gamma}_{\rm trig}$- It is defined as the probability for a prompt photon candidate to pass the `g40_loose` trigger given that it passes the experimental isolation and identification requirements. The integrated efficiency for $E_{\rm T} > 45$ GeV and all η[1] bins was found to be $(99.4^{+0.6}_{-0.2})\%$, Figure B.1. Other triggers used for the subsequent analysis rounds have similar efficiencies, *e.g.* see Table 2.5 and [43].

Reconstruction Efficiency ($\varepsilon^{\gamma}_{\rm rec}$) - This is the efficiency of reconstructing a photon given that it passes the cluster quality and experimental isolation requirements. It is computed as a function of $E_{\rm T}$ and $|\eta|$. Table B.1 quotes these results, where efficiencies between 70% and 86% are observed. Unlike the identification efficiency (see below), $\varepsilon^{\gamma}_{\rm rec}$ *decreases* with $E_{\rm T}$ for all $|\eta|$, as shown in Figure B.2. The decrease slows at high $E_{\rm T}$, as if reaching a plateau.

Identification Efficiency ($\varepsilon^{\gamma}_{\rm id}$) - This is the efficiency of true prompt photons to pass the identification, given that they pass the isolation requirement. It is also computed as a function of $E_{\rm T}$ and $|\eta|$. Table B.2 quotes these results, where efficiencies between 90 and 97% are observed. Unlike $\varepsilon^{\gamma}_{\rm rec}$, $\varepsilon^{\gamma}_{\rm id}$ *increases* with $E_{\rm T}$ for all $|\eta|$, as shown in Figure B.3. This increase also slows at high $E_{\rm T}$, as if reaching a plateau.

[1] The η referred to in this appendix is the one computed in the second sampling of ATLAS LAr calorimeter and sometimes is also denoted as $\eta^{\rm s2}$.

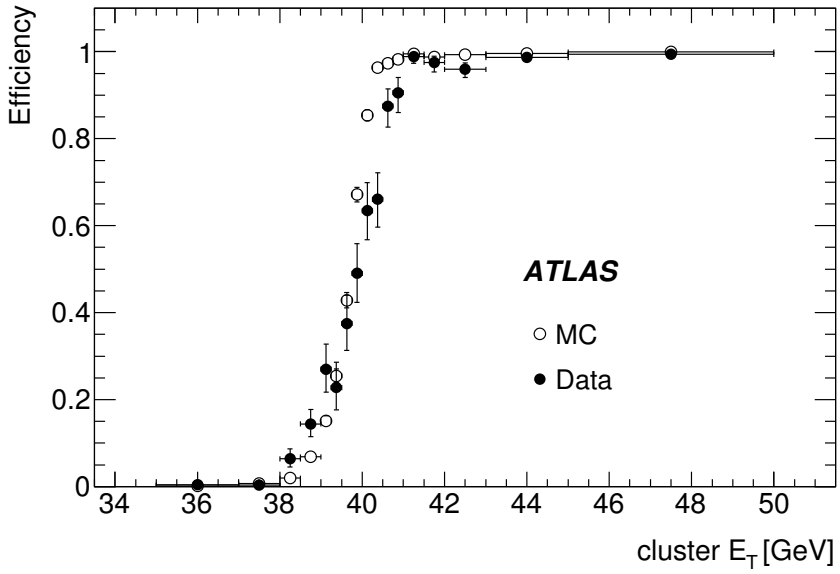

Figure B.1.: *Photon trigger efficiency with respect to the offline photon selection as measured in data (black dots) and MC (empty dots) for the g40_loose trigger, on photon candidates passing the tight identification criteria and with isolation energy lower than 3 GeV. From [49].*

	$\varepsilon^{\gamma}_{\rm rec}$ [%]			
E_T [GeV]	$\lvert\eta\rvert \in [0-0.6)$	$\lvert\eta\rvert \in [0.6-1.37)$	$\lvert\eta\rvert \in [1.52-1.81)$	$\lvert\eta\rvert \in [1.81-2.37)$
$[45,55)$	85.5 ± 0.2	86.9 ± 0.1	77.2 ± 0.3	78.6 ± 0.2
$[55,70)$	85.2 ± 0.2	86.6 ± 0.2	76.7 ± 0.4	78.0 ± 0.3
$[70,85)$	85.2 ± 0.3	86.1 ± 0.3	75.6 ± 0.6	77.4 ± 0.4
$[85,100)$	85.6 ± 0.2	85.5 ± 0.1	74.7 ± 0.3	76.1 ± 0.2
$[100,125)$	85.1 ± 0.2	85.9 ± 0.2	75.0 ± 0.3	76.6 ± 0.2
$[125,150)$	85.0 ± 0.3	85.2 ± 0.3	73.3 ± 0.6	75.0 ± 0.4
$[150,200)$	84.8 ± 0.4	84.2 ± 0.3	71.3 ± 0.7	74.4 ± 0.6
$[200,400)$	83.6 ± 0.2	83.4 ± 0.1	71.3 ± 0.3	73.7 ± 0.3

Table B.1.: *Isolated prompt photon reconstruction efficiency $\varepsilon^{\gamma}_{\rm rec}$ as a function of true photon $E_{\rm T}$ in four pseudorapidity intervals. The quoted errors are statistical only. From [49].*

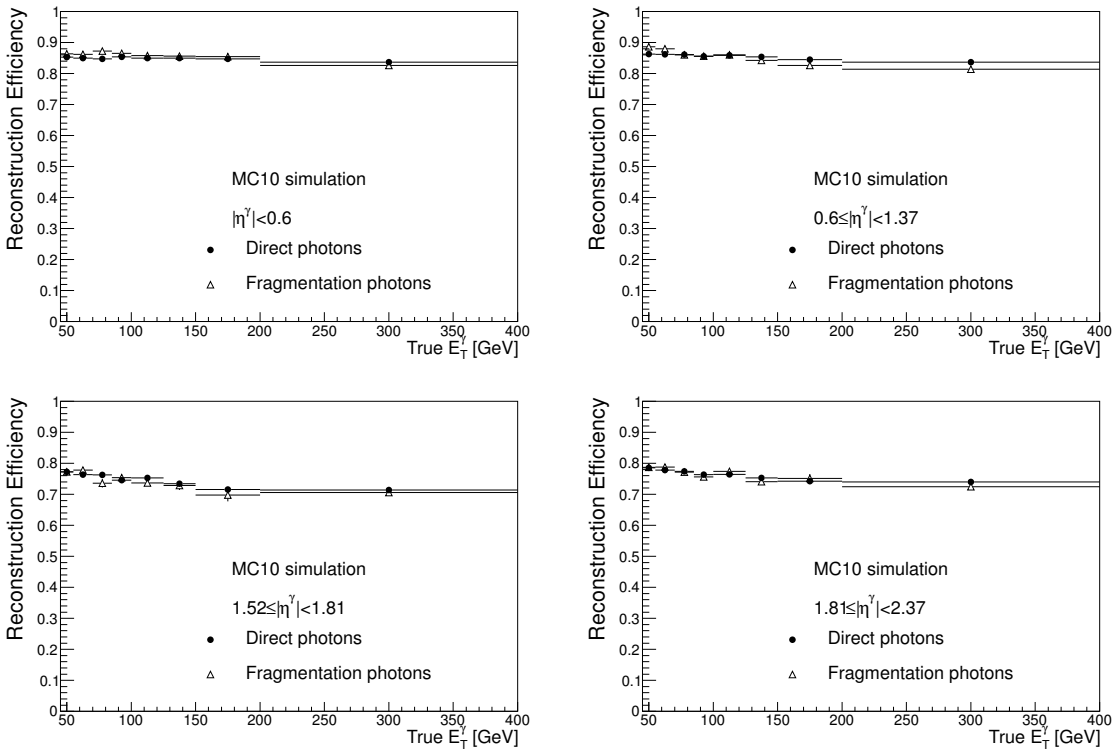

Figure B.2.: *$\varepsilon^{\gamma}_{\rm rec}$ plots corresponding to the results in Table B.1. From [49].*

	$\varepsilon_{\mathrm{id}}^{\gamma}$ [%]			
E_{T} [GeV]	$\lvert\eta\rvert \in [0-0.6)$	$\lvert\eta\rvert \in [0.6-1.37)$	$\lvert\eta\rvert \in [1.52-1.81)$	$\lvert\eta\rvert \in [1.81-2.37)$
$[45,55)$	91.3 ± 0.1	93.2 ± 0.1	93.0 ± 0.2	89.9 ± 0.2
$[55,70)$	93.1 ± 0.2	94.3 ± 0.1	94.4 ± 0.2	90.9 ± 0.2
$[70,85)$	93.6 ± 0.2	94.9 ± 0.2	94.8 ± 0.3	91.1 ± 0.3
$[85,100)$	94.6 ± 0.1	95.6 ± 0.1	95.8 ± 0.1	92.5 ± 0.1
$[100,125)$	94.7 ± 0.1	96.2 ± 0.1	96.0 ± 0.2	91.3 ± 0.2
$[125,150)$	95.1 ± 0.2	96.3 ± 0.1	95.0 ± 0.3	90.6 ± 0.3
$[150,200)$	94.7 ± 0.2	96.7 ± 0.2	96.7 ± 0.3	91.5 ± 0.4
$[200,400)$	95.2 ± 0.1	96.5 ± 0.1	97.0 ± 0.1	92.8 ± 0.1

Table B.2.: *Central values of the $\varepsilon_{\mathrm{id}}^{\gamma}$, after correcting the MC shower shapes to match those in data. These central values are computed for a mixture of direct and fragmentation photons from* PYTHIA. *The quoted errors are statistical only. From [49].*

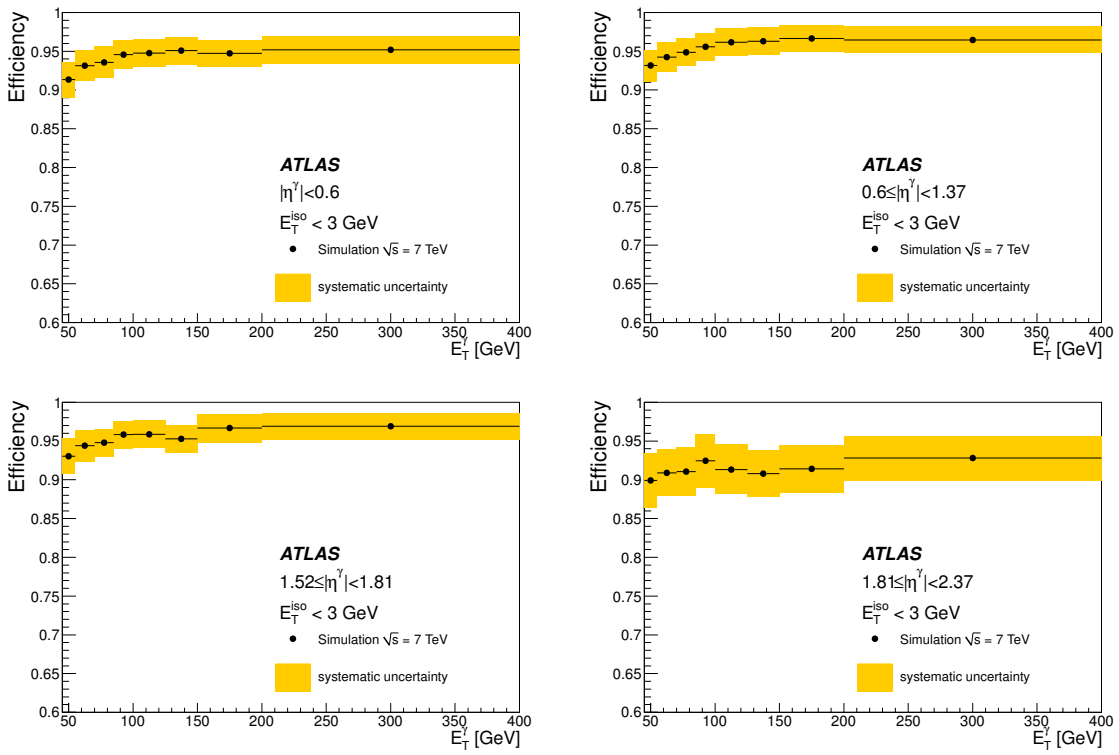

Figure B.3.: $\varepsilon_{\mathrm{id}}^{\gamma}$ *plots (as a function of the reconstructed photon E_{T}) for the results in Table B.2. From [49].*

B.3. Signal yield and Purity

Even with the great capabilities of ATLAS to reconstruct and identify photons, there is of course, some background contamination in the selected photon sample, mainly from "QCD jets" (π^0 decays). Photons from these jets are expected to be less isolated than prompt ones, so the isolation variable $E_{\mathrm{T}}^{\mathrm{iso}}$ is chosen as discriminating variable. The background contamination was estimated in this analysis using the "two-dimensional sidebands" (2D-sidebands) method, which uses the experimental shower shapes and $E_{\mathrm{T}}^{\mathrm{iso}}$ to define one signal region (**A**) and three control regions (**B, C** and **D**). The signal yield is then defined as,

$$N_{\mathbf{A}}^{\mathrm{sig}} = N_{\mathbf{A}}^{\mathrm{obs}} - N_{\mathbf{A}}^{\mathrm{bkg}} \tag{B.1}$$

The signal *purity* is defined as the signal yield from Equation (B.1) divided by the number of photon candidates in region **A**, which can also be re-expressed from the number of candidates seen in each region:

$$P = \frac{N_{\mathbf{A}}^{\mathrm{sig}}}{N_{\mathbf{A}}^{\mathrm{obs}}} = 1 - \frac{N_{\mathbf{B}}^{\mathrm{obs}} N_{\mathbf{C}}^{\mathrm{obs}}}{N_{\mathbf{A}}^{\mathrm{obs}} N_{\mathbf{D}}^{\mathrm{obs}}} \tag{B.2}$$

The obtained signal yield and corresponding purity are quoted, as functions of E_T and η, in Table B.3 and plotted as a function of E_{T} for the barrel η region in Figure B.4. The 2D-sidebands method assumes a negligible signal contamination in the control regions and that the shower shape variables and $E_{\mathrm{T}}^{\mathrm{iso}}$ are uncorrelated. Table B.3 and the example purity plots in Figure B.4 clearly show the background decreases with increasing photon E_{T}. This is to a large extent due to the isolation criteria, which is more efficient at large E_{T} where jets are more collimated and it becomes less likely that for example an high-energy π^0 remains isolated. This can also be appreciated in the $E_{\mathrm{T}}^{\mathrm{iso}}$ distributions in Figure B.5 where the background-enriched sample (non-tight candidates) extend to larger $E_{\mathrm{T}}^{\mathrm{iso}}$ values in the high E_{T} region compared to the signal-like (tight) candidates.

Another potential source of background is W boson events, where an electron from the W boson decay is misidentified as a photon. This background is, however, highly E_{T} dependent, due to the electron spectrum peaking approximately around $E_{\mathrm{T}} = m_W/2$, and is therefore expected to be small for high E_{T} photon events. The electron background was also found to be small in [49] and was hence neglected throughout the `ZfromGamma` analysis.

Signal yield				
E_{T} range [GeV]	$\lvert\eta^{\mathrm{s2}}\rvert \in [0.00; 0.60)$	$\lvert\eta^{\mathrm{s2}}\rvert \in [0.60; 1.37)$	$\lvert\eta^{\mathrm{s2}}\rvert \in (1.52; 1.81)$	$\lvert\eta^{\mathrm{s2}}\rvert \in [1.81; 2.37)$
$[45, 55)$	$22959 \pm 176^{+2092}_{-1686}$	$28146 \pm 215^{+3044}_{-2809}$	$10191 \pm 118^{+1304}_{-1336}$	$17017 \pm 172^{+2492}_{-2276}$
$[55, 70)$	$13629 \pm 131^{+1091}_{-887}$	$16082 \pm 154^{+1550}_{-1450}$	$5785 \pm 85^{+598}_{-700}$	$9722 \pm 126^{+1180}_{-1143}$
$[70, 85)$	$5052 \pm 77^{+351}_{-268}$	$6256 \pm 92^{+526}_{-540}$	$2210 \pm 51^{+166}_{-200}$	$3581 \pm 74^{+397}_{-391}$
$[85, 100)$	$2325 \pm 51^{+139}_{-114}$	$2746 \pm 57^{+201}_{-211}$	$916 \pm 32^{+88}_{-98}$	$1592 \pm 47^{+174}_{-159}$
$[100, 125)$	$1528 \pm 41^{+100}_{-74}$	$1896 \pm 47^{+131}_{-159}$	$594 \pm 25^{+42}_{-46}$	$991 \pm 36^{+101}_{-93}$
$[125, 150)$	$571 \pm 25^{+28}_{-25}$	$705 \pm 28^{+53}_{-51}$	$225 \pm 16^{+19}_{-22}$	$323 \pm 20^{+25}_{-21}$
$[150, 200)$	$361 \pm 20^{+21}_{-18}$	$399 \pm 21^{+35}_{-34}$	$135 \pm 12^{+14}_{-13}$	$205 \pm 16^{+17}_{-22}$
$[200, 400)$	$156 \pm 13^{+11}_{-11}$	$188 \pm 14^{+15}_{-24}$	$53 \pm 7^{+5}_{-7}$	$56 \pm 7^{+3}_{-3}$
Purity				
E_{T} range [GeV]	$\lvert\eta^{\mathrm{s2}}\rvert \in [0.00; 0.60)$	$\lvert\eta^{\mathrm{s2}}\rvert \in [0.60; 1.37)$	$\lvert\eta^{\mathrm{s2}}\rvert \in (1.52; 1.81)$	$\lvert\eta^{\mathrm{s2}}\rvert \in [1.81; 2.37)$
$[45, 55)$	$0.91^{+0.01+0.08}_{-0.01-0.06}$	$0.87^{+0.01+0.08}_{-0.01-0.07}$	$0.91^{+0.01+0.09}_{-0.01-0.10}$	$0.87^{+0.01+0.12}_{-0.01-0.11}$
$[55, 70)$	$0.93^{+0.01+0.06}_{-0.01-0.04}$	$0.90^{+0.01+0.07}_{-0.01-0.05}$	$0.94^{+0.02+0.06}_{-0.02-0.09}$	$0.89^{+0.01+0.10}_{-0.01-0.09}$
$[70, 85)$	$0.96^{+0.02+0.04}_{-0.02-0.04}$	$0.94^{+0.02+0.06}_{-0.02-0.05}$	$0.96^{+0.03+0.04}_{-0.03-0.05}$	$0.92^{+0.02+0.08}_{-0.02-0.09}$
$[85, 100)$	$0.97^{+0.03+0.03}_{-0.03-0.03}$	$0.97^{+0.03+0.03}_{-0.03-0.04}$	$0.97^{+0.03+0.03}_{-0.05-0.03}$	$0.93^{+0.04+0.07}_{-0.04-0.07}$
$[100, 125)$	$0.97^{+0.03+0.03}_{-0.04-0.03}$	$0.97^{+0.03+0.03}_{-0.03-0.04}$	$0.99^{+0.01+0.01}_{-0.06-0.02}$	$0.95^{+0.05+0.05}_{-0.05-0.07}$
$[125, 150)$	$0.98^{+0.02+0.02}_{-0.06-0.02}$	$0.99^{+0.01+0.01}_{-0.05-0.04}$	$0.98^{+0.02+0.02}_{-0.09-0.03}$	$0.97^{+0.03+0.03}_{-0.08-0.04}$
$[150, 200)$	$0.99^{+0.01+0.01}_{-0.07-0.03}$	$0.98^{+0.02+0.02}_{-0.07-0.04}$	$0.98^{+0.02+0.02}_{-0.12-0.03}$	$0.97^{+0.03+0.03}_{-0.10-0.06}$
$[200, 400)$	$1.00^{+0.00+0.00}_{-0.11-0.02}$	$0.98^{+0.02+0.02}_{-0.10-0.03}$	$1.00^{+0.00+0.00}_{-0.20-0.03}$	$1.00^{+0.00+0.00}_{-0.19-0.02}$

Table B.3.: *Signal yield and purity from the two-dimensional sidebands, for each $|\eta^{\mathrm{s2}}|$ region and E_{T} interval. The first error is statistical, the second systematic. From [49].*

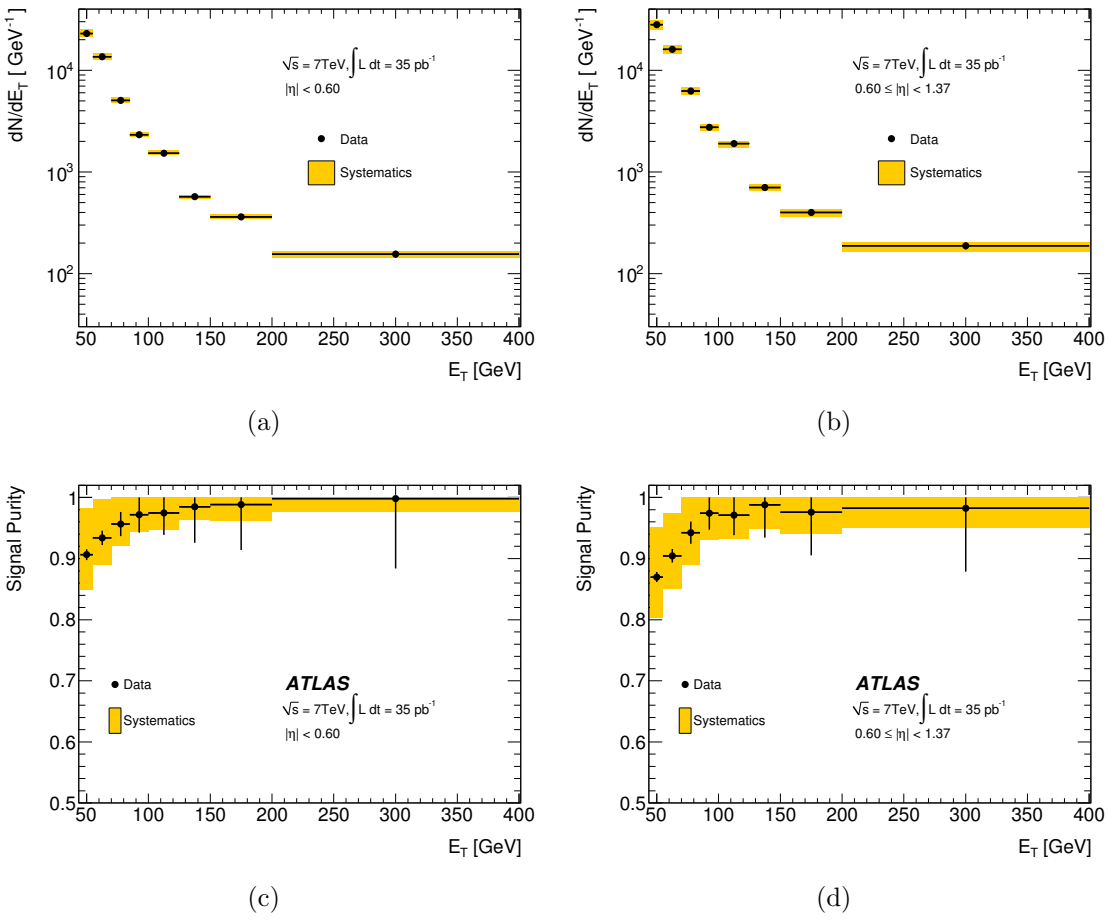

Figure B.4.: *Signal yield and corresponding purity with statistical errors as a function of* E_{T}*, for the barrel region region, as determined from the two-dimensional sidebands method in [49]. The yellow band represents the total systematic error. From [49].*

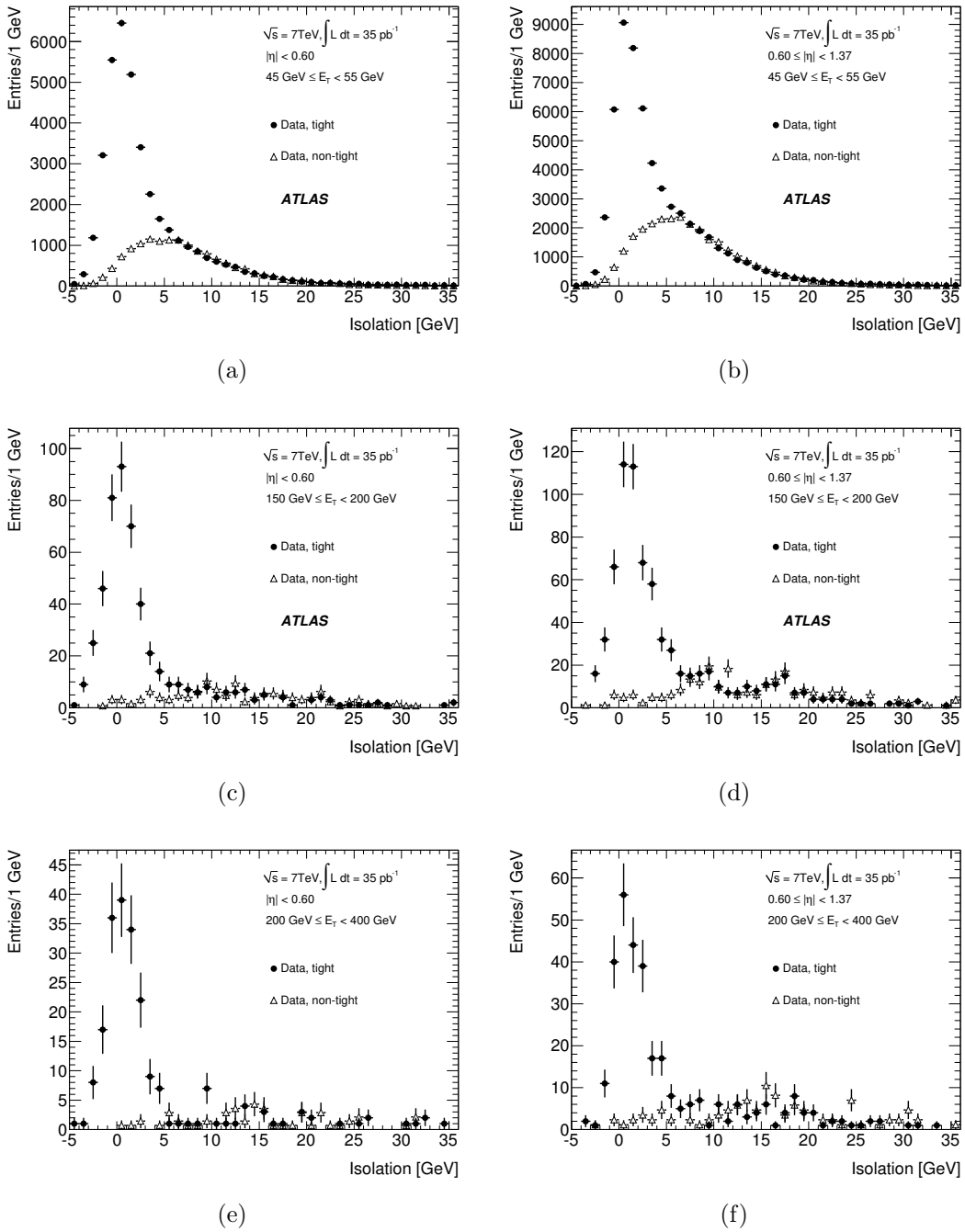

Figure B.5.: *The distributions for the calorimetric isolation variable $E_{\mathrm{T}}^{\mathrm{iso}}$, for tight (solid dots) and non-tight (open triangles) candidates in the barrel region (left column refers to $|\eta| < 0.6$, right column to $0.6 < |\eta| < 1.37$). Top to bottom rows means from low to high E_{T} (45 to 200 GeV). The non-tight distribution is normalized to the tight for $E_{\mathrm{T}}^{\mathrm{iso}} > 5$ GeV (non-isolated region). From [49].*

Appendix C.

Results from Previous Analyses

The aim of this appendix is to show some `ZfromGamma` results from previous analysis rounds (prior to Moriond'12) that are not provided in Chapter 5. The analyses will be presented as sub-sections in chronological order: Moriond'11, PLHC'11 and EPS'11. The structure/sectioning will be the same as in Chapter 5 and, unless otherwise stated, the general concepts discussed in the main sections apply to all these analyses.

As mentioned in the introduction of Chapter 5, the author produced most of the `ZfromGamma`-related results presented in the following sections, including the R&D that was required for the production of MC samples listed. With respect to the 0ℓ analysis, the author performed most of the work to obtain the CR1a-related results, except for the results presented in the sections titled "Context within the 0ℓ analysis" which concerns the CR1a implementation into the 0ℓ likelihood function, final background fitting and use for setting limits on SUSY models. All the results and plots showed from the other 0ℓ CRs and SRs were done by other members from the 0ℓ group in ATLAS.

C.1. Moriond'11 (35 pb^{-1})

This analysis corresponds to the first attempt to implement the `ZfromGamma` method for the first publication of the 0ℓ analysis [58]. The first documentation of the `ZfromGamma` method therefore appears in the 0ℓ supporting documentation, found in [63]. Overall, these first `ZfromGamma` results were promising in the sense that the data showed reasonably good agreement with *some* of the MC predictions; on the other hand, the MC samples used at the time were very limited and not very suited for this purpose (*e.g.* few generators and small statistics available, in particular after the 0ℓ high-p_{T} selections) and also many

aspects of the method were still in early developments. This was in fact a common trend of all the data-driven background estimation methods then, so within the 0ℓ analysis, the results were used only to validate the MC predictions and constrain some uncertainties. Because `ZfromGamma` was at the forefront of photon analyses in ATLAS at the time, the required $\gamma + X$ sample faced new issues which had not been covered by the SMDP analysis then [48], such as the increase in luminosity (35 pb^{-1} versus 0.880 pb^{-1}) and pileup conditions, a higher photon-p_{T} selection, and jet selections (the analysis in [48] was only inclusive), photon-jet overlap removal (see Section 5.4), the use of reconstructed $E_{\mathrm{T}}^{\mathrm{miss}}$ in photon events, etc.

C.1.1. Framework

The framework used in this analysis is specified in Section 5.1 and Table 5.1.

C.1.2. Event Samples

Data: The data was in `SUSYD3PD` format and included 2010 data periods A-I, amounting to $\int \mathscr{L} \mathrm{d}t \sim 35$ fb^{-1} after applying the Moriond'11 0ℓ GRL (see Table 5.2). The data streams used are listed in Table C.1.

Data Period	Data Stream
A-D	L1Calo
E-I	Egamma

Table C.1.: *Data streams used in the Moriond'11 analysis.*

Monte Carlo: The MC samples available for this analysis are listed in Tables C.2-C.4 and the production details in Table 5.7. The `ALPGEN` signal samples had a 2-jet filter applied at generator level, making them useful only after the 0ℓ "Dijet selection" had been applied (see Section C.1.4). The `PYTHIA` QCD sample contained fake photon candidates (*e.g.* π^0 and η decays) as well as prompt photon signal (*e.g.* produced by QED radiation emitted from quarks and by parton fragmentation). Another `PYTHIA` sample contained prompt photon signal from hard γ-jet scattering contributions (*e.g.* $q\bar{q} \to g\gamma$ or $qg \to q\gamma$).

Regarding matching data conditions, at the time of Moriond'11 the inclusion of a pileup component had only been implemented in a few samples (see Table 5.7); in this case, only for the `ALPGEN` samples, and also there was no official pileup reweighing tool like in the later analyses. Nevertheless, pileup effects were found to have negligible effects in this dataset for the 0ℓ analysis and `ZfromGamma` [63].

Sample ID	Name	Cross Section [pb]	Filter Eff.	k-factor	N_{gen}
108081	PythiaPhotonJet_Unbinned35	$1.7305 \cdot 10^{+4}$	0.60450	1.000	1998486
116390	AlpgenJimmyGamNp1_JetFilter_Nj2Et20	$7.4139 \cdot 10^{+4}$	0.10870	1.000	199718
116391	AlpgenJimmyGamNp2_JetFilter_Nj2Et20	$2.1474 \cdot 10^{+4}$	0.30995	1.000	199896
116392	AlpgenJimmyGamNp3_JetFilter_Nj2Et20	$5.8390 \cdot 10^{+3}$	0.46646	1.000	199848
116393	AlpgenJimmyGamNp4_JetFilter_Nj2Et20	$1.6224 \cdot 10^{+3}$	0.65008	1.000	199766

Table C.2.: *Moriond'11 Monte Carlo samples used to simulate the γ + jets signal, including cross section times filter efficiency, k-factor and the number of generated events in the sample.*

Sample ID	Name	Cross Section [pb]	Filter Eff.	k-factor	N_{gen}
105807	JF35_pythia_jet_filter	$5.4969 \cdot 10^{+7}$	1.000	1.000	4583202

Table C.3.: *Moriond'11 Monte Carlo samples used to simulate the SM background to the γ + jets signal from QCD, including cross section times filter efficiency, k-factor and the number of generated events in the sample.*

Sample ID	Name	Cross Section [pb]	Filter Eff.	k-factor	N_{gen}
115112	PythiaZnunuJet_Pt20	$1.2490 \cdot 10^{+3}$	1.0	1.000	49890
107710	AlpgenJimmyZnunuNp0_pt20_filt1jet	$3.5407 \cdot 10^{+3}$	$7.924433 \cdot 10^{-3}$	1.000	2999
107711	AlpgenJimmyZnunuNp1_pt20_filt1jet	$7.0170 \cdot 10^{+2}$	0.6112469	1.000	44487
107712	AlpgenJimmyZnunuNp2_pt20_filt1jet	$2.1700 \cdot 10^{+2}$	0.8896797	1.000	39491
107713	AlpgenJimmyZnunuNp3_pt20_filt1jet	$6.0160 \cdot 10^{+1}$	0.9689922	1.000	11995
107714	AlpgenJimmyZnunuNp4_pt20_filt1jet	$1.4640 \cdot 10^{+1}$	0.9900990	1.000	7993
107715	AlpgenJimmyZnunuNp5_pt20_filt1jet	$4.7100 \cdot 10^{+0}$	0.998004	1.000	2500

Table C.4.: *Moriond'11 Monte Carlo samples used to simulate the $Z_{\nu\nu}$ + jets signal, including cross section times filter efficiency, k-factor and the number of generated events in the sample.*

C.1.3. Inclusive Photon Sample ($\gamma + X$)

Event Selection: A combined and more technical version of Tables 5.8 and 5.9 for Moriond'11 is shown in Table C.5. It can be seen that the selection was the same as in the SMDP 880 nb^{-1} analysis [48], with the exception of the items highlighted in bold, which were added in order to include all the data periods used in the 0ℓ analysis (A-I). This was acceptable given the higher photon p_{T} cut set in `ZfromGamma` compared to [48], ensuring unprescaled triggers with $\sim 100\%$ efficiency. More clearly seen in Tables 5.8, the main difference in selection with respect to the later analyses was the smaller photon acceptance ($|\eta| < 1.81$, see Appendix B). The larger acceptance used in the later analyses therefore helped to reduce the required acceptance correction, entering the method through $A^{\gamma} \cdot \varepsilon^{\gamma}$ in Equation (5.8), shown in Table 5.17.

Requirement	Data	MC
Preselection		
GRL	**0ℓ GRL**	none
Trigger	`g10_loose` (A-E4 except 160975) **g20_loose (E5-F2 including 160975)** **g40_loose (G-I)**	`g10_loose`
Primary Vertex	At least 1 primary vertex with $\geq$3 tracks	same as in Data
Acceptance	$\lvert\eta^{\gamma}\rvert < 1.37$ or $1.52 \leq \lvert\eta^{\gamma}\rvert 1.81$ (η^{γ} = `ph_etas2`) **$p_{\mathrm{T}} > 45$ GeV (p_{T} = `ph_cl_pt`)**	"
Object Quality	`egamma::checkOQCluster` `Photon(run,ph_cl_eta,ph_cl_phi)` < 3	**OQmap (period I)**
Identification & Isolation		
Robust-Tight	`PhotonIDTool::PhotonCutsTight(3)`	same as in Data
Isolation	`ph_Etcone40_corrected` < 3 GeV	"

Table C.5.: *Moriond'11 event selection for the $\gamma + X$ sample. The selection is identical to [48, 114] except for the highlighted items.*

Results: The cutflow obtained for the $\gamma + X$ selection is shown in Table 5.10, which was validated with the SMDP group results quoted in [114]. For all the plots in this section, the MC is from the `PYTHIA` samples listed in Section C.1.2 (the `ALPGEN` signal samples were not used at this stage due to the 2-jet filter already discussed). The $\gamma +$ jets signal is normalised to the data luminosity and cross-section while the QCD background is normalised so that the sum of signal and background match the data.

The corresponding p_{T}, $|\eta|$, ϕ and shower shape distributions of the prompt-photon candidates passing the $\gamma + X$ selection (Table C.2) are shown in Figures 5.3(b), C.1 and C.3 respectively. As a consistency check, for photon $p_{\mathrm{T}} > 50$ GeV in Figure 5.3(b), there are 80 730 candidates, which is comparable to the number quoted in [48] for the same luminosity ($\sim$ 69 563), considering the SMDP number is after subtracting the background. As for the shower shape distributions, these were also consistent with the SMDP group equivalent found in [115] (the definitions of the shower shape variables can be found in [115] or [48]). The leading jet p_{T} distribution for this $\gamma + X$ sample is shown in Figure C.2.

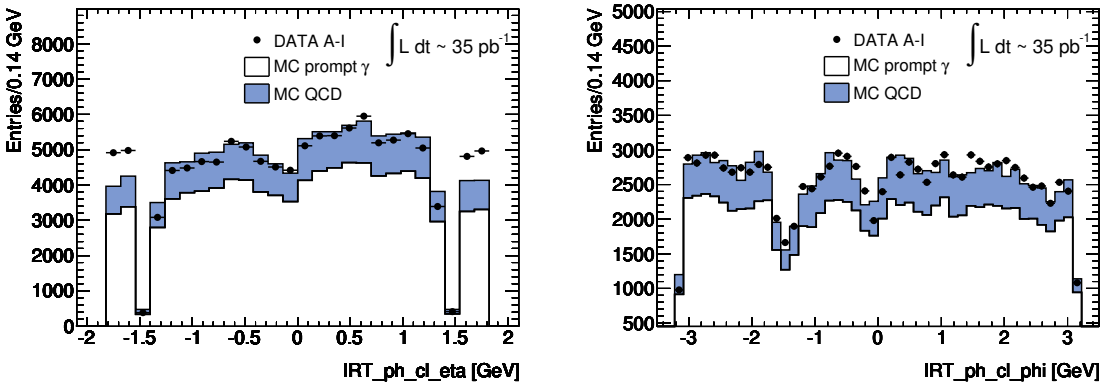

(a) (b)

Figure C.1.: *(a) Moriond'11 $|\eta|$ and (b) ϕ distributions for the prompt photon candidates in the $\gamma + X$ sample (Figure 5.3(b)).*

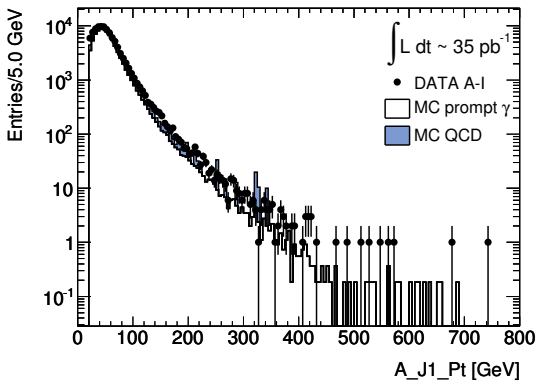

Figure C.2.: *Moriond'11 leading jet p_{T} distribution in the $\gamma + X$ sample.*

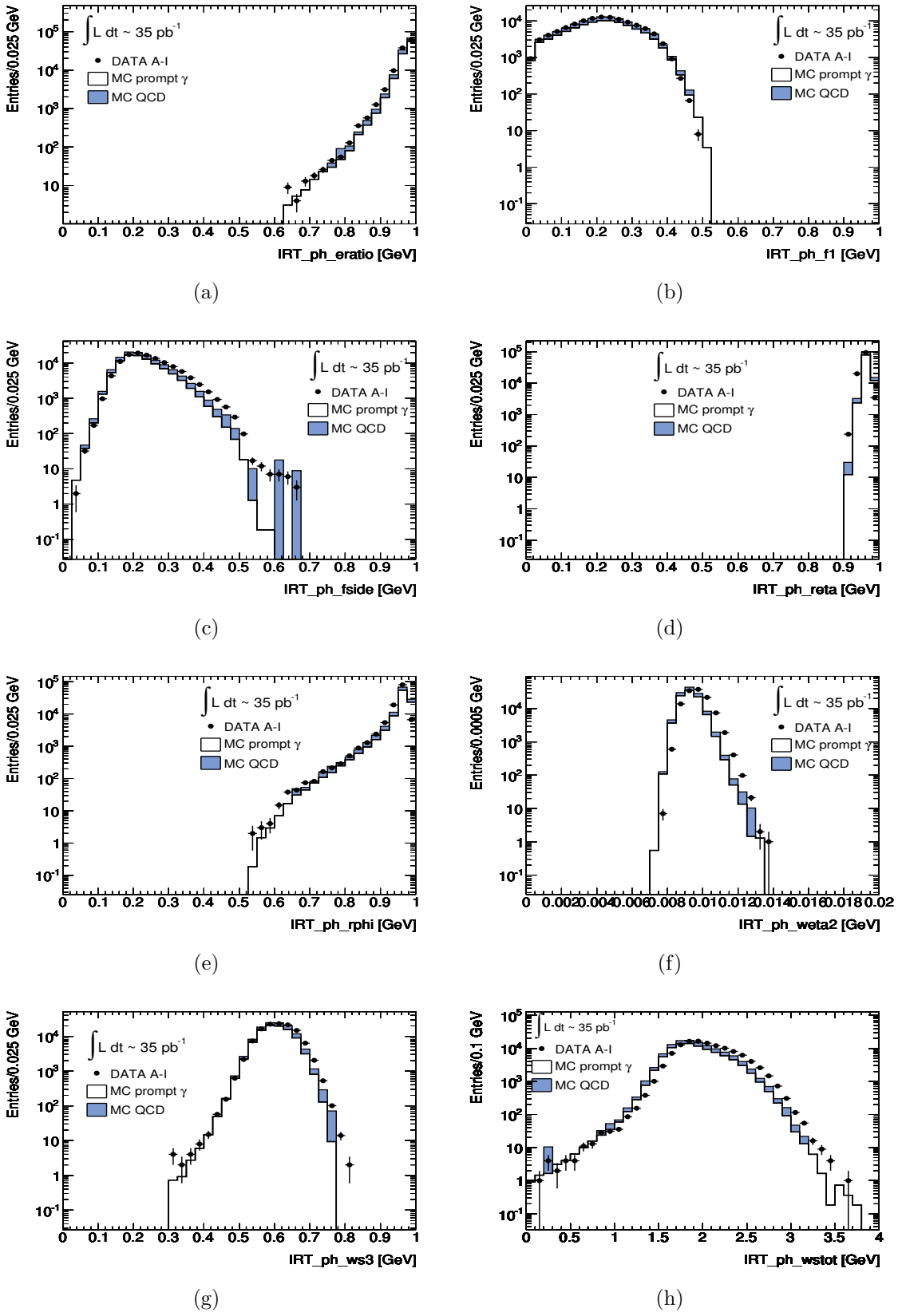

Figure C.3.: *Moriond'11 distributions of shower shape variables used in the "Robust-Tight" photon identification (Table C.5) for the prompt photon candidates in the $\gamma + X$ sample.*

C.1.4. Control Region Sample (CR1a)

CR1a object definition: This is specified in Section 5.4.1.

0ℓ Selection: Having applied the CR1a object definitions (Section 5.4) and 0ℓ object definitions in [63], the 0ℓ event selection applied is summarised in Table C.6 (a more detailed version can be found in [63]). Four signal regions A, B, C and D were defined (targeting light-$\tilde{q}\tilde{q}$, heavy-$\tilde{q}\tilde{q}$, $\tilde{g}\tilde{g}$ and $\tilde{g}\tilde{q}$ production, respectively). The "Pre-selection" without the $E_{\mathrm{T}}^{\mathrm{miss}}$ requirement defined in this case the Control Region (CR). The motivation for this was that the statistics in this CR were much larger that in the SR and hence a more precise cross-check between the data and MC could be made.

		A	B	C	D
Pre-selection	Number of required jets	≥ 2	≥ 2	≥ 3	≥ 3
	Leading jet p_{T} [GeV]	> 120	> 120	> 120	> 120
	Other jet(s) p_{T} [GeV]	> 40	> 40	> 40	> 40
	$E_{\mathrm{T}}^{\mathrm{miss}}$ [GeV]	> 100	> 100	> 100	> 100
Final selection	$\Delta\phi(\mathrm{jet}, E_{\mathrm{T}}^{\mathrm{miss}})_{\mathrm{min}}$	> 0.4	> 0.4	> 0.4	> 0.4
	$E_{\mathrm{T}}^{\mathrm{miss}}/m_{\mathrm{eff}}$	> 0.3	–	> 0.25	> 0.25
	m_{eff} [GeV]	> 500	–	> 500	> 1000
	m_{T2} [GeV]	–	> 300	–	–

Table C.6.: *Moriond'11 Criteria for admission to each of the four overlapping Signal Regions A to D. All variables are defined in [58].*

Results: For this part, some relevant results have been discussed in Section 5.4. Once the full CR1a selection is applied on the $\gamma + X$ sample, the remaining background is quite small, as shown in Figure 5.3(b) by the good agreement of data with MC signal. For this reason (as well as for the lack of suitable high-p_{T} background samples during this time), the plots that follow only show the $\gamma +$ jets MC signal from `PYTHIA` and `ALPGEN` (the latter only if a ≥ 2 jet selection has been applied) and the normalisation is to the data luminosity and cross-section. Figure C.4 shows the evolution with the 0ℓ selections (up to the CR stage, known as the "Dijet selection", see above) for channels A and C of $p_{\mathrm{T}}(\gamma_1)$ and the redefined $E_{\mathrm{T}}^{\mathrm{miss}} = p_{\mathrm{T}}(\gamma_1) + \not{E}_{\mathrm{T}}^{\mathrm{fake}\prime}$ (the latter being like a *smeared* version of $p_{\mathrm{T}}(\gamma_1)$, see Equations 5.1-5.3). Figures C.4(a)-C.4(b) show a very good agreement between data and the `PYTHIA` signal already at the $\gamma + X$ selection stage – a confirmation

that the background left is small. However, Figures C.4(c)-C.4(d) show that once the dijet selection is applied, a discrepancy between data and the PYTHIA signal becomes evident at low-p_{T}. In contrast, the ALPGEN signal does not suffer from this problem. Given that the data-PYTHIA discrepancy was found to be mitigated at higher photon-p_{T} and lower jet multiplicities, it was thought to be due to missing multijet events in PYTHIA. To further support this, a similar trend is observed for the leading jet-p_{T}, shown in Figure C.5, where in this case, the data-PYTHIA discrepancy is significant even before the dijet selection (Figure C.5(a)), and appears to grow with increasing p_{T} (contrary to the case of $p_{\mathrm{T}}(\gamma_1)$). Moreover, Figure C.2, which is equivalent to Figure C.5(a) but without including the QCD MC, further confirms that such discrepancy cannot be due to QCD background remnants but rather to the suspected missing multijet events in the PYTHIA signal. Figure C.4(e) shows the final CR1a $p_{\mathrm{T}}(\gamma_1)$ distribution for SR-A. In this case, the data-PYTHIA signal agreement is restored given the high $p_{\mathrm{T}}(\gamma_1)$ involved, *e.g.* see Table 5.16. The number of CR1a data events for each SR is shown in Table C.7 (column 3). In summary, the lack of multijet events was understood and was not because of problems with the PYTHIA model. Roughly speaking, the PYTHIA sample only contains events with $p_{\mathrm{T}}(j_2) < p_{\mathrm{T}}(\gamma)$, and the observed effect is due to the lack of events with the opposite p_{T} configuration. Such events should be produced by the dijet processes, with a photon produced by the parton shower, however, this contribution was not available statistically enough for this analysis.

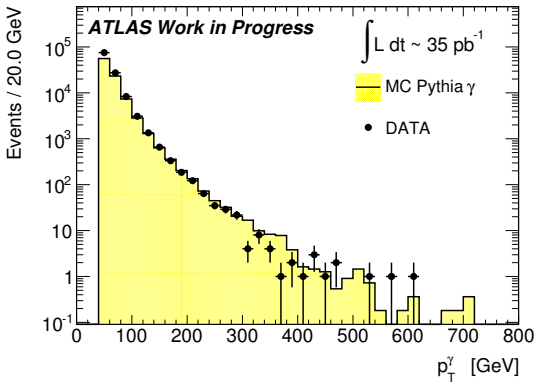

(a)

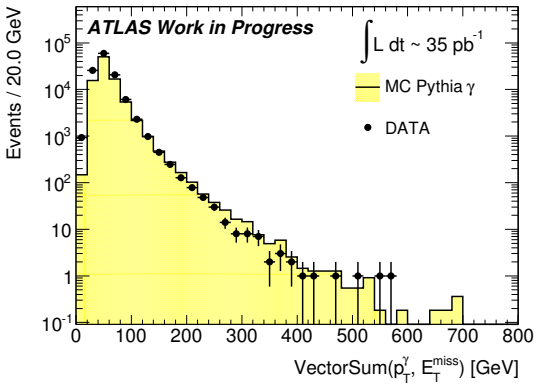

(b)

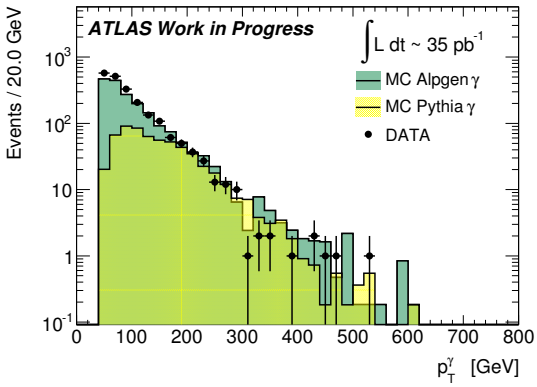

(c)

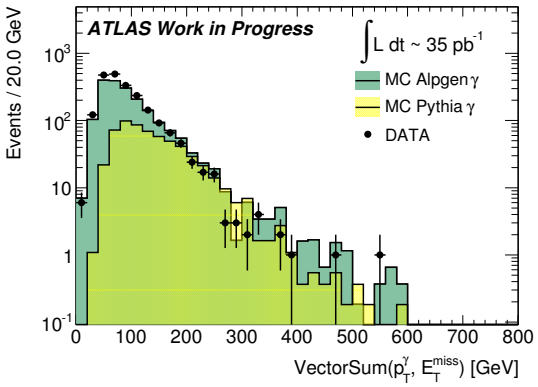

(d)

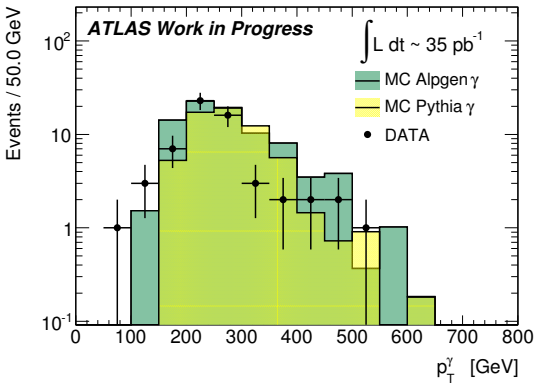

(e)

Figure C.4.: *Moriond'11 Left:* $p_{\mathrm{T}}(\gamma_1)$ *distribution for (a) the* $\gamma + X$ *sample, (c)* $\gamma + X$ *sample after the* 0ℓ *dijet selection and (e) after the full* 0ℓ *selection for SR-A. Right: The same distributions as on the left but after adding* $\not{E}_{\mathrm{T}}^{\mathrm{fake}\prime}$ *(see Section 5.4.1). The MC shown is the* `PYTHIA` *and* `ALPGEN` *signal.*

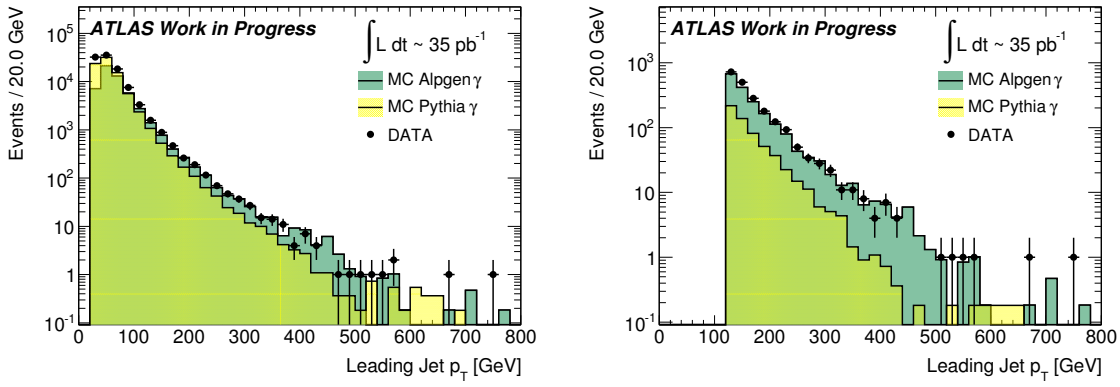

(a) (b)

Figure C.5.: *Moriond'11 Leading jet p_{T} distribution for (a) the $\gamma + X$ sample and (b) the $\gamma + X$ sample after the 0ℓ dijet selection. (a) is the same as Figure C.2 but without including the QCD MC.*

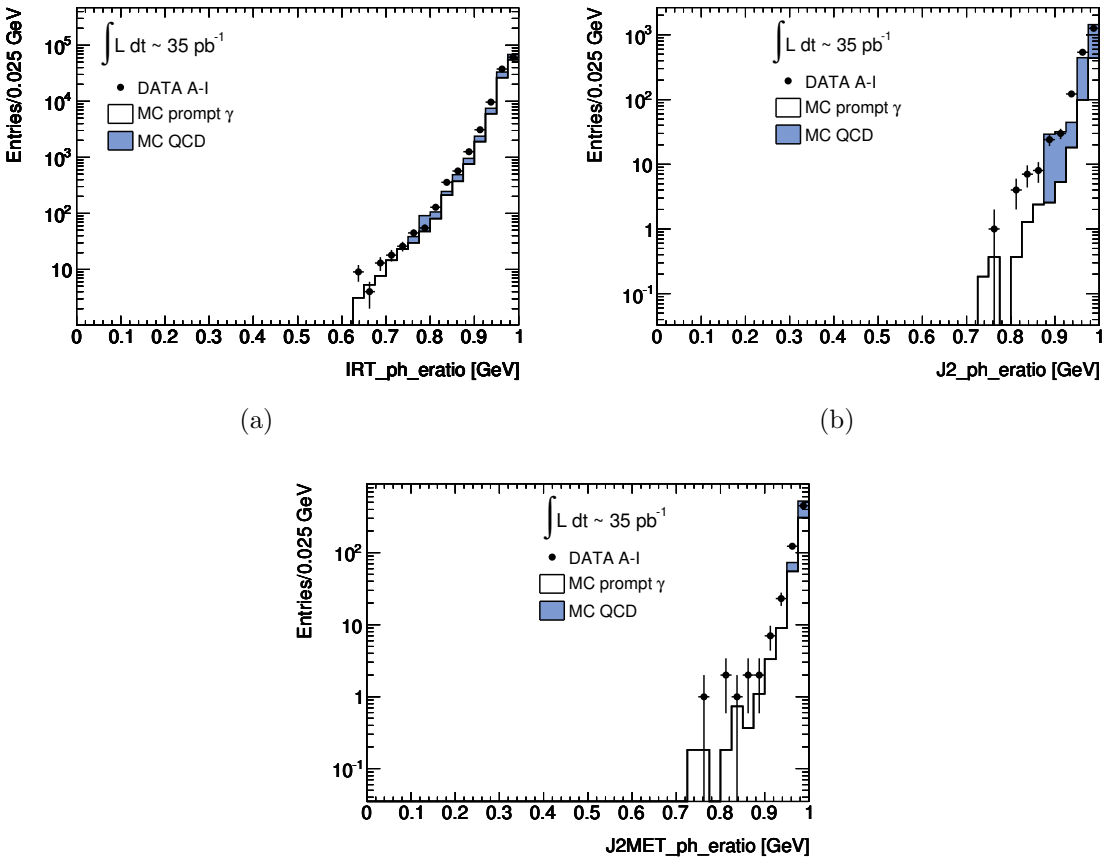

(a) (b)

(c)

Figure C.6.: *Moriond'11 Effect of* 0ℓ *selections on* E_{ratio} *– a shower shape variable used to make the photon identification. The plots show a beneficial impact on* $\varepsilon_{\mathrm{id}}^{\gamma}$ *since slightly higher values are expected from the narrower shape. (a)* $\gamma + X$ *sample; (b)* $\gamma + X$ *sample with* 0ℓ *Dijet selection and (c)* $\gamma + X$ *sample with* 0ℓ *Dijet and* $E_{\mathrm{T}}^{\mathrm{miss}}$ *selections. The MC shown is from* PYTHIA.

C.1.5. Transfer Function ($\mathbf{TF}_{Z_{\nu\nu}}$)

Unlike in the current implementation of the method, where the $A^{\gamma}(p_{\mathrm{T}}) \cdot \varepsilon^{\gamma}(p_{\mathrm{T}})$ and $R_{Z/\gamma}$ factors in the TF (Equation (5.6)) are obtained from prompt photon MC, during this time these values had to be obtained by other means because, as already emphasised, the prompt photon MC samples available then were not suited for such purposes.

- **Efficiency and Acceptance:** A separate value for efficiency and acceptance had to be estimated (unlike the current implementation where the combined $A^{\gamma}(p_{\mathrm{T}}) \cdot \varepsilon^{\gamma}(p_{\mathrm{T}})$ value is obtained).

  For the reasons already discussed in Sections 5.4.3 and 5.5.1, an overall efficiency value ε^{γ} was estimated from the SMDP prompt photon results in [48] as a p_{T}-η weighted-average of $\varepsilon^{\gamma}_{\mathrm{rec}} \cdot \varepsilon^{\gamma}_{\mathrm{id}}$, resulting in a fixed value of $\sim 80\%$. To further support this procedure (and as complement to the discussion of Figure 5.8) the evolution of another shower shape variable E_{ratio} (the asymmetry between the first and second maxima in the energy profile along η in the ATLAS ECAL) used for the photon ID requirement in Table C.5 is shown in Figure C.6. Again the 0ℓ selections reassure the $\varepsilon^{\gamma}_{\mathrm{id}}$ value from SMDP results can be used on the final CR1a sample as a conservative value.

  Regarding the acceptance correction A^{γ}, as discussed, given that the γ and $Z_{\nu\nu}$ η distributions converge at high-p_{T} (Figure 5.15), this correction is only to counteract the effect of the $\gamma + X$ selection in the SRs, which the $Z_{\nu\nu}$ is not subjected to. Hence, A^{γ} was calculated as the fraction in Figure 5.15 that fell outside the η range considered in the $\gamma + X$ selection. The result was cross-checked with the ratio of the $p_{\mathrm{T}}(\gamma_1)$ distributions in CR1a with and without the $\gamma + X$ selection step (see Equation (5.8)). The average value obtained was $\sim 75\%$.

- **Purity:** The value was also taken from the SMDP prompt photon results in [48] as a p_{T}-η weighted-average resulting in a fixed value of $\sim 90\%$.

- ***Z*/γ Ratio:** The value taken was from the then available result from `GAMBOS`, which at the time did not account for the variation in jet multiplicity.

TF stand-alone estimate of $Z_{\nu\nu}$ + jets: After the direct application of the TF to the CR1a event counts, the $Z_{\nu\nu}$ + jets background estimate results obtained for this analysis are shown in Table C.7 compared to `PYTHIA` and `ALPGEN`[1]. Despite the missing multijet events in `PYTHIA` discussed in Section C.1.4, this effect is mitigated in the SRs where only the high-p_{T} photon events are selected, and in particular SR-A which has the lowest jet multiplicity. Indeed, the results show that the data was consistent with `PYTHIA`. However, at this stage a data-`ALPGEN` discrepancy is observed (the MC statistical uncertainty is not shown but can be assumed to be smaller and the luminosity uncertainty was $\sim 11\%$). This data-`ALPGEN` discrepancy was investigated further and it was found to appear after the m_{eff} cut (the last cut in the 0ℓ selection). As an example, for the dijet channel (the one with the highest statistics), after the "Preselection" (see Table C.6), the `ALPGEN` result was 679 vs 657 ± 26 in data, whereas with the full selection, the discrepancy became larger (85 vs 60 ± 8). The corresponding distributions for these results are shown in Figure C.7 in the form of an estimated $Z_{\nu\nu}$ + jets $E_{\mathrm{T}}^{\mathrm{miss}}$ distribution for SRs A, C and D compared directly with the $Z_{\nu\nu}$ + jets signal (note that in the later analysis rounds, this kind of plots are show as a function of m_{eff} rather than $E_{\mathrm{T}}^{\mathrm{miss}}$). Due to the fixed value of photon efficiency used, this estimate should be more precise for $E_{\mathrm{T}}^{\mathrm{miss}} \gtrsim 100$ GeV. The integral of these distributions represents the number of $Z_{\nu\nu}$ + jets events quoted in columns 5 and 6 of Table C.7.

SR	m_{eff}	CR1a		$Z_{\nu\nu}$ + jets Estimate		$Z_{\nu\nu}$ + jets Signal
		data	Pythia/Alpgen	data	Pythia/Alpgen	Pythia/Alpgen
A	500	60	63.4 / 85.6	22 ± 5	26 ± 4 / 34	24 / 45
C	500	39	24.4 / 47.4	13 ± 4	10 ± 1 / 18	10 / 25
D	1000	1	0.6 / 3.8	0.5	0.3 / 1.8	0.0 / 0.8

Table C.7.: *Moriond'11 numbers of CR1a events from data and MC for each SR (columns 3-4) and the stand-alone estimate of $Z_{\nu\nu}$ + jets background in the SRs from data and MC (columns 5-6), compared to $Z_{\nu\nu}$ + jets MC (column 7). The MC statistical uncertainty is not shown but can be assumed to be small. The luminosity uncertainty was then $\sim 11\%$.*

[1]The results for SR-B are not shown because at the time the code to calculate the m_{T2} variable in Table C.6 had not been implemented in the `ZfromGamma` framework.

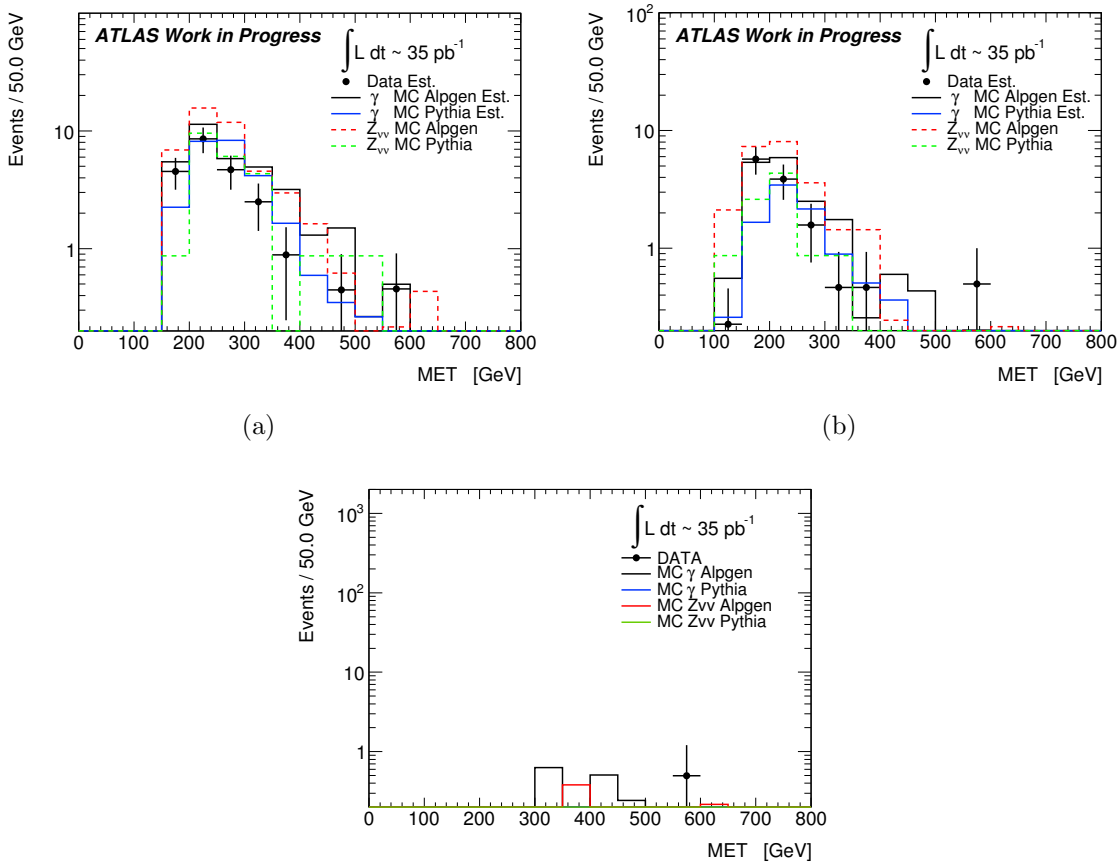

Figure C.7.: *Moriond'11 $Z_{\nu\nu}$ + jets $E_{\mathrm{T}}^{\mathrm{miss}}$ distributions in (a) SR-A, (b) SR-C, and (c) SR-D, from data and MC as estimated from CR1a using the TF, compared directly with $Z_{\nu\nu}$ + jets MC from* `PYTHIA` *and* `ALPGEN`*. The labels 'Data' and 'MC γ Alpgen/Pythia' indicate the TFs were applied to the CR1a data or MC events, whereas those labeled '$Z_{\nu\nu}$ + jets Alpgen/Pythia' show the raw MC $Z_{\nu\nu}$ + jets estimates for the SRs scaled to the data luminosity.*

C.1.6. Context within the 0ℓ analysis

Having been the first SUSY 0ℓ analysis with ATLAS data, data-driven background estimation methods were in early developments at the time. Hence, the results from these methods were used only to validate the MC prediction and constrain some uncertainties, but the central value for the background estimate was taken from MC as shown in the 0ℓ SRs m_{eff} distributions in Figure C.8 and represented numerically in Table C.8. From these, it was clear that the Z + jets and W + jets were the most dominant backgrounds, which further motivated the developments of the data-driven methods to estimate them, such as `ZfromGamma`. Similarly, this was also the first implementation of the `ZfromGamma` method and as mentioned, data-`ALPGEN` discrepancies had been found. At the time, CR1b was found more consistent with the $Z_{\nu\nu}$ + jets `ALPGEN` result and there were also published ATLAS W/Z results supporting the good agreement of data with `ALPGEN` [59]. This therefore motivated additional cross-checks of the method, like the '$Z_{\mu\mu}$ cross-check' described in Appendix D.1.

In the end, the 0ℓ results (Table C.8) were used to make the two interpretations shown in Figure C.9 (in a simplified and a constrained mSUGRA model, briefly explained in Section 5.6 and Section 1.2.2).

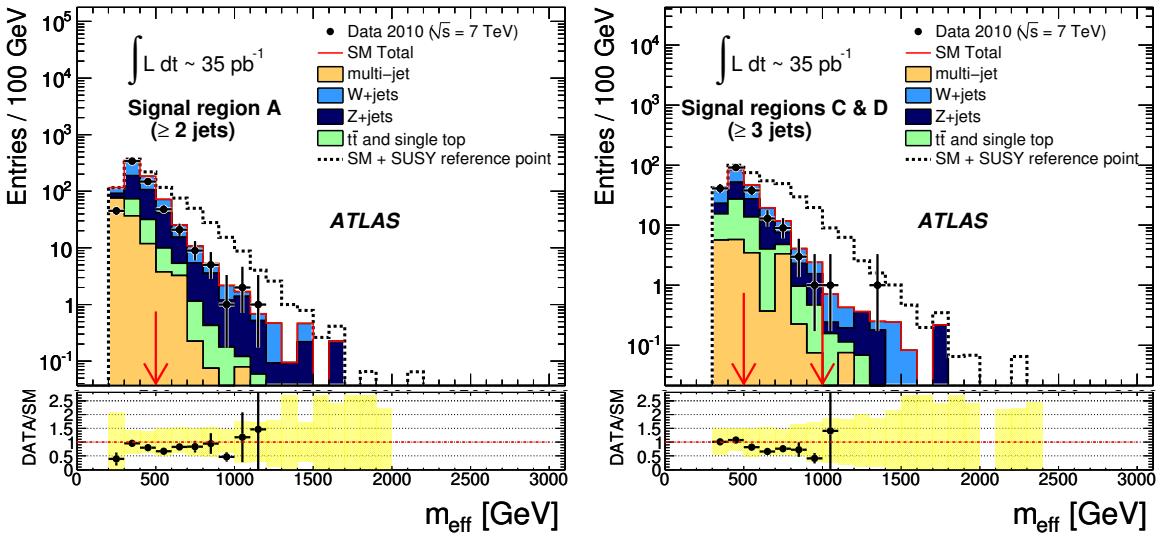

Figure C.8.: *Moriond'11 m_{eff} distribution for channels A and C/D prior to the m_{eff} cut (red arrows mark the start of a SR), in data and MC (W/Z + jets is from* `ALPGEN`*, $t\bar{t}$ and single top from* `MC@NLO` *and QCD from* `PYTHIA`*) and a mSUGRA reference point with $m_0 = 200$ GeV, $m_{1/2} = 190$ GeV, $A_0 = 0$, $\tan\beta = 3$ and $\mu > 0$. Black vertical bars show the statistical uncertainty from the data, while the yellow band shows the size of the SM MC uncertainty. From [58].*

	Signal region A	Signal region B	Signal region C	Signal region D
QCD	$7\ ^{+8}_{-7}$[u+j]	$0.6\ ^{+0.7}_{-0.6}$[u+j]	$9\ ^{+10}_{-9}$[u+j]	$0.2\ ^{+0.4}_{-0.2}$[u+j]
W+jets	50 ± 11[u] $^{+14}_{-10}$[j] $\pm$ 5[$\mathcal{L}$]	4.4 ± 3.2[u] $^{+1.5}_{-0.8}$[j] ± 0.5[$\mathcal{L}$]	$35 \pm$ 9[u] $^{+10}_{-\ 8}$[j] $\pm$ 4[$\mathcal{L}$]	1.1 ± 0.7[u] $^{+0.2}_{-0.3}$[j] ± 0.1[$\mathcal{L}$]
Z+jets	52 ± 21[u] $^{+15}_{-11}$[j] $\pm$ 6[$\mathcal{L}$]	4.1 ± 2.9[u] $^{+2.1}_{-0.8}$[j] ± 0.5[$\mathcal{L}$]	27 ± 12[u] $^{+10}_{-\ 6}$[j] ± 3[$\mathcal{L}$]	0.8 ± 0.7[u] $^{+0.6}_{-0.0}$[j] ± 0.1[$\mathcal{L}$]
$t\bar{t}$ and t	$10 \pm$ 0[u] $^{+\ 3}_{-\ 2}$[j] $\pm$ 1[$\mathcal{L}$]	0.9 ± 0.1[u] $^{+0.4}_{-0.3}$[j] ± 0.1[$\mathcal{L}$]	$17 \pm$ 1[u] $^{+\ 6}_{-\ 4}$[j] ± 2[$\mathcal{L}$]	0.3 ± 0.1[u] $^{+0.2}_{-0.1}$[j] ± 0.0[$\mathcal{L}$]
Total SM	118 ± 25[u] $^{+32}_{-23}$[j] ± 12[$\mathcal{L}$]	10.0 ± 4.3[u] $^{+4.0}_{-1.9}$[j] ± 1.0[$\mathcal{L}$]	88 ± 18[u] $^{+26}_{-18}$[j] ± 9[$\mathcal{L}$]	2.5 ± 1.0[u] $^{+1.0}_{-0.4}$[j] ± 0.2[$\mathcal{L}$]
Data	87	11	66	2

Table C.8.: *Moriond'11 Expected and observed numbers of events in the four 0ℓ SRs. Uncertainties shown are due to MC statistics, statistics in CRs, other sources of uncorrelated systematic uncertainty, and also the JER and lepton efficiencies [u], the JES [j], and the luminosity [$\mathcal{L}$]. From [58].*

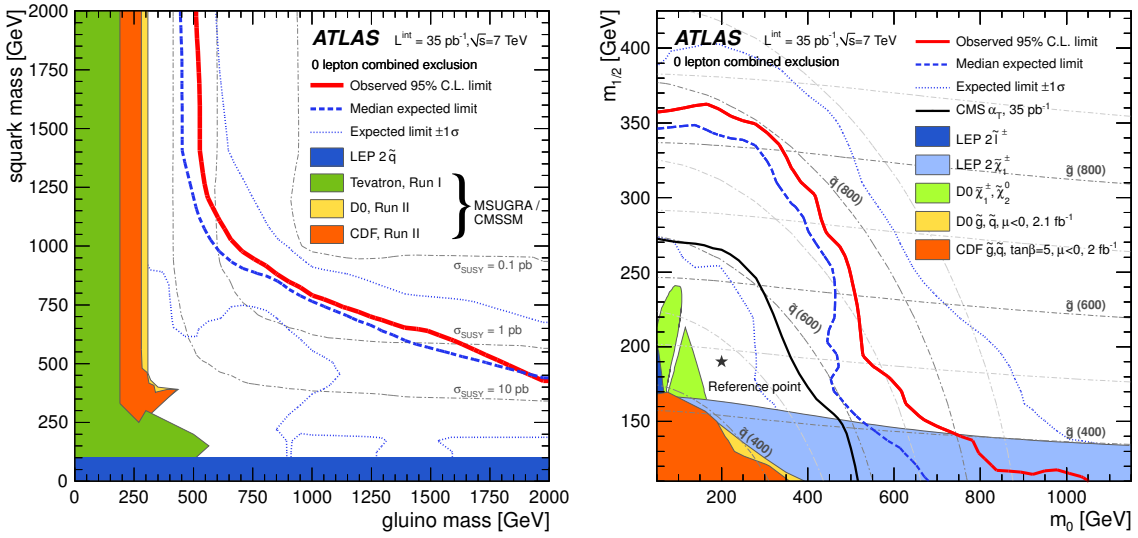

Figure C.9.: *Moriond'11 95% CL_s exclusion limits obtained by using the SR with the best expected sensitivity at each point in a simplified MSSM scenario with only strong production of gluinos and first- and second-generation squarks, and direct decays to jets and neutralinos (left); and in the (m_0 ; $m_{1/2}$) plane of MSUGRA/CMSSM for $\tan\beta = 3$, $A_0 = 0$ and $\mu > 0$ (right). The red lines show the observed limits, the dashed-blue lines the median expected limits, and the dotted blue lines the $\pm 1\sigma$ variation on the expected limits. Comparison with previous limits is illustrative only as some are derived in a different context. From [58].*

C.2. PLHC'11 (165 pb^{-1})

The results for this 0ℓ analysis were not published but rather presented at the PLHC'11 conference [65][2]. One highlight was that this was the first 0ℓ analysis using 2011 data (Moriond'11 used 2010 data). The corresponding `ZfromGamma` results were then documented in the PLHC'11 0ℓ internal note [102]. By this time, the `ZfromGamma` method had several improvements with respect to Moriond'11: new and more suitable MC samples, an improved photon selection and a better estimation of the TF; so the results, this time being significantly more solid and congruent, were used as the main $Z_{\nu\nu}$ + jets background estimate in the 0ℓ analysis. As for 0ℓ analysis itself, the main changes with respect to Moriond'11 were:

- The use of the data-driven methods to estimate the SM background (rather than from MC as previously done) from CRs (now defined from selections as close as possible to the SR but enriched in particular background processes) and TFs. In this case, five CRs were defined per SR.
- The introduction of a combined fit based on a likelihood function to obtain the total SM expectation. This fit accounted for CRs and SRs correlations and mutual-contamination.
- New SRs with increased sensitivity (from larger jet multiplicities and harder p_{T} cuts).
- Updated 0ℓ object definitions.
- The use of a "pileup reweighing" tool on the MC to match better the data conditions.

C.2.1. Framework

The framework used in this analysis is specified in Section 5.1 and Table 5.1.

C.2.2. Event Samples

Data: The data was in `SUSYD3PD` format and included 2011 data periods B-D, amounting to $\int \mathscr{L} \mathrm{d}t \sim 165$ pb^{-1} after applying the PLHC'11 0ℓ GRL (more details in Table 5.2).

[2] In this reference, CR1a was referred to as 'CR1' (see Section C.2.6), but here 'CR1a' will be kept to remain consistent with the rest of the sections.

Monte Carlo: The MC samples used in this analysis are listed in Tables C.9-C.10 and the production details in Table 5.7[3]. The new highlight was the availability of SHERPA samples for γ + jets and $Z_{\nu\nu}$ + jets. However, as suggested by the number of events generated and the plots below, their statistics at high-p_{T} were relatively poor and the PYTHIA γ + jets was better in this regard. On the other hand, as discussed in Appendix C.1, the PYTHIA signal suffered from missing multijet events, so for this analysis it was only used for illustration of such effect and to support the data-MC agreement at high-p_{T} where SHERPA lacked statistics. Another difference with respect to Moriond'11 was that samples to model the backgrounds to the γ + jets signal were no longer included in the plots. This was accepted at the time given the high-purity of the photon sample, in particular with the harder PLHC'11 SRs selections, as well as time constrains from the ATLAS MC production group to produce these samples. As for $Z_{\nu\nu}$ + jets MC, the PYTHIA sample was stopped and instead a SHERPA sample was used to be consistent with the γ + jets SHERPA estimate. The $Z_{\nu\nu}$ + jets ALPGEN samples used in Moriond'11 were still used for comparison purposes.

Regarding matching the new data-conditions, the MC production for PLHC'11 had more appropriate characteristics to match the pileup conditions such as an added pileup component ("mc10a" in Table 5.7) and a "pileup reweighing" (PR) tool also became available. At the time this tool was still in early developments and it was found to introduce an inefficiency of $\sim 50\%$ on the MC statistics [102].

In all the plots that follow, the MC is normalised to the data luminosity using the cross-sections listed and, unless otherwise stated, the PR tool is implemented using the "BCID-averaged reweighing", which was the default in the 0ℓ analysis.

Sample ID	Name	Cross Section [pb]	Filter Eff.	k-factor	N_{gen}
108081	PythiaPhotonJet_Unbinned35	$1.7305 \cdot 10^{+4}$	0.60450	1.000	999752
113715	SherpaY4JetsPt70	$1.5634 \cdot 10^{+3}$	1.000	1.000	199930

Table C.9.: *PLHC'11 Monte Carlo samples used to simulate the γ + jets signal, including cross section times filter efficiency, k-factor and the number of generated events in the sample.*

[3] Although some samples might appear to be the same in different analysis rounds, *e.g.* the PYTHIA signal in Tables C.9 and C.2, in general they have different production settings.

Sample ID	Name	Cross Section [pb]	Filter Eff.	k-factor	N_{gen}
119932	Z5jetstonunu30GeVScaleMT	$5.2941 \cdot 10^{+3}$	1.0	1.000	1699681
107710	AlpgenJimmyZnunuNp0_pt20_filt1jet	$3.5407 \cdot 10^{+3}$	$7.924433 \cdot 10^{-3}$	1.000	2999
107711	AlpgenJimmyZnunuNp1_pt20_filt1jet	$7.0170 \cdot 10^{+2}$	0.6112469	1.000	44487
107712	AlpgenJimmyZnunuNp2_pt20_filt1jet	$2.1700 \cdot 10^{+2}$	0.8896797	1.000	39491
107713	AlpgenJimmyZnunuNp3_pt20_filt1jet	$6.0160 \cdot 10^{+1}$	0.9689922	1.000	11995
107714	AlpgenJimmyZnunuNp4_pt20_filt1jet	$1.4640 \cdot 10^{+1}$	0.9900990	1.000	7993
107715	AlpgenJimmyZnunuNp5_pt20_filt1jet	$4.7100 \cdot 10^{+0}$	0.998004	1.000	2500

Table C.10.: *PLHC'11 Monte Carlo samples used to simulate the $Z_{\nu\nu}$ + jets signal, including cross section times filter efficiency, k-factor and the number of generated events in the sample.*

C.2.3. Inclusive Photon Sample ($\gamma + X$)

Event Selection: At the time, the "new" SMDP analysis with 35 pb^{-1} had just come out as an update of the 880 nb^{-1} analysis but it had not yet been strictly finalised, so the selection used by `ZfromGamma` from the preliminary documentation in [116] and outlined in Tables 5.8 and 5.9. The main changes with respect to Moriond'11 can be seen to be a larger photon acceptance (up to $|\eta| < 2.37$, see Appendix B) and a higher photon-p_{T} cut to suit the lowest unprescaled photon trigger for the new data periods included.

Results: The cutflow obtained for the $\gamma + X$ selection is shown in Table 5.10, which was validated with the SMDP group results in [116, 117]. The p_{T} distribution of the prompt photon candidates is shown in Figure C.10, where the good agreement of the data and the MC signal again corroborates the high-purity of the $\gamma + X$ sample. Also in Figure C.10, at low-p_{T} the data/MC ratio is lower for `SHERPA` than for `PYTHIA`, suggesting a potential overestimation from `SHERPA` of the $\gamma + X$ cross-section – `PYTHIA` seems more "data-like" since more background is expected at low-p_{T}, such as the Moriond'11 result in Figure 5.3(b). However, because both quickly converge around $p_{\text{T}}(\gamma_1) \sim 150$ GeV this was not investigated further.

C.2.4. Control Region Sample (CR1a)

0ℓ selection: Having applied the CR1a object definitions (Section 5.4) and 0ℓ object definitions in [102], the 0ℓ event selection applied is summarised in Table C.11 (the detailed version can be found in [102]). Five SRs were defined: SR-A was identical to Moriond'11 SR-A but with a harder m_{eff} cut, SR-B was identical to Moriond'11

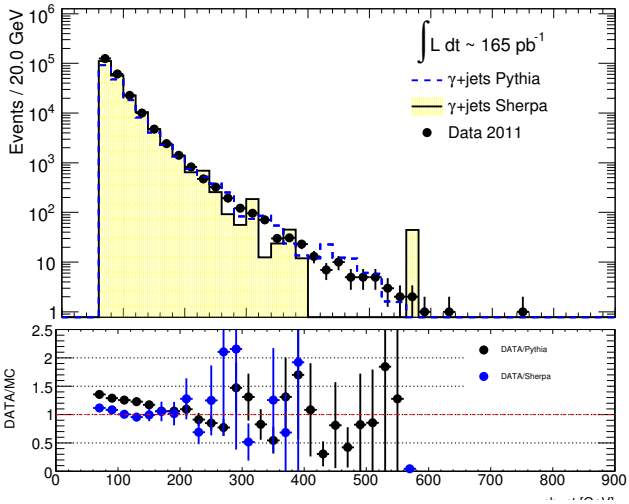

Figure C.10.: *PLHC'11 p_{T} distribution in data and MC of the prompt photon candidates in the $\gamma + X$ sample. The MC shown are the* `PYTHIA` *and* `SHERPA` *signals.*

SR-D. The four-jet SRs were all new. Note that SR-E used an 'inclusive' version of m_{eff}, m_{eff}(incl.), which includes all jets with $p_{\mathrm{T}} > 40$ GeV, and was in fact the first time the 0ℓ analysis used m_{eff}(incl.) before becoming the default last cut in Moriond'12.

Regarding the motivations to define these SRs, the jet multiplicity is motivated from the expected final states of $\tilde{q}\tilde{q}$, $\tilde{q}\tilde{g}$ and $\tilde{g}\tilde{g}$ production, mainly resulting in dijet, three-jet and four-jet events respectively, *e.g.* from $\tilde{q} \to q\tilde{\chi}_1^0$ and $\tilde{g} \to qq\tilde{\chi}_1^0$ (see Section 1.2.2). Cascade decays tend to increase the final-state multiplicity. The motivation for the $\Delta\phi$, $E_{\mathrm{T}}^{\mathrm{miss}}/m_{\mathrm{eff}}$ and m_{eff} cuts is discussed briefly in Section 5.4.2 and more explicitly in the 0ℓ documentation. SR-C and D were defined to increase sensitivity to different SUSY mass splittings, while the hardest SR, SR-E, was defined to boost the reach in the SUSY mass scale.

Results: For this part, some relevant results have been discussed in Section 5.4. Figure C.11 shows the prompt photon p_{T} evolution with the 0ℓ selections to define SR-A. Figure C.11(a) shows that at the stage of the $\gamma + X$ selection, the data already agrees quite well with both the `PYTHIA` and `SHERPA` signals. However, at the *dijet* selection stage (Figure C.11(b)), the missing multijet events in `PYTHIA` become evident (see Section C.1.4), whereas `SHERPA` does not show such a problem. This effect is more dramatic when looking at the p_{T} distribution of the softer jets in the event at this stage, like Figure C.12 which shows the effect is related to the second-leading jet (Figure C.12(b))

Requirement	Signal Region				
	A	B	C	D	E
$E_{\mathrm{T}}^{\mathrm{miss}}$ [GeV]	> 130				
Leading selected jet p_{T} [GeV]	> 130				
Second selected jet p_{T} [GeV]	>40	>40	>40	>40	>80
Third selected jet p_{T} [GeV]	–	>40	>40	>40	>80
Fourth selected jet p_{T} [GeV]	–	–	>40	>40	>80
$\Delta\phi$ $(i = 1, 2(, 3))$	>0.4				
$E_{\mathrm{T}}^{\mathrm{miss}}/m_{\mathrm{eff}}$	> 0.3 (2j)	> 0.25 (3j)	> 0.25 (4j)	> 0.25 (4j)	> 0.2 (4j)
m_{eff} [GeV]	> 1000 (2j)	> 1000 (3j)	> 500 (4j)	> 1000 (4j)	> 1100 (incl.)

Table C.11.: *PLHC'11 0ℓ SRs event selections. The quantities are defined elsewhere in the text or can be found in [102].*

whereas the leading jet distribution is only scaled (Figure C.12(a)). This effect is not due to a lack of statistics in the `PYTHIA` sample – Figure C.11(a) and Figure C.11(b) clearly show `SHERPA` has less high-p_{T} statistics than `PYTHIA`, and similarly the data-`PYTHIA` agreement is reasonably restored once the $E_{\mathrm{T}}^{\mathrm{miss}}$ cut is applied (Figures C.11(c)-(d)).

Figure C.13 shows an example CR1a $p_{\mathrm{T}}(\gamma_1)$ distribution for SR-C. Also shown in this figure, is the effect of the PR tool already mentioned, which clearly causes a significant loss in MC statistics. The typical percentage losses are quoted in Table C.12 for $\gamma +$ jets `SHERPA`. The CR1a m_{eff} distributions (prior to the m_{eff} cut) for each SR are shown in Figure C.14 where good data-MC signal agreement is seen, despite the limited MC statistics. The corresponding number of events are shown in Table C.15 for both data and MC (columns 2 and 3). The average photon-p_{T} and range of these events are quoted in Table 5.16.

Signal Region	MC statistics loss
A	41%
B	21%
C	10%
D	47%
E	100%

Table C.12.: *PLHC'11 percentage loss in MC statistics from using the PR tool on the $\gamma +$ jets* `SHERPA` *sample. For SR-C this effect is shown in Figure C.13.*

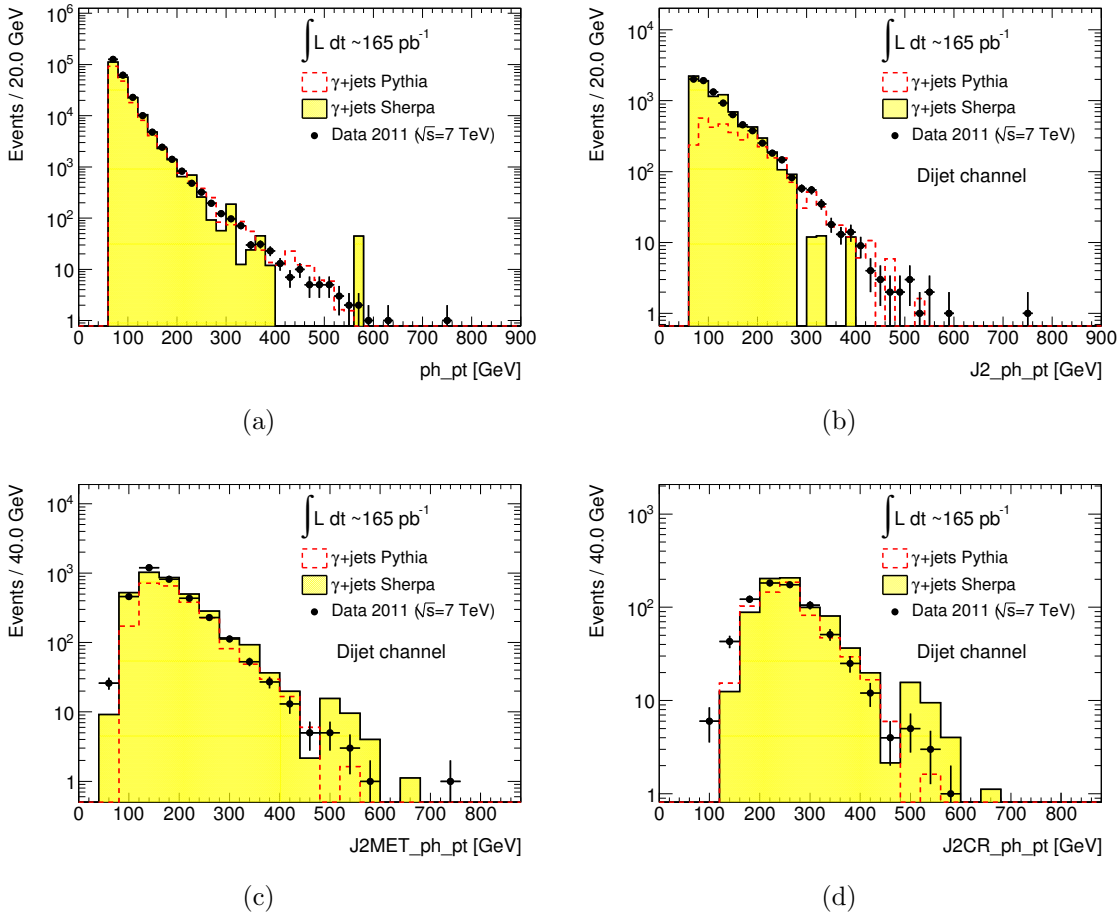

Figure C.11.: *PLHC'11 prompt photon p_{T} evolution with the CR1a selection for SR-A: (a) on the $\gamma + X$ sample (230 457 events), (b) after the dijet selection (8 557 events), (c) after the dijet selection and $E_{\mathrm{T}}^{\mathrm{miss}}$ cut (3 379 events), and (d) after the dijet selection, $E_{\mathrm{T}}^{\mathrm{miss}}$ cut and a softer m_{eff} cut (500 GeV). The MC shown are the* `PYTHIA` *and* `SHERPA` *signals.*

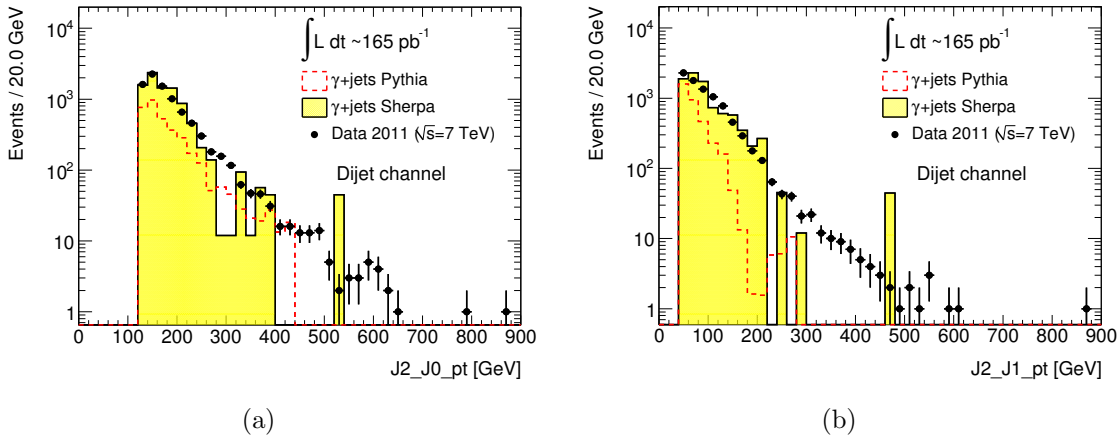

Figure C.12.: *PLHC'11 effect of missing multijets in $\gamma +$ jets* `PYTHIA` *for the (a) leading and (b) second-leading jet p_{T}.*

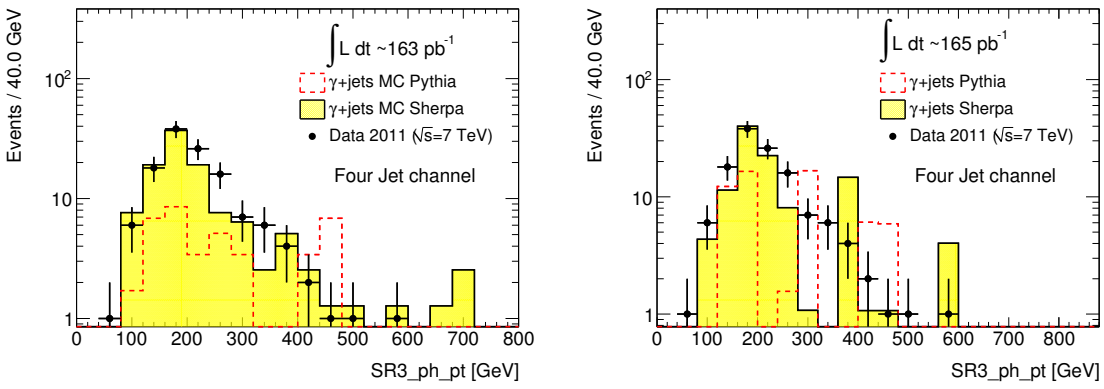

(a) (b)

Figure C.13.: *PLHC'11 prompt photon p_{T} distribution in SR-C, showing the effect of using the pileup reweighing (PR) tool on the MC: (a) without PR and (b) with PR, where a drop in MC statistics is clear. The MC shown is the* `PYTHIA` *and* `SHERPA` *signal.*

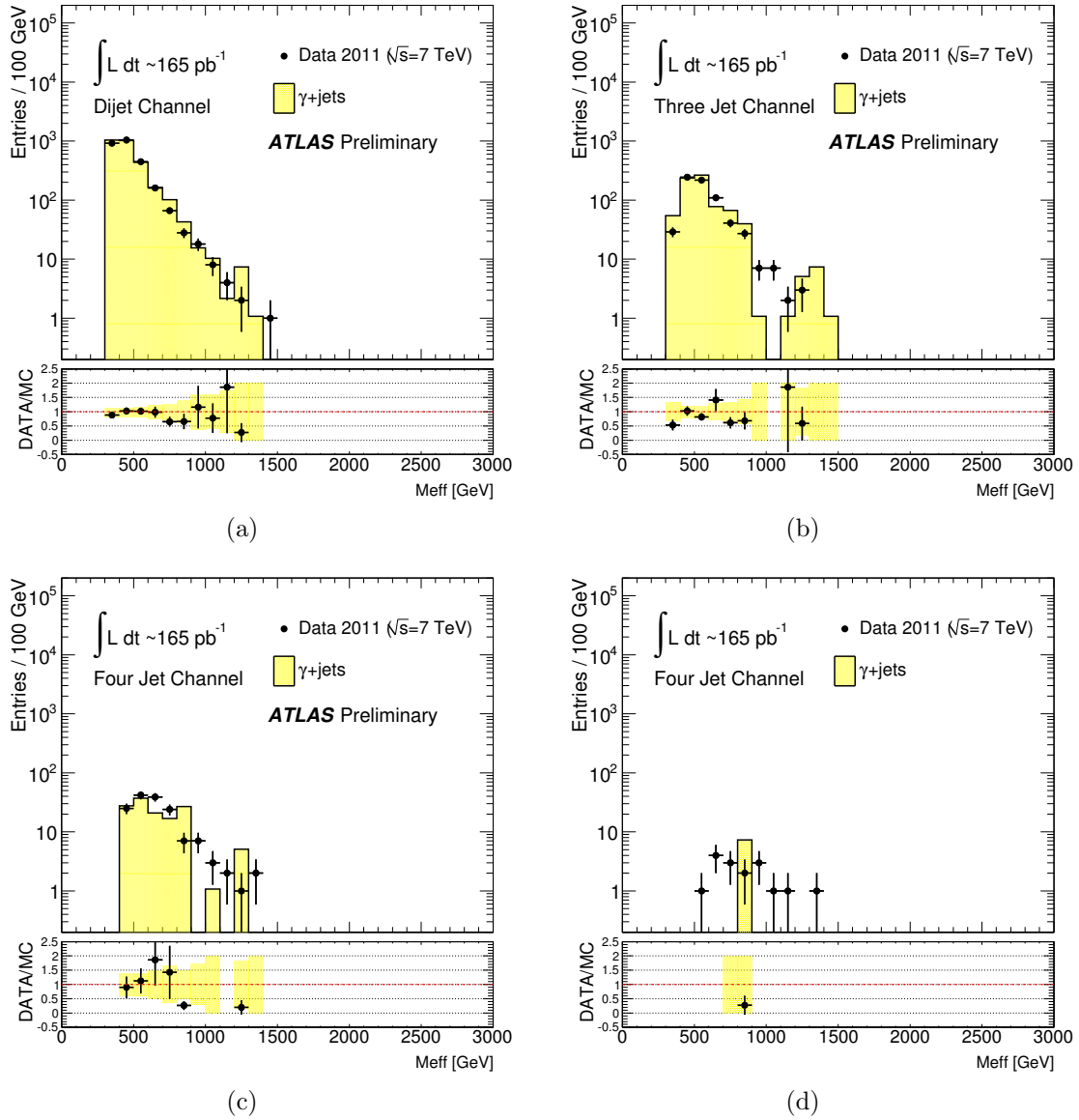

Figure C.14.: *PLHC'11 CR1a m_{eff} distributions in data and MC for SR-A (a), B (b) and C/D (c) and E (d). The MC shown is the* SHERPA *signal. The yellow band in the data/MC ratio denotes the size of the combined JER/JES and MC statistical uncertainties quoted in Tables C.13 and C.15 respectively.*

C.2.5. Transfer Function ($\mathbf{TF}_{Z_{\nu\nu}}$)

For this part, the highlight was that this was the first time for which it was possible to obtain part of the TF from MC rather than assuming SMDP results. The TF central values and associated uncertainties obtained are shown in Table C.13 and a summary of the procedures to calculate each of the factors now follows.

CR1a TF central value & uncertainties					
SR	A	B	C	D	E
Central Value	0.375	0.371	0.305	0.371	0.340
CR bckgrnd. (f_{bkg})	3%	3%	3%	3%	3%
$A^{\gamma} \cdot \varepsilon^{\gamma}$	22%	14%	7%	22%	30%
$\eta_{Z/\gamma}$	2%	2%	2%	2%	2%
JES/JER	$^{+1.4}_{-2.6}$ %	$^{+1.4}_{-2.6}$ %	$^{+1.4}_{-2.6}$ %	$^{+1.4}_{-2.6}$ %	$^{+1.4}_{-2.6}$ %
Pileup	4%	4%	4%	4%	4%
Trigger	$< 1\%$	$< 1\%$	$< 1\%$	$< 1\%$	$< 1\%$
Theory ($R_{Z_{\nu\nu}/\gamma}$)	15%	15%	15%	15%	15%

Table C.13.: *PLHC'11 Central values and associated uncertainties of the CR1a TFs. The meaning of the terms are explained elsewhere in the text.*

- **Efficiency and Acceptance:** These were also estimated for the first time using a bin-by-bin unfolding approach and as a combined $A^{\gamma} \cdot \varepsilon^{\gamma}$ correction factor to the TF as currently done. The original aim was to calculate it after the full CR1a selection to include all the effects arising from the SRs selections, as done in the current implementation (Section 5.5.1). However, due to the lack of MC statistics already mentioned (few events generated in the `SHERPA` sample and the inefficiency introduced by the PR tool), an integrated value calculated in SR-A with a *softer* m_{eff} cut (500 GeV) was used for all the TFs. The values obtained are shown in Figure C.15. Even so, using PR has an effect on this value as shown by Table C.14, although this is smaller than the overall assigned uncertainty quoted in Table C.13.

  The results were again cross-checked with SMDP results in [116] by resolving the different components: $A^{\gamma} \cdot \varepsilon^{\gamma} = A^{\gamma} \cdot \varepsilon^{\gamma}_{\text{rec}} \cdot \varepsilon^{\gamma}_{\text{id}}$. For $\varepsilon^{\gamma}_{\text{rec}}$, the SMDP result for photons with average p_{T} shown in Table 5.16 was estimated to be $\sim 83\% \pm 1\%$ and for $\varepsilon^{\gamma}_{\text{id}}$ $\sim 94\% \pm 1\%$. The A^{γ} was estimated from photon MC passing only the 0ℓ selection and bypassing the $\gamma + X$ selection using truth photon information and the result

obtained was practically identical to that shown in Table 5.17. Estimated this way, the value of $A^{\gamma} \cdot \varepsilon^{\gamma}$ was compared to that in Figure C.15 and their difference taken as the final uncertainty, shown in Table C.13 (row 3).

- **Purity:** Given the high and robust purity of the CR1a sample (Section 5.5.2), the remaining background was like in Moriond'11, neglected, and rather an uncertainity of 3% assigned to it, based on the maximum background estimate in [116] within the approximate photon p_{T} range of the CR1a candidates, as shown in Table C.13 (row 2).

- **Z/γ Ratio:** The value was again taken from `GAMBOS` but as an improvement with respect to the previous analysis, this time the variations with jet multiplicity, reconstruction effects and isolation criteria (Chapter 4 and Section 5.5.3) were at least considered this time by assigning a more conservative uncertainty of 15%, as shown in Table C.13 (row 8), given that the effects from PDFs largely cancel (a $< 5\%$ effect).

- **γ vs $Z_{\nu\nu}$ Pseudorapidity:** Given that the γ and $Z_{\nu\nu}$ η distributions are effectively identical in the SRs (*e.g.* Figures 5.15 and 4.14(b)), the difference found between $\gamma +$ jets and $Z_{\nu\nu} +$ jets MC was taken as the uncertainty, as shown in Table C.13 (row 4).

Other uncertainties that were assessed to be consistent with the rest of the 0ℓ analysis, also appearing in Table C.13, were:

- Pileup: This was obtained from the difference of using "BCID non-averaged reweighing" and the default (BCID averaged) in the PR tool.

- JES/JER: Jet energy scale and jet energy resolution uncertainties were assessed using the standard ATLAS tools provided by the Jet/ETmiss working group available at the time. More details can be found in [102].

- Trigger: This was with respect to the nearly 100% efficient photon trigger used in this analysis (`g60_loose`, see Appendix B).

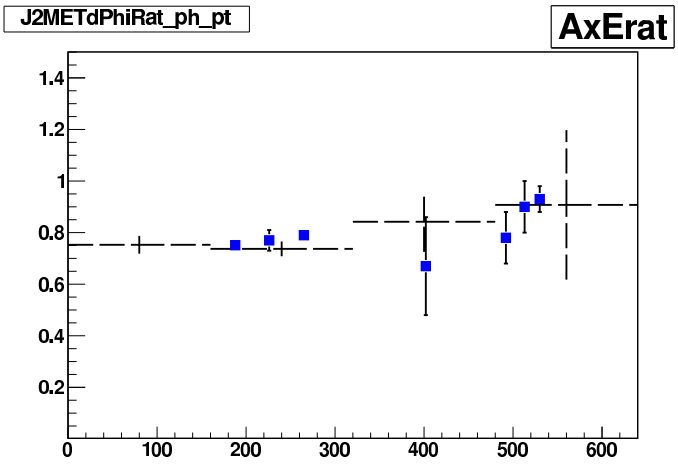

Figure C.15.: *PLHC'11 Combined acceptance and efficiency correction factor* $A^{\gamma}(p_{\mathrm{T}}) \cdot \varepsilon^{\gamma}(p_{\mathrm{T}})$ *for the CR1a TF in SR-A with softer* m_{eff} *cut (500 GeV), as obtained from* γ *+ jets* `SHERPA`*.*

Signal Region	$\langle A^{\gamma}(p_{\mathrm{T}}) \cdot \varepsilon^{\gamma}(p_{\mathrm{T}}) \rangle$	
	no PR	PR
A	0.93	0.99
B	0.78	0.78
C	0.77	0.69
D	0.90	0.61
E	0.67	0.00

Table C.14.: *PLHC'11 Effect of using the pileup reweighing tool on the integrated value of* $A^{\gamma}(p_{\mathrm{T}}) \cdot \varepsilon^{\gamma}(p_{\mathrm{T}})$ *in the SRs (Figure C.15).*

TF stand-alone estimate of $Z_{\nu\nu}$ + jets: After the direct application of the TF to the CR1a event counts, the $Z_{\nu\nu}$ + jets background estimate results obtained for this analysis are shown in Table C.15 compared to `SHERPA` and `ALPGEN`, where all the results are consistent within errors. Two examples to illustrate these results are shown in Figure C.16 for SR-A with softer m_{eff} cut and SR-C. The data-MC agreement is clearly best for the bin with the largest statistics, and the $Z_{\nu\nu}$ + jets `ALPGEN` sample describes better the data estimate in Figure C.16.

SR	CR1a		$Z_{\nu\nu}$ + jets Estimate		$Z_{\nu\nu}$ + jets Signal
	data	Sherpa	data	Sherpa	Sherpa/Alpgen
A	15	21	5.6 ± 1.5 (stat) ± 1.5 (syst)	8.4	3.5/6.0
B	12	15	4.5 ± 1.3 (stat) ± 1.1 (syst)	5.9	2.0/5.0
C	127	108	38.7 ± 3.4 (stat) ± 7.6 (syst)	35.3	30.9/34.3
D	8	6	3.0 ± 1.1 (stat) ± 0.8 (syst)	2.5	1.3/1.7
E	3	0	1.0 ± 0.6 (stat) ± 0.4 (syst)	0	0.4/0.4

Table C.15.: *PLHC'11 numbers of CR1a events from data and MC for each SR (columns 2-3) and the stand-alone estimate of $Z_{\nu\nu}$ + jets background in the SRs from data and MC (columns 4-5), compared to $Z_{\nu\nu}$ + jets MC (column 6). The MC statistical uncertainty is not shown but can be assumed to be small. The luminosity uncertainty was then ∼ 4.5% (Table 5.2).*

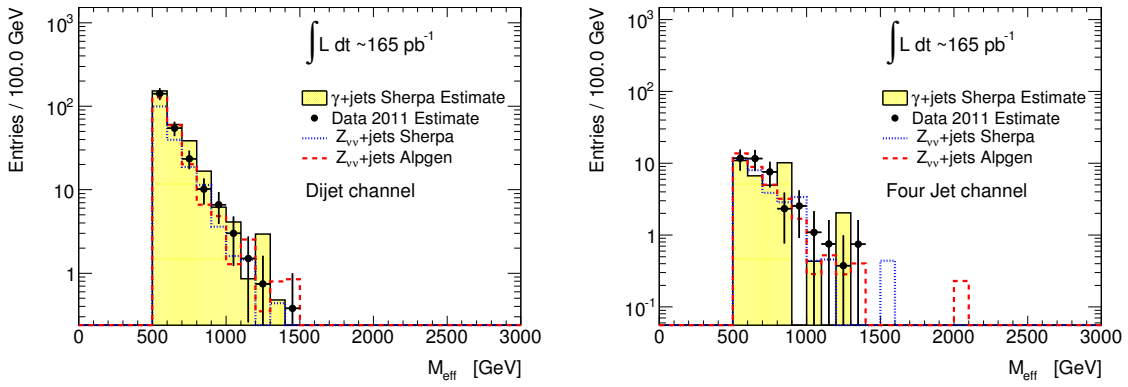

(a) (b)

Figure C.16.: *PLHC'11 $Z_{\nu\nu}$ + jets m_{eff} distributions in the 0ℓ (a) SR-A with softer m_{eff} cut (500 GeV) and (b) SR-C, as estimated from CR1a from data and MC using the TF, compared directly with $Z_{\nu\nu}$ + jets MC from* `SHERPA` *and* `ALPGEN`*. The labels 'Data 2011 Estimate' and 'γ + jets Sherpa estimate' indicate the TFs were applied to the CR1a data or MC events, whereas those labeled '$Z_{\nu\nu}$ + jets Sherpa/Alpgen' show the raw MC $Z_{\nu\nu}$ + jets estimates for the SRs scaled to the data luminosity.*

C.2.6. Context within the 0ℓ analysis

The 0ℓ SRs m_{eff} distributions (prior to the m_{eff} cut) are shown in Figure C.17, together with the 'raw' MC background expectations prior to the likelihood fitting procedure. The equivalent distributions for the CRs can be found in [102]. The corresponding event counts in the SRs and CRs are listed in Table C.16, where once again the rich statistics of CR1a become evident. SR-C was clearly the region with the largest statistics. The central values of the TFs used to translate the CR event counts into SR background estimates are quoted in Table C.17, featuring again the robustness of the CR1a TF accross all SRs (see Section 5.6.2). Tables like Table 5.24 which list the cross-TFs (Section 5.6.1) are not shown here but can be found in [102].

At the time of PLHC'11, there was no defined procedure to include both CR1a and CR1b into the same likelihood fit (unlike in the current implementation, see Section 5.6.1), so two different fits were done; one using CR1a and one using CR1b, shown in Tables C.19 and C.20 respectively, from which both estimates were considered consistent in SR-A, B and D, but not in SR-C (a $\sim 2\sigma$ discrepancy). However, despite SR-C being the SR with largest statistics, CR1b showed significantly larger uncertainties compared to the other CRs, as shown in Table C.18 (probably as a result of the CR1b-to-SR extrapolation) and also the corresponding TF central value was significantly different with respect to the others (see Table C.17). Another problem encountered was that the hardest SR, SR-E, showed too large statistical uncertainties for the likelihood fit to provide reliable results. Because of this, both of SR-C and SR-E were excluded from the final 0ℓ results presented at the PLHC'11 conference [65] and only CR1a was considered to estimate the $Z_{\nu\nu}$ + jets background estimate (hence it is referred in [65] simply as 'CR1'). This demonstrated the importance of the $Z_{\nu\nu}$ + jets background estimate in the 0ℓ analysis.

Given that no significant excess was found between the data and SM expectation, limits were set on the same SUSY models as in Moriond'11, shown in Figure C.18. Under these models, the gluino mass was excluded below 725 and up to 1025 GeV, while equal mass squarks and gluinos were excluded below 950 GeV. The larger jet multiplicities and harder selections of the PLHC'11 SRs improved the reach with respect to the Moriond'11 analysis.

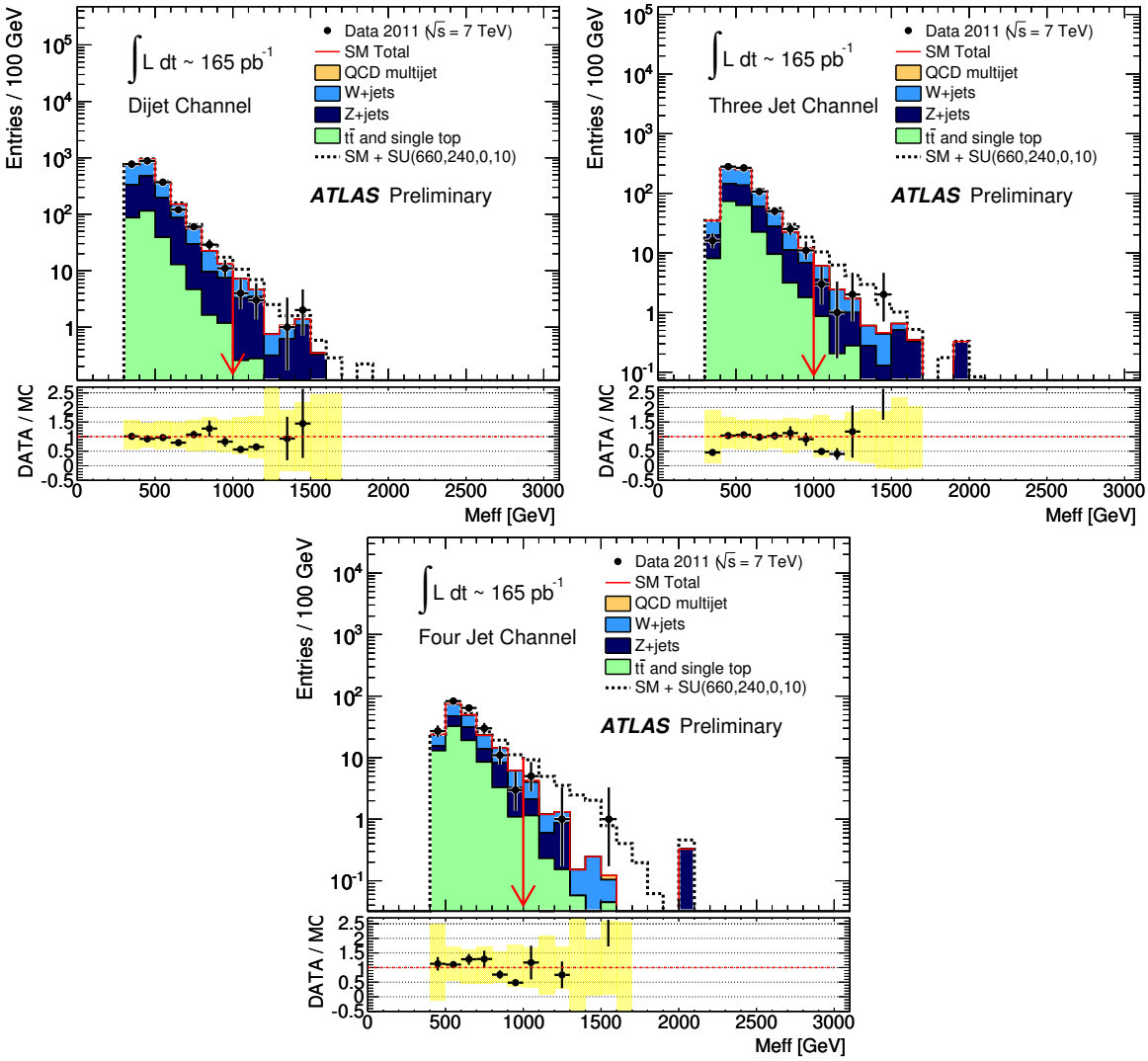

Figure C.17.: *PLHC'11 m_{eff} distributions for the ≥ 2 jet channel (top left), the ≥ 3 jet channel (top right) and the ≥ 4 jet channel (bottom), prior to the m_{eff} cut (red arrows indicate the start of a SR), in data and MC. For comparison, the dashed curve shows the expectation for an mSUGRA reference point with $m_0 = 660$ GeV, $m_{1/2} = 240$ GeV, $A_0 = 0$, $\tan\beta = 10$ and $\mu > 0$. This reference point is also indicated by the star on Figure C.18(b). Below each plot the data/MC ratio is shown. Black vertical bars show the statistical uncertainty from the data, while the yellow band shows the size of the combined SM MC statistical, JER and JES uncertainties. From [65].*

Region	Channel				
	A	B	C	D	E
SR	10	8	198	7	4
CR1a	15	12	127	8	3
CR1b	11	10	7	4	2
CR2	8	17	122	8	10
CR3	74	67	44	51	13
CR4	9	17	24	23	10

Table C.16.: *PLHC'11 data event counts in the* 0ℓ *SRs and CRs. From [102].*

Control region / process	Signal Region				
	A	B	C	D	E
CR 1a / $Z(\to \nu\nu)$+jets	0.38	0.37	0.3	0.37	0.34
CR 1b / $Z(\to \nu\nu)$+jets	0.65	0.65	12	0.66	0.0001
CR 2 / QCD jets	0.014	0.017	0.13	0.036	0.049
CR 3 / $W(\to \ell\nu)$+jets	0.09	0.081	2.1	0.075	0.085
CR 4 / $t\bar{t}$	0.048	0.075	4.2	0.07	0.082

Table C.17.: *PLHC'11 Summary of the central values of the CRs TFs in every channel. From [102].*

Uncertainty	Process (main CR)				
	Z+jets (CR1a)	Z+jets (CR1b)	QCD jets (CR2)	W+jets (CR3)	$t\bar{t}$ (CR4)
Central Value	0.3	12	0.13	2.1	4.2
JES	$^{+0}_{-2.2}$ %	$^{+20}_{-1.7}$ %	–	$^{+3.3}_{-2.5}$ %	$^{+5.9}_{-5.4}$ %
JER	1.4 %	11 %	–	2 %	4.1 %
CR bckgrnd.	3 %	–	–	–	–
γ acceptance.	7 %	–	–	–	–
$\gamma \to Z$ acc. corr.	2 %	–	–	–	–
Trigger	< 1 %	–	–	–	–
QCD seed	–	–	9.2 %	–	–
QCD Gaussian	–	–	23 %	–	–
QCD tail norm.	–	–	4.6 %	–	–
QCD tail stat.	–	–	11 %	–	–
l eff.	–	7.1 %	–	2.5 %	2.2 %
l scale.	–	16 %	–	1.2 %	1.5 %
l resoln.	–	1.9 %	–	0.77 %	0.45 %
b-tag/veto eff.	–	–	–	18 %	26 %
Theory	15 %	32 %	–	17 %	15 %
Pileup	4 %	–	–	1.4 %	5.3 %
MET CellOut	–	–	–	1.8 %	1.9 %
MC stat.	–	4.2 %	–	5.9 %	8.2 %

Table C.18.: *PLHC'11 uncertainties of the CRs TFs to SR-C (the SR with largest statistics). CR1b has significantly larger uncertainties and central value compared to the other CRs. From [102].*

Process	Signal Region				
	A	B	C	D	E
CR1a / $Z \to (\nu\nu)$+jets	5.61 ± 2.11	4.44 ± 1.6	38.55 ± 7.58	2.96 ± 1.33	0.01 ± 0.0
$W \to (\ell\nu)$+jets	6.2 ± 1.81	4.45 ± 1.59	57.43 ± 31.09	2.73 ± 1.3	0.0 ± 1.11
$t\bar{t}$+ Single Top	0.22 ± 0.33	1.01 ± 0.92	89.51 ± 37.53	1.41 ± 0.89	1.36 ± 0.55
QCD jets	0.05 ± 0.04	0.21 ± 0.07	12.28 ± 1.56	0.16 ± 0.11	0.0 ± 0.29
Total	12.08 ± 2.77	10.1 ± 2.34	197.77 ± 27.05	7.27 ± 1.71	1.37 ± 1.23
Data	10	8	198	7	4

Table C.19.: *PLHC'11 Fitted background components in each SR, compared with observation using CR1a. The Z + jets and W + jets are for most SRs the dominant backgrounds. From [102].*

Process	Signal Region				
	A	B	C	D	E
CR1a / $Z \to (\nu\nu)$+jets	7.1 ± 2.14	6.48 ± 2.07	82.69 ± 20.84	2.65 ± 1.43	0.0 ± 0.29
$W \to (\ell\nu)$+jets	6.17 ± 1.49	4.4 ± 1.13	57.46 ± 15.1	2.72 ± 0.79	0.67 ± 0.38
$t\bar{t}$+ Single Top	0.22 ± 0.26	1.0 ± 0.67	89.06 ± 16.27	1.41 ± 0.55	0.74 ± 0.29
QCD jets	0.05 ± 0.04	0.2 ± 0.07	11.48 ± 1.48	0.17 ± 0.1	0.67 ± 0.21
Total	13.55 ± 3.66	12.08 ± 3.72	240.69 ± 52.01	6.95 ± 2.08	2.08 ± 0.62
Data	10	8	198	7	4

Table C.20.: *PLHC'11 Fitted background components in each SR, compared with observation using CR1b. The Z+jets and W+jets are for most SRs the dominant backgrounds. From [102].*

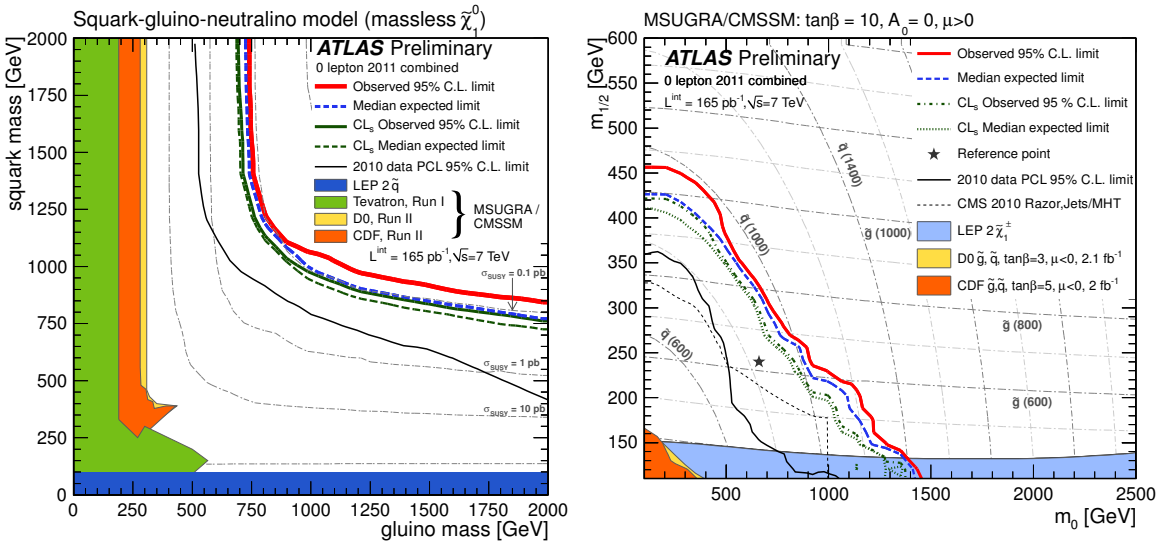

Figure C.18.: *PLHC'11 95% CL$_s$ exclusion limits obtained by using the SR with the best expected sensitivity at each point in (a) a simplified MSSM scenario with only strong production of gluinos and first- and second-generation squarks, and direct decays to jets and neutralinos; and in (b) the (m_0 ; $m_{1/2}$) plane of MSUGRA/CMSSM for $\tan\beta = 10$, $A_0 = 0$ and $\mu > 0$ (right). The red lines show the observed limits, the dashed-blue lines the median expected limits, and the dotted blue lines the $\pm 1\sigma$ variation on the expected limits. Comparison with previous limits is illustrative only as some are derived in a different context. From [58].*

C.3. EPS'11 (1.04 fb^{-1})

The results from this analysis round became the second publication of the 0ℓ analysis [54]. The corresponding `ZfromGamma` results are documented in the supporting 0ℓ documentation, found in [101]. Given the short time scale between EPS'11 and the previous analysis round (PLHC'11), not many improvements could be made to the `ZfromGamma` method, except for making used of two additional γ + jets `SHERPA` samples, which in the end turned out still insufficient for the harder SRs of EPS'11. As for 0ℓ analysis itself, the main changes with respect to PLHC'11 were:

- A significantly larger dataset (by almost an order of magnitude).
- A 'LAr hole' – a region in the ATLAS LAr calorimeter ($0 < \eta < 1.4$ and $-0.8 < \phi < -0.6$) that had a major electronics failure from data-period E onwards. In summary, the impact on the 0ℓ analysis from this was: for jets, the reconstruction was negligibly affected if the jet p_{T} was > 20 GeV but the mean energy loss was still $\sim 30\%$; for $E_{\mathrm{T}}^{\mathrm{miss}}$, both the scale and resolution were affected; for the CRs, the impact was negligible except for CR2 (QCD) given that substantial fake $E_{\mathrm{T}}^{\mathrm{miss}}$ could be generated by jets pointing into the hole. In addition, the γ + jets events which were never a worry to the 0ℓ analysis as none were expected to pass to the SRs (little true $E_{\mathrm{T}}^{\mathrm{miss}}$ is expect from such events, see Appendix D.2), became a concern. Similar to CR2, a high-p_{T} photon pointing into the hole could significantly contribute to the measured $E_{\mathrm{T}}^{\mathrm{miss}}$ and so, such event could potentially pass to the SRs. This was another case for which the `ZfromGamma` method proved useful and luckily the effect was found to be negligible, as described in Appendix D.2.1.

  In order to counteract all these effects, a 'LAr hole veto' was defined (and regarded as an 'event cleaning cut'), where the event was rejected if any of the leading-four jets had $p_{\mathrm{T}} > 30$ GeV and pointed into the hole. The impact of the LAr hole veto on the CRs was found to be negligible [101] and the overall decrease in SUSY signal acceptance to be no more than 15%.
- The incorporation of SR-C and E (Table C.11), which had been excluded in PLHC'11 to obtain the final limit plots.
- A procedure to incorporate both CR1a and CR1b into the likelihood fit to obtain a combined and more robust $Z_{\nu\nu}$ + jets background estimate.

- The use of "validation regions" (VRs) to cross-check CR3 ($W_{\ell\nu}$ + jets) and CR4 ($t\bar{t}$) and the removal of the theory uncertainties associated with the extrapolation in these CRs by applying the same m_{eff} cut as in the SRs (though the extrapolation in CR1b remained).
- Additional SUSY interpretations of the results, *e.g.* in Universal Extra Dimensions (UED) models [118].

C.3.1. Framework

The framework used in this analysis is specified in Section 5.1 and Table 5.1.

C.3.2. Event Samples

Data: The data was in `SUSYD3PD` format and included 2011 data periods B2-H4, amounting to $\int \mathscr{L} \mathrm{d}t \sim 1.035$ fb^{-1} after applying the EPS'11 0ℓ GRL (more details in Table 5.2).

Monte Carlo: The MC samples used in this analysis are listed in Tables C.21-C.22 and the production details in Table 5.7. The γ + jets `PYTHIA` sample from Table C.9 was no longer used because of the already known missing multijet events (Sections C.1.4 and C.2.4). The new highlight was the availability of a higher-p_{T} γ + jets `SHERPA` sample (referred to here as '`SHERPA`-140'). However, as will be shown in Section C.3.4, this proved still insufficient for the EPS'11 SRs. Again, background samples to the γ + jets signal were not included in the plots given the high-purity of the photon sample and time constrains to produce these samples (this issue was sorted for Moriond'12). As for $Z_{\nu\nu}$ + jets MC, the same `SHERPA` and `ALPGEN` samples as in PLHC'11 (albeit under different production settings, see Table 5.7) were used.

Regarding matching data-conditions, the MC production for EPS'11 ('mc10b' in Table 5.7) had more refined settings to match the pileup conditions than the PLHC'11 production ('mc10a'). The typical distribution of the number of interactions per event is shown in Figure C.19 for the γ + jets `SHERPA`-70 sample. However, it was not until Moriond'12 when the MC production was truly suited for 2011 data ('mc11'), as both EPS'11 and PLHC'11's production had been based on 2010 data with an added pileup component.

In all the plots that follow, the MC is normalised to the data luminosity using the cross-sections listed and the same pileup reweighing tool from PLHC'11 was implemented (see Section C.2.2).

Sample ID	Name	Cross Section [pb]	Filter Eff.	k-factor	N_{gen}
113715	SherpaY4JetsPt70	$1.5634 \cdot 10^{+3}$	1.000	1.000	199930
113716	SherpaY4JetsPt140	$9.7628 \cdot 10^{+1}$	1.000	1.000	199849

Table C.21.: *EPS'11 Monte Carlo samples to simulate the γ + jets signal, including cross section times filter efficiency, k-factor and the number of generated events in the sample.*

Sample ID	Name	Cross Section [pb]	Filter Eff.	k-factor	N_{gen}
119932	Z5jetstonunu30GeVScaleMT	$5.2941 \cdot 10^{+3}$	1.0	1.000	1699681
107710	AlpgenJimmyZnunuNp0_pt20_filt1jet	$3.572 \cdot 10^{+3}$	0.011	1.282	63482
107711	AlpgenJimmyZnunuNp1_pt20_filt1jet	$7.387 \cdot 10^{+2}$	0.611	1.282	909288
107712	AlpgenJimmyZnunuNp2_pt20_filt1jet	$2.229 \cdot 10^{+2}$	0.882	1.282	204942
107713	AlpgenJimmyZnunuNp3_pt20_filt1jet	$6.187 \cdot 10^{+1}$	0.968	1.282	140929
107714	AlpgenJimmyZnunuNp4_pt20_filt1jet	$1.563 \cdot 10^{+1}$	0.992	1.282	32980
107715	AlpgenJimmyZnunuNp5_pt20_filt1jet	$3.581 \cdot 10^{+0}$	0.998	1.282	9492

Table C.22.: *EPS'11 Monte Carlo samples to simulate the $Z_{\nu\nu}$ + jets signal, including cross section times filter efficiency, k-factor and the number of generated events in the sample.*

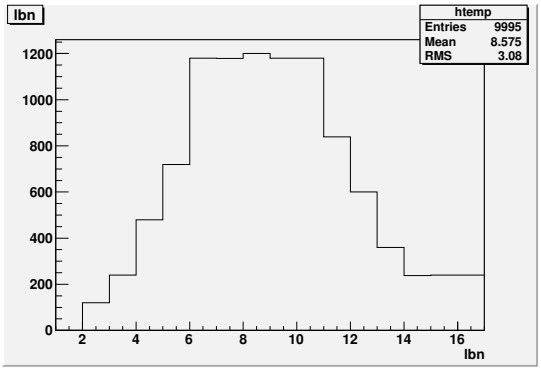

Figure C.19.: *EPS'11 Distribution of $\langle\mu\rangle$ in the γ + jets* `SHERPA`*-70 sample, to illustrate the MC production settings of the 'mc10b' to match the EPS'11 data conditions. The mean of $\langle\mu\rangle$ is indeed ~ 8, as quoted in Table 5.7.*

C.3.3. Inclusive Photon Sample ($\gamma + X$)

Event Selection: A slightly updated version of the photon selection with respect to the SMDP 35 pb^{-1} analysis [49] was implemented here, mainly to deal with the LAr hole problem discussed, as well as the new lowest unprescaled photon-trigger suitable for the EPS'11 dataset. The requirements are shown in Tables 5.8 and 5.9, which were largely based on the SMDP recommendations at the time [87]. Technically, the main changes were: an update of the 'photon cleaning' also related to the LAr hole (see Section 5.3.1); a higher photon-p_{T} cut (to suit the trigger); a harder PV requirement and the addition of a LAr error check.

Results: The results for the $\gamma + X$ selection just described were also presented at the EPS'11 conference as a separate analysis documented in [92]. The p_{T} distribution for the prompt photon candidates is shown in Figure C.20 for two isolation criteria; the one used in Table 5.8 and the then 'test' looser criteria of $E_{\mathrm{T}}^{\mathrm{iso}} < 5$ GeV. This was because the criterion used in the 880 nb^{-1} and 35 pb^{-1} SMDP analyses had been motivated by the lower photon-p_{T} acceptance and the consequently larger background contamination. However, for Moriond'12 onwards, $E_{\mathrm{T}}^{\mathrm{iso}} < 5$ GeV became the default criterion (note that the integrated luminosity of Figure C.20 is slightly lower than in the 0ℓ analysis because the EPS'11 SMDP GRL was used to obtain these plots). With the SMDP GRL, the number of prompt photon candidates was 529 481 with 3 GeV isolation and 628 497 with 5 GeV isolation. For Figure C.20(b), 5 candidates were found with $p_{\mathrm{T}} > 800$ GeV (4 unconverted, 1 converted); the highest-p_{T} unconverted photon had $p_{\mathrm{T}} \sim 960$ GeV and its event display is shown in Figure C.21.

The equivalent distribution to Figure C.20(a) but using the 0ℓ GRL is shown in Figure C.22 and the cutflow quoted in Table 5.10, which was found to be in very good agreement with the SMDP results in [92].

C.3.4. Control Region Sample (CR1a)

0ℓ selection: Having applied the CR1a object definitions (Section 5.4) and 0ℓ object definitions in [101], the discriminant 0ℓ event selections were identical to PLHC'11 (Table C.11). The detailed version, *e.g.* with the updated cleaning cuts, can be found in [101].

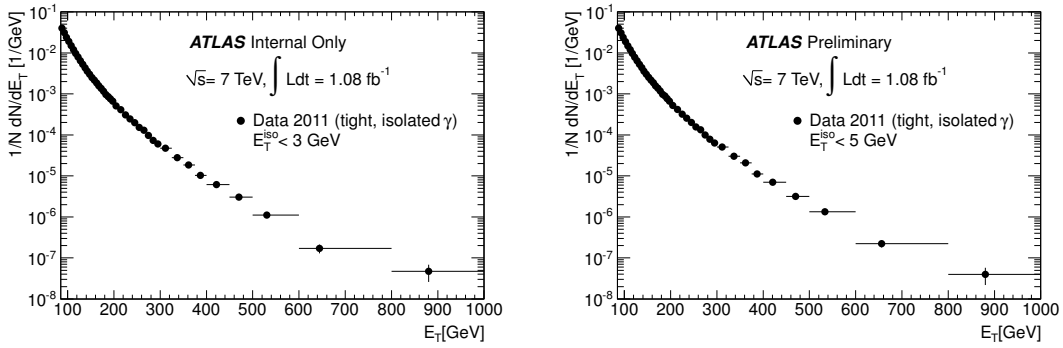

(a) (b)

Figure C.20.: *EPS'11 p_{T} distribution of the prompt photon candidates in the $\gamma + X$ sample from data, using two different isolation criteria: (a) the one used up to the EPS'11 analysis ($E_{\mathrm{T}}^{\mathrm{iso}} < 3$ GeV) and (b) a looser criterion used in Moriond'12 ($E_{\mathrm{T}}^{\mathrm{iso}} < 5$ GeV). The bins are of variable size and normalised to the total number of selected candidates. The marker positions correspond to the bin weighted averages. The integrated luminosity is slightly lower than in the 0ℓ analysis because the EPS'11 SMDP GRL was used for these plots. From [92].*

Results: For this part, some relevant results have been discussed in Section 5.4. Figure C.22 shows the prompt photon p_{T} evolution from the $\gamma + X$ selection to the CR1a selection for SR-A in data and the SHERPA-70 signal.

To get the MC CR1a m_{eff} distributions, the original plan was to continue using the SHERPA-70 sample, which had been used to produce for example Figure C.22. With this, the resulting m_{eff} distributions for all SRs are shown in Figure C.23 (prior to the m_{eff} cut). However, a significant data-MC discrepancy was found in the distribution for SR-C/D, as shown in Figure C.23(c). This issue was investigated further and found to be due to the pileup reweighing tool introducing a loss in statistics (see Appendix C.2.4). To support such conjecture, Figure C.24 shows the equivalent of Figure C.23 but without PR applied, and clearly the effect is negligible for all SRs except for SR-C/D, where a significant improvement in the data/MC agreement results. However, because the ultimate aim was to be as consistent as possible with the 0ℓ analysis, another solution was sought after to avoid not using this tool. For this, the SHERPA-140 sample with PR applied was investigated and, although it was found to be in good agreement with data at high-m_{eff}, it was discrepant at low-m_{eff}. Further investigation of this issue showed that there were missing low-p_{T} photon events in SHERPA-140 that could pass the SRs selections. This is illustrated in Figure C.25 where the m_{eff} distribution for SR-C/D is plotted versus $p_{\mathrm{T}}(\gamma_1)$ for both SHERPA-140 and SHERPA-70, from which is clear that SHERPA-70 events with photons of p_{T} lower than the generator-level cut of SHERPA-140 can certainly pass

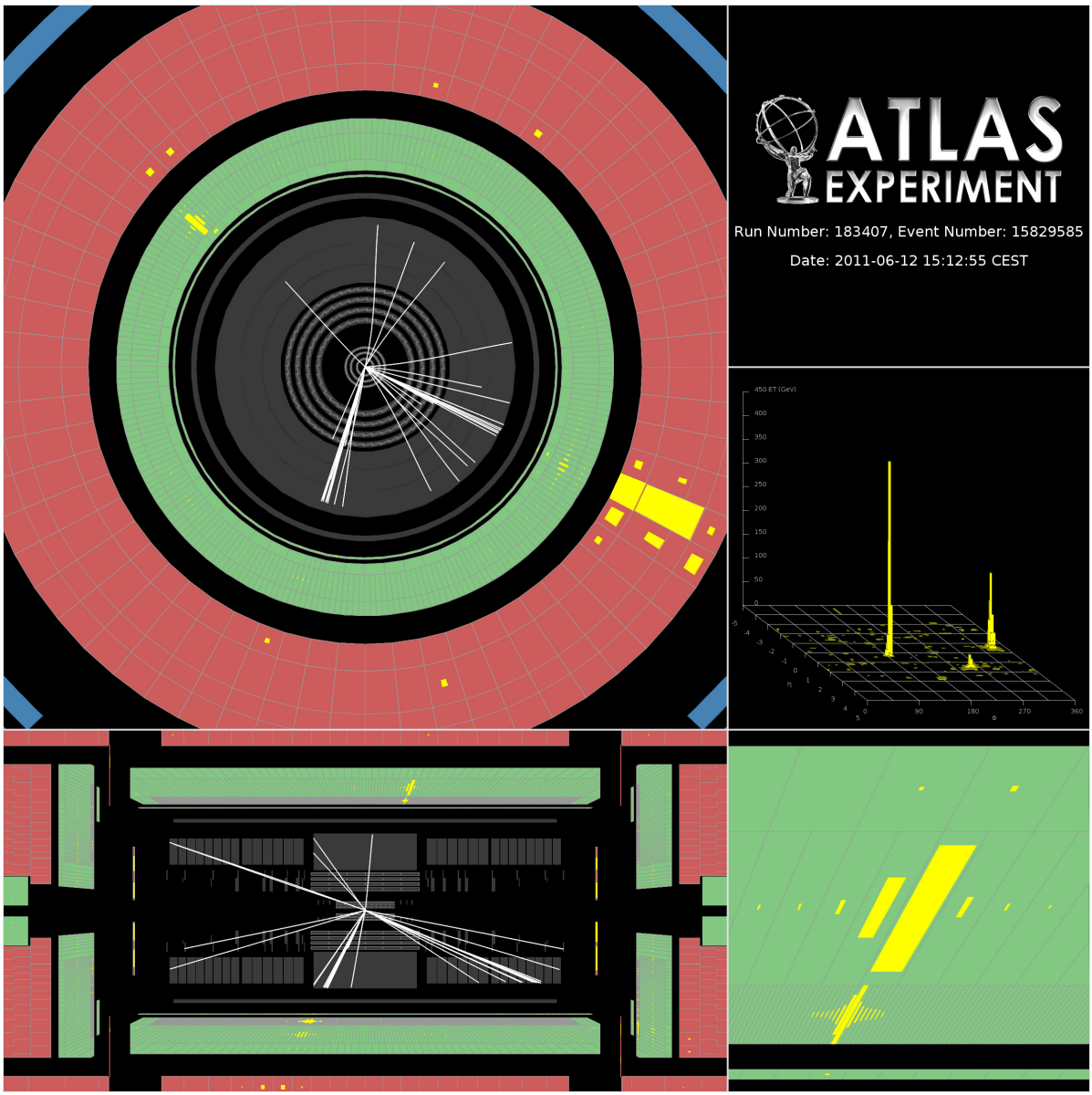

Figure C.21.: *EPS'11 Event display of event 15829585 in run 183407, showing the highest-p_{T} unconverted prompt photon candidate in the dataset using the SMDP GRL. The candidate has reconstructed p_{T} = 960 GeV and impacts at η = 0.35, ϕ = 2.44. It has $E_{\mathrm{T}}^{\mathrm{iso}} = -562$ MeV. The main balancing jet has reconstructed p_{T} = 918 GeVand impacts at η = -0.48, ϕ = -0.45; the event has reconstructed $E_{\mathrm{T}}^{\mathrm{miss}}$ = 22.5 GeV. The event display shows tracks with $p_{\mathrm{T}} > 2$ GeV.*

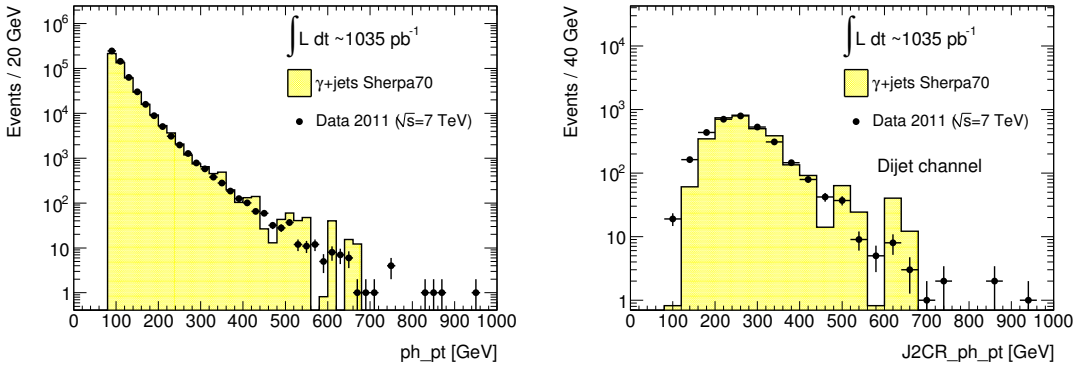

(a) (b)

Figure C.22.: *EPS'11 prompt photon p_{T} distribution in data and MC at different stages of the CR1a selection: (a) after the $\gamma + X$ selection and (b) after the CR1a selection for SR-A with a softer m_{eff} cut (500 GeV). The MC shown is the* SHERPA*-70 signal. Figure (a) is the equivalent of Figure C.20(a) but using the 0ℓ GRL.*

the SR-C/D selection (although the magnitude of the effect is misrepresented by the poor statistics of the SHERPA-70 sample). As additional evidence of this effect, Figure C.26 shows the CR1a $p_{\mathrm{T}}(\gamma_1)$ distribution for SR-C in SHERPA-70 and SHERPA-140 – clearly the lower p_{T} bins in SHERPA-140 have some events that are missing in SHERPA 70. In the end, the final consensus for the 0ℓ publication was to use SHERPA-140 for all CR1a m_{eff} plots with a scaling factor/correction applied at low m_{eff} and obtained from SHERPA-70. The result is shown in Figure C.27 and the scaling factors applied are listed in Table C.23. The number of events in these plots is shown in Table C.25 for both data and MC (columns 2 and 3) and the corresponding average $p_{\mathrm{T}}(\gamma_1)$ and range are quoted in Table 5.16.

SR	m_{eff} Range [GeV]					
	< 300	300 - 400	400 - 500	500 - 600	600 - 700	> 700
A	n/a	1.7747	1.1912	1.0	1.0	1.0
B	n/a	2.1003	1.3702	1.4215	1.0	1.0
C/D	n/a	1.6130	1.4007	1.0	1.0	1.0
E	n/a	n/a	n/a	n/a	n/a	1.0

Table C.23.: *EPS'11 Scaling factors applied on the* SHERPA*-140 CR1a m_{eff} distributions, obtained from the* SHERPA*-70 sample. The 'n/a' means the corresponding m_{eff} range had zero bin entries.*

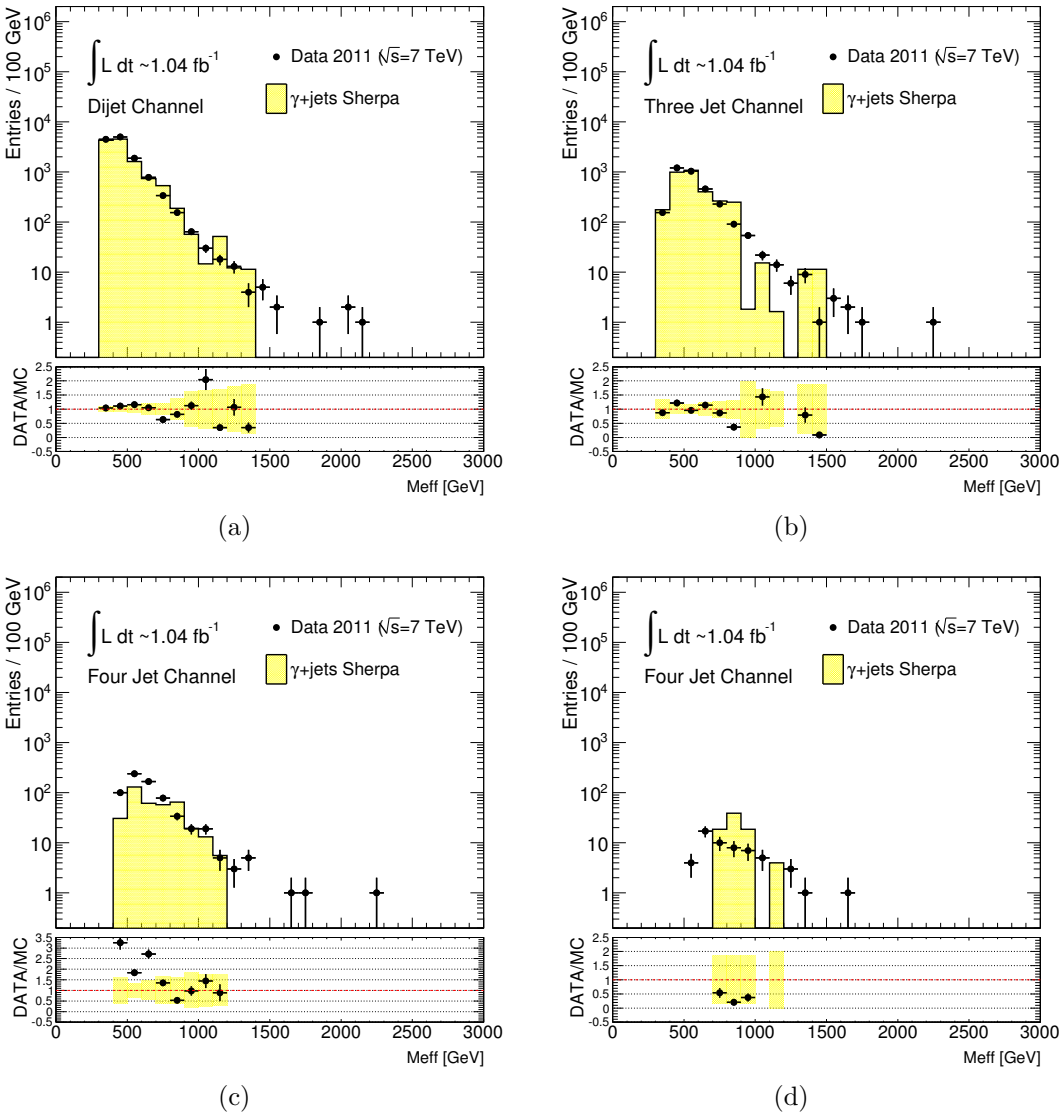

Figure C.23.: *EPS'11 CR1a m_{eff} distributions in data and MC for SR (a) A, (b) B, (c) C/D and (d) E. The MC shown is the* SHERPA-*70 with pileup reweighing applied. The yellow band in the data/MC ratio denotes the size of the combined JER/JES and MC statistical uncertainties.*

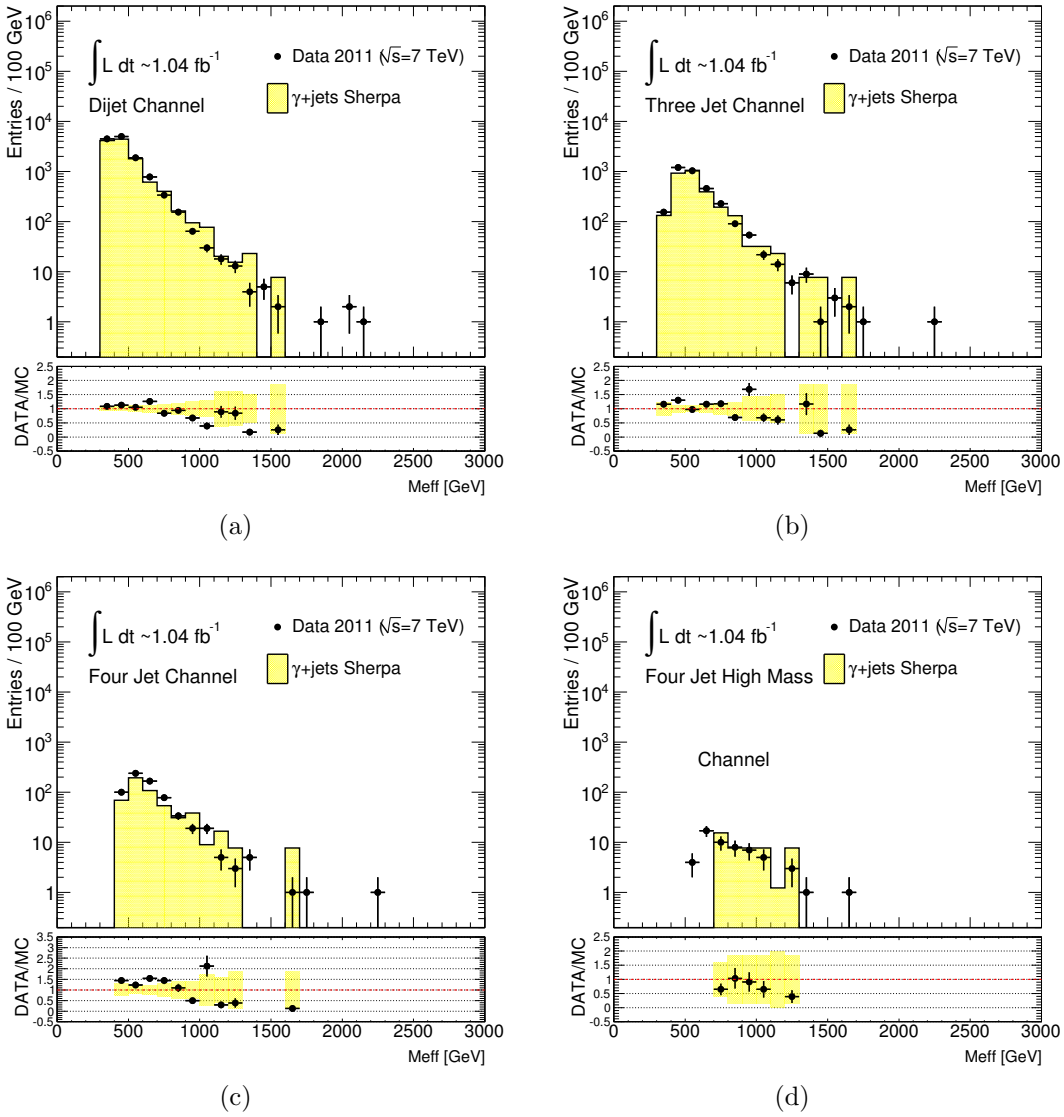

Figure C.24.: *EPS'11 CR1a m_{eff} distributions in data and MC for SR (a) A, (b) B, (c) C/D and (d) E. The MC shown is the* SHERPA*-70 without pileup reweighing applied. The yellow band in the data/MC ratio denotes the size of the combined JER/JES and MC statistical uncertainties.*

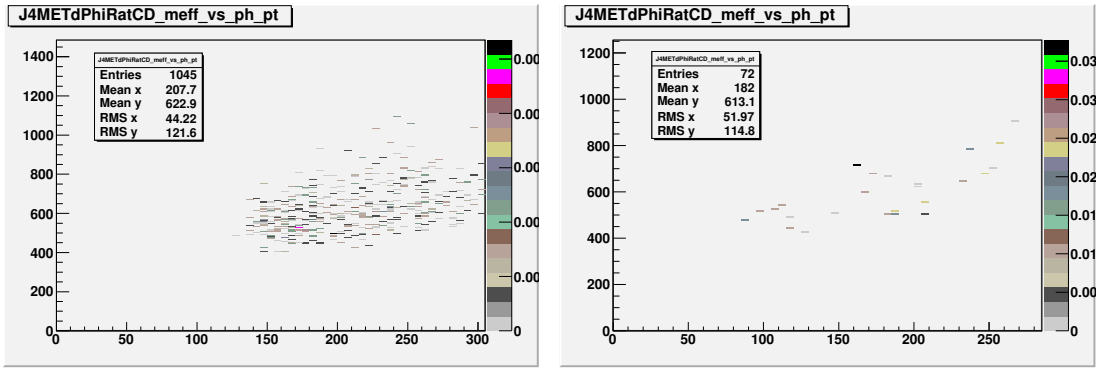

(a) (b)

Figure C.25.: *EPS'11 CR1a m_{eff} vs $p_{\text{T}}(\gamma_1)$ distributions in MC for SR-C/D prior to the m_{eff} cut. The MC shown is (a)* SHERPA*-70 without PR and (b)* SHERPA*-140 without PR. Note the statistics of the* SHERPA*-70 in are very limited (see Table C.21).*

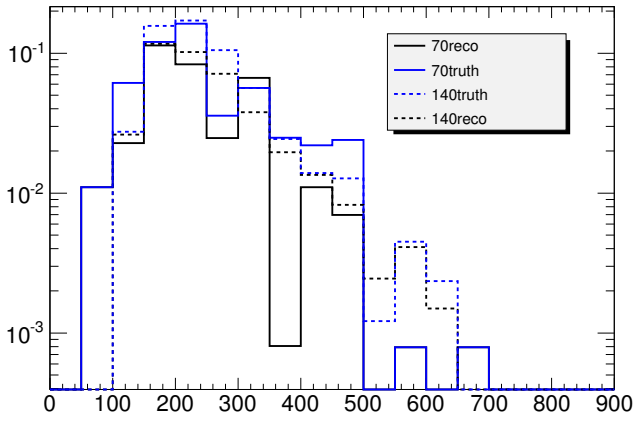

Figure C.26.: *EPS'11 true and reconstructed prompt photon p_{T} distribution in SR-C in* SHERPA*-70 and* SHERPA*-140. Both samples are normalised to the cross-section only.*

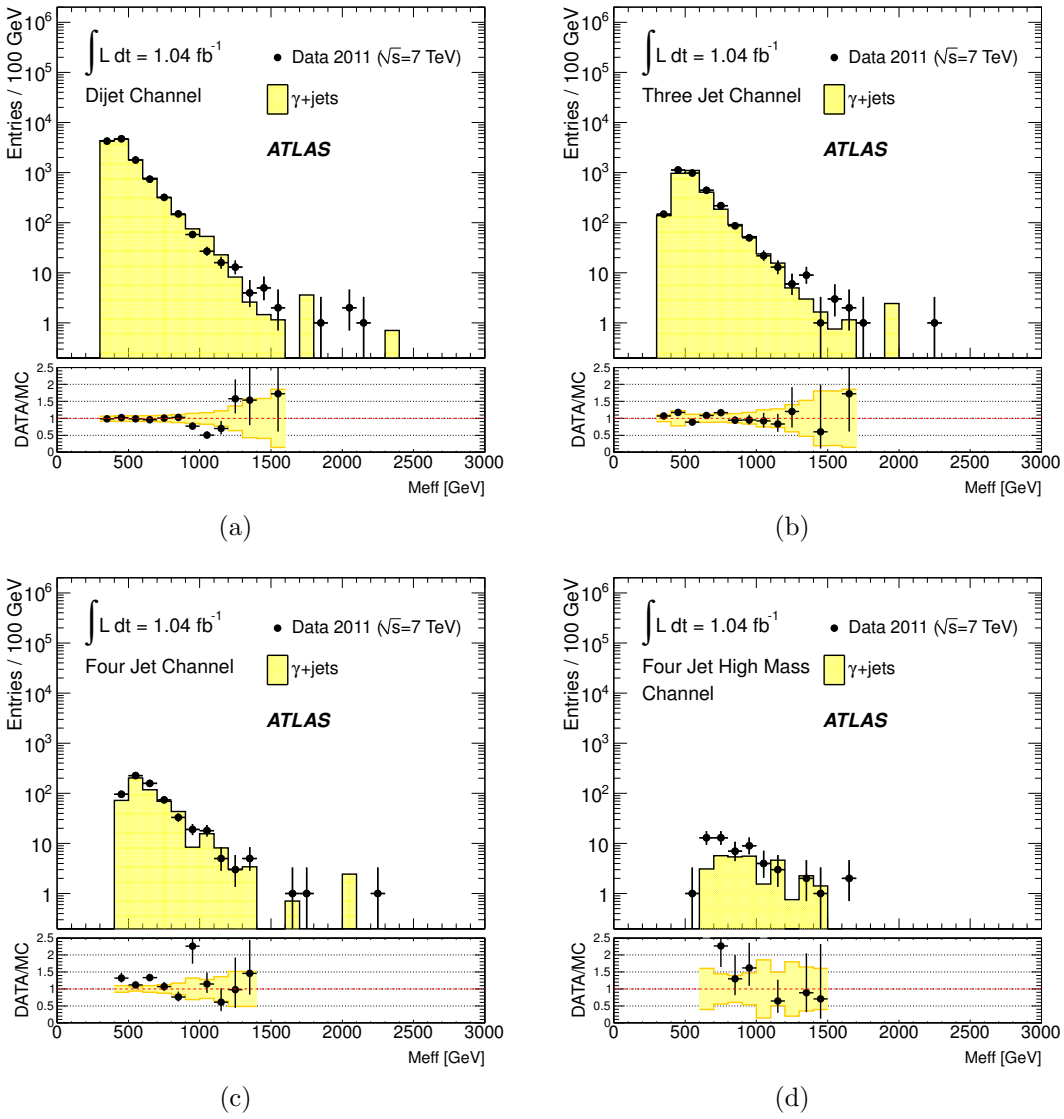

Figure C.27.: *EPS'11 final CR1a m_{eff} distributions in data and MC for SR (a) A, (b) B, (c) C/D and (d) E. The MC shown is the* SHERPA*-140 signal scaled by the* SHERPA*-70 signal at low m_{eff} by the factors in Table C.23. The yellow band in the data/MC ratio denotes the size of the combined JER/JES and MC statistical uncertainties and includes the error on the scaling factor.*

C.3.5. Transfer Function ($\mathbf{TF}_{Z_{\nu\nu}}$)

As mentioned, given the short time scale between PLHC'11 and EPS'11, it was not possible to further improve the calculation of the CR1a TFs with respect to what was done for PLHC'11. The TF central values and associated uncertainties obtained are shown in Table C.24 and a summary of the procedures to calculate each of the factors now follows.

Uncertainty	TF $Z_{\nu\nu}$ Est. from γ + jets				
	A	B	C	D	E
Central Value	0.376	0.382	0.339	0.39	0.34
CR bckgrnd. (f_{bkg})	5%	5%	5%	5%	5%
$A^{\gamma} \cdot \varepsilon^{\gamma}$	4.5%	5.0%	4.6%	6.5%	14.3%
$\eta_{Z/\gamma}$	2%	2%	2%	2%	2%
JES/JER	$^{+6.4\%}_{-8.2\%}$	$^{+8.5\%}_{-7.5\%}$	$^{+1.2\%}_{-2.9\%}$	$^{+4.3\%}_{-1.3\%}$	$^{+0\%}_{-0\%}$
Pileup ($A \times \varepsilon$)	0.3%	1.1%	0.3%	1.3%	1.9%
Trigger	$< 1\%$	$< 1\%$	$< 1\%$	$< 1\%$	$< 1\%$
Theory ($R_{Z_{\nu\nu}/\gamma}$)	15%	15%	15%	15%	15%

Table C.24.: *EPS'11 Central values and associated uncertainties of the CR1a TFs in the PLHC'11 analysis. The meaning of the terms are explained elsewhere in the text.*

- **Efficiency and Acceptance:** The same procedure as in PLHC'11 was followed.
- **Purity:** The same procedure as in PLHC'11 was followed (see Section C.2.5), except that the uncertainty assigned was increased from $\sim 3\%$ to $\sim 5\%$ to include the effects of electrons in W + jets decays misidentified as photons. The SMDP group had estimated this background to be around 1% for the photon-p_{T} range considered here [99].
- **Z/γ Ratio:** The same procedure as in PLHC'11 was followed.
- **γ vs $Z_{\nu\nu}$ Pseudorapidity:** The same procedure as in PLHC'11 was followed.

Other uncertainties that were assessed to be consistent with the rest of the 0ℓ analysis, also appearing in Table C.24, were:

- Pileup: The same procedure as in PLHC'11 was followed.

- JES/JER: The same procedure as in PLHC'11 was followed.
- Trigger: This was with respect to the nearly 100% efficient photon trigger used (`g80_loose`, see Appendix B).

TF stand-alone estimate of $Z_{\nu\nu}$+jets: After the application of the TF to the CR1a event counts, the $Z_{\nu\nu}$ + jets background estimate results obtained for this analysis are shown in Table C.25 compared to `SHERPA` and `ALPGEN`, where all the results are consistent within errors. Two examples to illustrate these results are shown in Figure C.28 for SR-A with softer m_{eff} cut and SR-C. Note that the $Z_{\nu\nu}$ + jets `ALPGEN` prediction includes a k-factors of 1.282 (see Table C.22) while the `SHERPA` equivalent does not, although this does not affect the data-driven CR1a estimate.

SR	CR1a		$Z_{\nu\nu}$ + jets Estimate		$Z_{\nu\nu}$ + jets Signal
	data	Sherpa	data	Sherpa	Sherpa/Alpgen
A	76	94	28.6 ± 3.3 (stat) ± 5.3 (syst)	38.9	16.6/36.3
B	59	54	22.6 ± 2.9 (stat) ± 4.2 (syst)	22.0	20.7/36.5
C	572	417	194.0 ± 8.1 (stat) ± 32.7 (syst)	158.5	181.2/235.7
D	35	34	13.7 ± 2.3 (stat) ± 2.4 (syst)	14.2	2.8/18.1
E	8	9	2.7 ± 1.0 (stat) ± 0.6 (syst)	3.5	4.0/4.0

Table C.25.: *EPS'11 numbers of CR1a events from data and MC for each SR (columns 2-3) and the stand-alone estimate of $Z_{\nu\nu}$ + jets background in the SRs from data and MC (columns 4-5), compared to $Z_{\nu\nu}$ + jets MC (column 6). The luminosity uncertainty was then ∼ 4.5% (Table 5.2).*

C.3.6. Context within the 0ℓ analysis

The 0ℓ SRs m_{eff} distributions (prior to the m_{eff} cut) are shown in Figure C.29 for data and the 'raw' MC background expectations (prior to the likelihood fitting procedure). Numerically, these distributions are represented by the SR event counts in Table C.26 (row 1) and the MC background expectations in Table C.27. The equivalent distributions for the CRs can be found in [101] and the respective event counts listed in Table C.26. The TFs central values used to translate the CR event counts into SR background estimates are presented in Table C.28. The version of Table C.28 actually fed into the likelihood fit is in the form of 'cross-TFs' (see Section 5.6.1), which takes into account

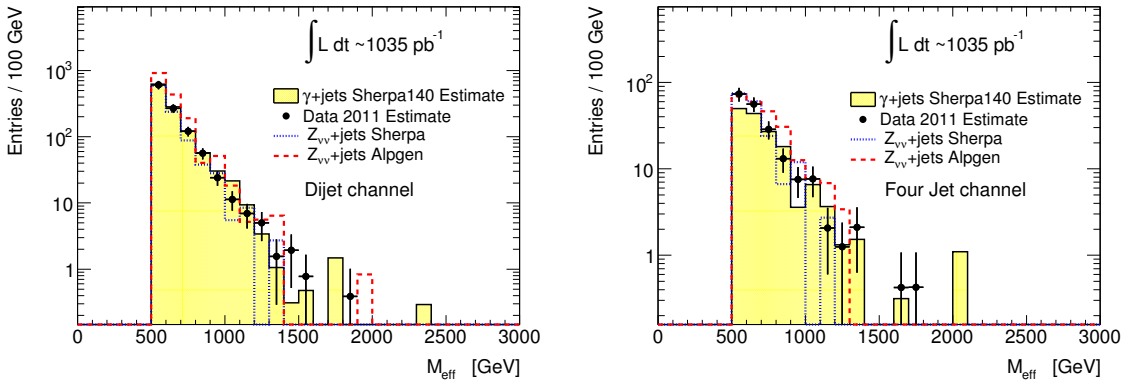

(a) (b)

Figure C.28.: *EPS'11 $Z_{\nu\nu}$ + jets m_{eff} distribution as estimated from CR1a, directly compared to $Z_{\nu\nu}$ + jets MC from* `SHERPA` *and* `ALPGEN` *for: (a) SR-A with softer m_{eff} cut (500 GeV) and (b) SR-C.*

correlations, mutual contamination, as well as the small correction to the CR1a TF from the additional background contribution arising from Z decays to misidentified charged leptons (see also Section 5.6.1). An example of this is shown in Table C.29 for SR-E and the rest can be found in [101].

In all these plots and numbers, the same features registered in PLHC'11 for CR1a were observed (large statistics, TF robustness and large contribution to the total SM expectation, see Section C.2.6), simply scaled by the EPS'11 increase in data luminosity when relevant.

Region	Channel				
	A	B	C	D	E
SR	58	59	1118	40	18
CR1a	76	59	572	35	8
CR1b	91	59	31	29	7
CR2	57	97	762	41	34
CR3	70	84	249	58	15
CR4	11	19	142	19	12

Table C.26.: *EPS'11 data event counts in the 0ℓ SRs and CRs. From [101].*

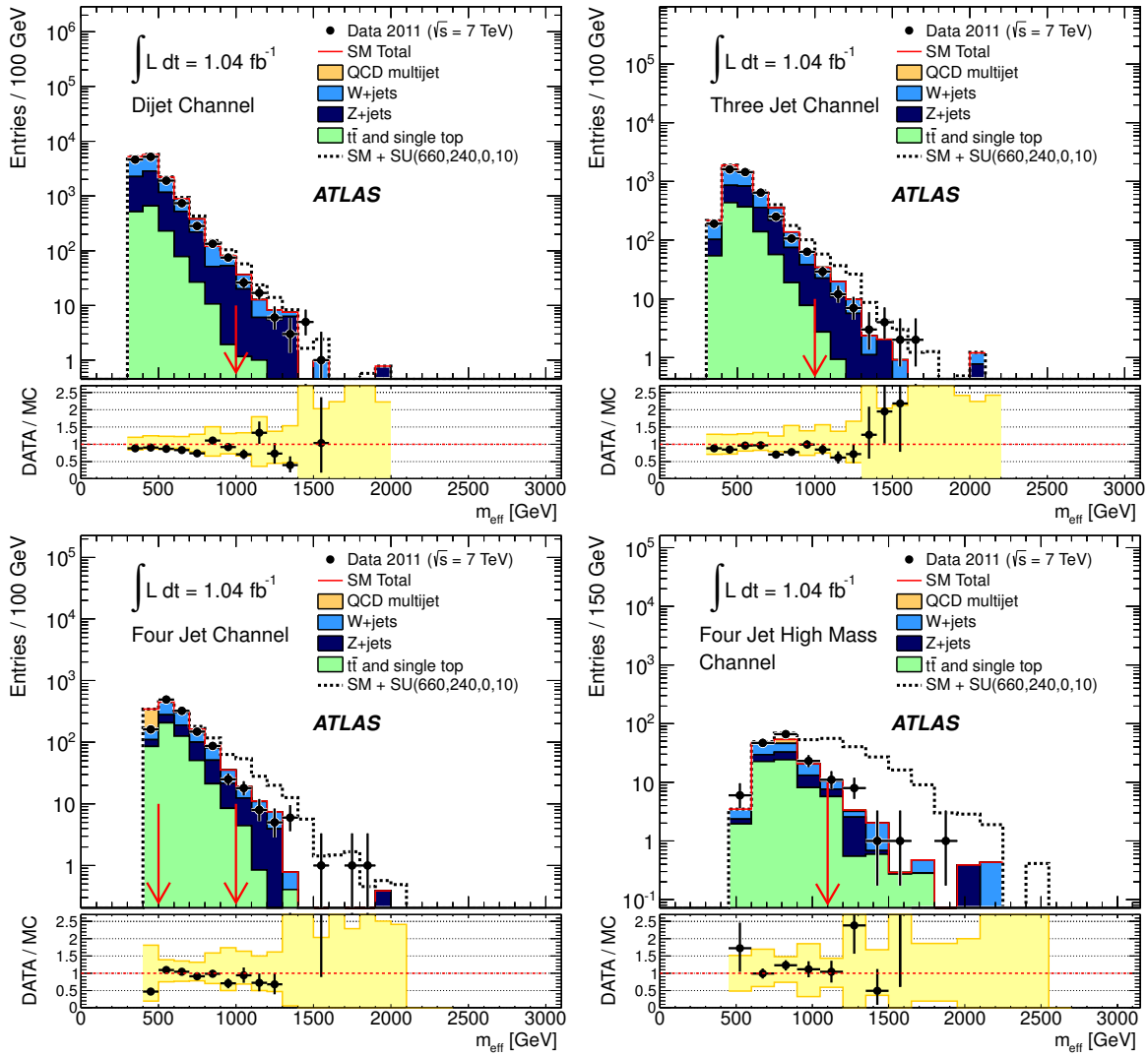

Figure C.29.: *EPS'11 m_{eff} distributions for SR A (top), B (top right), C/D (bottom left) and E (bottom right) prior to the m_{eff} cut in data, SM MC (the samples used are specified in [101]) and a mSUGRA reference point with $m_0 = 660$ GeV, $m_{1/2} = 240$ GeV, $A_0 = 0$, $\tan\beta = 10$ and $\mu > 0$ (this point is also indicated by the star on Figure C.30(b)). Red arrows mark the start of the SRs. Below each plot the ratio of the data to the SM expectation is provided. Black vertical bars show the statistical uncertainty from the data, while the yellow band shows the size of the systematic uncertainties from the MC simulation. From [54].*

SM process	Signal Region				
	A	B	C	D	E
Z+jets	36.6	37.6	245	18.8	4.28
W+jets	28.3	27	406	13.5	3.85
$t\bar{t}$ + Single Top	2.74	4.54	417	5.42	5.95
QCD jets	0.00177	0.00431	17.5	0.129	0.171
Total SM	67.6	69.1	1.09e+03	37.9	14.2

Table C.27.: *EPS'11 Summary of the MC expectations of each background component for all SRs. From [101].*

Control region / process	Signal Region				
	A	B	C	D	E
CR 1a / $Z(\to \nu\nu)$+jets	0.38	0.38	0.34	0.39	0.34
CR 1b / Z+jets	0.37	0.53	7.3	0.66	0.79
CR 2 / QCD jets	0.0072	0.012	0.052	0.022	0.063
CR 3 / W+jets	0.43	0.32	1.8	0.26	0.22
CR 4 / $t\bar{t}$ + single top	0.45	0.41	3.1	0.26	0.49

Table C.28.: *EPS'11 Summary of CRs TFs for all SRs. From [101].*

	Signal / Control Region					
	CR1a	CR1b	CR2	CR3	CR4	SR
Data	8	7	34	15	12	18
Targeted background	Z/γ+jets	Z/γ+jets	QCD multi-jet	W+jets	$t\bar{t}$ + single top	–
Transfer factor	0.374	0.812	0.063	0.196	0.372	–
Fitted Z/γ+jets	8.3	5.8	0.7	0.5	0.0	3.3
Fitted QCD multi-jet	–	–	29.8	0.8	0.6	2.1
Fitted W+jets	–	–	0.5	10.0	0.4	2.1
Fitted $t\bar{t}$ + single top	–	0.0	3.0	3.7	11.0	5.7
Fitted total background	8.3	5.9	34.0	15.0	12.0	13.1
Statistical uncertainty	±2.7	±1.2	±5.8	±3.9	±3.5	±1.9
Systematic uncertainty	±0.6	±1.7	±0.1	±0.1	±0.2	±2.5

Table C.29.: *EPS'11 Numerical inputs to and outputs from the likelihood fit to the CRs for SR-E. An entry '–' in rows 5–7 indicates that the process in that row is assumed not to contribute to the CR and hence excluded from the fit. All numerical entries give event counts, with the exception of the TFs row. From [102].*

As mentioned, one highlight in EPS'11 was the incorporation of both CR1a and CR1b into the likelihood fit to obtain a combined and better constrained $Z+$jets background estimate. With this, it was possible to incorporate SR-C that had been left out for PLHC'11. Similarly, SR-E could be incorporated, and so, this time it was possible to include all the SRs to obtain the best SUSY limits. Table C.30 shows the final results after the fitting procedure, with the $Z+$jets mean expectation constrained by the simultaneous measurements from CR1a and CR1b. The fitting was also performed using CR1a and CR1b individually and the results can be found in [101]. Overall, both approaches gave consistent estimates of the $Z+$jets background, although in SR-C the agreement was only at the limit of the fairly large uncertainties from CR1b.

In conclusion, the SM expectation results from the fit were once again compatible with data and so, in absence of a significant excess, limits were again set on the same SUSY models as in PLHC'11, shown in Figure C.30. However, this time all the SRs were used, taking the best expected limit at each point, obtained by comparing the observed number of SR events (s) with those from SM background plus SUSY signal ($s+b$) and using the CL_s prescription [24]. In the simplified model (Figure C.30(a)), gluino/squark masses below 700 GeV/875 GeV were excluded at the 95% C.L. for squark/gluino masses below 2 TeV, with the limit increasing to 1075 GeV for equal mass squarks and gluinos. In the mSUGRA/CMSSM models (Figure C.30(b)), equal mass squarks and gluinos were excluded below 950 GeV. The EPS'11 analysis again significantly improved the reach with respect to PLHC'11. Another EPS'11 highlight was the further interpretations performed, *e.g.* in Universal Extra Dimensions (UED) models, which are not shown here but can be found in [118].

Process	Signal Region				
	A	B	C	D	E
Z/γ+jets	$32.3 \pm 2.57 \pm 6.87$	$25.5 \pm 2.62 \pm 4.92$	$209 \pm 8.56 \pm 38.4$	$16.2 \pm 2.18 \pm 3.67$	$3.25 \pm 0.99 \pm 1.33$
W+jets	$26.4 \pm 3.97 \pm 6.69$	$22.6 \pm 3.45 \pm 5.56$	$349 \pm 30.3 \pm 122$	$13 \pm 2.18 \pm 4.65$	$2.08 \pm 0.837 \pm 1.07$
$t\bar{t}$+ Single Top	$3.5 \pm 1.56 \pm 1.59$	$5.9 \pm 2.01 \pm 2.24$	$425 \pm 39.4 \pm 84$	$3.99 \pm 1.27 \pm 2.02$	$5.67 \pm 1.75 \pm 1.94$
QCD jets	$0.22 \pm 0.059 \pm 0.24$	$0.92 \pm 0.12 \pm 0.46$	$34 \pm 1.5 \pm 29$	$0.73 \pm 0.14 \pm 0.5$	$2.1 \pm 0.37 \pm 0.82$
Total	$62.4 \pm 4.37 \pm 9.28$	$54.9 \pm 3.85 \pm 7.08$	$1.02e+03 \pm 40.9 \pm 144$	$33.9 \pm 2.9 \pm 6.23$	$13.1 \pm 1.91 \pm 2.49$
Data	58	59	1118	40	18

Table C.30.: *EPS'11 Fitted background components in each SR, compared with observation. The $Z+$ jets background is constrained by CR1a and CR1b, while the QCD, $W+$ jets and top backgrounds by CR2, CR3 and CR4, respectively. The values are quoted in the order "expectation +- stat uncert +- syst uncert". The $Z+$ jets and $W+$ jets are for most SRs the dominant backgrounds. From [102].*

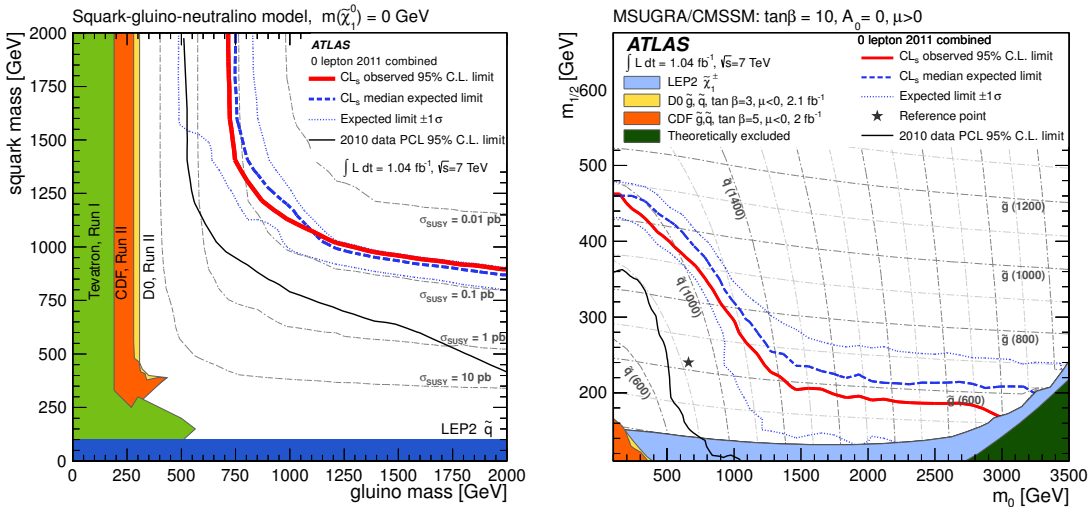

(a) (b)

Figure C.30.: *EPS'11 combined exclusion limits for simplified SUSY models with* $m(\tilde{\chi}_1^0) = 0$ *(left) and MSUGRA/CMSSM models with* $\tan\beta = 10$, $A_0 = 0$ *and* $\mu > 0$ *(right). The SR with the best expected limit at each point in the parameter plane is used. The dashed-blue line corresponds to the median expected 95% C.L. limit and the red line corresponds to the observed limit at 95% C.L. The dotted blue lines correspond to the* $\pm 1\sigma$ *variation in the expected limits. Also shown for comparison purposes in the figures are limits from the Tevatron and LEP (although some of these limits were produced under different models assumptions). The previous published ATLAS limits from this analysis (PLHC'11) are also shown. The mSUGRA reference point used in Figure C.29 is indicated by the star in the right-hand figure. From [101].*

Appendix D.

Supplementary cross-checks on the method

D.1. TF stand-alone estimate of $Z_{\mu\mu}$ + jets (Moriond'11)

At the time of the Moriond'11 analysis, the `ZfromGamma` method was still in early developments as it was the first time being implemented in ATLAS. As discussed in Appendix C.1, a few discrepancies were found between data and MC, which motivated the search for a cross-check of the validity of the method, that was independent of the 0ℓ analysis to eliminate potential biases coming from it. Referred here to as the '$Z_{\mu\mu}$ cross-check', a summary of it is now provided. Note, however, that this cross-check has not been repeated since Moriond'11, given the good agreement of the `ZfromGamma` results with the $Z_{\nu\nu}$ + jets MC prediction in all the subsequent analysis rounds.

The idea was to estimate the number of $Z_{\mu\mu}$ + jets events passing a simpler (and milder) selection than the 0ℓ SRs. This number was then to be compared to ATLAS Z + jets published results in [119]. For the event selection, the same inclusive photon sample $\gamma + X$ described in Appendix C.1.3 was defined. Then, the Moriond'11 0ℓ object definitions were applied in order to make a very simple inclusive jet channel selection: events were required to have at least one jet with $p_{\mathrm{T}} > 30$ GeV in order to match the selection in [119]. The resulting $p_{\mathrm{T}}(\gamma_1)$ distribution was then converted to a $p_{\mathrm{T}}(Z_{\mu\mu})$ distribution using the TF in Equation (5.6) but replacing the branching fraction $Br(Z \to \nu\nu)$ by $Br(Z \to \mu\mu)$. Table D.1 shows the results for this estimate for prompt photon candidates with $p_{\mathrm{T}}(\gamma_1) > 100$ GeV, where the estimate can be considered reliable

(given the high purity of the $\gamma + X$ sample in this regime). These results were compared to official ATLAS $Z_{\mu\mu}$ + jets results from [119] and found to be consistent within errors. The γ + jets `ALPGEN` sample used in Moriond'11 to obtain the stand-alone estimate of the $Z_{\nu\nu}$ + jets background could not be used for this cross-check due to the 2-jet filter it had at generator-level (see Appendix C.1.2). The corresponding $p_{\mathrm{T}}(Z_{\mu\mu})$ distribution representing the results from Table D.1 is shown in Figure D.1.

100 GeV $< p_{\mathrm{T}}(Z_{\mu\mu}) <$ 200 GeV		
$Z_{\mu\mu}$ + jets Estimate		$Z_{\mu\mu}$ + jets Data
data	Pythia	
$286 \pm 10(\mathrm{stat}) \pm 40(\mathrm{syst})$	$289 \pm 40(\mathrm{syst})$	$263 \pm 25(\mathrm{stat}) \pm 30(\mathrm{syst})$

Table D.1.: *Moriond'11 $Z_{\mu\mu}$ + jets estimate from γ + jets data and MC from* `PYTHIA` *compared to $Z_{\mu\mu}$ + jets data from [119].*

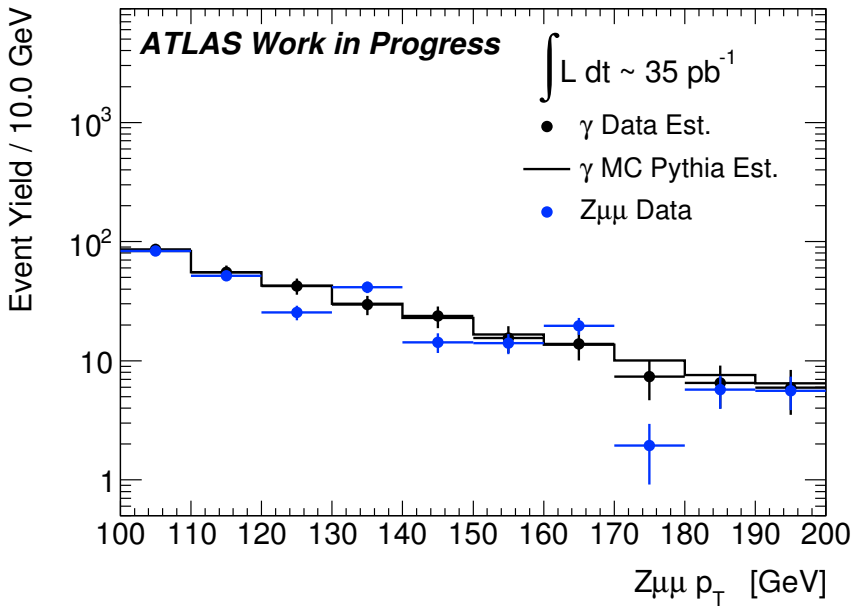

Figure D.1.: *Moriond'11 Estimated $p_{\mathrm{T}}(Z_{\mu\mu})$ distribution from the $\gamma+ \geq 1$ jet sample after correcting for acceptance, efficiency, purity and theoretical differences between the $Z_{\mu\mu}$ and γ bosons, compared to actual $Z_{\mu\mu}$ data from [119].*

D.2. γ + jets background in 0ℓ SRs

In all the 0ℓ analyses to date the contribution from γ+jets events to the total background estimate has been neglected so far. This has been widely accepted given that such events are not expected to pass the high $E_{\mathrm{T}}^{\mathrm{miss}}$ requirements characterising the SRs selections – the true $E_{\mathrm{T}}^{\mathrm{miss}}$ in γ + jets events is not expected to be large enough, as suggested by the typical values registered in even the highest $p_{\mathrm{T}}(\gamma_1)$ events *e.g.* see Table A.1. For this, CR1a proved useful once more to confirm such assumption.

The cross-check consisted in defining the CR1a sample as usual (see Section 5.4) except for the photon "neutrification" step (see Section 3.4). Such selection was applied to the `SHERPA` γ + jets samples listed in Section C.3.2 and indeed it was found that no events made it into the SRs, confirming that $\not{E}_{\mathrm{T}}^{\mathrm{fake}\prime} \sim 0$ in Equation (5.2) and so, a background contribution from γ + jets events in the 0ℓ SRs could be safely neglected.

However, there was one case for which this did not apply and an actual estimate for this background had to be calculated. This was for when the effects of the 'LAr hole' in the data could not be neglected, corresponding to the EPS'11 analysis round (see Appendix C.3). A summary of the method to calculate it and the results now follows.

D.2.1. The 'LAr hole' Example (EPS'11)

Due to the localised hardware problems in the LAr calorimeter described in Appendix C.3 and referred to in this note as the 'LAr hole', an estimate was made of the additional background arising from γ+jets events that passed the EPS'11 0ℓ SRs selections in the cases when the photon 'fell in the hole' and hence escaped detection and contributed to the event $E_{\mathrm{T}}^{\mathrm{miss}}$. This background is estimated using the γ + jets `SHERPA` samples listed in Table C.21.

The event selection is as follows: using truth information, if the truth prompt photon is outside the LAr hole region ($0 < \eta < 1.4$ and $-0.8 < \phi < -0.6$) the same event selection as for the SRs is applied *without* applying the additional "CR1a object definition" (see Section 5.4.1). However, for the cases when the truth photon does point into the LAr hole, the "CR1a object definition" *is* applied, which mimics the procedure used to estimate the $Z_{\nu\nu}$ + jets background using CR1a. Table D.2 shows the estimate central values and associated uncertainties for the γ + jets background due to the LAr hole. The systematic uncertainties are obtained by estimating the same background in a slightly

larger LAr hole region (± 0.1), identical to that which is used to define the LAr hole jet veto in the main SR selection (see [101]). The MC statistical uncertainty is computed from the unnormalised number of events in the SRs. The results show that this background is $\lesssim 8\%$ in the SRs considered, and decreases in the higher jet multiplicity channels. Moreover, the results are a 'conservative' estimate since by using the true prompt photon p_{T}, an inefficiency of 100% in the hole is assumed. This background, although small, was nevertheless included in the final 0ℓ likelihood fit.

SR	Events (unnormalised)	γ+jets background Estimate	Uncertainties		
			(sys)	(stat)	(tot)
A	5	3.8	39%	45%	59%
B	2	1.6	0%	71%	71%
C	13	7.2	29%	28%	40%
D	1	1.6	0%	100%	100%
E	0	0	0%	100%	100%

Table D.2.: *EPS'11 Estimate of the γ+jets background due to the LAr hole and associated uncertainties using γ + jets* `SHERPA` *MC.*

Appendix E.

List of Acronyms

ALICE A Large Ion Collider Experiment

AMSB Anomaly Mediated Supersymmetry Breaking

ATLAS A Toroidal LHC Apparatus

BCID Bunch Crossing Identification

B-L Baryon-Lepton

BSM Beyond-Standard-Model

B.R. / *Br* Branching Ratio

CDF Collider Detector at Fermilab

CERN European Organisation for Nuclear Research

CMS Compact Muon Solenoid

CMSSM Constrain Minimal Supersymmetric Standard Model

CP Charge-Parity

CR(s) Control Region(s)

CR1a Control Region 1a (the 0ℓ CR based on $\gamma + \text{jets}$)

CR1b Control Region 1b (the 0ℓ CR based on $Z_{\ell\ell} + \text{jets}$)

CR2 Control Region 2 (the 0ℓ CR based on QCD)

CR3 Control Region 3 (the 0ℓ CR based on $W_{\ell\nu} + \text{jets}$)

CR4 Control Region 4 (the 0ℓ CR based on $t\bar{t}$ and single top quark)

CS ATLAS Central Solenoid

CSC ATLAS Cathode Strip Chambers

EC ATLAS End Cap

ECAL ATLAS Electromagnetic Calorimeter

EM Electromagnetic

EMJES ATLAS numerical inversion jet calibration scheme

EPS'11 The analysis presented at the EPS conference in 2011

EW Electroweak

FCNC Flavour Changing Neutral Currents

FSR Final State Radiation

FWD ATLAS Forward

GMSB Gauge-mediated Supersymmetry Breaking

GRL Good Runs List

GUT Grand Unified Theories

HCAL ATLAS Hadronic Calorimeter

ID ATLAS Inner Detector / Identification

IP Interaction Point

ISR Initial State Radiation

JER Jet Energy Resolution

JES Jet Energy Scale

LAr Liquid Argon / ATLAS Liquid Argon Calorimeter

LHC Large Hadron Collider

LHCb Large Hadron Collider beauty Experiment

LO Leading Order

LSP Lightest Supersymmetric Particle

MC Monte Carlo

MDT ATLAS Monitored Drift Tubes

MET Missing Transverse Energy

Moriond'11 The analysis presented at the Moriond conference in 2011

Moriond'12 The analysis presented at the Moriond conference in 2012

MS ATLAS Muon Spectrometer

MSSM Minimal Supersymmetric Standard Model

mSUGRA Miniman Supergravity

NLO Next to Leading Order

NNLO Next to Next to Leading Order

NLSP Next to Lightest Supersymmetry Particle

OQ Object Quality

PDF(s) Parton Distribution Function(s)

pdf Poisson Probability Density Function

PLHC'11 The analysis presented at the PLHC conference in 2011

pQCD Perturbative QCD

PR Pileup Reweighing

PS Proton Synchroton

PSB Proton Synchroton Booster

PU Pileup

PV Primary Vertex

QED Quantum Electrodynamics

QCD Quantum Chromodynamics

RF Radio Frequency

RGE Renormalisation Group Equations

RPC R-parity Conservation / ATLAS Resistive Plate Chambers

RPV R-parity Violation

SCT ATLAS Silicon Tracker

SM Standard Model

SMDP Standard Model Direct Photon

SPS Super Proton Synchroton

SR(s) Signal Region(s)

SUGRA Supergravity

SUSY Supersymmetry

TF(s) Transfer Function(s) / Transfer Factor(s)

TGC ATLAS Thin Gap Chambers

TRT ATLAS Transition Radiation Tracker

UE Underlying Event

WIMP Weakly Interacting Massive Particle

0ℓ Zero Lepton (analysis)

Bibliography

[1] F. Halzen and A. Martin, *Quarks and Leptons: An introductory course in modern particle physics* (John Wiley and Sons, New York, USA, 1984).

[2] M. E. Peskin and D. V. Schroeder, *An Introduction to Quantum Field Theory (Frontiers in Physics)* (Westview Press, 1995).

[3] R. K. Ellis, W. J. Stirling, and B. R. Webber, *QCD and collider physics* (Cambridge Univ. Press, 2003).

[4] P. Skands, (2011), 1104.2863.

[5] Particle Data Group, K. Nakamura *et al.*, J. Phys. **G37**, 075021 (2010).

[6] S. P. Martin, (1997), hep-ph/9709356.

[7] A. Djouadi and S. Ferrag, Phys.Lett. **B586**, 345 (2004), hep-ph/0310209.

[8] M. Botje *et al.*, (2011), 1101.0538.

[9] T. Sjostrand and P. Z. Skands, JHEP **0403**, 053 (2004), hep-ph/0402078.

[10] D. Hanneke, S. Fogwell, and G. Gabrielse, Phys. Rev. Lett. **100**, 120801 (2008), 0801.1134.

[11] The ALEPH, DELPHI, L3, OPAL, SLD Collaborations, the LEP Electroweak Working Group, the SLD Electroweak and Heavy Flavour Groups, Phys. Rept. **427**, 257 (2006), hep-ex/0509008.

[12] MuLan Collaboration, D. Webber *et al.*, Phys.Rev.Lett. **106**, 041803 (2011), 1010.0991.

[13] The ATLAS Collaboration, Atlas public results, `https://twiki.cern.ch/twiki/bin/view/AtlasPublic`, 2011.

[14] C. A. Baker *et al.*, Phys. Rev. Lett. **97**, 131801 (2006), hep-ex/0602020.

[15] H. Georgi and S. L. Glashow, Phys. Rev. Lett. **32**, 438 (1974).

[16] Super-Kamiokande, K. Kobayashi *et al.*, Phys. Rev. **D72**, 052007 (2005), hep-ex/0502026.

[17] ATLAS Collaboration, G. Aad *et al.*, Phys.Lett. **B710**, 49 (2012), 1202.1408.

[18] WMAP Collaboration, J. Dunkley *et al.*, Astrophys.J.Suppl. **180**, 306 (2009), 0803.0586.

[19] D. Chung *et al.*, Phys.Rept. **407**, 1 (2005), hep-ph/0312378.

[20] S. Coleman and J. Mandula, Phys. Rev. **159**, 1251 (1967).

[21] R. Haag, J. T. Łopuszański, and M. Sohnius, Nuclear Physics B **88**, 257 (1975).

[22] L. Randall and R. Sundrum, Nucl.Phys. **B557**, 79 (1999), hep-th/9810155.

[23] Prospino2 website, `http://www.thphys.uni-heidelberg.de/~plehn/index.php?show=prospino&visible=tools`, 2012.

[24] A. L. Read, Journal of Physics G: Nuclear and Particle Physics **28**, 2693 (2002).

[25] The LHC Study Group, T. S. Pettersson and P. Lefèvre, editors, *The Large Hadron Collider: conceptual design (LHC White Book)*.CERN-AC-95-05 LHC (CERN, 1995).

[26] O. S. Bruning *et al.*, *LHC Design Report* (CERN, Geneva, 2004).

[27] LHC performance and statistics, `http://lhc-statistics.web.cern.ch/LHC-Statistics/#`, 2011.

[28] The ATLAS Collaboration, *ATLAS detector and physics performance*, Technical Design Report Vol. 1 (CERN, Geneva, 1999).

[29] The ATLAS Collaboration, *ATLAS detector and physics performance*, Technical Design Report Vol. 2 (CERN, Geneva, 1999).

[30] L. Evans and P. Bryant, Journal of Instrumentation **3**, S08001 (2008).

[31] K. Genser and P. Lebrun, Tevatron Report No. Beams–doc–1075, 2004 (unpublished).

[32] J. Slaughter *et al.*, Tevatron run ii luminosity, emittance and collision point size, in *Proceedings of the Particle Accelerator Conference*, pp. 1763 – 1765 vol.3, 2003.

[33] ATLAS Collaboration, G. Aad *et al.*, Eur.Phys.J. **C71**, 1630 (2011), 1101.2185.

[34] LPC, LHC luminosity plots for the 2011 proton run, `http://lpc.web.cern.ch/lpc/lumiplots.htm`, 2011.

[35] U. Egede, Thesis, `http://www.hep.lu.se/atlas/thesis/egede/thesis-node39.html#fig:Coordinate`, 2011.

[36] The ATLAS Collaboration, G. Aad *et al.*, JINST **3**, S08003 (2008).

[37] ATLAS detector photos, `http://atlas.ch/photos/`, 2011.

[38] ATLAS Collaboration, G. Aad *et al.*, Eur.Phys.J. **C70**, 723 (2010), 0912.2642.

[39] A. Collaboration, (2010), 1005.5254v1.

[40] CERN Report No. ATLAS-CONF-2010-006, 2010 (unpublished).

[41] ATLAS Collaboration, A. Airapetian *et al.*, (1996).

[42] The ATLAS Collaboration, *ATLAS Muon Spectrometer.* Technical Design Report (CERN, 1997).

[43] CERN Report No. ATLAS-CONF-2012-048, 2012 (unpublished).

[44] T. Perez Cavalcanti, CERN Report No. ATL-DAQ-PROC-2011-016, 2011 (unpublished).

[45] The ATLAS Collaboration, (2011), 1101.2185v1.

[46] A. Collaboration *et al.*, (2009), 0901.0512v4.

[47] ATLAS Collaboration, G. Aad *et al.*, Eur.Phys.J. **C72**, 1909 (2012), 1110.3174.

[48] Atlas Collaboration, G. Aad *et al.*, Phys.Rev. **D83**, 052005 (2011), 1012.4389, Long author list - awaiting processing.

[49] ATLAS Collaboration, G. Aad *et al.*, Phys.Lett. **B706**, 150 (2011), 1108.0253, Long author list - awaiting processing.

[50] M. Stockton, Event display photon / pi0, `https://atlas.web.cern.ch/Atlas/GROUPS/PHYSICS/EGAMMA/PublicPlots/20100721/display-photons/index.html`, 2010.

[51] CERN Report No. ATLAS-CONF-2010-036, 2010 (unpublished).

[52] M. Cacciari, G. P. Salam, and G. Soyez, JHEP **0804**, 063 (2008), 0802.1189.

[53] ATLAS Collaboration, G. Aad *et al.*, Eur.Phys.J. **C72**, 1844 (2012), 1108.5602.

[54] ATLAS Collaboration, G. Aad *et al.*, (2011), 1109.6572.

[55] ATLAS Collaboration, (2011), 1112.3832.

[56] S. Ask, M. Parker, T. Sandoval, M. Shea, and W. Stirling, JHEP **1110**, 058 (2011), 1107.2803.

[57] ATLAS Collaboration, G. Aad *et al.*, Phys.Lett. **B708**, 221 (2012), 1108.4908.

[58] Atlas Collaboration, G. Aad *et al.*, Phys.Lett. **B701**, 186 (2011), 1102.5290.

[59] ATLAS Collaboration, G. Aad *et al.*, Phys.Rev. **D85**, 032009 (2012), 1111.2690.

[60] Particle Data Group, K. Nakamura *et al.*, J. Phys. **G37**, 075021 (2010).

[61] G. Aad and et. al., Physics Letters B **706**, 150 (2011).

[62] C. Collaboration, (2009).

[63] A. Collaboration, CERN Report No. ATL-COM-PHYS-2010-1046, 2010 (unpublished), Support note of the jets+MET SUSY paper.

[64] Z. Bern *et al.*, Phys.Rev. **D84**, 114002 (2011), 1106.1423.

[65] CERN Report No. ATLAS-CONF-2011-086, 2011 (unpublished).

[66] M. Parker and D. Tovey, CERN Report No. ATLAS-COM-CONF-2012-037, 2012 (unpublished), Based on draft version 0.65 of the INT note.

[67] CDF Collaboration, T. Aaltonen *et al.*, Phys.Rev.Lett. **103**, 091803 (2009), 0905.4714.

[68] T. Sjostrand, S. Mrenna, and P. Z. Skands, Comput.Phys.Commun. **178**, 852 (2008), 0710.3820.

[69] F. A. Berends, H. Kuijf, B. Tausk, and W. T. Giele, Nucl. Phys. **B357**, 32 (1991).

[70] T. Sjostrand, S. Mrenna, and P. Z. Skands, JHEP **0605**, 026 (2006), hep-ph/0603175.

[71] M. Bahr *et al.*, Eur.Phys.J. **C58**, 639 (2008), 0803.0883, 143 pages, program and additional information available from http://projects.hepforge.org/herwig.

[72] T. Gleisberg *et al.*, JHEP **0902**, 007 (2009), 0811.4622.

[73] A. Martin, W. Stirling, R. Thorne, and G. Watt, Eur.Phys.J. **C63**, 189 (2009), 0901.0002.

[74] CTEQ Collaboration, H. Lai *et al.*, Eur.Phys.J. **C12**, 375 (2000), hep-ph/9903282.

[75] M. Gluck, E. Reya, and A. Vogt, Eur.Phys.J. **C5**, 461 (1998), hep-ph/9806404.

[76] CERN Report No. ATLAS-CONF-2011-058, 2011 (unpublished).

[77] A. Buckley *et al.*, Phys.Rept. **504**, 145 (2011), 1101.2599.

[78] M. Cacciari and G. P. Salam, Phys.Lett. **B641**, 57 (2006), hep-ph/0512210.

[79] Cacciari, m. and salam, g.p. and soyez, g., `http://fastjet.fr`.

[80] E. Maina, S. Moretti, and D. A. Ross, Phys.Lett. **B593**, 143 (2004), hep-ph/0403050.

[81] J. H. Kuhn, A. Kulesza, S. Pozzorini, and M. Schulze, JHEP **0603**, 059 (2006), hep-ph/0508253.

[82] U. Baur, Phys.Rev. **D75**, 013005 (2007), hep-ph/0611241.

[83] G. Bell, J. Kuhn, and J. Rittinger, Eur.Phys.J. **C70**, 659 (2010), 1004.4117.

[84] Zfromgamma twiki, `https://twiki.cern.ch/twiki/bin/view/AtlasProtected/ZfromGamma`.

[85] Zfromgamma twiki, `https://twiki.cern.ch/twiki/bin/view/AtlasProtected/ZfromGamma2010`, 2010.

[86] Rjets framework twiki, `https://twiki.cern.ch/twiki/bin/view/AtlasProtected/WZJratioAnalysis`.

[87] Zfromgamma twiki, `https://twiki.cern.ch/twiki/bin/view/AtlasProtected/ZfromGamma2011`, 2011.

[88] Zfromgamma twiki, `https://twiki.cern.ch/twiki/bin/view/AtlasProtected/ZfromGamma2012`, 2012.

[89] `https://twiki.cern.ch/twiki/bin/view/AtlasProtected/SUSYD3PDMaker`.

[90] C. ATLAS, CERN Report No. ATL-PHYS-PUB-2010-014, 2010 (unpublished).

[91] CERN Report No. ATLAS-CONF-2010-031, 2010 (unpublished).

[92] M. Kataoka *et al.*, CERN Report No. ATL-COM-PHYS-2011-867, 2011 (unpublished).

[93] ATLAS SM Direct Photon Working Group Recommendations, `https://twiki.cern.ch/twiki/bin/viewauth/AtlasProtected/SMDirectPhoton2011Common`.

[94] ATLAS SM Direct Photon Working Group Recommendations, `https://twiki.cern.ch/twiki/bin/viewauth/AtlasProtected/LArCleaningAndObjectQuality`.

[95] ATLAS SM Direct Photon Working Group Recommendations, `https://twiki.cern.ch/twiki/bin/viewauth/AtlasProtected/PhotonFudgeFactors`.

[96] ATLAS SM Direct Photon Working Group Recommendations, `https://twiki.cern.ch/twiki/bin/viewauth/AtlasProtected/CaloIsolationCorrections`.

[97] ATLAS Egamma Group Energy Rescaler Tool, `https://twiki.cern.ch/twiki/bin/view/AtlasProtected/EnergyRescaler`.

[98] ATLAS Collaboration, G. Aad *et al.*, (2012), 1203.3161.

[99] R. Ishmukhametov, R. Daya, and R. Stroynowski, CERN Report No. ATL-COM-PHYS-2011-721, 2011 (unpublished), Supporting note of latest 2010 SM inclusive photon cross section measurement, approved by ATLAS and submitted for publication.

[100] S. Asai *et al.*, CERN Report No. ATL-COM-PHYS-2011-1736, 2011 (unpublished), Supporting documentation for SUSY 0-lepton Moriond 2012 paper.

[101] S. Asai *et al.*, CERN Report No. ATL-PHYS-INT-2011-085, 2011 (unpublished).

[102] S. Asai *et al.*, CERN Report No. ATL-PHYS-INT-2011-055, 2011 (unpublished).

[103] CERN Report No. ATLAS-CONF-2011-032, 2011 (unpublished).

[104] R. Bruneliere, M. Baak, J. Lundberg, M. C. Rammensee, and T. J. Khoo, CERN Report No. ATL-PHYS-INT-2011-032, 2011 (unpublished).

[105] Search for new physics in the multijets + missing transverse energy final state in 7 tev proton-proton collisions, 2012.

[106] Search for supersymmetry in hadronic final states using mt2 with the cms detector

at 7 tev, 2012.

[107] Search for supersymmetry with the razor variables at cms, 2012.

[108] CMS Supersymmetry Physics Results, `https://twiki.cern.ch/twiki/bin/view/CMSPublic/PhysicsResultsSUS`.

[109] CERN Report No. ATLAS-CONF-2011-156, 2011 (unpublished).

[110] ATLAS Collaboration, G. Aad *et al.*, (2011), 1111.4116.

[111] ATLAS Collaboration, (2011), 1112.3832.

[112] CERN Report No. ATLAS-CONF-2011-130, 2011 (unpublished).

[113] ATLAS Collaboration, G. Aad *et al.*, Phys.Rev. **D85**, 012006 (2012), 1109.6606, 18 pages plus author list (30 pages total), 9 figures, 4 tables, final version to appear in Physical Review D.

[114] ATLAS SM Direct Photon Working Group Recommendations for 2010 analysis, `https://twiki.cern.ch/twiki/bin/viewauth/AtlasProtected/PhotonCrossSection2010`.

[115] CERN Report No. ATLAS-CONF-2010-077, 2010 (unpublished).

[116] H. Abreu *et al.*, CERN Report No. ATL-PHYS-INT-2011-037, 2011 (unpublished).

[117] ATLAS SM Direct Photon Working Group Recommendations, `https://twiki.cern.ch/twiki/bin/viewauth/AtlasProtected/PhotonCrossSection2011`.

[118] T.-J. Khoo, M. Rammensee, Z. Rurikova, N. Kanaya, and P. De Jong, CERN Report No. ATLAS-COM-CONF-2011-183, 2011 (unpublished).

[119] H. Bauchemin *et al.*, CERN Report No. ATL-COM-PHYS-2011-141, 2011 (unpublished).

List of Figures

List of Tables